The power of power corrections

Marinissen, C.B.

Publication date
2025
Document Version
Final published version

Citation for published version (APA):
Marinissen, C. B. (2025). *The power of power corrections*. [Thesis, fully internal, Universiteit van Amsterdam].

The Power of Power Corrections

Coenraad Marinissen

The Power of Power Corrections

ACADEMISCH PROEFSCHRIFT

ter verkrijging van de graad van doctor
aan de Universiteit van Amsterdam
op gezag van de Rector Magnificus
prof. dr. ir. P.P.C.C. Verbeek
ten overstaan van een door het College voor Promoties ingestelde commissie,
in het openbaar te verdedigen in de Aula der Universiteit
op woensdag 7 mei 2025, te 14.00 uur

door
Coenraad Benjamin Marinissen
geboren te Vlissingen

Promotiecommissie

Promotor:	prof.dr. E.L.M.P. Laenen	Universiteit van Amsterdam
Copromotor:	dr. M.L. Vonk	Universiteit van Amsterdam
Overige leden:	dr C.N. Cheng	Universiteit van Amsterdam
	dr W.J. Waalewijn	Universiteit van Amsterdam
	dr. J. de Vries	Universiteit van Amsterdam
	prof. dr. T.W. Grimm	Utrecht University
	dr. L. Vernazza	INFN Torino

Faculteit der Natuurwetenschappen, Wiskunde en Informatica

ISBN: 978-94-93431-34-8

Cover by Kalle

Printed by www.proefschriftspecialist.nl

Het promotieonderzoek beschreven in dit proefschrift werd verricht aan de Universiteit van Amsterdam, alsmede aan het Nationaal instituut voor subatomaire fysica (Nikhef).

UNIVERSITEIT VAN AMSTERDAM

Nikhef

List of publications

This thesis is based on:

[1] E. Laenen, C. Marinissen and M. Vonk, *Resurgence analysis of the Adler function at* $\mathcal{O}(1/N_f^2)$, *JHEP* **09** (2023) 103 [`2302.13715`].

[2] J. ter Hoeve, E. Laenen, C. Marinissen, L. Vernazza and G. Wang, *Region analysis of QED massive fermion form factor*, *JHEP* **02** (2024) 024 [`2311.16215`].

[3] C. Marinissen, A. van Spaendonck and M. Vonk, *Resurgence of large order relations*, *Adv. Theor. Math. Phys.* **28** (2024) 2657 [`2312.12497`].

[4] R.v. Bijleveld, E. Laenen, C. Marinissen, L. Vernazza and G. Wang. To appear.

Other work:

[1] C.B. Marinissen, R. Rahn and W.J. Waalewijn, *..., 83106786, 114382724, 1509048322, 2343463290, 27410087742, ... efficient Hilbert series for effective theories*, *Phys. Lett. B* **808** (2020) 135632 [`2004.09521`].

[2] S. Calò, C. Marinissen and R. Rahn, *Discrete symmetries and efficient counting of operators*, *JHEP* **05** (2023) 215 [`2212.04395`].

[3] L. Di Luzio, S. Hoof, C. Marinissen and V. Plakkot, *Catalogues of Cosmologically Self-Consistent Hadronic QCD Axion Models*, `2412.17896`.

Contents

Chapter 1.

Introduction

Fundamental physics focuses on understanding the fundamental laws that govern the universe at the deepest level. In particle physics this has resulted in a theoretical framework that describes the elementary particles – the smallest building blocks of matter forming everything from atoms and molecules to stars and galaxies. This so-called Standard Model of particle physics (SM) is more than just a catalog of particles, it is a quantum field theory (QFT) that describes how the fundamental particles interact. However, calculating the processes directly is highly complex, making theoretical predictions not an easy task.

Physicists and mathematicians have worked hard to overcome this challenge. The basic idea is to start with a simpler version of the system, where an exact solution is known, and then "perturb" this solution by adding small corrections that approximate the effect of more complex interactions. This approach can be implemented in a framework called *perturbation theory*, where one expands the solution F of the hard problem in terms of a small parameter α, often the coupling constant which represents the strength of the interaction. To be more precise, one can write

$$F(\alpha) = \sum_{n=0}^{\infty} f_n \, \alpha^n \, , \tag{1.1}$$

where it is known how to calculate the perturbative corrections f_n. If the coupling constant α is small, each additional term in the series becomes progressively smaller, so that the sum in Eq. (1.1) can be truncated when the desired precision is reached. This led to many precise predictions.

Despite its succes, perturbation theory applied to QFT is plagued by numerous infinities, so that, at face value, perturbation theory loses its predictive power. Well-known are the so-called ultraviolet (UV) infinities. Theorists have dealt with UV infinities using renormalization, a process to systematically remove these infinities by redefining the parameters (such as mass and charge) at each order of perturbation theory [8]. However, this does not mean that we are out of the woods. Often the coefficients in Eq. (1.1) grow as $f_n \sim A^{-n} n!$, with A some constant. This causes the perturbative series to be *asymptotic*: at first decreasing with increasing order, but then succumbing to the factorial growth. In particular, the series of Eq. (1.1) has zero radius of convergence and diverges irrespective of the size of α. Once again, even aided by renormalization, perturbation theory is haunted by infinity and it may seem that perturbation theory is flawed again. However, the mathematical framework of *resurgence* introduced by the mathematician Écalle [9] – building on the work of Borel [10] – allows us to turn the divergent series into proper functions. In particular, resurgence shows that the factorial growth of the coefficients indicates the presence of *non-perturbative* effects that are non-analytic at $\alpha = 0$, generally of the form

$$e^{-A/\alpha} F^{(1)}(\alpha)\,, \tag{1.2}$$

where $F^{(1)}(g)$ is some function that admits a perturbative expansion on its own.

In the first part of this thesis, I will study non-perturbative QFT using resurgence. I will consider formal aspects of resurgence as well as one of the more practical applications of resurgence: *renormalons* [11]. In the context of renormalons, non-perturbative effects like Eq. (1.2) scale as Λ/Q, with Λ the QCD scale parameter and Q the scale of the problem at hand. Non-perturbative effects in QCD are proportional to this ratio and often referred to as *power corrections*.

In the second part of this thesis, I will study a different type of power correction that becomes relevant when a scattering process involves two, or more, widely seperated scales. In this case, each coefficient of the power series Eq. (1.1) contains large logarithms of the type $\alpha^n \log^m \xi \sim 1$, with m up to $2n-1$, and ξ a ratio of the widely separated scales. To obtain precise predictions, one cannot just truncate the perturbative series, but one needs to *resum* these large logarithms to all orders in α. This is a very common situation at hadron colliders; different scales may arise due to the presence of particles with very different masses, or have a dynamical origin following from the value of kinematic observables. Key to the resummation program are *factorization theorems*, which determine how the scattering amplitude factorizes into simpler (single scale) universal objects. By writing evolution equations for these objects, we can eventually find an all-order formula where the large logarithms are resummed.

In order to appreciate resurgence and factorization, we need to dive deeper into both topics.

1.1. Resurgence

Resurgence analysis suggests that we should supplement asymptotic series with additional nonperturbative contributions like (1.2), which can be united in what is known as a *transseries*. In its simplest form, such a transseries can be written as

$$F(\vec{\sigma}, \alpha) = \sum_{n=0}^{\infty} \sigma_n \, F^{(n)}(\alpha) \, \mathrm{e}^{-n \frac{A}{\alpha}} \,, \tag{1.3}$$

where $F^{(n)}(\alpha) = \sum_{h=0}^{\infty} f_h^{(n)} \alpha^h$ are called *transseries sectors* and they are usually all asymptotic series. From a physics point of view, one can often think of the transseries as the semiclassical expansion of a path integral which yields a sum over saddle point contributions. In this interpretation, nA is the instanton action of the n-th saddle point solution, where each saddle point contribution is weighted by a parameter σ_n in the transseries whose value is determined by boundary conditions imposed on the path integral. However, transseries structures like Eq. (1.3) can be used to describe a much broader class of physical phenomena like quantum tunneling, soliton waves, D-branes, and most notable for this thesis: renormalons.

Although asymptotic series diverge, a finite value can still be assigned to these series using the method of *Borel summation* [10]. This summation technique plays a central role in the theory of resurgence and provides a way to resum asymptotic series up to arbitrary precision. In fact, Écalle showed that Borel summation lies at the basis of a systematic procedure for finding missing nonperturbative contributions. Moreover, he showed that these are intricately connected to one another in an algebraic sense that he formulated in his *alien calculus*.

At the heart of alien calculus are the so-called *alien derivatives* $\Delta_{\ell A}$, which give rise to relations between different transseries sectors. In particular the alien derivative is a differential operator whose action on the transseries sectors is given by

$$\Delta_{\ell A} F^{(n)}(\alpha) \propto F^{(n+\ell)}(\alpha) \,, \tag{1.4}$$

where the constants of proportionallity depend on the specific transseries we are studying. Alien derivatives are abstract operators that are generically hard to compute with. However, a so-called *bridge equation* can make the bridge between ordinary calculus of derivatives and alien calculus. Such bridge equations therefore play a central role in practical applications of resurgence.

Before resurgence was developed by Écalle, it was already known that there is a connection between transseries sectors. A famous example of this stems from the seventies: Bender and Wu studied the large n behaviour of the perturbative energy levels E_n of the quartic anharmonic oscillator [12] and showed that their large order behaviour could be recovered from studying the one-instanton sector of the 'negatively coupled' quartic oscilator [13]. Resurgence is even more universal and also higher instanton sectors may contribute in the large order behaviour of the perturbative coefficients. Schematically, such *large order relations* are of the form:

$$\begin{tikzcd}
\boxed{f^{(0)}_{k\gg1}} & & \boxed{f^{(1)}_h} \arrow[ll, bend right] & + & \boxed{f^{(2)}_h} \arrow[llll, bend right] & + & \boxed{f^{(3)}_h} \arrow[llllll, bend right, "\text{“Predicting”}"'] & + & \cdots
\end{tikzcd}$$

where the subscript $k \gg 1$ denotes the large order behaviour of the perturbative coefficients. What is less known is that the arrows can be reverted and that resurgence can be used to study non-perturbative physics by starting from the perturbative information:

$$\begin{tikzcd}
\boxed{f^{(0)}_{k\gg1}} \arrow[rr, bend right] \arrow[rrrr, bend right] \arrow[rrrrrr, bend right, "\text{“Decoding”}"'] & & \boxed{f^{(1)}_h} & + & \boxed{f^{(2)}_h} & + & \boxed{f^{(3)}_h} & + & \cdots
\end{tikzcd}$$

This is in fact the reason for the name resurgence. If one takes enough perturbative coefficients and starts digging deep enough, one eventually finds all other non-perturbative transseries sectors.

1.2. Factorization

The key to understanding and using perturbative methods to calculate high energy interactions between particles is the idea of factorization. Factorization separates a process into parts that can be calculated independently, where each factor depends only on physics happening on one distance scale. This approach is essential in QCD, where it allows one to isolate short-distance effects (high-energy, perturbative) from long-distance effects (low-energy, non-perturbative). As already highlighted above, factorization is also one of the main ingredients for resummation, which is needed when standard perturbative calculations break down due to large logarithmic terms.

Factorization analyses can be developed using a *diagrammatic approach* within the full theory, i.e. QED or QCD, where factorization theorems are derived from first principles. See e.g. [14–18] for seminal papers. An alternative approach to factorization – which has become popular in the last two decades – is by means of an effective theory, such as the *soft-collinear effective field theory* (SCET) [19–21]. In this context, factorization theorems are constructed at the Lagrangian level, where soft and collinear modes in the scattering process are defined through independent fields.

In this thesis, we will follow the more traditional, diagrammatic approach, to factorization. In particular, we will focus on the decay of an off-shell photon of invariant mass Q into a massive fermion anti-fermion pair of mass m, which in turn can be expressed in terms of two form factors F_1 and F_2. Such form factors – often called Sudakov form factors due to the early work of Sudakov on the resummation of the leading logarithms [22] – have been a prototype amplitude for factorization studies. For the purpose of this thesis, we consider the small mass expansion of the form factors, i.e. $m \ll Q$. The *leading power* (LP) term of this expansion is known to factorize [23, 24]:

$$V^\mu = J \otimes \bar{J} \otimes H^\mu \otimes S\,, \tag{1.5}$$

where the *jet functions* J and $\bar{J}$ collect the modes *collinear* to the fermion anti-fermion pair respecitvely. The *hard function* H^μ and *soft function* S collect the hard and soft modes of this process. The jet and soft function can be given universal operator matrix definitions and therefore be applied to other processes as well. The process dependence resides in the hard function. The first step in proving the factorization formula Eq. (1.5) is to understand the regions of the space of loop momenta that give the LP contributions. After appropriate approximations it is then possible to convert the leading contributions into the form of the factorization theorem.

The study of power corrections in scattering processes at hadron colliders has received increasing attention in the past few years due to its importance for precision physics. In [25], such a study was initiated for the *next-to-leading power* (NLP) correction to Eq. (1.5) and in particular how this can also be cast into a factorization theorem. In this thesis, we consider the NLP corrections to the form factors F_1 and F_2 in two complementary approaches. First, by analyzing the loop momentum regions responsible for the NLP contributions using the so-called *method of regions*. Second, by proposing operator matrix definitions for new NLP jet functions, which serve as key ingredients in the NLP factorization theorem proposed by [25].

1.3. Outline

The structure of this thesis is as follows. In chapter 2, we introduce the mathematical framework of resurgence and provide more context to what was discussed already in Sec. 1.1. Our goal with this chapter is that a first time reader can become familiar with the fundamentals of the topic. Chapter 3 delves into more formal and advanced aspects of resurgence, focusing on the resurgence structure of large-order relations. In chapters 4 and 5, we turn to one of the key applications of resurgence: the study of renormalons. Chapter 4 covers the basics of this non-perturbative phenomenon, particularly as it manifests in QED and QCD. Toward the end of the chapter, we introduce a novel method for analyzing renormalons using resurgence. Building on this, in chapter 5 we apply these resurgence techniques to explore the renormalon contributions to the Adler function.

The latter part of the thesis shifts focus to aspects of factorization. In chapter 6, we provide a concise review of factorization from a diagrammatic perspective. In particular, we review the LP factorization theorem for the QED massive form factors. Here, we hihglight how the so-called method of expansion by momentum regions can be used to verify such a theorem. To pave the way for NLP factorization, we employ the method of regions in chapter 7 to analyze the two-loop massive form factors up to NLP accuracy. Building on these results, in chapter 8 we propose operator matrix definitions for NLP jet functions and validate them by comparison with the findings of the previous chapter.

Finally, in chapter 9 we summarize the key results and conclusions of this thesis. Additional details and background on the calculations presented throughout this work are provided in four appendices.

Chapter 2.

Resurgence

This chapter is based on Secs. 2 and 3 and App. B of [1] and on Sec. 2 of [3].

In this introductory chapter, we delve into the method of *resurgence*, a set of mathematical techniques based on the groundbreaking work by J. Écalle [9]. The problem that resurgence addresses is that of asymptotic series. These divergent series, while seemingly problematic, encode profound information about the underlying non-perturbative structure of the theory. This brings us to the main objective of this chapter: the understanding of asymptotic behaviour of perturbative series and its relation to non-perturbative sectors. As we show in this chapter, by leveraging the tools of resurgence we can systematically bridge the gap between these two realms, uncovering the rich interplay between the perturbative and non-perturbative.

In recent years, resurgence techniques have become more popular among physicists and have been applied to a wide range of physical models. These include (but definitely are not limited to) the Painlevé I equation [26–29], quantum mechanics [30–34], quantum field theories [35–38], hydrodynamics [39, 40], two-dimensional gravity [41, 42], topological strings [43–46] and many more.

While not every detail of this chapter is essential for understanding the later sections of this thesis, our aim here is to introduce the mathematical framework of resurgence in a way accessible to readers encountering the topic for the first time. For this purpose, we will primarily follow the notation and presentation of [47], which in our opinion is well suited to introduce the topic in a pedagogical way. For further background information, we refer the interested reader to [48–50] or the review sections of [27].

2.1. Borel summation of asymptotic expansions

Assume that some physical problem provides us with a power series in some coupling constant α:

$$F(\alpha) = \sum_{n=0}^{\infty} f_n \, \alpha^{n+1} \,, \tag{2.1}$$

where we have included an extra power of α on the left for later convenience. We will further assume that this series is asymptotic, of the *Gevrey-1* type – that is: we assume that as $n \to \infty$, the coefficients f_n grow factorially as

$$\frac{f_n A^{n+\beta}}{\Gamma(n+\beta)} \sim c + \mathcal{O}\left(1/g\right) , \tag{2.2}$$

for some nonzero complex constants A, c and a real constant β. In most of what follows, we will assume for simplicity that β is an integer. The results in this chapter are easily generalized to the case of noninteger β, see e.g. Sec. 2.6.

Due to the factorial growth of the coefficients f_n in Eq. (2.2), the series in Eq. (2.1) does not converge for any nonzero value of α. When Eq. (2.1) arises in a physics setting this is a problem, as one would expect the series $F(\alpha)$ to not just be purely formal but to describe a *function* that has a finite value for some range of α-values. The usual way to cure this problem is to take the *Borel transform* of the series:

$$F(\alpha) = \sum_n f_n \alpha^{n+1} \quad \to \quad \mathcal{B}[F](t) = \sum_n \frac{f_n}{\Gamma(n+1)} t^n, \tag{2.3}$$

where t is the (complex) Borel transformation parameter conjugate to α. In the literature, one often encounters different definitions of the Borel transform. That is, the definition given in Eq. (2.3) is a special case of the more general Borel transform $\mathcal{B}_\nu$, defined by dividing in Eq. (2.3) by $\Gamma(n+2-\nu)$ instead. As we show in App. A.1, the different definitions are closely related and lead to equivalent results.

For asymptotic series whose coefficients grow factorially, the compensating factorial in the denominator in Eq. (2.3) leads to a finite radius of convergence. In this case one may endeavour to sum the Borel transformed series, and after that invert the transform to obtain a "Borel-summed" expression for the original series. To make the inversion precise one traditionally defines the *Borel sum* as the Laplace transform of $\mathcal{B}[F]$:

$$\mathcal{S}_0[F](\alpha) = \int_0^\infty dt\, \mathcal{B}[F](t)\, e^{-\frac{t}{\alpha}} . \tag{2.4}$$

Notice that instead of integrating along the real positive line, one can integrate in a different direction θ in the complex t-plane for which the integral converges. This leads to a Borel sum $\mathcal{S}_\theta[F]$ where the integration in Eq. (2.4) is now from 0 to $e^{\mathrm{i}\theta}\infty$. We will need this more general definition in what follows.

It might appear as if the process of Borel transforming and then Borel summing is a tautology, since the integral reinstates the factorial growth, e.g.

$$\int_0^\infty dt\, t^n\, e^{-\frac{t}{\alpha}} = \Gamma(n+1)\alpha^{n+1}. \tag{2.5}$$

However, in many cases one can now first perform the infinite sum $\mathcal{B}[F](t)$ and analytically continue to the whole complex t-plane (or a multiple cover thereof) minus a discrete set of points where the analytic continuation of $\mathcal{B}[F](t)$ has singularities. Next the integral in Eq. (2.4) can be performed. The effect is that integration and summation are interchanged. One can show that for Gevrey-1 series, this leads to a finite function $\mathcal{S}_0[F]$ [10].

The Borel transform $\mathcal{B}[F](t)$ can still have singularities in the complex t plane, which are in fact related to the factorial growth. A simple example illustrates this point.

Example 2.1.1. *In Eq.* (2.3) *let us choose* $f_n = n!A^{-n}$*. In that case we have*

$$\mathcal{B}[F] = \sum_{n=0}^{\infty} \left(\frac{t}{A}\right)^n = \frac{A}{A-t}\,, \tag{2.6}$$

leading to a pole at $t = A$*. As another example, consider* $f_0 = 0$ *and* $f_n = -(n-1)!A^{-n}$ *for* $n > 0$*. The Borel transform is then*

$$\mathcal{B}[F](t) = -\sum_{n=1}^{\infty} \frac{1}{n}\left(\frac{t}{A}\right)^n = \log\left(1 - \frac{t}{A}\right)\,, \tag{2.7}$$

which leads to a branch cut running from A *to* ∞*. In both Eqs.* (2.6) *and* (2.7)*, the series after the first equal sign converges for* $|t| < |A|$*. The second equals sign contains the analytic continuation of this convergent series into a multi-valued function on the entire* t*-plane except for* $t = A$*, where the function has a logarithmic branch point in the case of Eq.* (2.7)*.*

When the singularities of $\mathcal{B}[F](t)$ lie on the integration contour from 0 to ∞ in Eq. (2.4) one can deform the contour such that one integrates either slightly above the singularity under an angle $\theta = 0^+$, or below the singularity under an angle $\theta = 0^-$. Deciding to integrate either above or below for the example Eq. (2.6) e.g. leads to an ambiguity

$$\mathcal{S}_{0^+}[F] - \mathcal{S}_{0^-}[F] = 2\pi \mathrm{i}\, A\, e^{-\frac{A}{\alpha}}. \tag{2.8}$$

Other singularities in the complex t plane will influence the integral in Eq. (2.4); the contour may be chosen in many ways, adding sensitivity to other singularities in the Borel plane as well. Notice the non-perturbative aspect of the ambiguities like in Eq. (2.8) via the exponent $e^{-A/\alpha}$.

The Borel transform followed by the Laplace transform solves exactly the problem we mentioned earlier: it turns an asymptotically divergent series in α into a finite function of α. One can show that for Gevrey-1 series a particular asymptotic expansion of that function around $\alpha = 0$ is the original expansion $F(\alpha)$ that we started with. While this solves our problem, this is certainly not the end of the story: the construction depends on the integration path in the Laplace transform, and therefore the function one arrives at is generally not unique. As it turns out, this non-uniqueness is a virtue rather than a problem.

2.2. From Borel summation to alien calculus

In physics, singularities and divergences are usually regarded as troublesome. However, in a resurgence context, all the information about an asymptotic series and the associated non-perturbative data is encoded in the singularity structure of its Borel transform. Before discussing how to systematically extract this information, we need to introduce some concepts and terminology.

A function whose expansion gives a formal power series $F(\alpha)$ is said to be a *simple resurgent function* if the Borel transform $\mathcal{B}[F](t)$ has only simple poles or logarithmic branch cuts as singularities. That is, near each singularity, say at $t = \omega$, we have that

$$\mathcal{B}[F](t) = \frac{a}{2\pi\mathrm{i}\,(t-\omega)} + \Psi(t-\omega)\frac{\log(t-\omega)}{2\pi\mathrm{i}} + \Phi(t-\omega)\,, \tag{2.9}$$

for some $a \in \mathbb{C}$ and where the functions Ψ, Φ are analytic around the origin. More generally, the Borel transform can also contain other singularities, e.g. double or higher order poles as is the case for the Adler function discussed in Chapter 5. However, most of our discussion in this chapter is focused on the simplest case of a single pole and a log-branch cut that are commonly considered in the literature. In Sec. 2.6 we then give the necessary details to extend the resurgence analysis needed for the discussion of the Adler function.

To obtain a better understanding of the Borel singularities in Eq. (2.9), we introduce *alien calculus* [9]. The fundamental object in alien calculus is the linear differential operator Δ_ω, the *alien derivative*, which acts on simple resurgent functions. Being a derivative, it satisfies the Leibniz rule when acting on a product of simple resurgent functions. Furthermore, for those functions it has a rather simple expression: by rewriting $\Psi(t)$ in Eq. (2.9) as the Borel transform of a resurgent function $G(\alpha)$, i.e. $\mathcal{B}[G](t) = \Psi(t)$, the alien derivative at a singular point ω is

$$\Delta_\omega F(\alpha) = a + G(\alpha)\,. \tag{2.10}$$

When ω is not a singular point of $\mathcal{B}[F](t)$, then $\Delta_\omega F(\alpha) = 0$. In other words, the alien derivatives fully encode the singular properties of the Borel transforms of simple resurgent functions. We emphasize that α in Eq. (2.10) cannot take the same value as ω as they are variables in different planes.

Next, let us consider a direction θ in the complex plane of the Borel variable t along which $\mathcal{B}[F]$ has singularities. Such a singular direction is known as a *Stokes line*, since as we shall see Stokes' phenomenon [51, 52] occurs there. Because of the singularities on the integration path, the Borel summation $\mathcal{S}_\theta[F]$ is no longer well-defined. Of course, the singularities are easily avoided by integrating slightly to the left or right of the direction θ, leading to summations that we denote by $\mathcal{S}_{\theta^+}[F]$ and $\mathcal{S}_{\theta^-}[F]$ respectively. These different summations lead to an ambiguity and one may ask how these two distinct functions are related. They are in fact connected by the *Stokes automorphism* $\mathfrak{S}_\theta$, or its related *discontinuity* Disc_θ. These are defined as

$$\mathcal{S}_{\theta^+} = \mathcal{S}_{\theta^-} \circ \mathfrak{S}_\theta = \mathcal{S}_{\theta^-} \circ (1 - \mathrm{Disc}_\theta)\,. \tag{2.11}$$

One can show (see e.g. [50]) that these operators can be expressed in terms of the alien derivatives via the exponential map

$$\mathfrak{S}_\theta = \exp\left[\sum_{\{\omega_\theta\}} e^{-\frac{\omega_\theta}{\alpha}} \Delta_{\omega_\theta}\right], \tag{2.12}$$

where the set $\{\omega_\theta\}$ denotes all the singular points along the θ-direction. The main point now is that if we know the Stokes automorphisms (or equivalently, the alien derivatives), then we also know how to relate the different summations. Consequently, at least in principle a full reconstruction anywhere in the complex α plane, including non-perturbative contributions, of the function $F(\alpha)$ is then possible.

It is convenient to define the *pointed alien derivative*, related to the ordinary alien derivative by

$$\dot{\Delta}_\omega \equiv e^{-\frac{\omega}{\alpha}} \Delta_\omega. \tag{2.13}$$

This turns out to be a useful operator as it commutes with the usual derivative (see again [50] for details), i.e.

$$[\dot{\Delta}_\omega, \partial_\alpha] = 0. \tag{2.14}$$

This will momentarily be used to derive a bridge equation.

2.3. Transseries and bridge equations

From the relation between Stokes automorphisms and alien derivatives, Eq. (2.12), we notice that the ambiguity arising in Borel summation is non-perturbative in α, being of order $e^{-\frac{\omega}{\alpha}}$. This implies that the non-perturbative solution we are trying to construct must contain such non-perturbative exponential contributions. As we will see in a moment, resurgence can be captured in a universal way through transseries [53]. Transseries are generalizations of perturbative series by the inclusion of terms with non-perturbative (non-analytic) factors like $e^{-\frac{\omega}{\alpha}}$. Factors of this type are called *transmonomials*.

Let us start by assuming that our resurgent function arises as a solution to some problem depending on a single boundary condition, i.e. we consider the single parameter transseries Ansatz

$$F(\alpha,\sigma) = \sum_{n=0}^{\infty} \sigma^n e^{-n\frac{A}{\alpha}} \Psi^{(n)}(\alpha)\,, \qquad \text{with} \qquad \Psi^{(n)}(\alpha) = \alpha^{\beta_n} \sum_{h=0}^{\infty} f_h^{(n)} \alpha^h\,, \tag{2.15}$$

where $\Psi^{(0)}$ is simply a perturbative series, as in Eq. (2.1), and $\Psi^{(n)}$, for $n \geq 1$, are the non-perturbative contributions. The transseries parameter σ counts the number of $e^{-\frac{A}{\alpha}}$ factors [47] and parameterizes different choices of the boundary condition.[1] The β_n are called the *characteristic exponents*; we discuss their role in resurgence at the end of Sec. 2.6. In the resurgence literature, $\Psi^{(n)}$ is often called the *n-instanton sector*, even though in practice n may count solitons, renormalons, or some other non-perturbative physical quantity. To avoid confusing readers with a high-energy background, we shall call these quantities the *n-th non-perturbative sector* instead.

After introducing an intuitive pictorial representation of non-perturbative transseries sectors and their interrelations in the form of the *alien chain* in the next subsection, it will be straightforward in Sec. 2.6 to generalize this one-parameter transseries to

---

[1] This specific choice of the transseries Ansatz is useful to introduce the various resurgence concepts in this chapter. In chapter 3, we will be more generic by introducing resurgence without assuming an underlying transseries.

multi-parameter transseries, by including further non-perturbative monomials like $e^{+A/\alpha}$, $\log(\alpha)$, etc.

We saw that the alien derivatives play an important role in the construction of the complete non-perturbative solution to a problem. It is however still unclear how to compute these derivatives in a systematic way. This is done through the construction of the *bridge equations*, so named because they form a bridge between the ordinary calculus of derivatives and alien calculus. Assume for the moment that $F(\alpha,\sigma)$ is the solution to some differential equation (in the variable α). From Eq. (2.14) we get that acting on this equation with $\dot{\Delta}_\omega$ yields a new, linear differential equation to which $\dot{\Delta}_\omega F(\alpha,\sigma)$ is a solution. At the same time, acting on the original equation with ∂_σ shows that $\partial_\sigma F(\alpha,\sigma)$ is a solution to the *same* equation.

Example 2.3.1. *Consider the non-linear differential equation*

$$\partial_\alpha F(\alpha,\sigma) = 6 + F(\alpha,\sigma)^3\,. \tag{2.16}$$

Acting on this with $\dot{\Delta}_\omega$ *yields*

$$\partial_\alpha \dot{\Delta}_\omega F(\alpha,\sigma) = 3F(\alpha,\sigma)^2 \cdot \dot{\Delta}_\omega F(\alpha,\sigma)\,, \tag{2.17}$$

which is a new, linear differential equation for $\dot{\Delta}_\omega F(\alpha,\sigma)$*. Similarly, acting with* ∂_σ *leads to the same equation as Eq.* (2.17)*, with* $\dot{\Delta}_\omega F(\alpha,\sigma)$ *replaced by* $\partial_\sigma F(\alpha,\sigma)$*.*

Supposing the new linear differential equation is of first order (as is natural for a problem with a single boundary condition) we conclude that the two new solutions must be proportional to each other, i.e.

$$\dot{\Delta}_\omega F(\alpha,\sigma) = S_\omega(\sigma)\partial_\sigma F(\alpha,\sigma)\,, \tag{2.18}$$

where $S_\omega(\sigma)$ is a proportionality factor which still may depend on σ. This relation is Écalle's bridge equation [9]; it indeed presents a bridge between the alien derivatives and the regular ones. By substituting $\dot{\Delta}_\omega = e^{-\frac{\omega}{\alpha}}\Delta_\omega$ and expanding the transseries, the LHS equals

$$\dot{\Delta}_\omega F(\alpha,\sigma) = \sum_{n=0}^{\infty} \sigma^n e^{-\frac{nA+\omega}{\alpha}} \Delta_\omega \Psi^{(n)}(\alpha)\,, \tag{2.19}$$

while the RHS yields

$$S_\omega(\sigma)\partial_\sigma F(\alpha,\sigma) = S_\omega(\sigma)\sum_{n=0}^{\infty} n\,\sigma^{n-1} e^{-n\frac{A}{\alpha}}\Psi^{(n)}(\alpha)\,. \tag{2.20}$$

Both sides must be equal term by term according to the powers of σ and $e^{-\frac{A}{\alpha}}$. To this end, [27] defined a notion of *degree* as

$$\deg\left(\sigma^n e^{m\frac{A}{\alpha}}\right) = n + m\,. \tag{2.21}$$

Since the transseries Eq. (2.15) has degree $\deg(F(\alpha,\sigma)) = 0$, it follows that the bridge equation can only contain nontrivial information at $\omega = \ell A$, $\ell \in \mathbb{Z}$. Thus, for transseries of this type we expect singularities in the Borel plane at $\omega = A$ but also at integer multiples of A – something which we will also see for the Adler function in chapter 5. Note that here $\ell = 0$ is excluded because the Borel transform is regular at the origin. Furthermore, $\dot{\Delta}_{\ell A} F(\alpha,\sigma)$ only contains positive powers of σ, so we can write the proportionality constant as a formal power series expansion

$$S_{\ell A}(\sigma) = \sum_{k=0}^{\infty} S_\ell^{(k)} \sigma^k\,. \tag{2.22}$$

Taking the degree of both Eqs. (2.19) and (2.20) implies that $S_\ell^{(k)}$ is only nonzero at $k = 1-\ell$, and therefore, writing $S_\ell^{(1-\ell)} \equiv S_\ell$, we have that

$$S_{\ell A}(\sigma) = S_\ell\, \sigma^{1-\ell}, \quad \ell \leq 1\,. \tag{2.23}$$

The bridge equation Eq. (2.18) now reads

$$\sum_{n=0}^{\infty} \sigma^n e^{-(n+\ell)\frac{A}{\alpha}} \Delta_{\ell A} \Psi^{(n)}(\alpha) = \sum_{n=0}^{\infty} S_\ell\, n\, \sigma^{n-\ell} e^{-n\frac{A}{\alpha}} \Psi^{(n)}(\alpha)\,, \tag{2.24}$$

or equivalently

$$\Delta_{\ell A}\Psi^{(n)}(\alpha) = \begin{cases} 0 & \ell > 1, \\ (n+\ell) S_\ell \Psi^{(n+\ell)} & \ell \leq 1, \quad \ell \neq 0\,, \end{cases} \tag{2.25}$$

where we used that $\Psi^{(n)} = 0$ for all $n < 0$. Although the alien derivative has an involved definition, the final result for the alien derivative is surprisingly simple, and works purely algebraically on the building blocks of the transseries, Eq. (2.15). We can compute all alien derivatives as long as the yet unknown constants $\{S_1, S_{-1}, S_{-2}, ...\}$ are known. We refer to these constants as *Stokes constants.* In general, computing Stokes constants is a difficult task which depends on the specific system that one tries to solve, and we shall not need to do so in this thesis.

For simple resurgent functions with a single parameter, we now have two equations for the alien derivative, i.e. Eqs. (2.10) and (2.25). Comparing the two yields

$$\mathcal{B}[\Psi^{(n)}](t) = \frac{a}{2\pi\mathrm{i}\,(t-\ell A)} + \frac{\mathsf{S}_{n\to n+\ell}}{2\pi\mathrm{i}}\,\mathcal{B}[\Psi^{(n+\ell)}](t-\ell A)\log(t-\ell A) + \text{regular}\,, \tag{2.26}$$

where 'regular' stands for a function that is analytic (and therefore non-singular) at $t = \ell A$. In other words, near the singularity $t = \ell A$ of $\mathcal{B}[\Psi^{(n)}](t)$, we find the *resurgence* of the the $\Psi^{(n+\ell)}$ sector. In this expression, the so-called *Borel residues* $\mathsf{S}_{n\to n+\ell}$ are constants that can be expressed in terms of the Stokes constants via Eqs. (2.11), (2.12) and (2.25).

Example 2.3.2. *For example we find*

$$\mathsf{S}_{n\to n+1} = -(n+1)S_1, \quad \mathsf{S}_{n\to n+2} = -\frac{1}{2}(n+1)(n+2)S_1^2\,, \quad \textit{etc.} \tag{2.27}$$

and similarly

$$\mathsf{S}_{n\to n-2} = -(n-1)S_{-1}, \quad \mathsf{S}_{n\to n-2} = -(n-2)\left(S_{-2} + \frac{1}{2}(n-1)S_{-1}^2\right)\,, \quad \textit{etc.} \tag{2.28}$$

See [27] for closed-form expressions for all Borel residues.

2.4. One-dimensional alien chain

Instead of entering the world of alien calculus, we will follow the more pedagogical picture of the *alien chain* developed in [47] as it will help us build an intuitive language in which resurgence can be better understood. For example, in the case of a single boundary condition, Stokes' automorphism Eq. (2.12) can be fully computed using Eq. (2.25) (see e.g. [27]), but once one needs to generalize to multi-parameter transseries, the equations can become quite intricate. Instead, for practical situations, the simple setup of the alien chain can be used and generalizations will come naturally. (For multi-parameter transseries, we will introduce alien *lattices* in Sec. 2.6.)

From the point of view of the alien chain, the sectors $\Psi^{(n)}$ of the transseries, Eq. (2.15), are viewed as nodes:

$$\boxed{\Psi^{(0)}} \qquad \boxed{\Psi^{(1)}} \qquad \boxed{\Psi^{(2)}} \qquad \boxed{\Psi^{(3)}} \qquad \boxed{\Psi^{(4)}} \qquad \boxed{\Psi^{(5)}} \qquad \cdots$$

which will be connected by alien derivatives to form a chain. We can then reinterpret the resurgence equation, Eq. (2.25), as a set of allowed resurgence "motions" along this chain. That is, there is only one type of forward motion (i.e. with ℓ positive) because of the constraint that $\Delta_{\ell A}\Psi^{(n)} = 0$ for $\ell > 1$. However, from the fact that nonzero $\ell \leq 1$ can give nonvanishing alien derivatives, we see that there are multiple backwards motions. Recall that (for real and positive A) to compute the Stokes automorphism Eq. (2.12) at $\theta = 0$ one only needs alien derivatives with $\ell > 0$, whereas the Stokes automorphism at $\theta = \pi$ only requires $\ell < 0$. Therefore, we never need to consider combinations of forward and backward motions together.

Example 2.4.1. *As an example, there is only one forward path to go from* $\Psi^{(1)}$ *to* $\Psi^{(4)}$ *by repeatedly acting with* Δ_A*:*

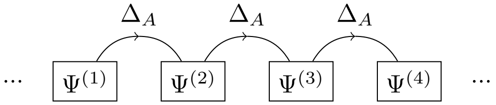

However, there are multiple backwards motions to go from $\Psi^{(4)}$ *to* $\Psi^{(1)}$ *using different combinations of* Δ_{-A}*,* Δ_{-2A} *and* Δ_{-3A}*:*

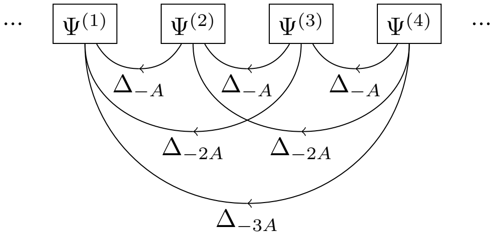

Before we can compute Stokes' automorphism using allowed motions on the alien chain, we need to introduce some further terminology and set up some computational rules. We denote a step $\mathcal{S}_{n\to m}$[2] as a single link connecting two nodes n and m on the chain and a path $\mathcal{P}$ as a combination of consecutive steps. The length $\ell(\mathcal{P})$ of a path is then defined as the number of steps composing the path:

$$\ell(\mathcal{P}) = \#\{\mathcal{S}_{n\to m} \in \mathcal{P}\}\,. \tag{2.29}$$

Looking at the proportionality factor on the RHS of Eq. (2.25), we see that it is natural to define the weight w of a step $\mathcal{S}_{n\to m}$ in terms of the Stokes constants S_k as

$$w(\mathcal{S}_{n\to m}) = mS_{m-n}\,. \tag{2.30}$$

---

[2] Note to be confused with the Borel residues of Eq. (2.26), which have a similar notation.

The weight of a path is then simply the product of the weights of the steps that make up the path

$$w(\mathcal{P}) = \prod_{\mathcal{S}_i \in \mathcal{P}} w(\mathcal{S}_i)\,. \tag{2.31}$$

Finally, it is convenient to define a "statistical factor" [47] linking two nodes as

$$\mathrm{SF}_{(n\to m)} = \sum_{\mathcal{P}(n\to m)} \frac{w(\mathcal{P})}{\ell(\mathcal{P})!}\,, \tag{2.32}$$

where the sum is over all allowed paths linking nodes n and m. Equipped with these definitions, let us now see how they turn up in the calculation of Stokes automorphisms, through a specific example.

Example 2.4.2. *Reviewing Eqs.* (2.12) *and* (2.25)*, we notice that the actual form of Stokes' automorphism depends on the object it acts on. Focusing on the example of the transseries sector* $\Psi^{(3)}$*, it follows from the allowed motions on the alien chain that this sector has singularities both in the* $\theta = 0$ *and* $\theta = \pi$ *directions. As the only allowed forward motions consist of repeated actions of* Δ_A*, we see that the Stokes automoprhism in the* $\theta = 0$ *direction takes a simple form:*

$$\begin{aligned}\mathfrak{S}_0 \Psi^{(3)} &= \exp\left(e^{-\frac{A}{\alpha}}\Delta_A\right)\Psi^{(3)} \\ &= \left[1 + e^{-\frac{A}{\alpha}}\Delta_A + \frac{1}{2!}\left(e^{-\frac{A}{\alpha}}\Delta_A\right)^2 + \frac{1}{3!}\left(e^{-\frac{A}{\alpha}}\Delta_A\right)^3 + \ldots\right]\Psi^{(3)} \\ &= \Psi^{(3)} + 4S_1 e^{-\frac{A}{\alpha}}\Psi^{(4)} + \frac{20}{2!}S_1^2 e^{-2\frac{A}{\alpha}}\Psi^{(5)} + \frac{120}{3!}S_1^3 e^{-3\frac{A}{\alpha}}\Psi^{(6)} + \ldots \end{aligned} \tag{2.33}$$

In the $\theta = \pi$ *direction, the Stokes automorphism does not take such a simple form, as there are multiple allowed backward motions on the alien chain. Luckily, when acting on* $\Psi^{(n)}$*,* $n > 0$*, the possible set of backward paths is finite. For* $\Psi^{(3)}$ *we obtain*

$$\begin{aligned}\mathfrak{S}_\pi \Psi^{(3)} &= \exp\left(\sum_{\ell=1}^{3} e^{\ell\frac{A}{\alpha}}\Delta_{-\ell A}\right)\Psi^{(3)} \\ &= \left[1 + \sum_{\ell=1}^{3} e^{\ell\frac{A}{\alpha}}\Delta_{-\ell A} + \frac{1}{2!}\left(\sum_{\ell=1}^{3} e^{\ell\frac{A}{\alpha}}\Delta_{-\ell A}\right)^2 + \frac{1}{3!}\left(\sum_{\ell=1}^{3} e^{\ell\frac{A}{\alpha}}\Delta_{-\ell A}\right)^3 + \ldots\right]\Psi^{(3)} \\ &= \Psi^{(3)} + 2S_{-1}e^{\frac{A}{\alpha}}\Psi^{(2)} + \left(S_{-2} + S_{-1}^2\right)e^{2\frac{A}{\alpha}}\Psi^{(1)}\,. \end{aligned} \tag{2.34}$$

Having computed these actions explicitly, let us now translate these results to the terminology we introduced above. We see that under the action of $\mathfrak{S}_0$ *on* $\Psi^{(3)}$ *we obtain an infinite sum of higher sectors* $\Psi^{(n\geq 3)}$*: the nodes on the alien chain that can* *be reached by forward motions. The coefficients of the terms containing these sectors can be expressed in terms of statistical factors Eq. (2.32). For example going from* $\Psi^{(3)} \to \Psi^{(4)}$*, we see that there is only a single path, of length* $\ell = 1$ *and weight* $w = 4S_1$*. Furthermore, we have to include a non-perturbative factor* $e^{-\frac{A}{\alpha}}$*. Likewise, the path to go from* $\Psi^{(3)} \to \Psi^{(5)}$ *has length* $\ell = 2$ *with weight* $w = 20S_1^2$*. In order to get the correct coefficient of the* $\Psi^{(5)}$ *term, we have to multiply by* $\frac{1}{2!}$ *and a non-perturbative term, i.e.* $SF_{(3\to5)}e^{-2\frac{A}{\alpha}}$ *in total. Similarly, the coefficient in front of* $\Psi^{(6)}$ *is* $SF_{(3\to6)}e^{-3\frac{A}{\alpha}}$ *etc. Adding up all different terms for all possible paths gives the full action of* $\mathfrak{S}_0$ *on* $\Psi^{(3)}$*.*

For the full action of $\mathfrak{S}_\pi$*, we need to consider the allowed backward motions. Again, there is only a single path of length* $\ell = 1$ *to go from* $\Psi^{(3)} \to \Psi^{(2)}$*, leading to a statistical factor SF=* $2S_{-1}$ *and non-perturbative term* $e^{\frac{A}{\alpha}}$*. To go from* $\Psi^{(3)} \to \Psi^{(1)}$ *however, we have two allowed paths. One has* $\ell = 1$ *with* $w = S_{-2}$*, and the other path has* $\ell = 2$ *with* $w = 2S_{-1}^2$*, so* $SF_{(3\to1)} = S_{-2} + S_{-1}^2$*. In both cases we need to multiply by the non-perturbative factor* $e^{2\frac{A}{\alpha}}$*. Adding all terms for all possible paths again gives the action of the Stokes automorphism.*

To summarize what we have learned: $\mathfrak{S}_0\Psi^{(n)}$ (resp. $\mathfrak{S}_\pi\Psi^{(n)}$) is a sum over all forward (backward) paths linking nodes to the right (left) of $\Psi^{(n)}$, i.e. the terms in this sum can be written as

$$\mathfrak{S}_0\Psi^{(n)} = \Psi^{(n)} + \sum_{m>n} \mathrm{SF}_{(n\to m)} e^{-(m-n)\frac{A}{\alpha}} \Psi^{(m)}, \tag{2.35}$$

and likewise for $\mathfrak{S}_\pi\Psi^{(n)}$, where the only difference is that one should sum over $m < n$.

2.5. Large order behaviour and asymptotics

With the knowledge of the previous sections, we can now return to our main goal: the understanding of asymptotic behaviour of perturbative series in QFT and its relation to non-perturbative sectors. In fact, the resurgent structure is even more general and can be used to relate the asymptotic series of all non-perturbative sectors to each other. To see this, we apply Cauchy's theorem

$$\begin{aligned} f(\alpha) &= \oint_{\mathcal{C}} \frac{dy}{2\pi \mathrm{i}} \frac{f(y)}{y-\alpha} \\ &= -\int_0^{\infty} \frac{dy}{2\pi \mathrm{i}} \frac{\mathrm{Disc}\,_0 f(y)}{y-\alpha} - \int_0^{-\infty} \frac{dy}{2\pi \mathrm{i}} \frac{\mathrm{Disc}\,_\pi f(y)}{y-\alpha} + \oint_{(\infty)} \frac{dy}{2\pi \mathrm{i}} \frac{f(y)}{y-\alpha}, \end{aligned} \tag{2.36}$$

where we assumed discontinuities only in the $\theta = 0$ and $\theta = \pi$ directions. See Fig. 2.1 for the deformation of the contour to go from the first to the second line in Eq. (2.36).

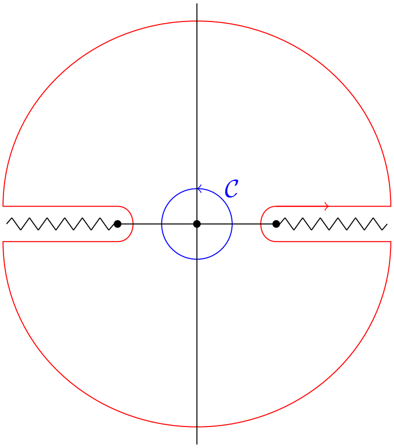

Figure 2.1.: In blue, (the inner contour) we show the contour $\mathcal{C}$ of the first line of the Cauchy integral, Eq. (2.36). In red (the outer contour) the deformed contour of the second line in that equation is shown. The zigzag lines on the right and left denote the rays where Disc_0 and Disc_π occur.

Notice that we deformed the contours even further such that the first two integrals in Eq. (2.36) start from 0.

For example, we can apply this to the perturbative sector $\Psi^{(0)}(\alpha)$. The discontinuities of this sector are easily computed using the rules from the previous subsection:

$$\mathrm{Disc}_0\Psi^{(0)} = (1-\mathfrak{S}_0)\Psi^{(0)} = -\sum_{\ell=1}^{\infty} S_1^\ell e^{-\ell\frac{A}{\alpha}}\Psi^{(\ell)}, \qquad \text{and} \qquad \mathrm{Disc}_\pi\Psi^{(0)} = 0\,. \tag{2.37}$$

In many cases, the integral around infinity vanishes (we will come back to this in chapter 3), yielding

$$\sum_{k=0}^{\infty} f_k^{(0)}\alpha^k = \sum_{\ell=1}^{\infty}\frac{S_1^\ell}{2\pi\mathrm{i}}\int_0^\infty dy\frac{e^{-\ell\frac{A}{y}}y^{\beta_\ell}}{y-\alpha}\sum_{h=0}^{\infty} f_h^{(\ell)}y^h\,. \tag{2.38}$$

By expanding around $\alpha = 0$, we can match equal powers in α on both sides of this equation and perform the y-integrations, after which we arrive at a remarkable connection between the perturbative and non-perturbative expansions:

$$f_k^{(0)} \simeq \sum_{\ell=1}^{\infty}\frac{S_1^\ell}{2\pi\mathrm{i}}\sum_{h=0}^{\infty} f_h^{(\ell)}\frac{\Gamma(k-h-\beta_\ell)}{(\ell A)^{k-h-\beta_\ell}}\,. \tag{2.39}$$

Here, we used a $\simeq$ symbol instead of an equals sign to indicate that this relation only describes the behavior as $k\to\infty$. In particular, we have exchanged the sum over h

and the integral in Eq. (2.38), which is only allowed formally – leading e.g. to the fact that $\Gamma(k-h-\beta_\ell)$ may be ill-defined when h is large compared to k.

In words: Eq. (2.39) states that the asymptotic behaviour of the perturbative coefficients $f_k^{(0)}$ is completely determined by the non-perturbative expansion coefficients $f_h^{(\ell)}$. We will call relations like Eq. (2.39) *large order relations* which we discuss in more depth in the next chapter. Furthermore, in chapter 5 we shall explain in detail how one can unpack large order relations systematically, and decode from the perturbative coefficients the non-perturbative ones.

We can repeat this derivation to obtain large order relations for other non-perturbative sectors as well. The key ingredient is to rewrite Cauchy's theorem in terms of the Stokes discontinuities, so that from the rules discussed in the previous subsection, one can write down large order relations by looking at allowed motions on the alien chain. Let us note that of course all of this is only possible if the non-perturbative sectors indeed have an asymptotic expansion (as opposed to a convergent or even finite one) – we shall see later that this is not always the case, e.g. for the Adler function.

To be explicit, we substitute Eq. (2.35) into Cauchy's theorem to get

$$\begin{aligned}\Psi^{(n)}(\alpha) = \sum_{\ell>n} \frac{\mathrm{SF}_{(n\to\ell)}}{2\pi\mathrm{i}} \int_0^{\infty} dy \frac{e^{-(\ell-n)\frac{A}{y}}}{y-\alpha} \Psi^{(\ell)}(y) \\ + \sum_{\ell<n} \frac{\mathrm{SF}_{(n\to\ell)}}{2\pi\mathrm{i}} \int_0^{-\infty} dy \frac{e^{-(\ell-n)\frac{A}{y}}}{y-\alpha} \Psi^{(\ell)}(y)\,. \end{aligned} \tag{2.40}$$

Again expanding around $\alpha=0$, matching equal powers in α and performing the y-integrals, one finds

$$f_k^{(n)} \sim \sum_{\ell\neq n} \frac{\mathrm{SF}_{(n\to\ell)}}{2\pi\mathrm{i}} \chi_{(n\to\ell)}(k)\,, \tag{2.41}$$

where it is convenient to define the large order factor[3]

$$\chi_{(n\to\ell)}(k) = \sum_{h=0}^{\infty} f_h^{(\ell)} \frac{\Gamma(k+\beta_n-h-\beta_\ell)}{((\ell-n)A)^{k+\beta_n-h-\beta_\ell}}\,. \tag{2.42}$$

Thus, Eqs. (2.41) and (2.42) show how, using the alien chain formalism, the asymptotic behaviour of expansion coefficients in non-perturbative sectors encodes all expansion coefficients in other non-perturbative sectors.

---

[3] Note that we define these factors slightly different from [47], as we include an explicit factor of $\Gamma(k)/A^k$.

2.6. Generalizations and extensions

There are many generalizations of the concepts and constructions we have seen so far, but in this thesis we only need two of them. First, we will need the concept of *multi-parameter transseries.* Second, we need to consider transseries with terms that include logarithmic factors. In this section, we follow the exposition in [27, 47]. We finish with a short discussion on the types of singularities in the Borel plane that are different than those discussed so far.

As we will see, for the Adler function in chapter 5, it is not enough to capture all the non-perturbative contributions with a single exponential transmonomial $e^{-\frac{A}{\alpha}}$. Instead, we need to allow for more such exponentials, $e^{-\frac{A_i}{\alpha}}$. In fact, two exponents seem to suffice for the Adler function at the order we are interested in, but we shall be somewhat more general. Thus, by writing $\boldsymbol{A} = (A_1, ..., A_k)$, a typical Ansatz for a k-parameter transseries solution to a non-linear problem is

$$F(\alpha, \boldsymbol{\sigma}) = \sum_{\boldsymbol{n}\in\mathbb{N}_0^k} \boldsymbol{\sigma}^{\boldsymbol{n}} e^{-\frac{\boldsymbol{n}\cdot\boldsymbol{A}}{\alpha}} \Psi^{(\boldsymbol{n})}(\alpha)\,, \qquad \text{with} \qquad \Psi^{(\boldsymbol{n})}(\alpha) = \alpha^{\beta_{\boldsymbol{n}}} \sum_{h=0}^{\infty} f_h^{(\boldsymbol{n})} \alpha^h\,. \tag{2.43}$$

Here we used the notation $\boldsymbol{\sigma}^{\boldsymbol{n}} = \prod_{i=1}^{k} \sigma_i^{n_i}$. Understanding the resurgence properties of such a transseries is again best understood in terms of the alien derivatives Δ_ω. For the one-parameter transseries, a key ingredient in the calculation of alien derivatives was the bridge equation Eq. (2.25). In the case of the multi-parameter transseries, the bridge equation usually takes the form

$$\Delta_{\boldsymbol{\ell}\cdot\boldsymbol{A}} \Psi^{(\boldsymbol{n})}(\alpha) = \boldsymbol{S}_{\boldsymbol{\ell}} \cdot (\boldsymbol{n}+\boldsymbol{\ell}) \Psi^{(\boldsymbol{n}+\boldsymbol{\ell})}\,, \qquad \boldsymbol{\ell} \neq \boldsymbol{0}\,, \tag{2.44}$$

where for each combination $\boldsymbol{\ell}\cdot\boldsymbol{A}$ we now need a whole vector of Stokes parameters $S_{\boldsymbol{\ell}} = (S_{\boldsymbol{\ell}}^{(1)}, ..., S_{\boldsymbol{\ell}}^{(k)})$ with the following general constraint:

$$S_{\boldsymbol{\ell}}^{(j)} = 0 \qquad \text{if} \qquad \ell_i \geq 1 + \delta_{ij}, \quad \forall i \in \{1, \ldots, k\}\,. \tag{2.45}$$

Eqs. (2.44) and (2.45) can be derived by generalizing the steps we took in Sec. 2.3 to the case of a multi-parameter transseries. The Borel singularities of the sectors $\Psi^{(\boldsymbol{n})}$ lie at positions $t = \boldsymbol{\ell}\cdot\boldsymbol{A}$ in the Borel plane, with $\boldsymbol{\ell} \in \mathbb{Z}^k$ with entries bounded from below by Eq. (2.44). Thus Eq. (2.26) becomes

$$\mathcal{B}[\Psi^{(\boldsymbol{n})}](t) = \frac{a}{2\pi\mathrm{i}\,(t-\boldsymbol{\ell}\cdot\boldsymbol{A})} + \frac{\mathsf{S}_{\boldsymbol{n}\to\boldsymbol{n}+\boldsymbol{\ell}}}{2\pi\mathrm{i}}\, \mathcal{B}[\Psi^{(\boldsymbol{n}+\boldsymbol{\ell})}](t-\boldsymbol{\ell}\cdot\boldsymbol{A}) \log(t-\boldsymbol{\ell}\cdot\boldsymbol{A}) + \text{regular}, \tag{2.46}$$

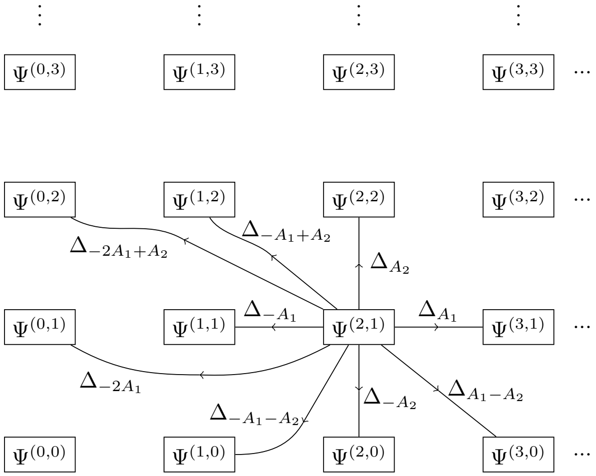

Figure 2.2.: Two-dimensional alien lattice. We show all allowed motions of a single step starting from node $\Psi^{(2,1)}$. Compared to the allowed motions for the one-dimensional alien chain, we observe a much richer structure of allowed resurgence motions.

where the *Borel residues* $\mathsf{S}_{\boldsymbol{n}\to\boldsymbol{n}+\boldsymbol{\ell}}$ can be computed in terms of the Stokes parameters $S^{(i)}_{\boldsymbol{\ell}}$ using Eq. (2.44).

In Sec. 2.4, we explained how, in the one-parameter case, the bridge equation translates to a set of allowed motions along an *alien chain* of non-perturbative sectors. Furthermore, we gave computational rules for the computation of Stokes discontinuities and large order formulae for the asymptotic behaviour of transseries. The natural extension for multi-parameter transseries is to think of the sectors $\Psi^{(\boldsymbol{n})}$ as living on a k-dimensional *alien lattice*. The computational rules outlined in the previous subsections are then to a large extent unaltered, the main exception being that we have a richer structure of allowed resurgence motions on the (multi-dimensional) alien lattice.

Example 2.6.1. *Consider the two-dimensional case* $k = 2$ *(see Fig. 2.2), and consider all the motions consisting of a single step starting from the node* $\Psi^{(2,1)}$*. Similar to what happens for the one-parameter transseries, the constraints in the bridge equation Eq.* (2.44) *lead to only two types of forward motion in the* $\boldsymbol{\ell} = (1,0)$ *and* $\boldsymbol{\ell} = (0,1)$ *directions:* Δ_{A_1} *and* Δ_{A_2}*. In other words, starting from node* $\Psi^{(2,1)}$*, the only way to reach*[4] *node* $\Psi^{(2,3)}$ *with purely forward motions is by acting with* Δ_{A_2} *twice. For pure backwards motion we have, as before, more options. In the example in Fig. 2.2, we see the allowed purely backwards motions consisting of a single step, obtained by acting*

---

[4] As will shortly be made clear, the concept of reaching a node means that the corresponding sector then occurs in the large order description of the coefficients of the original sector.

with Δ_{-A_1}*,* Δ_{-A_2}*,* Δ_{-2A_1} *and* $\Delta_{-A_1-A_2}$*. This means that from* $\Psi^{(2,1)}$ *one can reach node* $\Psi^{(0,1)}$ *using either* Δ_{-2A_1} *or twice* Δ_{-A_1}*.*

The example shows that we now also have a type of mixed forward and backward motion, obtained by acting with $\Delta_{-A_1+A_2}$, $\Delta_{-2A_1+A_2}$ and $\Delta_{A_1-A_2}$. However, similarly to pure forward motion, the constraint of the bridge equation limits the forward part of the motion in particular to minimal step sizes. E.g. acting with $\Delta_{-A_1+2A_2}$ does not lead to an allowed motion. Finally, we should emphasize that for paths of multiple steps it is not allowed to mix single steps with different directions, similar to the fact that one could not mix forward and backward motion in the one-parameter case. The reason for this is that for the computation of the Stokes automorphism, Eq. (2.12), in a singular direction

$$\theta_{\boldsymbol{\ell}} = \arg(\boldsymbol{\ell} \cdot \boldsymbol{A}) \,, \tag{2.47}$$

one only requires alien derivatives in the $\boldsymbol{\ell}$-direction. To clarify this with an example, note that to reach node $\Psi^{(0,3)}$ starting from $\Psi^{(2,1)}$ one can act with $\Delta_{-A_1+A_2}$ twice, but the path where one first acts with $\Delta_{-2A_1+A_2}$ and subsequently with Δ_{A_2} is a combination that does not occur in any Stokes automorphism.

For the computational rules, the concepts of step, path, their length, etc. stay unchanged in the multi-parameter setting. However, as we now have a vector of Stokes coefficients, the weight of a step, Eq. (2.30), becomes an inner product

$$w(\mathcal{S}(\boldsymbol{n} \to \boldsymbol{m})) = \boldsymbol{m} \cdot \boldsymbol{S}_{\boldsymbol{m}-\boldsymbol{n}} \,. \tag{2.48}$$

The expression for Stokes' automorphism acting on $\Psi^{(\boldsymbol{n})}$ in the singular direction $\theta_{\boldsymbol{\ell}} = \arg(\boldsymbol{\ell} \cdot \boldsymbol{A})$, is now given by the sum over all paths linking the node $\Psi^{(n)}$ to $\Psi^{(\boldsymbol{n}+m\boldsymbol{\ell})}$, with $m > 0$:

$$\mathfrak{S}_{\theta_{\boldsymbol{\ell}}} \Psi^{(\boldsymbol{n})} = \Psi^{(\boldsymbol{n})} + \sum_{m>0} \mathrm{SF}_{(\boldsymbol{n} \to \boldsymbol{n}+m\boldsymbol{\ell})} e^{-m \frac{\boldsymbol{\ell} \cdot \boldsymbol{A}}{\alpha}} \Psi^{(\boldsymbol{n}+m\boldsymbol{\ell})}. \tag{2.49}$$

Likewise, the large order relation Eq. (2.41) becomes

$$f_k^{(\boldsymbol{n})} \simeq \sum_{\boldsymbol{\ell} \neq \boldsymbol{n}} \frac{\mathrm{SF}_{(\boldsymbol{n} \to \boldsymbol{\ell})}}{2\pi \mathrm{i}} \chi_{(\boldsymbol{n} \to \boldsymbol{\ell})}(k) \,, \tag{2.50}$$

with

$$\chi_{(\boldsymbol{n} \to \boldsymbol{\ell})}(k) = \sum_{h=0}^{\infty} f_h^{(\boldsymbol{\ell})} \frac{\Gamma(k + \beta_{\boldsymbol{n}} - h - \beta_{\boldsymbol{\ell}})}{((\boldsymbol{\ell} - \boldsymbol{n}) \cdot \boldsymbol{A})^{k + \beta_{\boldsymbol{n}} - h - \beta_{\boldsymbol{\ell}}}} \tag{2.51}$$

the generalization of the large order factor, Eq. (2.42). These generalizations to multi-parameter transseries will all play a role when we study the Adler function.

As a final note on multi-parameter transseries, we want to mention that it might be the case that despite what we have said, one finds that the action of an operator like Δ_{2A_i}, for some value of i, is non-zero. One possibility is that there is an additional transseries parameter related to an exponential transmonomial $e^{-\frac{2A_i}{\alpha}}$. As a result, a sector with exponential $e^{-\frac{2A_i}{\alpha}}$ lies on top of a sector with $\left(e^{-\frac{A_i}{\alpha}}\right)^2$. In [54], which studies the all-order resurgence of factorially divergent series associated to a renormalon in six-dimensional scalar ϕ^3 theory, such a transseries was actually found with three transseries parameters and exponential transmonomials $e^{-\frac{A_i}{\alpha}}$, $e^{-\frac{2A_i}{\alpha}}$ and $e^{-\frac{3A_i}{\alpha}}$. A second way in which the action of Δ_{2A_i} does not vanish is that it might be the case that the problem at hand does not allow for a bridge equation of the form Eq. (2.44). In other words, the bridge equation does not lead to the constraint that Δ_{2A_i} vanishes. We will come back to this in our discussion of the Adler function in Secs. 5.1 and 5.2.

Next, we discuss transseries with logarithmic transmonomials $\log(\alpha)$. Note that in the literature, see e.g. [26, 27, 47, 54], both multi-parameter transseries and logarithmic factors often occur in the case of *resonant* transseries, which are transseries where multiple A_i add up to 0 in such a way that logarithmic factors must occur to solve the problem at hand. Although for the Adler function we have two exponents $A_1 = -A_2$ and logarithmic factors do occur, in its transseries the two effects are not related and our transseries is not resonant.

One can of course add logarithmic transmonomials to the general multi-parameter transseries Eq. (2.43). However, despite the fact that we need such a multi-parameter transseries for the Adler function, we will see in Sec. 5.2 that the part of the transseries with logarithms effectively looks like a one parameter transseries. Therefore, here we only discuss how to extend the one-parameter transseries of Eq. (2.15) by including logarithmic transmonomials.

The one-parameter transseries Ansatz with logarithms becomes:

$$F(\alpha,\sigma) = \sum_{n=0}^{\infty} \sigma^n e^{-n\frac{A}{\alpha}} \Psi^{(n)}(\alpha), \quad \text{with} \quad \Psi^{(n)}(\alpha) = \sum_{p=0}^{p_n} \log^p(\alpha) \sum_{h=0}^{\infty} f_h^{(n)[p]} \alpha^{h+\beta_n^{[p]}}, \tag{2.52}$$

where we included an expansion in logarithmic powers of α up to some finite logarithmic power p_n. Note that in doing this, we add a new transmonomial $\log(\alpha)$ to the transseries, but *not* a new transseries parameter $\hat{\sigma}$ in addition to σ. The reason for this is that the addition of logs generally does not change the location of singularities in the Borel plane, so there are no new Stokes automorphisms that would act on such a parameter. For similar reasons, we consider all of the $f_h^{(n)[p]}$ to belong to the same non-perturbative sector and we will always draw them as a single box in alien chains and lattices.

The derivation of the bridge equation, Eq. (2.25), is unaltered (and thus the allowed motions along the alien chain are the same), but when we apply Cauchy's residue theorem to obtain large order relations, we get additional and more complicated integrals. To be precise, when we expand Eq. (2.40) around $\alpha = 0$, we additionally need to perform integrals of the form

$$\int_0^\infty dy\; y^s e^{-m\frac{A}{y}} \log^p(y)\,, \tag{2.53}$$

for some s, m and p. These integrals can be evaluated exactly, and it is straightforward to show that this yields the following large order relation for the perturbative coefficients

$$\begin{aligned} f_k^{(0)[0]} \sim \sum_{\ell=1}^{\infty} \frac{S_1^\ell}{2\pi\mathrm{i}} \sum_{h=0}^{\infty} f_h^{(\ell)[0]} \frac{\Gamma(k-h-\beta_\ell^{[0]})}{(\ell A)^{k-h-\beta_\ell^{[0]}}} \\ + \sum_{\ell=1}^{\infty} \frac{S_1^\ell}{2\pi\mathrm{i}} \sum_{h=0}^{\infty} \sum_{p=1}^{p_\ell} f_h^{(\ell)[p]} \left. \frac{\left[\log(\ell A) - \partial_g\right]^p \Gamma(g)}{(\ell A)^{k-h-\beta_\ell^{[p]}}} \right|_{g=k-h-\beta_\ell^{[p]}}, \end{aligned} \tag{2.54}$$

where the first term is analogous to (2.39) and the second follows from the logarithmic transmonomials. One can derive similar equations for the large order behaviour of the coefficients of the non-perturbative sectors.

Although most of our discussion in Sec. 2 was focused on the case of a single pole and a log-branch cut, we finish this section with a short discussion on other types of singularities in the Borel plane that might appear. Indeed we will need this in the upcoming sections for the Adler function. In fact, the characteristic exponents $\beta_{\boldsymbol{n}}$ we added in the transseries Ansatz already allow for higher order poles in the Borel plane. Looking at Eqs. (2.42) and (2.50), we notice that these characteristic exponents play a role in the large order behaviour of the perturbative and non-perturbative coefficients. To see how this translates to the Borel plane, consider a formal power series $F(\alpha)$ and its Borel transform

$$F(\alpha) = \sum_{n=0}^{\infty} \Gamma(n-\beta)\,\alpha^{n+1} \qquad \Longrightarrow \qquad \mathcal{B}[F](t) = \frac{\Gamma(-\beta)}{(1-t)^{-\beta}}, \tag{2.55}$$

where we assumed that $\beta < 0$. In particular, $\beta = -1, -2, -3, ...$ correspond to a single, double, triple pole etc. in the Borel plane.

Furthermore, the sectors with logarithms in the transseries Ansatz Eq. (2.52) yield new types of singularities. As an example, consider the $p = 1$ terms of Eq. (2.54) with $\partial_g \Gamma(g) = \Gamma(g)\psi(g)$ (with $\psi(z) = \frac{\mathrm{d}}{\mathrm{d}z} \log \Gamma(z)$ the digamma function), i.e. consider the formal series

$$G(\alpha) = \sum_{k=0}^{\infty} \Gamma(k-\beta)\psi(k-\beta)\, \alpha^{k+1} \tag{2.56}$$

with $\beta < 0$ again. Its Borel transform is given by

$$\mathcal{B}[G](t) = -\Gamma(-\beta) \frac{\log(1-t) - \psi(-\beta)}{(1-t)^{-\beta}}, \tag{2.57}$$

and we indeed observe that these terms lead to a type of singularity we have not considered so far. We will discuss the role of these Borel singularities for the Adler function when we encounter them in Secs. 5.1 and 5.2.

2.7. Numerical methods

Richardson transforms, Padé approximants and conformal transformations are often-used as numerical methods in the resurgence literature because they are well-suited to extract as much information as possible from a limited set of perturbative data. Since we make considerable use of these methods in this thesis, we discuss them here in some detail. See [55] for a more extensive exposition.

2.7.1. Richardson transforms

Consider a sequence $\mathbb{S}(k)$ which we know how to compute numerically for arbitrary k, and has an expansion of the form

$$\mathbb{S}(k) = s_0 + \frac{s_1}{k} + \frac{s_2}{k^2} + \ldots . \tag{2.58}$$

Our first aim is to calculate s_0, which we can do by computing $\lim_{k\to\infty} \mathbb{S}(k)$. However, it might well be that one needs to compute $\mathbb{S}(k)$ for many and large values of k to confidently judge the limit. The *Richardson transform* [56, 57] is a method to accelerate this process and enable one to reach the desired limit with (significantly) fewer values of k. It is defined recursively by

$$\begin{aligned}
&\mathrm{RT}[\mathbb{S}](k,0)=\mathbb{S}(k), \\
&\mathrm{RT}[\mathbb{S}](k,N)=\mathrm{RT}[\mathbb{S}](k+1,N-1)+\frac{k}{N}\Big(\mathrm{RT}[\mathbb{S}](k+1,N-1)-\mathrm{RT}[\mathbb{S}](k,N-1)\Big)\,,
\end{aligned} \tag{2.59}$$

where we denote the N^{th} Richardson transform of $\mathbb{S}(k)$ by $\mathrm{RT}[\mathbb{S}](k,N)$.

Example 2.7.1. *Consider the case for $N=1$, which corresponds to*

$$RT[\mathbb{S}](k,1)=\mathbb{S}(k+1)+k\Big(\mathbb{S}(k+1)-\mathbb{S}(k)\Big)=s_0+\frac{s_1-s_2}{k^2}+\mathcal{O}\Big(\frac{1}{k^3}\Big)\,. \tag{2.60}$$

Clearly the limit $\lim_{k\to\infty} RT[\mathbb{S}](k,1)=s_0$ has a faster rate of convergence than $\mathbb{S}(k)$, as the subleading part proportional to s_1 now scales as $\mathcal{O}\Big(1/k^2\Big)$. Since the Richardson transform $RT[\mathbb{S}](k,N)$ cancels the subleading terms in $\mathbb{S}(k)$ up to order $1/k^N$, the estimate of s_0 thus becomes better when both k and N increase,

We can also find a closed form, in terms of $\mathbb{S}(k),\mathbb{S}(k+1),\ldots,\mathbb{S}(k+N)$, for the N^{th} Richardson transform by solving the following set of equations for s_0:

$$\begin{aligned}
\mathbb{S}(k)&=s_0+\frac{s_1}{k}+\ldots+\frac{s_N}{k^N} \\
\mathbb{S}(k+1)&=s_0+\frac{s_1}{k+1}+\ldots+\frac{s_N}{(k+1)^N} \\
&\vdots \\
\mathbb{S}(k+N)&=s_0+\frac{s_1}{k+N}+\ldots+\frac{s_N}{(k+N)^N}
\end{aligned} \tag{2.61}$$

where we truncated the series in Eq. (2.58) after the N^{th} term. The solution for s_0, up to order $\mathcal{O}(1/k^{N+1})$, is given by

$$s_0\approx \mathrm{RT}[\mathbb{S}](k,N)=\sum_{n=0}^{N}(-1)^{n+N}\frac{(k+n)^N}{n!(N-n)!}\mathbb{S}(k+n)+\mathcal{O}\Big(\frac{1}{k^{N+1}}\Big). \tag{2.62}$$

Example 2.7.2. *Let us see how the Richardson transform works in practice by considering the function*

$$f(u)=\frac{1}{1+\frac{u}{2}}+\frac{\log(1-u)}{u}=\sum_{k=0}^{\infty}\bigg(\Big(-\frac{1}{2}\Big)^k-\frac{1}{k+1}\bigg)u^k. \tag{2.63}$$

If one is only given numerical values for the first, say 40, coefficients $\mathbb{T}(k)$*:*

$$\mathbb{T}(k) = \left(-\frac{1}{2}\right)^k - \frac{1}{k+1}\,, \tag{2.64}$$

one can use the Richardson transform to extract the leading growth of these coefficients:

$$\mathbb{T}(k) \approx -\frac{1}{k} + \frac{1}{k^2} + ... \tag{2.65}$$

where the ellipsis contains terms for both the subleading $\frac{1}{k}$ *behaviour and the* $(-\frac{1}{2})^k$ *term. In Fig. 2.3a we show the coefficients* $\mathbb{T}(k)$ *in blue for* $1 \leq k \leq 40$*, together with their second Richardson transform. Here we used Eq.* (2.62) *to calculate the Richardson transform as the direct formula has a faster implementation than the recursive formula given in Eq.* (2.59)*. We see that the Richardson transform gives a clear acceleration of the series to the value* $s_0 = 0$ *with*

$$RT[\mathbb{T}(k)](38,2) = -0.0000156286508329897 7613 \tag{2.66}$$

Higher order Richardson transforms give even better estimates of s_0*.*

We may go even further and extract s_1*, by constructing the sequence*

$$k\big(\mathbb{T}(k) - 0\big) \approx -1 + \frac{1}{k} + ... \tag{2.67}$$

This converges to -1 *in the* $k \to \infty$ *limit. In Fig. 2.3b we see this sequence together with its second Richardson transform, showing again good convergence towards* -1*:*

$$RT\big[k\big(\mathbb{T}(k) - 0\big)\big](38,2) = -0.9999841284122182302 \tag{2.68}$$

One can naturally continue this process and also extract the coefficients s_i*,* $i > 1$*. Also the* $(-\frac{1}{2})^k$ *term of* $\mathbb{T}(k)$ *can be extracted and we show how this can be done in chapter 5. For now we highlight the fact that this term does not spoil the above convergence towards* s_0 *and* s_1*.*

2.7.2. Padé approximants and Borel-Padé summation

Consider an analytic function $f(u)$, or even a formal power series

$$f(u) = \sum_{k=0}^{\infty} a_k u^k\,. \tag{2.69}$$

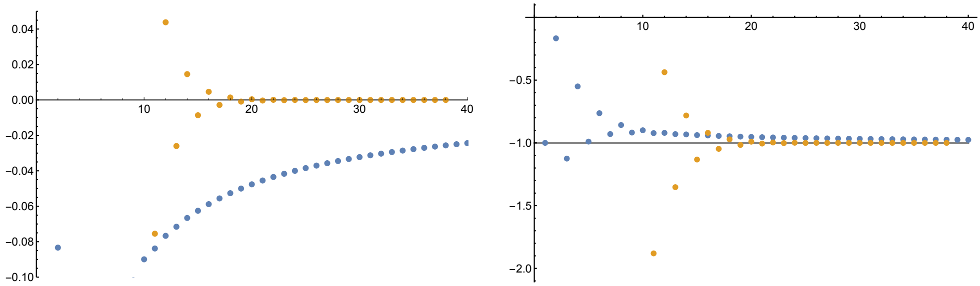

(a) **(b)**

Figure 2.3.: In (a), we show the coefficients c_k (bottom curve, blue), Eq. (2.64), together with their second Richardson transform (top curve, orange). In (b), we show the sequence $k\big(\mathbb{T}(k) - 0\big)$ (top curve, blue) of Eq. (2.67), again with the second Richardson transform (bottom curve, orange).

One can define the *Padé approximant* of $f(u)$ [58, 59] as

$$\mathcal{P}_{N,M}[f](u) \equiv \frac{\sum_{n=0}^{N} b_n u^n}{\sum_{m=0}^{M} c_m u^n} \,. \tag{2.70}$$

This rational function should be thought of as an approximation to $f(u)$ itself: the coefficients b_n and c_n are precisely chosen such that the first $N + M + 1$ coefficients of the Taylor expansions of $f(u)$ and $\mathcal{P}_{N,M}[f](u)$ agree. (Note that the Padé approximant has $N + M + 2$ coefficients in total, but an overall scaling of these coefficients has no effect on the rational function.) Given a power series $f(u)$, software packages like `Mathematica` can compute Padé approximants up to around 100 coefficients exactly, and even further numerically. In practice, one usually computes the *diagonal* Padé approximant of order N, $\mathcal{P}_N[f](u)$ (defined as $\mathcal{P}_{N,M}[f](u)$ with $M = N$), and we shall always do so in this thesis.

The main use of Padé approximants lies in the fact that they can encode singularities. If for example $f(u)$ describes a function with a pole at some point $u_0 \neq 0$, a truncated Taylor expansion of $f(u)$ will not 'see' such a pole easily, simply because a Taylor expansion is a polynomial which has a finite value at u_0. The Padé approximant, on the other hand, by construction must have a number of poles, and essentially always[5] one of these will turn out to be near u_0.

This ability of Padé approximants to encode singularities of $f(u)$ goes even further: a Padé approximant can also spot more complicated singularities in $f(u)$ such as

---

[5] In rare cases where a singularity does not show up, it can be made visible by changing the order of the Padé approximant. As a check, we have always compared Padé approximants at slightly different orders for the computations in this thesis.

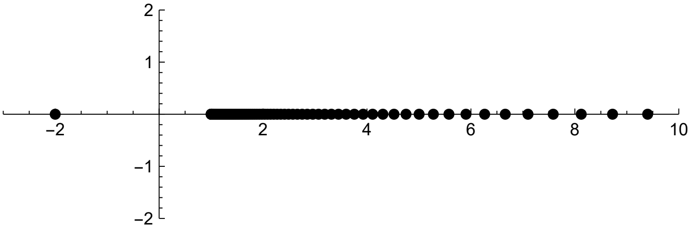

Figure 2.4.: Poles of the order 120 diagonal Padé approximant to the function in Eq. (2.63). One clearly sees the (single) pole at $u = -2$ as well as the mimicked branch cut starting at $u = 1$.

logarithmic branch cuts. Of course the rational function $\mathcal{P}_N[f](u)$ does not have such branch cuts, but for large N it does have a large number of poles, and these poles can accumulate into half-lines that start at some point u_0, thus mimicking a branch cut, not only in a pictorial way but also in the sense that integrals around branch cuts are well-approximated by integrals around the poles.

For a real power series, the coefficients in the Padé approximant will also be real. In general, this leads to Padé poles that are also at real locations, but occasionally 'spurious' poles occur when the denominator of the Padé approximant has two non-real complex conjugate zeroes. The occurrence of such spurious poles is usually not very problematic, as they occur sporadically and can often be removed by taking a slightly higher or lower order Padé approximant.

Example 2.7.3. *To illustrate the process of Padé approximation, let us once again look at the example Eq.* (2.63)*. The function $f(u)$ has a simple pole at $u = -2$ and a logarithmic branch cut starting at $u = 1$. Using the exact Taylor expansion in Eq.* (2.63)*, and from that result computing $\mathcal{P}_{120}[f](u)$ using* `Mathematica`*, we find a rational function whose poles we plot in Fig. 2.4. Both the single pole at $u = -2$ and the accumulation of all other poles to mimick the branch cut at $u = 1$ are clearly visible in the figure.*

In this thesis, we use Padé approximants in two different ways. First of all, we use these approximants to spot singularities for functions (usually in the Borel plane) for which we only have a finite number of expansion coefficients available. A second application of Padé approximants is that they can be used to replace an actual Borel transform $\mathcal{B}[F](t)$ of an asymptotic series before doing the Laplace transform. That is, instead of computing

$$\mathcal{S}[F](g) \approx \int_0^\infty dt\, \mathcal{B}[F]_N(t)\, e^{-\frac{t}{g}} \tag{2.71}$$

using an Nth order Taylor expansion of $\mathcal{B}[F](t)$, one instead computes

$$\mathcal{S}[F](g) \approx \int_0^\infty dt\, \mathcal{PB}_N[F](t)\, e^{-\frac{t}{g}}\,, \tag{2.72}$$

with $\mathcal{PB}_N \equiv \mathcal{P}_N \circ \mathcal{B}$. The reason why this is useful is that it does not make much sense to Laplace transform a Taylor series of a Borel transform directly: such a Taylor series is simply a polynomial, and its Laplace transform does nothing but reinsert factors of $n!$ in front of the nth coefficient of $\mathcal{B}[F](t)$ – that is, it simply returns a cut-off version of the original asymptotic series, which when we make N larger and larger will still diverge for any value of the parameter.

If instead of directly Laplace transforming a Borel plane power series one takes a diagonal Padé approximant first, the resulting functions are much better behaved. There are two reasons for this: first of all in a Laplace transform of the form Eq. (2.72) the function $\mathcal{PB}_N[F](t)$ behaves very nicely as $t \to \infty$: it simply becomes a constant, so the total integral including the decaying exponential converges very fast. More importantly, however, as we have seen $\mathcal{PB}_N[F](t)$ encodes the singularities of $\mathcal{B}[F](t)$ very well, and these singularities contain information about the non-perturbative contributions to the function $O(g)$ that we are trying to approximate – non-perturbative contributions that 'cure' the asymptotic growth of the power series expansion.

As a result, whenever we want to numerically compute an inverse Laplace transform of a Borel transform whose analytical form is unknown, we use a Padé approximant. This procedure is known as Borel-Padé summation or sometimes Borel-Écalle-Padé summation; further details can be found in e.g. [27, 47].

2.7.3. Conformal transformations

As we saw earlier in this chapter, very often there is a dominant Borel singularity at, say, $t = A$ – corresponding with the leading divergence of the associated asymptotic series – and the subdominant singularities are at $t = nA$ for $n \geq 2$. In the case there are branch cut singularities and if one tries to approximate the Borel transform using a Padé approximant, it might be hard to distinguish the different singularities as the branch cuts are mimicked by the accumulation of Padé poles. To pull the branch cuts apart, one can take a conformal map before taking the Padé approximant [60, 61]. To be specific, the conformal mapping

$$\mathcal{C} : t \to -\frac{4zA}{(1-z)^2} \tag{2.73}$$

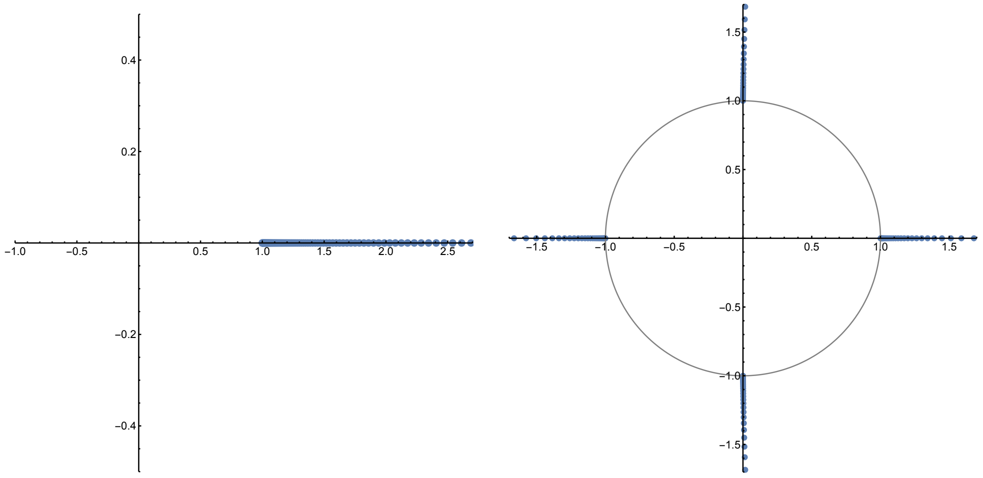

(a) **(b)**

Figure 2.5.: In (a), we show the poles of the diagonal Padé approximant $\mathcal{PB}_{140}[F](t)$ of Eq. (2.74). As the poles of different branch cuts are hard to distinguish, we show in (b) the Padé singularities after applying the conformal map Eq. (2.73) to the Borel plane. We clearly observe that the different branch cuts are pulled apart with $z = -1$ and $z = \pm\mathrm{i}$ corresponding to $t = 1$ and $t = 2$ in the left figure respectively. Furthermore, the second branch point of both logarithms at $t = \infty$ is made visible in (b) with an accumulation of poles near $z = 1$.

maps the half-line $[A, \infty)$ in the t-plane to the unit circle in the z-plane. E.g. $t = A$ gets mapped to $z = -1$, $t = 2A$ gets mapped to $z = \pm\mathrm{i}$ etc. Again, an example may be best to illustrate the usefulness of the conformal mapping.

Example 2.7.4. *Consider the following Borel transform:*

$$\mathcal{B}[F](t) = \log(1-t) + \log(2-t)\,, \tag{2.74}$$

which has two branch cuts starting at $t = 1$ *and* $t = 2$*. In Fig. 2.5a we show the poles of the diagonal Padé approximant* $\mathcal{PB}_{140}[F](t)$ *and clearly observe an accumulation of poles at* $t = 1$*. However, it is not clear if the poles near* $t = 2$ *correspond to the branch cut of* $\log(2-t)$*, or are still a representation of the branch cut of* $\log(1-t)$*. To pull the different branch cuts apart, we can apply the conformal mapping of Eq.* (2.73)*. Fig. 2.5b shows the Padé poles of the order* $N = 140$ *Padé approximant after taking the conformal mapping. The different branch cuts at* $t = 1$ *and* $t = 2$ *are mapped to* $z = -1$ *and* $z = \pm\mathrm{i}$ *respectively and are now easily distinguishable. Both logarithms* $\log(1-t)$ *and* $\log(2-t)$ *also have a second branch point at* $t = \infty$*, which gets mapped to the finite location at* $z = 1$ *by the conformal mapping and subsequently made visible by the*

Padé approximant. The above observations are easily verified with a small calculation:

$$\begin{aligned} \mathcal{CB}[\log(1-t)](z) &= 2\log(1+z) - 2\log(1-z) \\ \mathcal{CB}[\log(2-t)](z) &= \log(2) + \log(z+\mathrm{i}) + \log(z-\mathrm{i}) - 2\log(1-z)\,, \end{aligned} \tag{2.75}$$

with $\mathcal{CB} = \mathcal{C}\circ\mathcal{B}$*. We indeed see four different logarithmic branch points appearing in the* z*-plane.*

Chapter 3.

Resurgence of large order relations

This chapter is based on [3].

Let us consider an asymptotic perturbative series in some variable[1] z:

$$\varphi^{(0)}(z) = \sum_{g=0}^{\infty} \varphi_g^{(0)} z^{g+1} \,. \tag{3.1}$$

From the previous chapter, we learned that the perturbative coefficients $\varphi_g^{(0)}$ in Eq. (3.1) are related to other non-perturbative coefficients $\varphi_h^{(n)}$. These relations are collected in so-called *large order relations* – which we encountered already in Sec. 2.5 and in particular Eq. (2.39) – and repeat here for clarity in the simplified case that $\beta_\ell = 0$:

$$\frac{\varphi_g^{(0)}}{\Gamma(g)} \simeq \sum_{\ell=1}^{\infty} \frac{S_1^\ell}{2\pi \mathrm{i}} \sum_{h=0}^{\infty} (kA)^{g-h} \frac{\Gamma(g-h)}{\Gamma(g)} \varphi_h^{(\ell)} \,. \tag{3.2}$$

As explained below Eq. (2.39), this should be understood to hold in the large g limit. Originally, large order relations of this type appeared in [26].

As said already in the introduction of this thesis, the study of the large order behaviour of asymptotic series in physics predates the conception of resurgence and large order relations. Many other implicit and explicit discussions of large order behaviour have appeared over the years, e.g. [62–64]. To the best of our knowledge, the first (leading instanton) large order formulas of the form in Eq. (3.2) appeared in [65] and subsequently also in [43, 44, 66] before being generalized to the multi-instanton version of Eq. (3.2) from [27] in the context of ODEs and matrix models.

In the more recent mathematics literature, the focus of resurgence research has not been on large order behaviour as much as it has been in the physics literature, but Écalle and Sharma described a method to study large order relations in [67], and most of the essectial techniques needed to discuss large order behaviour can be found in the textbook [68]. In 2020, Sauzin used these techniques to study the large order

---

[1] For most physicists it might feel strange to use g as a summation variable as it is often used as the coupling constant in which one expands perturbative series. However for those feeling uncomfortable at the moment, hang on, as for most of this chapter we are actually interested in expansions in $1/g$ around $g = \infty$.

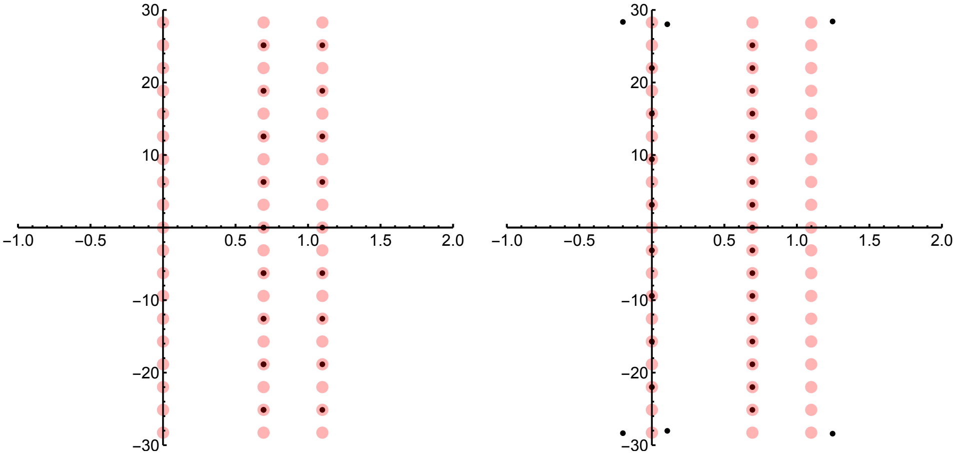

(a) **(b)**

Figure 3.1.: Borel transform of the Adler function large order expansion – discussed in more detail in chapter 5. The black dots are the singularities of the Borel-Padé transform of the $1/g$ expansion of Eq. (3.2) for $\ell = 1$. The red transparent disks are added to aid the eye and are positioned at $\log(\ell) + \pi i n$, with $\ell = 1, 2, 3$ and $n \in \mathbb{Z}$. The two plots show the contributions to the large order relation coming from the two leading nonperturbative sectors. The spurious black dots with imaginary part $\sim \pm 9\pi\mathrm{i}$ in the right hand plot are a result of numerical instabilities.

behavior of the asymptotic 'Stirling series' that occurs when expanding the logarithm of the gamma function [69].

The applications of large order relations go beyond toy models: in chapter 5 we will study the resurgent structure of the Adler function, and use large order relations to extract higher nonperturbative sectors that have an interpretation as renormalon contributions. Without turning to details yet, let us give a small preview of what we will encounter in chapter 5. For each ℓ in Eq. (3.2) the ratio of gamma functions yields a new asymptotic series in $1/g$, which in the context of the Adler function (as in many other examples of asymptotic series) is studied by plotting poles of the Padé approximant to its Borel transform. This leads to the plots shown in Fig. 3.1, where the black dots indicate the singularities of the Borel transform of these series, which in turn should determine nonperturbative contibutions to the large order relation. In fact, it was this interesting singularity structure – somewhat reminiscent of the 'peacock patterns' observed in [70] – that led us to the question which underlying structure gives rise to these patterns.

The observed pattern is not specific to the Adler function: it also appears for a variety of other models – see e.g. Fig. 3.2, which displays a similar plot for a toy model

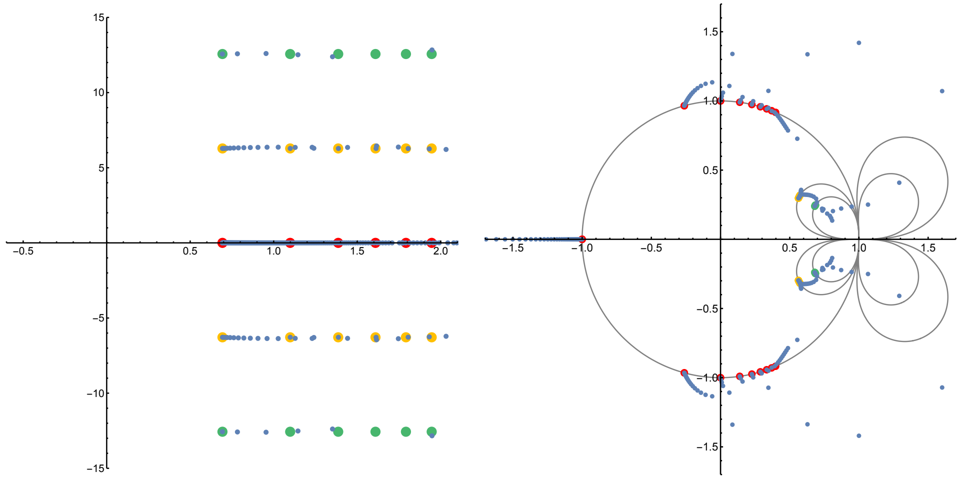

(a) **(b)**

Figure 3.2.: In (a), we show the singularities of the Borel-Padé transform of Eq. (3.2) for $\ell = 1$ for the quartic free energy. Similar to the plots shown in Fig. 3.1, we observe singularities at $\log(k) + 2\pi i n$, but now for integers $k \geq 2$ and $n \in \mathbb{Z}$. As the singularities are branch cuts (mimicked by the accumulation of poles of the Padé approximant), the poles corresponding to different branch cuts are hard to distinguish. In (b), we therefore show the Padé singularities after applying a conformal map to the Borel plane – recall Sec. 2.7.3 – which maps the singularities on the positive real axis to the unit circle; the images of some other lines with imaginary part $2\pi n$ are also drawn. We clearly observe that the branch cuts are pulled apart and can therefore conclude that the poles on the real axis in (a) belong to different branch cuts. We refer to example 3.2.2 for more details.

that we will study extensively later in this chapter. In this case, the Padé poles line up to mimic branch cuts (rather than poles) in the Borel transform of the large order expansion, but the repeating structure of singularities is essentially the same. These observations are particularly interesting in light of the fact that the $1/g$ expansion of Eq. (3.2) *itself* takes the form of a transseries [27, 71]. These two ingredients form the starting point of this chapter.

Throughout this chapter, we provide numerous examples to illustrate various concepts and to numerically verify our statements. As these examples are primarily meant to support the more abstract concepts, we keep the examples small and refrain from too many details. Many more details will be given in chapter 5, when we perform the resurgence analysis of the Adler function.

In this chapter, we study the resurgent structure of the transseries that large order relations constitute. Before we do so, we review in Sec. 3.1 the tools from resurgence that are necessary for the rest of the chapter. In Secs. 3.2.1 and 3.2.2, we show how the resurgent structure of large order relations can be understood using the so-called Stirling transform, which repackages all the coefficients into new series that appear in the large order relation Eq. (3.2). In particular, these new series make the repeated pattern in the imaginary direction in Figs. 3.1 and 3.2a manifest, leading to an underlying geometric structure that we dub the *Borel cylinder*. We subsequently derive the Stokes phenomenon [51, 52] in Sec. 3.2.3, and explain how it relates to the Stokes phenomenon of the original asymptotic expansion. In doing so, we test to what extent the resummation of the large order relation describes the perturbative coefficients *exactly*: when we resum Eq. (3.2) for finite g, can we calculate the perturbative coefficients $\varphi_g^{(0)}$ to arbitrary precision? We will find that the answer to this question is often 'yes', even in cases where one ignores potential contributions to the large order relation coming from a Cauchy integral at infinity. Finally in Sec. 3.2.4, we will formulate 'exact' large order relations, and see that this resummation establishes a natural extension of the large order relation to non-integer and even complex values of g. Sec. 3.3 is devoted to a test of the exact large order relation for a toy model called the quartic partition function and Sec. 3.4 finishes with our conclusions and an outlook.

3.1. From Stokes constants to Borel residues

In the previous chapter we gave a 'classical' introduction of resurgence, where we assumed that our resurgent function arises from a problem that has a bridge equation, i.e. we assumed a particular form of the underlying transseries – recall e.g. Eq. (2.18) for the one-parameter transseries. This was in particular useful to explain the important resurgence concepts, however in many applications, such a bridge equation is hard to derive or even non-existent – see in particular chapter 5. Therefore, in this section we will be more generic by introducing resurgence without assuming an underlying bridge equation or transseries. Instead, we start from the setting of a *simple resurgent function* – introduced in Eq. (2.9) – where the Borel transform only has poles and logarithmic branch cuts as its singularities. We will in particular be interested in the case of logarithmic singularities, but this is not a very strong restriction as we can switch to a different Borel transform – see App. A.1.

In this chapter, we will be mostly interested in what happens at a single Stokes line. Without loss of generality, by rotating the complex z variable and the corresponding Borel transform variable t if necessary, we may assume that this Stokes line is the positive real axis. The Stokes line can contain more than a single singularity, but we do make the assumption that any singularities on it are at $t = \ell A$ for $\ell \in \mathbb{Z}_{>0}$.

This is often a reasonable assumption; for example, there may be multi-instanton or renormalon configurations in our physical problem, and those would lead to precisely such a pattern of singularities.

Taking these assumptions into account, let us then assume that near some singularity $t = \ell A$, the Borel transform of the perturbative series Eq. (3.1) has the form

$$\mathcal{B}[\varphi^{(0)}](t) = \frac{\mathsf{S}_{0\to\ell}}{2\pi i}\ \mathcal{B}[\varphi^{(\ell)}](t-\ell A)\ \log(t-\ell A) + \text{regular}, \tag{3.3}$$

which is just a particular instance of Eq. (2.26). The main difference with Eq. (2.26) is that the Borel residues $\mathsf{S}_{0\to\ell}$ are now assumed to be general and not necessarily expressed in terms of Stokes constants via a bridge equation as in e.g. Example 2.3.2. Of course, there is some freedom in scaling $\mathsf{S}_{0\to\ell}$ and $\varphi^{(\ell)}$ in opposite ways; usually this freedom is fixed by requiring that the leading term in $\varphi^{(\ell)}$ is unity.

Quite common in the theory of resurgence is that the relation (3.3) generalizes to the other formal power series $\varphi^{(k)}$ as well: we have that

$$\mathcal{B}[\varphi^{(k)}](t) = \frac{\mathsf{S}_{k\to k+\ell}}{2\pi i}\ \mathcal{B}_0[\varphi^{(k+\ell)}](t-\ell A)\ \log(t-\ell A) + \text{regular}, \tag{3.4}$$

for integers k, ℓ such that $k \geq 0$ and $k+\ell \geq 0$. In this chapter, we will use the terminology that the sectors *know about each other*.

An important observation is that the Borel residues $\mathsf{S}_{0\to\ell}$ are formally *multivalued*, since there are in general many paths γ along which we can analytically continue the Borel transform from $t = 0$ to $t = \ell A$. Therefore, to properly define the Borel residues $\mathsf{S}_{0\to\ell}$, we must commit to a convention with regards to these paths. A standard convention is the one shown in Fig. 3.3 on the left side, where we analytically continue the Borel transform above the Stokes line to the singularity of interest. We will come back to this ambiguity in Sec. 3.1.2.

3.1.1. Stokes phenomenon

Whenever we encounter a Stokes line, we are interested in computing the discontinuity

$$\text{disc}\varphi^{(0)}(z) = (\mathcal{S}_+ - \mathcal{S}_-)\varphi^{(0)}(z)\,. \tag{3.5}$$

In this chapter, whenever it is clear what the singular direction θ is, we will omit the angle, e.g. denote the lateral Borel sums with angles infinitesimally larger or smaller than θ by $\mathcal{S}_+\varphi^{(0)}$ and $\mathcal{S}_-\varphi^{(0)}$ respectively. In computing the discontinuity in Eq. (3.5), it is important that the Laplace integrals for both $\mathcal{S}_+$ and $\mathcal{S}_-$ do not cross any branch

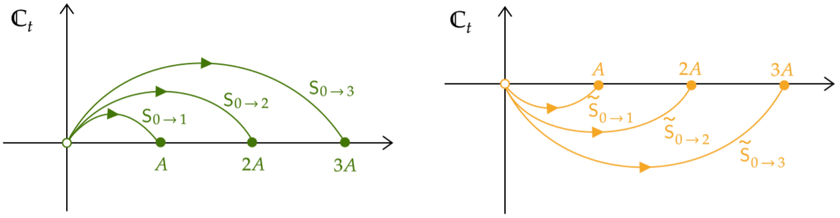

Figure 3.3.: Conventions for the description (3.3) of the Borel transforms near singularities at $t = \ell A$: on the left the standard convention (continuation above the Stokes line) and on the right an alternative convention (continuation below the Stokes line).

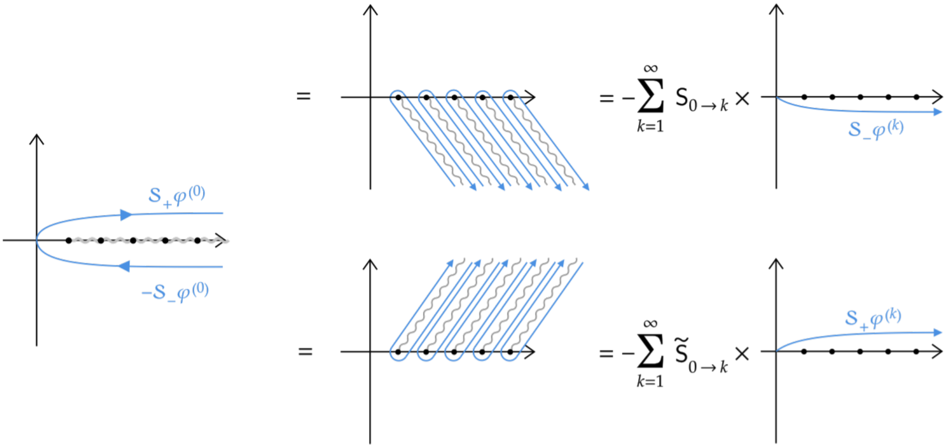

Figure 3.4.: Considering the *difference* of lateral resummations, there are two natural choices: we either let all branch cuts (and thus the Hankel contours) run off to infinity below the real line (upper graphs) or we let them run off to infinity above real line (lower graphs).

cuts associated to the logarithmic contributions to the Borel transform Eq. (3.3). One may achieve this by aligning all branch cuts with the Stokes line (see the left hand side of Fig. 3.4), but a more conventient choice is to let all branch cuts go off to infinity in a diagonal direction and deform the integration contour into a sum of so-called *Hankel contours*, as depicted in the middle of Fig. 3.4.

By decomposing the integration contour in terms of Hankel contours around individual singularities in this way, we can use Eq. (3.3) to find[2]

$$(\mathcal{S}_+ - \mathcal{S}_-)\varphi^{(0)}(z) = -\mathcal{S}_- \left(\sum_{k=1}^{\infty} \mathsf{S}_{0\to k}\, \varphi^{(k)}(z)\, \mathrm{e}^{-kA/z} \right). \tag{3.6}$$

More suggestively, we can write this as

$$\mathcal{S}_+\varphi^{(0)}(z) = \mathcal{S}_- \left(\varphi^{(0)}(z) - \sum_{k=1}^{\infty} \mathsf{S}_{0\to k}\, \varphi^{(k)}(z)\, \mathrm{e}^{-kA/z} \right), \tag{3.7}$$

which tells us that the Borel summation along one side of the Stokes line is equal to the resummation along the other side when we modify the asymptotic expansion in the appropriate way. This is a manifestation of *Stokes phenomenon.* Using the *Stokes automorphism* $\mathfrak{S}$ defined by $\mathcal{S}_+ = \mathcal{S}_- \circ \mathfrak{S}$, – recall Eq. (2.11) – we can write an equivalent statement in terms of asymptotic expansions which reads

$$\mathfrak{S}\varphi^{(0)}(z) = \varphi^{(0)}(z) - \sum_{k=1}^{\infty} \mathsf{S}_{0\to k}\, \varphi^{(k)}(z)\, \mathrm{e}^{-kA/z}. \tag{3.8}$$

Similarly, for Eq. (3.4), the action of the Stokes automorphism Eq. (3.8) generalizes to

$$\mathfrak{S}\varphi^{(k)}(z) = \varphi^{(k)}(z) - \sum_{\ell=1}^{\infty} \mathsf{S}_{k\to k+\ell}\, \varphi^{(k+\ell)}(z)\, \mathrm{e}^{-\ell A/z}\,, \tag{3.9}$$

for generic sectors $\varphi^{(k)}$. Comparing to Eq. (2.35), we see that we obtained a similar formula for Stokes' automorphism, where the Borel residues are replaced by the statistical factor. To be precise:

$$\mathrm{SF}_{n\to m} = -\mathsf{S}_{n\to m}\,, \tag{3.10}$$

which also yields a formula to compute Borel residues in the case of a one-parameter transseries – recall example 2.3.2.

So far, we have not made any assumptions about an underlying transseries, but the above expressions Eqs. (3.8) and (3.9) show that it is useful to unite the formal,

---

[2] Here, we have exchanged the order of summation over k and integration in t. This is an operation that, especially in a resurgence setting, has to be treated with care, but since the sums over k (as opposed to those over g) generally have a nonzero radius of converge, this exchange of sums and integrals can often be put on solid footing.

asymptotic power series $\varphi^{(n)}$ in a transseries,

$$\Phi(\vec{\sigma}, z) = \sum_{n=0}^{\infty} \sigma_n \, \varphi^{(n)}(z) \, \mathrm{e}^{-nA/z} \,. \tag{3.11}$$

In the above expression we have assigned weigths σ_n, i.e. the transseries parameters, to each transseries sector $\varphi^{(n)}$; these are all collected in the single vector $\vec{\sigma}$ on the left hand side. The advantage of introducing these parameters is that we can now also view any asymptotic expansion before the Stokes jump Eq. (3.9) – that is, simply $\varphi^{(k)}$ – as a transseries with $\sigma_n = \delta_{n,k}$. In fact, one may be more general and think of the Stokes automorphism as mapping one transseries expansion – with particular values of σ_n and summed above the Stokes line using the $\mathcal{S}_+$ procedure – to another one – with other values of σ_n and summed below the Stokes line using the $\mathcal{S}_-$ procedure.

Using the transseries notation, we can write the action of the Stokes automorphism as an action on the transseries parameters:

$$\mathfrak{S}\Phi(\vec{\sigma}, z) = \Phi(\mathbb{S} \cdot \vec{\sigma}, z) \,. \tag{3.12}$$

Effectively, we are multiplying the (infinite) vector $\vec{\sigma}$ with an (infinite) lower-triangular *Stokes matrix* $\mathbb{S}$ whose elements are given by the Borel residues

$$(\mathbb{S})^{n}{}_{m} = \begin{cases} -\mathsf{S}_{m\to n} & \text{for } m < n \\ 1 & \text{for } m = n \\ 0 & \text{for } m > n \,, \end{cases} \qquad = \begin{pmatrix} 1 & 0 & 0 & \cdots \\ -\mathsf{S}_{0\to 1} & 1 & 0 & \cdots \\ -\mathsf{S}_{0\to 2} & -\mathsf{S}_{1\to 2} & 1 & \cdots \\ \cdots & \cdots & \cdots & \cdots \end{pmatrix} \tag{3.13}$$

for integers $m, n \geq 0$. In particular, this means that we have the following action on a single transseries parameter

$$\mathfrak{S} : \sigma_n \mapsto \sigma_n - \sum_{m=0}^{n-1} \sigma_m \mathsf{S}_{m\to n} \,. \tag{3.14}$$

This generic description expresses the Stokes phenomenon in terms of an *infinite* set of Borel residues.

Example 3.1.1. *In section 3.3 we will introduce the quartic free energy – a popular toy model to study resurgence (see e.g. [71]). Throughout this section and the next, we will occasionally refer forward to aspects of this example to clarify the material. The* *quartic free energy has a two-parameter transseries solution that can be written as*

$$F(x,\sigma,\rho) = \sum_{n=0}^{\infty} \sigma^n F^{(n)}(x) \mathrm{e}^{-nA/x} + \rho\,, \tag{3.15}$$

where the $F^{(n)}(x)$ *are formal power series in* x*. Their Borel transforms have a Stokes line along the positive real axis and therefore* $F(x,\sigma,\rho)$ *undergoes a Stokes transition. Despite the fact that there are an infinite number of transseries sectors* $F^{(n)}$*, it turns out that setting* $\sigma_n = \sigma^n$ *is a convenient parametrization under which the Stokes automorphism along the* $\arg(x) = 0$ *direction acts as*

$$\mathfrak{S}_0 F(x,\sigma,\rho) = F(x,\sigma + S_1,\rho)\,. \tag{3.16}$$

Thus we can reduce the number of degrees of freedom for this particular transition to one parameter σ *and one Stokes constant* S_1*. These relate to our generic formulation* (3.11) *and* (3.9) *when*

$$\mathsf{S}_{k\to k+l} = -\binom{k+l}{k} S_1^l\,. \tag{3.17}$$

The second parameter ρ *is irrelevant for the above argument; it only plays a role when we consider another Stokes transition across the negative real axis.*

3.1.2. Multivalued Borel residues

As we mentioned in Sec. 3.1.1, the Borel residues $\mathsf{S}_{k\to k+\ell}$ depend on the path along which we analytically continue the Borel transforms from one point to another. In computing the discontinuity along a Stokes line, Eq. (3.6), we assumed that the Hankel contours run off to infinity *below* the Stokes line, meaning that we could use the Borel residues $\mathsf{S}_{k\to k+\ell}$ as defined by paths *above* the Stokes line – the convention in the left of Fig. 3.3. Alternatively, we could consider diagonal Hankel contours *above* the Stokes line, in which case we would need to use a different set of residues that we denote by $\tilde{\mathsf{S}}_{k\to k+\ell}$ and which correspond to analytic continuation of the Borel transforms along paths *below* the Stokes line, as in Fig. 3.3 on the right.

To relate the two sets of Borel residues, we observe that both choices should describe the same discontinuity:

$$\begin{aligned}\text{Disc}\ \varphi^{(0)} &= -\mathcal{S}_-\left(\sum_{k=1}^{\infty}\mathsf{S}_{0\to k}\varphi^{(k)}\mathrm{e}^{-kAz}\right) = -\mathcal{S}_-\left(\mathfrak{S}-1\right)\varphi^{(0)} \\ &= -\mathcal{S}_+\left(\sum_{k=1}^{\infty}\tilde{\mathsf{S}}_{0\to k}\varphi^{(k)}\mathrm{e}^{-kAz}\right) = -\mathcal{S}_+\left(1-\mathfrak{S}^{-1}\right)\varphi^{(0)}\,. \end{aligned} \tag{3.18}$$

The top (bottom) line in this equation is obtained by letting the Hankel contours run to infinity below (above) the real line, as shown by the diagrams in the top (bottom) of Fig. 3.4. Eq. (3.18) implies that two conventions lead to two *distinct* transseries expansions that after the appropriate lateral resummation should reproduce the *same* discontinuity. Hence, these respective transseries must consist of different linear combinations of the formal power series $\varphi^{(k)}$, and therefore they are defined by two distinct sets of residues $\{\mathsf{S}_{k\to k'}\}$ and $\{\tilde{\mathsf{S}}_{k\to k'}\}$. To reproduce the same discontinuity, the two transseries expressions should be related via

$$\mathfrak{S}\left(\sum_{k=1}^{\infty}\tilde{\mathsf{S}}_{0\to k}\varphi^{(k)}\mathrm{e}^{-kAz}\right) = \sum_{k=1}^{\infty}\mathsf{S}_{0\to k}\varphi^{(k)}\mathrm{e}^{-kAz}. \tag{3.19}$$

If we know one set of residues, we can derive the other set straightforwardly by using this equation and the Stokes automorphism Eq. (3.9). Using the Stokes matrix $\mathbb{S}$ we can interpret the above equation as saying that

$$\mathbb{S}\cdot\begin{pmatrix}0\\ \tilde{\mathsf{S}}_{0\to 1}\\ \tilde{\mathsf{S}}_{0\to 2}\\ \tilde{\mathsf{S}}_{0\to 3}\\ \dots\end{pmatrix} = \begin{pmatrix}0\\ \mathsf{S}_{0\to 1}\\ \mathsf{S}_{0\to 2}\\ \mathsf{S}_{0\to 3}\\ \dots\end{pmatrix} \tag{3.20}$$

Solving this equation for the first three Borel residues $\tilde{\mathsf{S}}_{0\to k}$, we find that

$$\begin{aligned}\tilde{\mathsf{S}}_{0\to 1} &= \mathsf{S}_{0\to 1}\\ \tilde{\mathsf{S}}_{0\to 2} &= \mathsf{S}_{0\to 2}+\mathsf{S}_{0\to 1}\mathsf{S}_{1\to 2}\\ \tilde{\mathsf{S}}_{0\to 3} &= \mathsf{S}_{0\to 3}+\mathsf{S}_{0\to 1}\mathsf{S}_{1\to 3}+\mathsf{S}_{0\to 2}\mathsf{S}_{2\to 3}+\mathsf{S}_{0\to 1}\mathsf{S}_{1\to 2}\mathsf{S}_{2\to 3}\,. \end{aligned} \tag{3.21}$$

The general solution is

$$\tilde{\mathsf{S}}_{k\to k+\ell} = \sum_{r=1}^{\ell} \sum_{k=k_0<\ldots<k_r=k+\ell} \prod_{j=0}^{r-1} \mathsf{S}_{k_j\to k_{j+1}} \,. \tag{3.22}$$

Note that all the 'one-step' residues $\mathsf{S}_{k\to k+1} = \tilde{\mathsf{S}}_{k\to k+1}$ are equal. This is as expected, since their respective paths are in the same homotopy class (see figure 3.3). Of course, for the 'multi-step' residues, we could have chosen even more complicated homotopy classes for the paths, going above some singularities and below others, or even circling the singularities several times – but the two conventions above are clearly the most natural ones. Regardless of the conventions that we pick, any complete set of residues contains the same information about the resurgence relations (3.3) as any other complete set.

Example 3.1.2. *For the quartic free energy, whose Borel residues* $\mathsf{S}_{k\to k+\ell}$ *were given in* (3.17)*, one can also calculate the alternative set of Borel residues using* (3.22)*, leading to*

$$\tilde{\mathsf{S}}_{k\to k+\ell} = (-1)^{\ell} \binom{k+\ell}{k} S_1^{\ell} \,. \tag{3.23}$$

These are again expressed in powers of a single Stokes constant S_1*.*

3.1.3. Derivation of large order formulas

We already derived large order relations in Sec. 2.5, but let us now give a slightly different derivation in terms of Borel residues to keep the discussion as generic as possible. Again, we use Cauchy's theorem to write

$$\begin{aligned} \frac{\varphi_g^{(0)}}{g!} &= \oint_0 \frac{\mathrm{d}t}{2\pi\mathrm{i}} \frac{\mathcal{B}[\varphi^{(0)}](t)}{t^{g+1}} && (3.24) \\ &= \sum_{k\geq 1} \mathsf{S}_{0\to k} \int_{H_{kA}^-} \frac{\mathrm{d}t}{(2\pi\mathrm{i})^2} \frac{\mathcal{B}[\varphi^{(k)}](t-kA)}{t^{g+1}} \log(t-kA) + \oint_\infty \frac{\mathrm{d}t}{2\pi\mathrm{i}} \frac{\mathcal{B}[\varphi^{(0)}](t)}{t^{g+1}} \,, && (3.25) \end{aligned}$$

where in the second line we deformed the contour around $t=0$ to a contour around infinity and in the process picked up various Hankel contours associated to singularities that the Borel transform has. Given our definition of the Stokes automorphism, each of these Hankel contours H_{kA}^- grabs the k-th singularity located at kA and 'leaves' the Borel plane below the positive real axis – as shown in figure 3.4. For the rest of this computation we will assume that the contribution around infinity vanishes and therefore ignore it – but we will come back to this assumption in Secs. 3.2.4 and 3.3.3.

By an appropriate shift, the right hand side can now be rewritten as

$$\frac{\varphi_g^{(0)}}{g!} = -\sum_{k\geq 1} \mathsf{S}_{0\to k} \int_0^{\infty - \mathrm{i}\epsilon} \frac{\mathrm{d}t}{2\pi\mathrm{i}} \, \frac{\mathcal{B}[\varphi^{(k)}](t)}{(t+kA)^{g+1}} \,, \tag{3.26}$$

where ϵ is an infinitesimally small positive number, causing the contour to run below the singularities. We can then replace the Borel transforms by their Taylor series around $t = 0$ and integrate term by term with respect to t, which produces the familiar asymptotic large order relations that read[3]

$$\frac{2\pi\mathrm{i}\, \varphi_g^{(0)} A^g}{\Gamma(g)} \simeq -\sum_{k\geq 1} \mathsf{S}_{0\to k} k^{-g} \sum_{h\geq 0} \frac{\Gamma(g-h)}{\Gamma(g)} (kA)^h \varphi_h^{(k)} \,. \tag{3.27}$$

This is the same form of the large order formulas that we already derived in Sec. 2.5, but with the statistical factor replaced by minus the Borel residues.

3.2. Resurgence of the large order transseries

We finished the previous section with the usual form of the large order relation, connecting the coefficients in the perturbative sector of a transseries to the coefficients in its nonperturbative sectors. An important observation (already underlying e.g. [27]) is now that this formula itself has the form of a transseries: by writing

$$k^{-g} = e^{-g\log(k)} \tag{3.28}$$

we see that it has 'instanton actions' $\log(2), \log(3), \log(4)$ etc. We shall call this transseries the *large order transseries*. The nature of this transseries is slightly different from the ones we have discussed so far, though; in particular, the instanton actions are not all integer multiples of a finite set of 'basis actions', and they are (by the nature of the logarithmic function) not single-valued. One may therefore wonder about the resummation of this transseries, whether it also has a Stokes automorphism, how its Stokes data are related to those of the original transseries, and so on. It is to those questions that we turn in this section.

---

[3] To anticipate our discussion in section 3.2.4, where we will want to extend these expressions to complex values of g, we already write $\Gamma(g)$ rather than $(g-1)!$ on the left hand side of this equation.

3.2.1. The Stirling transform

For each k in the large order transseries Eq. (3.27), the ratios of gamma functions can be expanded in powers of $1/g$. This yields a formal power series in $1/g$ for each k, whose coefficients encode the perturbative fluctuations $\varphi_h^{(k)}$ around the k-th instanton sector. For $k = 1$, the first few terms of this series read

$$-\mathsf{S}_{0\to 1}\left(\varphi_0^{(1)} + \frac{A\varphi_1^{(1)}}{g} + \frac{A\varphi_1^{(1)} + A^2\varphi_2^{(1)}}{g^2} \right. \\ \left. + \frac{A\varphi_1^{(1)} + 3A^2\varphi_2^{(1)} + A^3\varphi_3^{(1)}}{g^3} + \mathcal{O}(g^{-4})\right) . \tag{3.29}$$

Because the 1-instanton coefficients $\varphi_h^{(1)}$ grow factorially as h becomes large, the above power series will generically be asymptotically divergent as well. In fact, this is the case for all k-sectors in the large order relation Eq. (3.27).

Working out a few more orders in Eq. (3.29), we find that the integer coefficients appearing in the series correspond to *Stirling numbers of the second kind* [72]. The above series therefore constitutes what we will call a *rescaled Stirling transform* of the first instanton series. Let us elaborate: a formal power series $\psi(z) = \sum_{n\geq 0} a_n z^{-n}$ defines a sequence of coefficients a_n whose Stirling transform is another sequence of coefficients b_n defined by

$$b_n = \sum_{k=0}^{n} \left\{ {n \atop k} \right\} a_k \,, \tag{3.30}$$

where the integers $\left\{ {n \atop k} \right\}$ are the Stirling numbers of the second kind; see App. A.2 for a definition. We then say that the formal power series

$$\tilde{\psi}(g) = \sum_{n=0}^{\infty} b_n g^{-n} \tag{3.31}$$

is the Stirling transform of the series $\psi(z)$. Furthermore, we can rescale the argument $z \to z/A$ in $\psi(z)$ to obtain a new series in z^{-1}:

$$\psi\left(\frac{z}{A}\right) = \sum_{n=0}^{\infty} \left(a_n A^n\right) z^{-n} \,. \tag{3.32}$$

Finally, we introduce a formal power series $\hat{\psi}(g)$ which is the Stirling transform of this rescaled series, and which looks as follows:

$$\begin{aligned} \hat{\psi}(g) &= \sum_{n=0}^{\infty}\sum_{k=0}^{n}\left\{ {n \atop k} \right\}\left(a_k A^k\right) g^{-n} \\ &= a_0 + \frac{Aa_1}{g} + \frac{Aa_1 + A^2 a_2}{g^2} + \frac{Aa_1 + 3A^2 a_2 + A^3 a_3}{g^3} + \mathcal{O}(g^{-4})\,. \end{aligned} \tag{3.33}$$

This series is what we call the rescaled Stirling transform of $\psi(z)$ and it matches exactly the series expansion (3.29) of the large order relation (3.27). If we now identify the coefficients a_h with the coefficients $\varphi_h^{(1)}$ of the one-instanton sector of our original transseries, then we conclude that the asymptotic expansion for $k = 1$ in Eq. (3.27) is the rescaled Stirling transform of that one-instanton series. More generally, the asymptotic expansion in $1/g$ of the large order transseries in its nonperturbative sector multiplying $k^{-g} = e^{-g \log k}$ can be expressed as a rescaled Stirling transform of the k-instanton series of the original transseries, where the scaling factor is kA instead of A.

Having understood that the asymptotic expansions appearing in the large order relations are actually rescaled Stirling transforms of the original instanton series, we can define

$$\hat{\varphi}^{(k)}(g) = \sum_{n=0}^{\infty}\sum_{\ell=0}^{n}\left\{ {n \atop \ell} \right\}\left(\varphi_\ell^{(k)}\,(kA)^\ell\right) g^{-n}\,, \tag{3.34}$$

and rewrite the asymptotic large order relations (3.27) as

$$\frac{2\pi\mathrm{i}\varphi_g^{(0)} A^g}{\Gamma(g)} \simeq -\sum_{k=1}^{\infty} \mathsf{S}_{0\to k}\hat{\varphi}^{(k)}(g)\,\mathrm{e}^{-g\log(k)}\,. \tag{3.35}$$

Thus, Eq. (3.35) allows us to order the contributions by size where the one-instanton coefficients $\varphi_h^{(1)}$ determine the leading expansion in $1/g$, and higher instanton coefficients $\varphi_h^{(k)}$ determine nonperturbative contributions to the large order transseries that are exponentially suppressed as $\mathrm{e}^{-g\log(k)}$.

Example 3.2.1. *Let us test Eq.* (3.35) *by performing a resurgent large order analysis at leading instanton order* $k = 1$*. (We will perform tests for higher* k *below in example 3.2.4.) To this end (see also [71]), we study the large order growth of perturbative coefficients* $F_g^{(0)}$ *of the quartic free energy, which we already briefly introduced in example 3.1.1.*

The large order relation for the quartic free energy is exactly of the form of Eq. (3.35)*, with instanton sectors* $F^{(k)}$ *that carry an instanton action* $A = 3/2$ *and with Borel residues* $\mathsf{S}_{0\to k}$ *expressed in terms of a Stokes constant* $S_1 = -2$ *by Eq.* (3.17)*. To test Eq.* (3.35)*, we call the sequence on the left hand side of this equation* r_g *and plot the ratio*

$$\frac{r_g}{S_1 \hat{\varphi}_0^{(1)}} \simeq 1 + \mathcal{O}(g^{-1})\,, \tag{3.36}$$

for g up to 500 in the first plot of Fig. 3.5. This indeed convergences towards 1 as g becomes large. Likewise, in the second plot, we test the expected subleading g^{-1}*-behaviour by plotting the ratio*

$$g\frac{r_g - S_1 \hat{\varphi}_0^{(1)}}{S_1 \hat{\varphi}_1^{(1)}} \simeq 1 + \mathcal{O}(g^{-1})\,, \tag{3.37}$$

which again converges towards 1 in the large g limit. We can similarly test the g^{-N} *contributions to the leading sector of Eq.* (3.35) *by summing the right hand side of Eq.* (3.34) *(for* $k = 1$*) up to order* $n = N - 1$*. We then plot the difference between the (exact) left and (truncated) right hand side of Eq.* (3.34) *for values of g up to 500, where we divide by the expected* g^{-N} *contribution at that order so that we expect the rescaled difference to become 1 at large g. In Fig. 3.5 we see that indeed both sides of Eq.* (3.35) *match up to order* g^{-12} *(where the only reason to stop is not to make the figure too large), confirming the validity of the Stirling numbers appearing in Eq.* (3.34)*.*

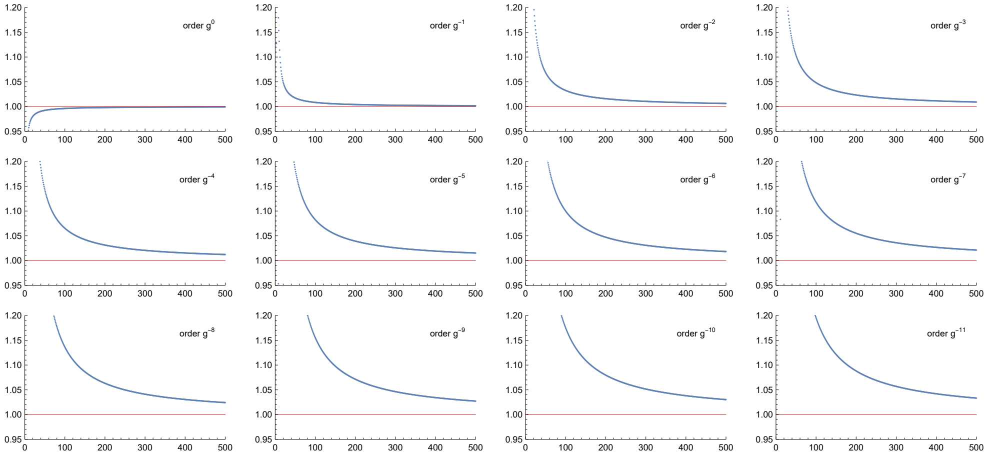

Figure 3.5.: A test of the rescaled Stirling transform appearing in Eq. (3.35), for the leading $k = 1$ sector and up to order g^{-12}.

At this point, we have established how the large order transseries (3.35) is constructed in terms of the instanton coefficients $\varphi_h^{(k)}$ of the original transseries. Still, the question remains whether the newly constructed large order transseries is truly a *resurgent* transseries, in the sense that the Borel transforms of its formal power series $\hat{\varphi}^{(k)}(g)$ know about each other like the original series $\varphi^{(k)}(g)$ do in Eq. (3.4). In order to answer this question, we want to derive similar resurgence relations for the Borel transforms of the rescaled Stirling transforms $\hat{\varphi}^{(k)}$. The first question to address is therefore what the Borel planes of these series look like.

It so happens that the Stirling transforms of functions have a rather interesting property when it comes to their Borel transforms: consider the Stirling transform $\tilde{\psi}(g)$ – defined through Eqs. (3.30) and (3.31) from the series $\psi(z)$. Its Borel transform, assuming as usual that it converges and through analytic continuation defines a function, has the following simple form:

$$\mathcal{B}_0[\,\tilde{\psi}\,](t) = \mathcal{B}_0[\,\psi\,](\mathrm{e}^t - 1)\,. \tag{3.38}$$

Two remarks are in order. First of all, notice that this simple form of the Borel transform is true for the 0-Borel transform. Its generic n-Borel transform is straightforwardly obtained through differentiation – see App. A.1-A.2 – yielding a Borel transform that is less simple. To keep the formulas concise, we therefore switch to the 0-Borel transform from now on in the remainder of this chapter and leave out the subscript. Subsequently, the rescaled Stirling transform $\hat{\psi}(g)$ given by Eq. 3.33, also has a Borel transform that relates to $\mathcal{B}[\,\psi\,]$ as follows:

$$\mathcal{B}[\,\hat{\psi}\,](t) = \mathcal{B}[\,\psi\,]\left(A(\mathrm{e}^t - 1)\right)\,. \tag{3.39}$$

As a result, we find that the 0-Borel transforms of the asymptotic series $\hat{\varphi}^{(k)}(g)$ appearing in the large order relations can be expressed explicitly in terms of the Borel transforms of the original instanton series $\varphi^{(k)}$, using their proper rescaling:

$$\mathcal{B}[\hat{\varphi}^{(k)}](t) = \mathcal{B}[\varphi^{(k)}]\left(kA(\mathrm{e}^t - 1)\right)\,. \tag{3.40}$$

We provide derivations of these statements in App. A.2.

The above relations already reveal the underlying reason for the appearance of the towers of singularities in the Borel plane that we discussed in the introduction: the Borel transforms (3.40) of the rescaled Stirling series are functions of e^t and are therefore invariant under $t \to t + 2\pi\mathrm{i}$. As a result, any singularity in the Borel plane of the original instanton series $\mathcal{B}[\varphi^{(k)}]$ reappears as a tower of evenly spaced singularities in the Borel plane of $\mathcal{B}[\hat{\varphi}^{(k)}]$. As we explain in the next subsection, this 'translational symmetry' also explains why it makes sense to write k^{-g} as $\mathrm{e}^{-g\log(k)}$ in terms of the 'multivalued instanton action' $\log(k)$ in the large order transseries (3.35).[4]

3.2.2. Resurgent structure

Now that we have seen that the Borel transforms of the rescaled Stirling transforms of the $\varphi^{(k)}(z)$ can be expressed in terms of the Borel transforms of these instanton series themselves, we can derive resurgence relations like Eq. (3.4) for the rescaled Stirling transforms. Using Eq. (3.40), we obtain

$$\begin{aligned}
\mathcal{B}[\hat{\varphi}^{(k)}](t) &= \mathcal{B}[\varphi^{(k)}]\big(kA(\mathrm{e}^t-1)\big) \qquad (3.41)\\
&= \frac{\mathsf{S}_{k\to k+\ell}}{2\pi\mathrm{i}}\mathcal{B}[\varphi^{(k+\ell)}]\big(kA(\mathrm{e}^t-1)-\ell A\big)\log\big(kA(\mathrm{e}^t-1)-\ell A\big)+\text{regular}\\
&= \frac{\mathsf{S}_{k\to k+\ell}}{2\pi\mathrm{i}}\mathcal{B}[\hat{\varphi}^{(k+\ell)}]\left(t-\log\left(\frac{k+\ell}{k}\right)\right)\log\left(t-\log\left(\frac{k+\ell}{k}\right)\right)+\text{regular}\,,
\end{aligned}$$

where in going from the first to the second line we expanded $s\equiv kA(\mathrm{e}^t-1)$ around $s=\ell A$ using the ordinary resurgence relations Eq. (3.4). In the last line we expanded the logarithm around $s=\ell A$ and used Eq. (3.40) to go back to the Borel transform of $\hat{\varphi}^{(k+\ell)}$. Notice that we are just interested in the singular terms in these expressions; the higher order terms in the expansion of the logarithm only yield regular terms, since they multiply a Borel transform which is analytic at $s=\ell A$.

The resurgence relations given in Eq. (3.41) for the transseries sectors $\hat{\varphi}^{(k)}$ of the large order transseries are quite similar to Eq. (3.4) which describe the resurgence of the original transseries sectors $\varphi^{(k)}$. We observe in particular that the large order transseries sectors labeled by k and $k+\ell$ are connected by the same Borel residues $\mathsf{S}_{k\to k+\ell}$ that occurred for the original transseries. An important difference lies in the fact that the locations of the Borel singularities are completely different from those of the original transseries. Within the original transseries, the k-instanton sector knows about the $(k+\ell)$-sector by expanding $\mathcal{B}[\varphi^{(k)}](t)$ around $t=\ell A$. In the case of our large order transseries, the k-sector knows about the $(k+\ell)$-sector by expanding $\mathcal{B}[\hat{\varphi}^{(k)}](t)$ around $t=\log\left(\frac{k+\ell}{k}\right)$. In fact, due to the $t\sim t+2\pi\mathrm{i}$ symmetry of Eq. (3.40), we can add any integer multiple of $2\pi\mathrm{i}$ to the location of a given singularity of $\mathcal{B}[\hat{\varphi}^{(k)}](t)$ to find another singularity from which the same $(k+\ell)$-sector resurges with the same Borel residue $\mathsf{S}_{k\to k+\ell}$.

---

[4] In a different context, the change of variables $s=kA(\mathrm{e}^t-1)$ is the *uniformizing map* in [61] for a Borel transform with a single singularity at $s=-kA$.

Summarizing this discussion, the Borel transform $\mathcal{B}[\hat{\varphi}^{(k)}](t)$ will have singularities at

$$\mathcal{A}^{(k)}_{\ell,n} = \log\left(\frac{k+\ell}{k}\right) + 2\pi\mathrm{i}n \qquad \text{for } k+\ell>0\ ,\ \ell\neq 0 \text{ and } n\in\mathbb{Z}\,, \tag{3.42}$$

from which the $(k+\ell)$-sector resurges with residue $\mathsf{S}_{k\to k+\ell}$. When we lift the condition that $k+\ell>0$, which happens for example in the case with two opposite primitive instanton actions $A_1=-A_2$, we can also get singularities at

$$\tilde{\mathcal{A}}^{(k)}_{\ell,n} = \log\left(-\frac{k+\ell}{k}\right) + (2n+1)\pi\mathrm{i} \qquad \text{for } k+\ell<0\ ,\ \ell\neq 0 \text{ and } n\in\mathbb{Z}\,. \tag{3.43}$$

This pattern of singularities is for example relevant for the plots shown in Fig. 3.1 at the beginning of this chapter. One can write similar formulas for more general cases (which we will not consider further in this thesis) when there are several primitive instanton actions $A_1, A_2, \ldots$, even when there is no relation between them, where the addition of πi in Eq. (3.43) changes.

Using the above notation, the resurgence relations in Eq. (3.41) can be written compactly as

$$\mathcal{B}[\hat{\varphi}^{(k)}](t)\bigg|_{t=\mathcal{A}^{(k)}_{\ell,n}} = \frac{\mathsf{S}_{k\to k+\ell}}{2\pi i}\ \mathcal{B}[\hat{\varphi}^{(k+\ell)}]\left(t-\mathcal{A}^{(k)}_{\ell,n}\right)\ \log\left(t-\mathcal{A}^{(k)}_{\ell,n}\right) + \text{regular}\,, \tag{3.44}$$

which also makes the similarity to Eq. (3.4) more manifest. As for ‘ordinary’ resurgence, these large order resurgence relations tell us that when we integrate around any singularity $\mathcal{A}^{(k)}_{\ell,n}$ in the Borel plane, we can extract the formal power series $\hat{\varphi}^{(k+\ell)}$. In the spirit of Sec. 3.1, this suggests that we should unite all these series into what we call the *generic large order transseries*

$$\Phi(\sigma_{k,n}, g) = \sum_{n=-\infty}^{\infty}\sum_{k=1}^{\infty}\sigma_{k,n}\ \hat{\varphi}^{(k)}(g)\,\mathrm{e}^{-g\mathcal{A}^{(1)}_{k,n}} = \sum_{n=-\infty}^{\infty}\Phi_n(\vec{\sigma}_n, g)\,. \tag{3.45}$$

The parameters $\sigma_{k,n}$ are again transseries parameters associated to sectors (k,n). In Sec. 3.2.3 we will see how the Stokes automorphism acts on these parameters. In anticipation of what is to come, it is also useful to write the above *full transseries* Φ, as an infinite sum over ‘horizontal’ *subtransseries* Φ_n. The large order transseries Eq. (3.35) is then obtained by setting $\sigma_{k,n}=-\mathsf{S}_{0\to k}\delta_{n,0}$. Note that the locations $\mathcal{A}^{(k)}_{\ell,n}$ of the Borel singularities in the k-th Borel plane correspond to the relative *distances* between the instanton actions of the sectors $(k+\ell, m+n)$ and (k,m) in the large order transeries:

$$\mathcal{A}^{(k)}_{\ell,n} = \mathcal{A}^{(1)}_{k+\ell,m+n} - \mathcal{A}^{(1)}_{k,m}\,, \tag{3.46}$$

for arbitrary integers m. These distances are visible in the Borel plane of the leading sector – see also the singularities shown in Fig. 3.1. The fact that the singularities of the Borel transforms correspond to relative distances between instanton actions holds in general, but is often concealed by the fact that in ordinary transseries these actions lie on a semi-lattice generated by a single primitive instanton action A. For the large order transseries, on the other hand, there are infinitely many primitive instanton actions $\log(p)$ for p prime.

We conclude that the large order transseries is truly a resurgent transseries, just like the original transseries. The only differences are that its singularities no longer depend on the instanton action A of the original transseries, and that each singularity associated to a sector $k+\ell$ is copied at locations shifted by integer multiples of $2\pi\mathrm{i}$ in the Borel plane of $\mathcal{B}[\hat{\varphi}^{(k)}]$. The domain of the variable t in terms of which the Borel transforms $\mathcal{B}[\hat{\varphi}^{(k)}]$ are defined is thus effectively a cylinder that we will henceforth call the *Borel cylinder*. This cylinder provides the best way to structure the singularities found in Figs. 3.1 and 3.2 that we encountered at the beginning of this chapter; we discuss this further in example 3.2.2 below.

Example 3.2.2. *Let us see whether in examples we can reproduce the singularity structure* $\mathcal{A}^{(k)}_{\ell,n}$ *and* $\tilde{\mathcal{A}}^{(k)}_{\ell,n}$ *that is described in Eqs.* (3.42) *and* (3.43). *Since we do not have closed form expressions for the various Borel transforms, we make use of Padé approximants – see Sec. 2.7.2 – to mimic their singularity structure. The singularities* $\mathcal{A}^{(1)}_{\ell,n}$ *and* $\tilde{\mathcal{A}}^{(1)}_{\ell,n}$*, as approximated by the Padé approximant of* $\mathcal{B}[\hat{\varphi}^{(1)}]$*, were already shown in Figs. 3.1 and 3.2 at the beginning of this chapter, for the Adler function and the quartic free energy respectively. As further evidence for the structure, we also consider the second rescaled Stirling transform for the quartic free energy. In Fig. 3.6 we plot the singularities of the Padé approximant of the Borel transform* $\mathcal{B}[\hat{F}^{(2)}]$ *of this series.*

Starting with Fig. 3.1a for the Adler function, we clearly observe singularities at the anticipated positions $t = \mathcal{A}^{(1)}_{\ell,n}$ *with* $\ell = 1, 2$. *For Fig. 3.1b, besides singularities at* $t = \mathcal{A}^{(1)}_{\ell,n}$ *with* $\ell = 2$, *we also notice singularities at positions* $t = \tilde{\mathcal{A}}^{(1)}_{\ell,n}$ *, with* $\ell = 1, 2$. *This is a consequence of the fact that the Adler function has two opposite primitive instanton actions* $A_1 = -A_2$, *which as we have explained leads to additional contributions in the large order relation* (3.35) *that scale with* $(-k)^{-g} = e^{-g\log(k)\pm\pi\mathrm{i}}$, *leading in turn to Eq.* (3.43).

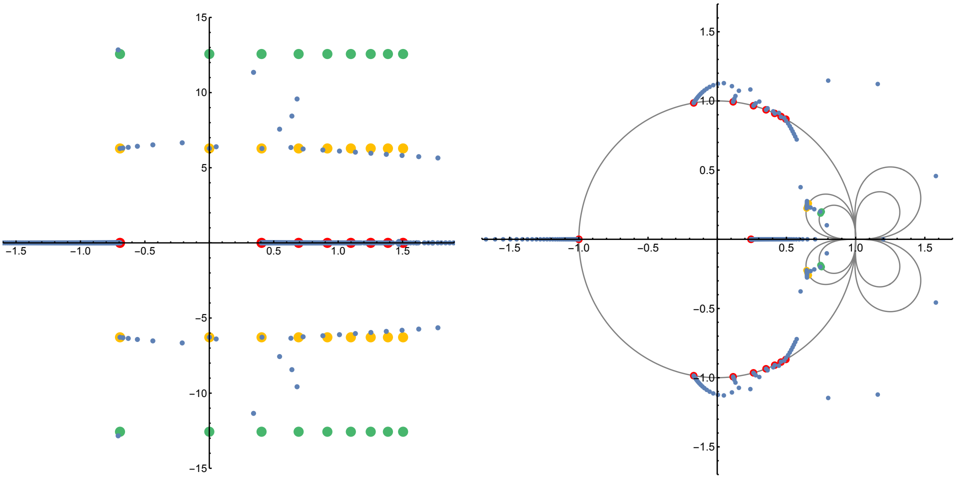

(a) **(b)**

Figure 3.6.: In (a), we show the singularities of the diagonal order 800 Padé approximant of $\mathcal{B}[\hat{F}^{(2)}](t)$. As the branch cuts are mimicked by an accumulation of poles, the poles corresponding to different branch cuts on the real line are hard to distinguish. We therefore show in (b) the order 300 diagonal Padé approximant of $\mathcal{B}[\hat{F}^{(2)}]$ after applying the conformal map of Eq. (3.47). The branch cuts positioned on the positive real line are now pulled apart as they are mapped to the unit circle. The singularity at $t = \log(1/2) = -\log(2)$ of Fig. (a) gets mapped to $z \approx 0.24$. Furthermore, the 'flower-like' curves in the z-plane correspond to $\Im(t) = \pm 2\pi\mathrm{i}$ and $\Im(t) = \pm 4\pi\mathrm{i}$. Unfortunately, the branch cut starting at $z \approx 0.24$ 'uses' many poles of the Padé approximant, so we only observe a limited number of singularities starting on these curves. As a result, the branch cuts at $\Im(t) \pm 2\pi n i$ for $n \neq 0$ are instead best viewed in the original t-plane.

For Figs. 3.2a and 3.6a we observe singularities at $t = \mathcal{A}^{(1)}_{\ell,n}$ *and* $t = \mathcal{A}^{(2)}_{\ell,n}$ *respectively. However, as the branch cuts on the real axis are mimicked by the accumulation of Padé poles along, it is hard to distinguish the branch cuts starting at different points. We have therefore applied a conformal mapping*

$$t = -\frac{4z \log\left(\frac{k+1}{k}\right)}{(1-z)^2}\,, \tag{3.47}$$

which maps the half-line $[\log\frac{k+1}{k}, \infty)$ *to the unit circle in the* z*-plane, where in particular* $t = \log\frac{k+1}{k}$ *gets mapped to* $z = -1$*. The resulting figures for the Padé approximants of these conformally mapped series are shown in Figs. 3.2b and 3.6b for* $k = 1$ *and* $k = 2$ *respectively. We observe that the branch cuts starting on the real positive* t*-axis are now pulled apart in the* z*-plane and become clearly visible.*

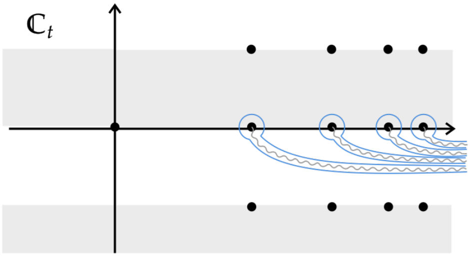

Figure 3.7.: The Hankel contours $H^{-}_{\log(1+\ell)}$ along which we integrate in Eq. (3.50).

3.2.3. Stokes automorphism

In the previous section, we have verified that the large order transseries Eq. (3.35) and its generic version Eq. (3.45) truly form *resurgent* transseries by establishing the resurgent structure (3.44) of their nonperturbative sectors. For practical purposes, we are often interested in resumming the sectors $\hat{\varphi}^{(k)}$ that appear in these large order transseries. The reason for this – as explained elaborately in chapter 5 – is that we often want to use the large order behaviour of the perturbative coefficients $\varphi_g^{(0)}$ – which may be easy to obtain in specific examples – to decode the nonperturbative coefficients $\varphi_h^{(k)}$ of the k-instanton sector, which may not be so easy to obtain by other methods, for example because the nonperturbative effects in the underlying physical problem are not *a priori* known. To achieve such a decoding, we need to first 'remove' all sectors $\hat{\varphi}^{(k')}$ for which $k' < k$ from the large order transseries before we can read off the coefficients in the k-th sector. The only effective way to do this is by resumming these series $\hat{\varphi}^{(k')}$ and substracting them from the left hand side of the large order transseries. As is so often the case, to achieve this we need to decide along which contour in the Borel plane – or here: the Borel cylinder – we resum, and different choices are related by a Stokes phenomenon. In this subsection we discuss various contours and use the resurgence relations of Eq. (3.44) as well as consistency of resummation to derive the Stokes phenomenon of the generic large order transseries.

As we saw in Eq. (3.42), the singularities of the large order transseries sectors $\hat{\varphi}^{(k)}$ accumulate along horizontal lines separated by integer multiples of $2\pi\mathrm{i}$. There are two natural resummations $\mathcal{S}_{0^+}$ and $\mathcal{S}_{0^-}$, whose contours go above and below the singularities on the real positive line respectively:

$$\mathcal{S}_{0^\pm}\hat{\varphi}^{(k)}(g) = g\int_0^{\infty\pm\mathrm{i}\epsilon} \mathcal{B}[\hat{\varphi}^{(k)}](t)\,\mathrm{e}^{-gt}\mathrm{d}t\,. \tag{3.48}$$

We can then define the discontinuity operator

$$\operatorname{Disc}_0 = \mathcal{S}_{0^+} - \mathcal{S}_{0^-}\,, \tag{3.49}$$

in order to study the Stokes phenomenon as discussed in Sec. 3.1.1. The discontinuity of the first large order transseries sector $\hat{\varphi}^{(1)}$ can readily be computed, and yields

$$\begin{aligned}\operatorname{Disc}_0 \hat{\varphi}^{(1)} &= \sum_{\ell=1}^{\infty} \mathsf{S}_{1\to 1+\ell}\; g \int_{H^-_{\log(1+\ell)}} \frac{\mathrm{d}t}{2\pi\mathrm{i}}\, \mathcal{B}[\hat{\varphi}^{(1+\ell)}](t-\log(1+\ell))\log\left(t-\log(1+\ell)\right)\mathrm{e}^{-gt} \\ &= -\sum_{\ell=1}^{\infty} \mathsf{S}_{1\to 1+\ell}\,\mathrm{e}^{-g\log(1+\ell)}\mathcal{S}_{0^-}\hat{\varphi}^{(1+\ell)}\,,\end{aligned} \tag{3.50}$$

where the Hankel contours $H^-_{\log(1+\ell)}$ are shown in Fig. 3.7. We can repeat this computation for generic sectors $\hat{\varphi}^{(k)}$ and find that

$$\operatorname{Disc}_0 \hat{\varphi}^{(k)} = -\sum_{\ell=1}^{\infty} \mathsf{S}_{k\to k+\ell}\,\mathrm{e}^{-g\log\left(\frac{k+\ell}{k}\right)}\mathcal{S}_{0^-}\hat{\varphi}^{(k+\ell)}\,. \tag{3.51}$$

Note that the instanton actions that appear correctly correspond to the singularities $\mathcal{A}^{(k)}_{l,0}$ in Eq. (3.42). From the discontinuity of the large order transseries sectors $\hat{\varphi}^{(k)}$, we extract the Stokes phenomenon

$$\mathfrak{S}_0\hat{\varphi}^{(k)} = \hat{\varphi}^{(k)} - \sum_{\ell=1}^{\infty} \mathsf{S}_{k\to k+\ell}\,\hat{\varphi}^{(k+\ell)}\,\mathrm{e}^{-g\log\left(\frac{k+\ell}{k}\right)}\,, \tag{3.52}$$

which is the direct analogue of Eq. (3.9) for the original transseries. The action of the Stokes automorphism can be formulated within the horizontal subtransseries $\Phi_n(g,\vec{\sigma}_n)$ of Eq. (3.45) as follows:

$$\mathfrak{S}_0\Phi_n\left(g,\vec{\sigma}_n\right) = \Phi_n\left(g,\mathbb{S}_0\cdot\vec{\sigma}_n\right)\,, \tag{3.53}$$

or at the level of individual transseries parameters as

$$\mathfrak{S}_0 : \sigma_{k,n} \mapsto \sigma_{k,n} - \sum_{j=1}^{k-1}\sigma_{j,n}\mathsf{S}_{j\to k}\,. \tag{3.54}$$

This mapping should be compared to Eq. (3.14) for the original transseries. The matrix $\mathbb{S}_0$ is essentially the same as $\mathbb{S}$ given in Eq. (3.13), but with the ‘zeroth’ row and column removed. Since a $\hat{\varphi}^{(0)}$ sector does not exist in the large order transseries, we can assume such a sector to vanish identically and naturally extend the Stokes matrix $\mathbb{S}_0$ to include also a $j=0$ contribution in Eq. (3.54), in which case we simply have

$$\mathbb{S}_0 = \mathbb{S}\,. \tag{3.55}$$

The equivalence of the Stokes matrix associated to the Stokes phenomenon of the large order transseries across the positive real axis, to that of the ordinary transseries, also means the following. If we consider our large order transeries (3.35) and study its Stokes phenomenon in the *anti-clockwise* direction, given by the inverse automorphism $\mathfrak{S}_0^{-1}$ or equivalently by the inverse Stokes matrix $\mathbb{S}^{-1}$, we retrieve the alternative Borel residues by virtue of Eq. (3.20):

$$\mathbb{S}^{-1}\cdot\begin{pmatrix} 0 \\ \mathsf{S}_{0\to1} \\ \mathsf{S}_{0\to2} \\ \mathsf{S}_{0\to3} \\ \cdots \end{pmatrix} = \begin{pmatrix} 0 \\ \tilde{\mathsf{S}}_{0\to1} \\ \tilde{\mathsf{S}}_{0\to2} \\ \tilde{\mathsf{S}}_{0\to3} \\ \cdots \end{pmatrix}. \tag{3.56}$$

Said otherwise, we have that

$$\mathfrak{S}_0\left(\sum_{k=1}^{\infty}\tilde{\mathsf{S}}_{0\to k}\hat{\varphi}^{(k)}(g)\mathrm{e}^{-g\log(k)}\right) = \sum_{k=1}^{\infty}\mathsf{S}_{0\to k}\hat{\varphi}^{(k)}(g)\mathrm{e}^{-g\log(k)}\,. \tag{3.57}$$

That is, the large order transseries with transseries parameters $\tilde{\mathsf{S}}_{0\to k}$ resummed *above* the positive real line (with $\mathcal{S}_{0^+}$) is equivalent to the large order transseries with parameters $\mathsf{S}_{0\to k}$ resummed *below* the positive real line (with $\mathcal{S}_{0^-}$). This equation is the direct analogue of Eq. (3.19) for the original transseries.

We can generalize the discontinuity $\mathrm{Disc}_{\,0}$, across singularitities that lie on the positive real line of the Borel plane, to Stokes transitions with discontinuities that we will label $\mathrm{Disc}_{\,n}$ and that arise from singularities $\mathcal{A}_{l,n}^{(k)}$ on other horizontal lines with fixed n – see Fig. 3.8. For completeness, let us derive the Stokes automorphisms for these transitions and see how they alter the transeries parameters $\sigma_{k,n}$.

Consider the contours shown in Fig. 3.8 on the left, which define Borel summations

$$\mathcal{S}_{n^\pm}\hat{\varphi}^{(k)}(g) = g\int_{2\pi\mathrm{i}n}^{\infty+2\pi\mathrm{i}n\pm\mathrm{i}\epsilon}\mathcal{B}[\hat{\varphi}^{(k)}](t)\,\mathrm{e}^{-gt}\mathrm{d}t\,. \tag{3.58}$$

By the symmetry of the Borel cylinder, these resummations can be related to Eq. (3.48) as follows:

$$\mathcal{S}_{n^\pm}\hat{\varphi}^{(k)}(g) = \mathrm{e}^{-2\pi \mathrm{i} n g}\mathcal{S}_{0^\pm}\hat{\varphi}^{(k)}(g)\,. \tag{3.59}$$

For integer g, the prefactor on the right hand side equals 1, reflecting the symmetry of the Borel cylinder under translations by $2\pi\mathrm{i}$. In what follows, we will also be interested in cases with non-integer g (where for real g we can mathematically think of the factors of $\mathrm{e}^{-2\pi \mathrm{i} n g}$ as transition functions on a nontrivial $U(1)$-bundle over the Borel cylinder), so we will keep these factors explicit in our formulas. We can now define discontinuities $\mathrm{Disc}_{\,n} = \mathcal{S}_{n^+} - \mathcal{S}_{n^-}$, which can be expressed as

$$\mathrm{Disc}_{\,n}\,\hat{\varphi}^{(k)}(g) = \mathrm{e}^{-2\pi \mathrm{i} n g}\,\mathrm{Disc}_{\,0}\,\hat{\varphi}^{(k)}(g)\,. \tag{3.60}$$

In terms of Stokes automorphisms we then have

$$\mathfrak{S}_n\hat{\varphi}^{(k)}(g) = \hat{\varphi}^{(k)}(g) - \mathrm{e}^{-2\pi \mathrm{i} n g}\sum_{\ell=1}^{\infty}\mathsf{S}_{k\to k+\ell}\,\hat{\varphi}^{(k+\ell)}(g)\,\mathrm{e}^{-g\log\left(\frac{k+\ell}{k}\right)}\,. \tag{3.61}$$

We note that the sectors $\varphi^{(k+\ell)}$ and the Stokes residues $\mathsf{S}_{k\to k+\ell}$ appear, as was to be expected, but with an instanton action that is shifted by $-2\pi\mathrm{i}n$.

Next, we can derive the action of this Stokes automorphism on the subtransseries of Eq. (3.35):

$$\mathfrak{S}_n\Phi_m(\vec{\sigma}_m, g) = \Phi_m(\vec{\sigma}_m, g) + \Phi_{m+n}\left((\mathbb{S}-\mathrm{I})\cdot\vec{\sigma}_m, g\right)\,, \tag{3.62}$$

where I is an infinite identity matrix. As a consistency check, note that Eqs. (3.61) and (3.62) reduce to Eqs. (3.52) and (3.53) respectively when we set $n = 0$. For the full transseries, we find that

$$\mathfrak{S}_n\Phi(\sigma, g) = \sum_{m=-\infty}^{\infty}\Phi_m(\vec{\sigma}_m + (\mathbb{S}-\mathrm{I})\cdot\vec{\sigma}_{m-n}, g)\,, \tag{3.63}$$

or at the level of individual transseries parameters we find

$$\mathfrak{S}_n : \sigma_{k,m} \mapsto \sigma_{k,m} + \sum_{j=1}^{k-1}\sigma_{j,m-n}\mathsf{S}_{j\to k}\,. \tag{3.64}$$

Having derived the actions of the Stokes automorphisms $\mathfrak{S}_n$, we can now consistently resum the (generic) large order transseries along any of the contours shown in Fig. 3.8

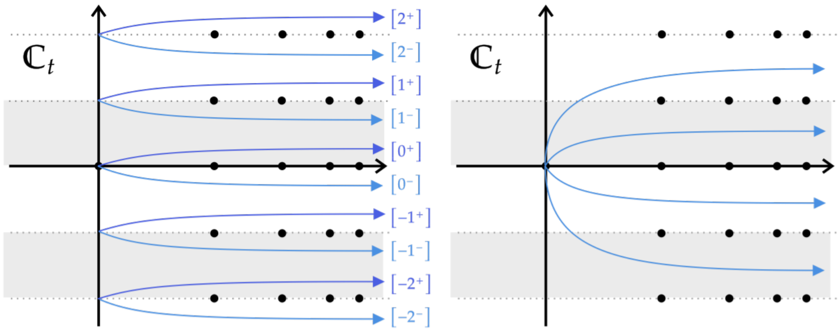

Figure 3.8.: On the left we show the contours $[n^{\pm}]$ corresponding to the resummations $\mathcal{S}_{n^{\pm}}$ defined in Eq. (3.58). Once we have derived the Stokes phenomena $\mathfrak{S}_n$ across the nth horizontal ray of singularities, we are able to resum the large order transseries along any of the contours shown on the right.

on the right, running from $t = 0$ to $t = +\infty$. Changing the contour prescription can then straightforwardly be compensated for by applying the appropriate automorphism $\mathfrak{S}_n$ to the transseries. For example, as a consequence of Eq. (3.57) we know that the following two resummations are equal:

$$\mathcal{S}_{0^+}\left(\sum_{k\geq 1}\tilde{\mathsf{S}}_{0\to k}\hat{\varphi}^{(k)}\mathrm{e}^{-g\log(k)}\right) = \mathcal{S}_{0^-}\left(\sum_{k\geq 1}\mathsf{S}_{0\to k}\hat{\varphi}^{(k)}\mathrm{e}^{-g\log(k)}\right). \tag{3.65}$$

We can extend this to any of the contours shown on the right of Fig. 3.8 using our automorphisms $\mathfrak{S}_n$.

Recall that the original motivation for resumming large order transseries sectors was to decode the higher instanton fluctuations $\varphi_h^{(k)}$ from the large order behaviour of the perturbative coefficients $\varphi_g^{(0)}$. In general we only know those coefficients for nonnegative integers g. Within that context, the factor $\mathrm{e}^{-2\pi i n g}$ therefore reduces to the identity and all Stokes automorphisms $\mathfrak{S}_n$ are equal to $\mathfrak{S}_0$. Thus, for these purposes, the discussion above simplifies greatly and we can simplify the generic large order transseries Eq. (3.45) to

$$\Phi(\vec{\sigma}_0, g) = \sum_{k=1}^{\infty} \sigma_{k,0}\,\hat{\varphi}^{(k)}(g)\mathrm{e}^{-g\log(k)}\,. \tag{3.66}$$

Example 3.2.3. *We can test the relation Eq.* (3.60) *between different discontinuities numerically for the* $k = 1$ *sector of the quartic free energy. As already explained* *in example 3.2.2, we do not have a closed form expression for the Borel transform* $\mathcal{B}[\hat{F}^{(1)}](t)$*, but we can numerically approximate this function using Padé approximants. In particular, the singularities of the Padé approximant encode the singularities of* $\mathcal{B}[\hat{F}^{(1)}](t)$*. To test Eq.* (3.60)*, we replaced* $\mathcal{B}[\hat{F}^{(1)}](t)$ *by its diaganal Padé approximant of order* N*,* $\mathcal{PB}_N[\hat{F}^{(1)}](t)$*, and performed the integration required to compute the discontinuity numerically.*

Since this computation does not require the perturbative coefficients, we can test it for any g*, not necessarily integer. In particular we have tested the relation between the discontinuities at* $n = 0$ *and* $n = -1$ *for diverse values of* g*. For example, taking* $g = 5/3$ *yields*

$$\begin{aligned} \mathrm{Disc}_{\,0}\hat{F}^{(1)}(g) &\approx -0.20236122\ldots + 0.00000000\ldots\mathrm{i}\,, \\ \mathrm{e}^{-2\pi\mathrm{i}g}\,\mathrm{Disc}_{\,-1}\hat{F}^{(1)}(g) &\approx -0.20236165\ldots + 0.00000496\ldots\mathrm{i}\,, \end{aligned} \tag{3.67}$$

which nicely matches to five decimal places. To obtain Eq. (3.67)*, we took the diagonal Padé approximant of order* $N = 800$*. This high order is necessary for producing enough singularities near* $\mathcal{A}^{(1)}_{k,-1}$ *to compute* $\mathrm{Disc}_{\,-1}\hat{F}^{(1)}(g)$ *with sufficient accuracy. Including even more terms should increase the accuracy of the match even further.*

In the next subsection we will see that ‘horizontal’ resummations like Eq. (3.65) naturally appear in the derivation of what we will call *exact large order relations.*

3.2.4. Exact large order relations

In the previous subsection we learned that the large order transseries inherits the resurgence structure – expressed in terms of the Stokes matrix $\mathbb{S}$ – from the original transseries, despite its distinct singularity structure. We derived the Stokes automorphism $\mathfrak{S}_n$ for multiple ‘horizontal’ Stokes transitions that allow us to relate the different resummation prescriptions shown in Fig. 3.8 on the right. We arrived at these results by starting with the conventional large order relation Eq. (3.27) that we derived at the end of Sec. 3.1.3. Many properties of the large order transseries that we have discussed can also be derived in a more direct way, as we demonstrate in this section.

Let us therefore take a step back and consider the large order relation in its integral form Eq. (3.26), which we repeat here for convenience and where we have again discarded the contribution from infinity:

$$\frac{\varphi^{(0)}_g}{g!} = -\sum_{k\geq 1}\mathsf{S}_{0\to k}\int_0^{\infty-\mathrm{i}\epsilon}\frac{\mathrm{d}t}{2\pi\mathrm{i}}\,\frac{\mathcal{B}[\varphi^{(k)}](t)}{(t+kA)^{g+1}}\,. \tag{3.68}$$

In Sec. 3.1.3 we asymptotically expanded the right hand side of this expression by expanding the Borel transform $\mathcal{B}[\varphi^{(k)}](t)$ as a power series in t and performing the integral term by term. Let us now present a different approach: we first introduce the variable $u = \log(t + kA)$ which allows us to rewrite the expression as

$$\frac{\varphi_g^{(0)}}{g!} = -\sum_{k\geq 1} \mathsf{S}_{0\to k} \int_{\log(kA)}^{\infty - \mathrm{i}\epsilon} \frac{\mathrm{d}u}{2\pi\mathrm{i}}\, \mathcal{B}[\varphi^{(k)}](\mathrm{e}^u - kA)\, \mathrm{e}^{-gu}\,. \tag{3.69}$$

Subsequently, we shift the integration variable to $v = u - \log(kA)$ and obtain

$$\frac{2\pi\mathrm{i}\,\varphi_g^{(0)} A^g}{\Gamma(g)} = -\sum_{k\geq 1} \mathsf{S}_{0\to k} \mathrm{e}^{-g\log(k)} \left(g \int_0^{\infty - \mathrm{i}\epsilon} \mathrm{d}v\, \mathcal{B}[\varphi^{(k)}](kA(\mathrm{e}^v - 1))\, \mathrm{e}^{-gv} \right). \tag{3.70}$$

On the right hand side we recover the Borel transform (3.40) of the rescaled Stirling transforms $\hat{\varphi}^{(k)}$ that we studied before. This equation expresses the perturbative coefficient $\varphi_g^{(0)}$ as the resummation of the large order transseries (3.35) along the contour below the positive real axis. Whenever the sum over k on the right hand side converges, which is generally the case in examples, Eq. (3.70) is an exact relation that is also valid for finite g. We will therefore call this expression the *exact large order relation* from now on.

The brief computation above reproduces much of the hard work of this section: it allows us to rederive the resurgence relations Eq. (3.44) and singularity structure Eq. (3.42) and subsequently the automorphisms $\mathfrak{S}_n$ that we found in the previous section. Most importantly, it assigns a distinct contour $[0^-]$ to our large order transseries with residues $\mathsf{S}_{0\to k}$ along which its resummation computes the correct value for the perturbative coefficients $\varphi_g^{(0)}$.

The right hand side of the exact large order relation constitutes a function of g that we can expand in a large g limit. Eq. (3.70) tells us that one possible transseries expansion is the large order transseries Eq. (3.35), which after resummation along the $[0^-]$ contour gives back the same function. If we repeat the computation above, but with Hankel contours running above the real positive t axis in Eq.(3.68) – see again the bottom graphs in Fig. 3.4 – then we obtain a similar expression:

$$\frac{2\pi\mathrm{i}\,\varphi_g^{(0)} A^g}{\Gamma(g)} = -\sum_{k=1}^{\infty} \tilde{\mathsf{S}}_{0\to k} \mathrm{e}^{-g\log(k)} \left(g \int_0^{\infty + \mathrm{i}\epsilon} \mathrm{d}v\, \mathcal{B}[\varphi^{(k)}](kA(\mathrm{e}^v - 1))\, \mathrm{e}^{-gv} \right). \tag{3.71}$$

This is simply the $[0^+]$-resummation of the large order transseries with the alternative Borel residues $\tilde{\mathsf{S}}_{0\to k}$. The resulting function is of course equal to (3.70):

$$\begin{aligned}\frac{2\pi\mathrm{i}\,\varphi_g^{(0)}A^g}{\Gamma(g)} &= \mathcal{S}_{0^+}\left(-\sum_{k=1}^{\infty}\tilde{\mathsf{S}}_{0\to k}\mathrm{e}^{-g\log(k)}\hat{\varphi}^{(k)}(g)\right)\\ &= \mathcal{S}_{0^-}\left(-\sum_{k=1}^{\infty}\mathsf{S}_{0\to k}\mathrm{e}^{-g\log(k)}\hat{\varphi}^{(k)}(g)\right)\,. \end{aligned} \tag{3.72}$$

The equality of both resummations is consistent with the Stokes automorphism Eq. (3.57) that we derived in the previous subsection, and can be seen as an alternative derivation of that equation. More generally, by considering Eq. (3.69) and substituting $v = u - \log(kA) + 2\pi\mathrm{i}n$ where n is any integer, we can see that

$$\begin{aligned}\frac{2\pi\mathrm{i}\varphi^{(0)}A^g}{\Gamma(g)} &= \mathrm{e}^{-2\pi\mathrm{i}ng}\,\mathcal{S}_{n^+}\left(-\sum_{k=1}^{\infty}\tilde{\mathsf{S}}_{0\to k}\mathrm{e}^{-g\log(k)}\hat{\varphi}^{(k)}(g)\right)\\ &= \mathrm{e}^{-2\pi\mathrm{i}ng}\,\mathcal{S}_{n^-}\left(-\sum_{k=1}^{\infty}\mathsf{S}_{0\to k}\mathrm{e}^{-g\log(k)}\hat{\varphi}^{(k)}(g)\right)\,, \end{aligned} \tag{3.73}$$

which is consistent with Eq. (3.59). In example 3.2.4, we check the exact relation Eq. (3.70), and in particular Eq. (3.72), for the quartic free energy.

Example 3.2.4. *We consider again the quartic free energy introduced already in previous examples. In particular, recall example 3.2.1 where we tested the large order transseries* (3.35) *for* $k = 1$. *We performed the test by applying ratio tests on*

$$r_g \equiv \frac{2\pi\mathrm{i}A^g}{\Gamma(g)}F_g^{(0)} \tag{3.74}$$

in the large g*-limit. We can now also perform tests for* $k > 1$ *by resumming the asymptotic large order relation, i.e. we can test the exact large order relation* (3.70)*. Similar to example 3.2.3, we do not have an exact Borel transform* $\mathcal{B}[\hat{F}^{(k)}](t)$ *at our disposal, so we replace this function by its (diagonal) Padé approximant in the integration and define*

$$r_g^{(k)} \equiv S_1^k\mathrm{e}^{-g\log(k)}\int_0^{\infty-\mathrm{i}\epsilon} dv\,\mathcal{PB}\_N[\hat{F}^{(k)}](v)e^{-gv}\,. \tag{3.75}$$

A numerical evaluation of the integral yields, for example for $g = 20$*:*

$$\begin{aligned} r_{20} &\approx \qquad\qquad\qquad\qquad\qquad\qquad 1.386394325206770660\,\mathrm{i}\,,\\ r_{20}-r_{20}^{(1)} &\approx 0.000000879112757638 + 0.000000000111827370\,\mathrm{i}\,,\\ r_{20}-(r_{20}^{(1)}+r_{20}^{(2)}) &\approx 0.000000000000643417 - 0.000000000223651298\,\mathrm{i}\,,\\ r_{20}-(r_{20}^{(1)}+r_{20}^{(2)}+r_{20}^{(3)}) &\approx -0.000000000000643249 - 0.000000000000010324\,\mathrm{i}\,. \end{aligned} \tag{3.76}$$

To obtain these numbers, we used the $N = 100$ *diagonal Padé approximant. We observe that* $r_{20}^{(1)}$ *already matches the exact value* r_{20} *to* 7 *decimal places and adding further* $r_{20}^{(k)}$ *improves the approximation even further.*

In [27], a nice way to visualize approximations with an increasing number of nonperturbative sectors was introduced. In Fig. 3.9a, we compare r_g *to the resummed large order relation for* $1 \leq g \leq 30$ *and up to twelve nonperturbative sectors in this way. The vertical axis shows the precision, defined by*

$$\log_{10}\left|\frac{r_g}{r_g - \sum_{k=1}^{n} r_g^{(k)}}\right|\,, \tag{3.77}$$

and n *ranging from 1 to 12. In Fig. 3.9b, we also test Eq.* (3.71) *by changing the integration path in Eq.* (3.75) *to the* $[0^+]$ *contour and using the Borel residues Eq.* (3.23) *– i.e. we replace* S_1^k *by* $-(-S_1)^k$*. It is important to realize that we must do* both *replacements: the large order relation only gives exact results when we use the Borel residues that correspond to the chosen integration contour. We observe that once we do this, both resummations of the large order transseries match the exact values* r_g *with an extraordinarily small error.*

In Sec. 3.1.3 we discussed the derivation of the classical 'asymptotic' large order relation which expresses the large g behaviour of the perturbative coefficients $\varphi_g^{(0)}$ in terms of the large order transseries shown in Eq. (3.35). In the present section we learned that we can also express those same perturbative coefficients as the resummation of the large order transseries, without invoking any large g limit. It is therefore natural to wonder if Eq. (3.70) is an *exact* large order relation, in the sense that its right hand side computes the perturbative coefficients $\varphi_g^{(0)}$ also at *finite* g to arbitrary precision. Figs. 3.9a and 3.9b support this idea, as both resummations describe the perturbative coefficients with extraordinary precision. Let us discuss this possibility of exactness somewhat further.

One possible objection that one might raise against this assertion is that a finite number of perturbative coefficients $\varphi_g^{(0)}$ can be changed 'by hand' by adding a polynomial to $\varphi^{(0)}(z)$, without altering the instanton coefficients that determine the

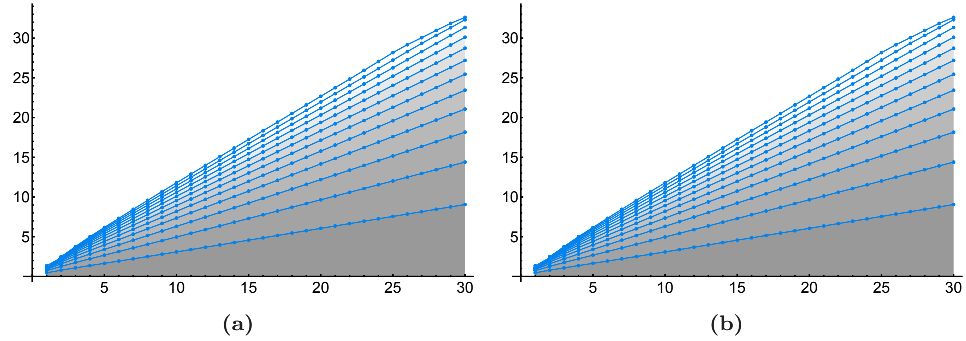

Figure 3.9.: In (a) we show the precision – defined by Eq. (3.77) – of the resummed large order transseries along the $[0^-]$ contour. We plotted the values for g ranging from 1 to 30 and n ranging from 1 to 12. In (a) we used an integration contour below the real line as in Eq. (3.75). In (b) we show a similar plot where we used an integration path along the $[0^+]$ contour instead.

resummation on the right hand side of Eq. (3.70). Therefore, how can that equation be used to exactly compute all $\varphi_g^{(0)}$? As we will explain now, this apparent contradiction is resolved by the contribution at infinity to the Laplace transform that appeared in Eq. (3.25) but that we have ignored in what followed.

Imagine that indeed we wish to alter a select number of perturbative coefficients by adding a polynomial to the original series $\varphi^{(0)}(z)$ as follows:

$$\tilde{\varphi}^{(0)}(z) = \varphi^{(0)}(z) + \sum_{g=0}^{G} a_g z^{-g}\,, \tag{3.78}$$

thereby altering the values of $\varphi_g^{(0)}$ with $g \leq G$ to $\tilde{\varphi}_g^{(0)} = \varphi_g^{(0)} + a_g$. Clearly, the large order behaviour of the perturbative coefficients $\tilde{\varphi}_g^{(0)}$ is unaffected by such a modification and hence the instanton coefficients $\tilde{\varphi}_h^{(k)} = \varphi_h^{(k)}$ also remain unchanged. However, the exact large order relation for $\tilde{\varphi}_g^{(0)}$ at finite $g \leq G$ must differ from the original by a_g. To see how this happens, we first note that the Borel transform of our new series $\tilde{\varphi}^{(0)}$ reads

$$\mathcal{B}[\tilde{\varphi}^{(0)}](t) = \mathcal{B}[\varphi^{(0)}](t) + \sum_{h=0}^{G} \frac{a_h}{h!} t^h\,. \tag{3.79}$$

The first term on the right hand side, when inserted into Eq. (3.25), yields the familiar exact large order relation of $\varphi_g^{(0)}$ when we follow the contour deformation as explained in Sec. 3.1.3. The second term on the right hand side, however, leads to poles at $t = 0$

and $t=\infty$. If we deform the contour away from zero to $t=\infty$ we obtain

$$\frac{\tilde{\varphi}_g^{(0)}}{g!} = \Big(\text{exact large order relation of } \varphi_g^{(0)}\Big) + \sum_{h=0}^{G} \frac{a_h}{h!} \frac{1}{2\pi \mathrm{i}} \oint_{t=\infty} t^{h-g-1}\, \mathrm{d}t\,. \tag{3.80}$$

An elementary residue computation shows that the latter term is simply $a_g/g!$, as required. We can even extend the argument to the case that $G=\infty$, as long as the power series that is then added in Eq. (3.78) has a non-zero radius of convergence: the large order behaviour is unaltered and therefore the instanton coefficients of the large order relation will remain unchanged. The Borel transform of such a series with a nonzero radius of convergence will moreover be analytic in the whole complex plane and hence, as with the polynomial, a residue computation at infinity will again simply add the coefficient $a_g/g!$ to the exact large order relation. In the next section, we will discuss a contribution at infinity of this kind in some more detail for the quartic partition function.

A final interesting aspect of the exact large order relation is the fact that, since the right hand side is now a function of g, we can carry out the resummation even when g is not a positive integer. In fact, we can resum the large order transseries for arbitrary complex values of g. If we regard the perturbative coefficients as a prescription to assign values $\varphi_g^{(0)}$ to positive integers g, one can wonder whether the resummation of the large order transseries for arbitrary g provides a natural extension of this map $\varphi_g^{(0)}:\mathbb{N}\to\mathbb{C}$ to the complex domain. We will discuss this question for a specific example in the next section.

3.3. A worked out example

In the previous section we derived the *exact* large order relation, Eq. (3.70), for the perturbative coefficients of an asymptotic transseries. Although our derivation of this relation is only valid for integer values of g – for example because in the Cauchy integral representation of Eq. (3.24) one can only extract residues when g is integer – nothing prevents us from studying the resulting equation for generic real or even complex values of g. In this section, we want to find out to what extent the large order relation is truly exact. We do so by studying the example of the *quartic partition function* – closely related to the quartic free energy that featured in several previous examples – for which the perturbative coefficients $\varphi_g^{(0)}$ have a closed form expression which admits a natural extension[5] to complex g.

---

[5] We will be careful in using the word ‘extension’ rather than (analytic) ‘continuation’, since a function which is only known at integer values of g does not have a unique analytic continuation

3.3.1. Quartic integral and free energy

So far in this chapter, we have used the quartic free energy in various examples to illustrate some of the concepts and perform numerical checks on the formulas we derived. For the purpose of the storyline, we kept the examples small and restricted ourselves to the necessary details, postponing a more detailed introduction of the model to the present section. Of course, the quartic model is a favorite toy model in many resurgence studies, so the interested reader can find many further applications of this model elsewhere, notably in [71].

Let us start by considering the quartic partition function

$$Z(\hbar) = \frac{1}{2\pi} \int_\Gamma dw \, e^{-\frac{1}{\hbar}V(w)} \,, \tag{3.81}$$

where $V(w)$ is a quartic potential defined by

$$V(w) = \frac{1}{2}w^2 - \frac{\lambda}{24}w^4 \,, \tag{3.82}$$

and Γ is an infinite contour in the complex w-plane chosen such that the integral converges. The parameters $\hbar$ and λ can be arbitrary nonzero complex numbers. One can think of Eq. (3.81) as a zero-dimensional path integral, hence the name 'partition function' for $Z(\hbar)$.

By defining $x \equiv \lambda\hbar$ and changing the variable $w \to \sqrt{\hbar}\, w$, Eq. (3.81) can be written as[6]

$$Z(x) = \frac{1}{\sqrt{2\pi}} \int_{\tilde{\Gamma}} dw \, e^{-\frac{1}{2}w^2 + \frac{x}{24}w^4} \,, \tag{3.83}$$

where $\tilde{\Gamma}$ is the curve obtained from Γ by the above rescaling. The partition function can be shown to satisfy the second-order linear differential equation

$$16x^2 Z''(x) + (32x - 24)Z'(x) + 3Z(x) = 0 \,. \tag{3.84}$$

In the next subsection, we will consider the transseries solution to this differential equation and test the exact large order relation, Eq. (3.70), for this transseries.

Before we do so, let us introduce the quartic *free energy* $F = \log Z$, which is the model we discussed in the examples 3.1.1 and 3.2.1 – 3.2.4. Using Eq. (3.84), it is straightforward to show that F satisfies the following nonlinear second order

---

to complex values of g. Thus, our extensions will not be unique – our claim, rather, is that in a resurgence setting they constitute a natural choice.

[6] For convenience, we change the overall normalisation by a factor $\sqrt{\hbar}/(2\pi)$; see [71] for more details.

differential equation:

$$16x^2F''(x) + 16x^2\left(F'(x)\right)^2 + (32x - 24)F'(x) = 0\,. \tag{3.85}$$

Being a *second* order ODE, the solution to Eq. (3.85) has two integration constants and is therefore described by a *two*-parameter transseries which turns out to have the form

$$F(x,\sigma,\rho) = \sum_{n=0}^{\infty}\sigma^n\,e^{-\frac{nA}{x}}\sum_{g=0}^{\infty}F_g^{(n)}x^g + \rho\,, \tag{3.86}$$

with instanton action $A = 3/2$ and σ and ρ the transseries parameters. This expression was used in example 3.1.1. As Eq. (3.85) is a non-linear ODE, one obtains infinitely many instanton sectors $F^{(n)}$ with evenly spaced actions nA, leading to the pattern of Borel plane singularities of Fig. 3.3. By plugging the transseries Eq. (3.86) into Eq. (3.85), one can obtain recursive relations to determine the instanton coefficients $F_g^{(n)}$ that can be found in App. B of [71].[7]

3.3.2. Test of the exact large order relations

We want to test the exact large order relation, Eq. (3.70), for the quartic partition function. We therefore need the solution to the second-order linear ODE of Eq. (3.84), which takes the form

$$\mathcal{Z}(\sigma_0,\sigma_1,x) = \sigma_0 Z^{(0)}(x) + \sigma_1\,\mathrm{e}^{-\frac{A}{x}}Z^{(1)}(x)\,, \tag{3.87}$$

with the same instanton action $A = 3/2$ as for the quartic free energy, but now only two asymptotic series:

$$\begin{aligned}
Z^{(0)}(x) &= \sum_{n=0}^{\infty} Z_g^{(0)}x^n\,, \qquad & Z_g^{(0)} &= \left(\frac{2}{3}\right)^g\frac{(4g)!}{2^{6g}\,(2g)!\,g!}\,,\\
Z^{(1)}(x) &= \sum_{n=0}^{\infty} Z_g^{(1)}x^n\,, \qquad & Z_g^{(1)} &= -\frac{\mathrm{i}}{\sqrt{2}}\left(-\frac{2}{3}\right)^g\frac{(4g)!}{2^{6g}\,(2g)!\,g!}\,.
\end{aligned} \tag{3.88}$$

---

[7] In [71], the instanton sectors $F_g^{(n)}$ are labeled as $F_g^{(n,0)}$. Furthermore, because the integration constant ρ is simply an additive constant, the two-parameter transseries in (3.86) is dubbed a '1.5-parameter' transseries there.

The corresponding 0-Borel transforms of the two asymptotic sectors can be expressed in closed form in terms of hypergeometric functions and are given by[8]

$$\begin{aligned}\mathcal{B}[Z^{(0)}](t) &= {}_2F_1\left(\frac{1}{4},\frac{3}{4},1;\frac{2t}{3}\right)\,,\\ \mathcal{B}[Z^{(1)}](t) &= -\frac{\mathrm{i}}{\sqrt{2}}{}_2F_1\left(\frac{1}{4},\frac{3}{4},1;-\frac{2t}{3}\right)\,.\end{aligned} \tag{3.89}$$

With the expressions for the partition function at our disposal, we can now plug these results into Eq. (3.70). The exact large order relation for the coefficients $Z_g^{(0)}$ consists of only a single term on the right hand side:

$$Z_g^{(0)} = -\frac{S_1}{2\pi\mathrm{i}}\,\Gamma(g+1)A^{-g}\int_0^{\mathrm{e}^{-\mathrm{i}\theta}\infty}\mathrm{d}t\,\mathcal{B}[Z^{(1)}]\left(\frac{3}{2}(\mathrm{e}^t-1)\right)\mathrm{e}^{-gt}\,, \tag{3.90}$$

where $\theta=\arg(g)$ and the Stokes constant reads $S_1=-2$. Let us explain the integration path in Eq. (3.90). The extension of our exact large order relation to generic real and positive g is straightforward, but in the case of complex g we need to be careful: when the real part of g, $\Re(g)$, is negative, any Laplace integral going from 0 to $+\infty$ along the real t-axis will not converge. Hence we need to adjust the angle along which we integrate as we move g through the complex plane. The correct way to do this is to set the angle of integration to $-\theta$. This will moreover ensure that the Laplace integral converges as rapidly as possible, which is desirable from a numerical computational point of view.

If we regard the perturbative coefficients $Z_g^{(0)}$ in Eq. (3.88) as obtained from a function whose domain consists of integers $g\in\mathbb{N}$, then this function admits a natural extension to the domain of complex numbers:

$$Z_g^{(0)} = \left(\frac{2}{3}\right)^g\frac{\Gamma(4g+1)}{2^{6g}\,\Gamma(2g+1)\Gamma(g+1)}\,, \tag{3.91}$$

i.e. we replace the factorials by gamma functions.[9] The first question that we want to address is whether the exact large order relation can reproduce the exact value of $Z_g^{(0)}$, defined in this way, for real positive g. The answer to this question is shown in the upper graph of Fig. 3.10a for the real part of $Z_g^{(0)}$. (One obtains similar plots for its imaginary part.) The solid red line plots the *exact value* of Eq. (3.91), and the round blue markers are computed using the right hand side of Eq. (3.90). The triangular

---

[8] Notice that in [71], the 1-Borel transform was used.

[9] Strictly speaking we also need to define c^g for constant c as $e^{g\log c}$ and pick a branch for the logarithm, but we can ignore this subtlety in what follows and simply assume that c^g is always extended in the 'natural' way from integer g.

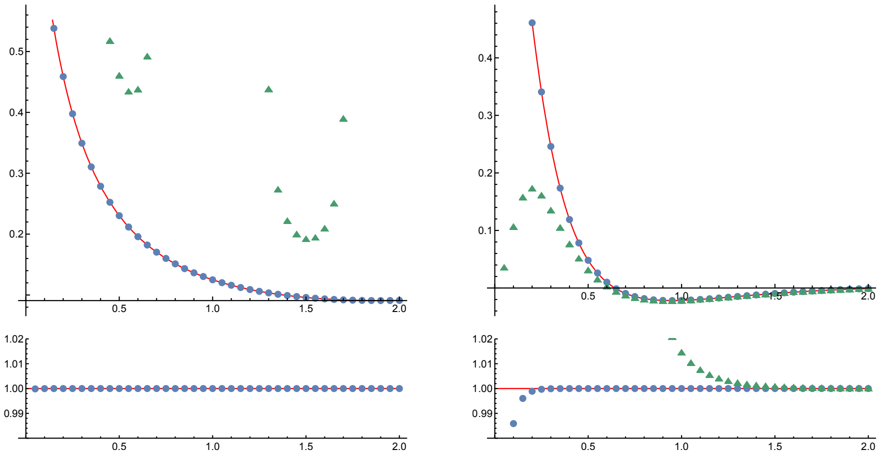

(a) arg$(g) = 0$ **(b)** arg$(g) = 0.45\pi$

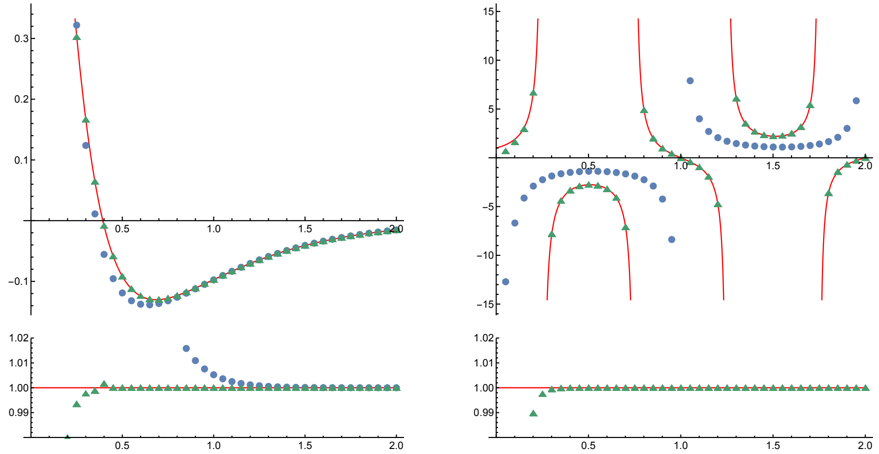

(c) arg$(g) = 0.55\pi$ **(d)** arg$(g) = \pi$

Figure 3.10.: Results of the numerical integration of the exact large order relation for the quartic partition function for four different values of arg(g) and with $|g|$ (horizontal axis) ranging from 0 to 2. In the upper graphs in each panel, we show in red (solid line) the real part of the *exact* value of $Z_g^{(0)}$, Eq. (3.91). The round blue markers display the numerical results for Eq. (3.90), whereas the green triangle markers show the results for Eq. (3.92), with Stokes' phenomenon taken into account. The Stokes phenomenon, which occurs at arg$(g) = \pi/2$, explains why the blue markers match the red line in Figs. (a) and (b), and the green markers do so in (c) and (d). In the lower graphs in each panel, we show the ratio of the exact and computed values. We achieve a good accuracy for $|g| > 0.5$, whereas for smaller values of $|g|$, the numerical accuracy decreases due to the exponential factor in the Laplace integral which becomes large in this regime. In (d), we shifted $|g|$ by $1/1000$ in the numerical integrations to avoid computing ratios of infinities. The lower graph shows that even close to the singularities, the exact large order relation works to great accuracy.

green markers in this plot will be explained shortly. The lower graph depicts the ratio between the exact and computed values. Clearly, the two expressions match nicely also for non-integer g. Notice that there are no singularities on the integration path – i.e. on the real positive line – of Eq. (3.90), so we do not need to deform the contour here.

We can also consider *negative real* values of g. For this, we need to rotate the phase of g from 0 to π and rotate the direction of the integration contour in Eq. (3.90) to $-\infty$ in the opposite direction, as we explained before. In Fig. 3.10d we show the result. At first sight our conjecture of exactness of Eq. (3.90) seems to fail, as the blue markers clearly fail to accurately describe the analytic expression for $Z_g^{(0)}$. However, there is a simple reason for this: the Borel transform $\mathcal{B}[Z^{(1)}]\left(\frac{3}{2}(\mathrm{e}^t-1)\right)$ has numerous singularities along the imaginary axis, and these induce a Stokes phenomenon when the integration contour crosses this axis. Hence, when we rotate the contour of integration to the negative axis in the Borel plane, we pick up nonperturbative corrections that we need to include. Taking these nonperturbative contributions into account we find for $\Re(g)$ *negative* that

$$Z_g^{(0)} = -\frac{S_1}{2\pi\mathrm{i}}\,\Gamma(g+1)A^{-g}\left(1-\frac{2\mathrm{e}^{2\pi\mathrm{i}g}}{1+\mathrm{e}^{4\pi\mathrm{i}g}}\right)\int_0^{\mathrm{e}^{-\mathrm{i}\theta}\infty}\mathcal{B}Z^{(1)}\left(A(\mathrm{e}^t-1)\right)\mathrm{e}^{-gt}\mathrm{d}t\,, \quad (3.92)$$

The nonperturbative corrections are therefore described by including the additional factor

$$-\frac{2\mathrm{e}^{2\pi\mathrm{i}g}}{1+\mathrm{e}^{4\pi\mathrm{i}g}}\,, \quad (3.93)$$

as we derive in App. A.3. Using Eq. (3.92) we obtain the *green* (triangular) markers in the different panels of Fig. 3.10. Indeed, these markers describe the exact values of the perturbative coefficients for $\Re(g) < 0$, as one can see in Fig. 3.10d.

Now, we can also test the exact large order relation for complex values of g. The most interesting values are those for which the integration contour in the Borel plane is near the Stokes line. To clearly see the Stokes phenomenon, we have therefore tested the exact large order relation for $\arg(g) = 0.45\pi$ (Fig. 3.10b) and $\arg(g) = 0.55\pi$ (Fig. 3.10c). Before the Stokes phenomenon takes place – which happens at $\theta = 0.5\pi$ – we observe that the blue markers obtained using Eq. (3.90) correctly describe $Z_g^{(0)}$. Conversely, the green markers Eq. (3.92) describe $Z_g^{(0)}$ correctly after the Stokes phenomenon has occurred. Note that in particular the difference between the blue and green markers in Figs. 3.10b and 3.10c becomes more significant when g is very small, since – as is always the case for a Stokes transition – the two differ by a nonperturbative, exponentially small contribution in the large g expansion.

3.3.3. Discussion

The analysis in this section has shown that for the quartic partition function, the exact large order relation, Eq. (3.92), describes the natural extension of the perturbative coefficients, Eq. (3.91), to the complex g-plane to high numerical precision. To make this work, we needed to account for the Stokes phenomenon, showing that this phenomenon plays an equally important role for large order transseries as it does for 'ordinary' ones.

It is important to realize, though, that as the perturbative coefficients $\varphi_g^{(0)}$ are only defined for positive integers g, the extension to complex g is in general not unique. The extension of the factorials to gamma functions was the natural choice – in a sense, we make the same choice as one does when using the Laplace integral (which defines the gamma function) in Eq. (2.4) to reintroduce the factorials after having performed a Borel transform. Less natural options are certainly available: one could for example extend the factorials to Hadamard's gamma function, but with this replacement Eqs. (3.90) and (3.91) would no longer lead to the same result.

One may now wonder whether the exact large order relation for complex g only worked for this specific example, or if it works in general. Let us first emphasize that for more complicated (non-linear) examples one cannot even give a 'natural' extension of $\varphi_g^{(0)}$ to complex values of g. Furthermore, deriving the integral expression of the exact large order relation by other means that provide a natural smooth g-dependence – as we were able to do in App. A.3 for Eq. (3.90) – is not possible in general. In fact, we can turn things around and say that the exact large order relation itself defines the most natural extension to the complex g-plane of $\varphi_g^{(0)}$. Of course, as the example of the partition function shows, if we want to *define* an extension to complex g in this way, Stokes' pheneomenon must be taken into account carefully. A final subtlety is that we have ignored a potential contribution at infinity in the Cauchy integral that is used to extract $\varphi_g^{(0)}$ from the Borel transform, also when we took g non-integer. Let us now discuss this subtlety for the quartic parition function.

To this end, let us ask under which conditions a contribution at infinity of the form

$$\oint_{\infty} \frac{\mathrm{d}t}{2\pi \mathrm{i}} \frac{\mathcal{B}[\varphi^{(0)}](t)}{t^{g+1}}\,, \tag{3.94}$$

is nonzero. In the explicit example of the quartic partition function, we already found a match between the resummed large order transseries without such a contribution and the exact value of the perturbative coefficients for values of g throughout the complex plane. This seems to suggest that in this example the contribution at infinity vanishes for any g, but is this really the case?

Because we have an explicit expression for the Borel transform of the quartic partition function, we can expand it around $t = \infty$ and obtain

$$\mathcal{B}[Z^{(0)}](t) \simeq t^{-\frac{1}{4}} \sum_{n=0}^{\infty} a_n \left(\frac{1}{\sqrt{t}} \right)^n , \tag{3.95}$$

where the coefficients a_n depend on a branch choice at infinity of the hypergeometric function. Since the Borel transform goes to zero as t approaches infinity, the integral of Eq. (3.94) vanishes for $\Re(g) > 0$: consider a circular path C_R of radius R, then the integral scales as

$$\int_{C_R} \frac{\mathrm{d}t}{2\pi \mathrm{i}} \frac{\mathcal{B}[Z^{(0)}](t)}{t^{g+1}} \simeq \mathcal{O}\left(R^{-g-1/4} \right) , \tag{3.96}$$

which for $\Re(g) > 0$ vanishes as $R \to \infty$. When we complexify g and rotate into the half-plane where $\Re(g) < 0$, the situation is complicated. Formally, the contribution at infinity should diverge and therefore the exact large order relation should break down. However, this is not what we found in this section: remarkably, the exact large order relation seems to hold, even when $\Re(g) < 0$, if we account for the Stokes phenomenon of $\mathcal{B}[Z^{(1)}]\left(\frac{3}{2}(\mathrm{e}^t - 1)\right)$. It is noteworthy, however, that the integrand of Eq. (3.94), when we plug in the expansion Eq. (3.95), has a simple pole – with residue a_n – at infinity whenever $g = -\frac{1}{4} - \frac{n}{2}$ for a nonnegative integer n. These are exactly the values of g for which both sides of the large order relation (3.92) diverge and where a finite contribution a_n would be neglectable anyway – see also Fig. 3.10d. Formally, this argument is invalidated by the fact that the residue is defined as the coefficient of the simple pole in a Laurent series expansion in t, which the above series is not – it is an expansion in fractional powers of t. Yet, the fact that the series has simple poles for the same values of g for which the coefficient $Z_g^{(0)}$ diverges, does not seem like a coincidence.

It would be interesting to better understand the nature of the contribution at infinity and how in the end it does or does not contribute to the exact large order relation for complex values of g, as well as to what extent this holds true for other transseries. In this regard, note that this example is much simpler than generic large order transseries, since there is only a single instanton sector and hence no Stokes transitions $\mathfrak{S}_n$ across horizontal lines on the Borel cylinder to account for. In fact, 'unwrapping' the Borel cylinder for a fully nonlinear problem, one would find an infinite number of diagonal Stokes lines in the large order Borel plane, each containing a single primitive instanton action plus all its positive integer multiples. Combining all of the corresponding Stokes automorphisms into a single one that rotates from the positive to the negative real t-axis seems to be a very difficult task.

Finally, let us comment on the nature of the Stokes phenomenon, computed in Eq. (A.21), of the Borel transform $\mathcal{B}[\hat{Z}^{(1)}](t) \equiv \mathcal{B}[Z^{(1)}]\left(\frac{3}{2}(\mathrm{e}^t - 1)\right)$ in the example of the quartic partition function. Usually, when an asymptotic series undergoes a Stokes phenomenon, it 'jumps' by an exponentially small factor $\mathrm{e}^{-A/z}$ multiplied by a *diferent* asymptotic series. On the contrary, here we observe that the series $\hat{Z}^{(1)}(x)$ jumps by an exponentially small factor multiplied by *itself*. This phenomenon is known as *self-resurgence* and appears also in the context of WKB solutions (see e.g. section 5 of [73]). Using asymptotic large order relations, we have checked explicitly that the higher order terms of the formal power series $\hat{Z}^{(1)}(x)$ probe the lower order terms of that exact same series. From the dependence on $e^t - 1$, one sees that the singularities at $t = 2\pi i n$ for nonzero integers n in the Borel cylinder of $\mathcal{B}[\hat{Z}^{(1)}]$ correspond to the origin in the original Borel plane of $\mathcal{B}[Z^{(1)}]$. This shows that there is actually a nonzero Borel residue at the origin on the other sheets of the multisheeted (original) Borel plane – i.e. if one takes a path around some of the other singularities. This is a particular example of the multivaluedness of the Borel residues that we discussed in Sec. 3.1.2. This particular type of Stokes phenomenon for large order transseries appears in this example because both $Z^{(0)}$ and $Z^{(1)}$ know about each other – that is: $\mathsf{S}_{0\to 1}$ and $\mathsf{S}_{1\to 0}$ are both nonzero. In the context of nonlinear ODEs, one always has that the residues $\mathsf{S}_{k\to 0}$ vanish, and hence the same effect does not occur in the Borel cylinders of the first sector $\mathcal{B}[\hat{\varphi}^{(1)}]$ – see e.g. Figs. 3.1a, 3.1b and 3.2a. Even in those examples, though, it does occur for the higher sectors $\mathcal{B}[\hat{\varphi}^{(k>1)}]$ – see e.g. Fig. 3.6a, where we do find singularities at $t = 2\pi i n$ for integer $n \neq 0$.

3.4. Conclusion

Large order relations are a powerful tool for decoding fluctuations in higher nonperturbative sectors. They have been used extensively in a wide variety of physical models. In this chapter, originally motivated by the desire to understand the repeating singularity structure found in Fig. 3.1, we have taken a closer look at the generic underlying transseries structure of these large order relations. We have argued that for rather generic transseries – only assuming the resurgent structure of Eq. (3.4) – we can fully explain this observed singularity structure, as described by Eq. (3.42). We have seen that the large order transseries is constructed out of rescaled Stirling transforms $\hat{\varphi}^{(k)}$ of the original instanton sectors, and that these formal power series have a Borel cylinder rather than a Borel plane: $t \sim t + 2\pi\mathrm{i}$.

We derived the Stokes automorphism $\mathfrak{S}_0$ of the large order transseries across the positive real axis of this Borel cylinder, which turns out to be qualitatively the same as that of the original transseries, expressed in terms of the Stokes matrix $\mathbb{S}$ in Eq. (3.13). After establishing further automorphisms $\mathfrak{S}_n$ across copies of the positive real axis, we obtained a clear and unambiguous resummation procedure for the large order transseries which, after establishing the exact large order relations Eq. (3.73), is expected to compute the perturbative coefficients $\varphi^{(0)}$ *exactly* in many cases. We have checked the 'exactness' of this statement for the quartic partition function, where we found that the exact large order relation holds, even for complex values of g, and that Stokes phenomenon for the large order transseries plays an important role to make this happen.

From a practical point of view, what we have gained is a clear understanding of the precise contour along which one is supposed to resum the large order transseries sectors with a given set of Borel residues in order to succesfully probe higher order instanton coefficients $\varphi_h^{(k>1)}$. Having established a clear understanding of its Stokes phenomenon, we can now also resum the large order transseries along other contours using the automorphisms $\mathfrak{S}_n$. We would like to stress that our analysis makes no assumptions about the Stokes data of the underlying transseries: we formulated our results in terms of generic Borel residues rather than specific Stokes constants.

From a more conceptual point of view, it is interesting that the *exact* large order relation does not only compute the perturbative coefficients $\varphi_g^{(0)}$, but also allows us to extend them to complex values of g. It is striking that the exact large order relation for the quartic partition function, which we tested thoroughly in Sec. 3.3, seems to work for *all* complex values of g – if we take the Stokes phenomenon explained in App. A.3 into account – and does not seem to be spoiled by the contribution at infinity in the Cauchy integral. Of course, this is only a single example, but it would be interesting to see more examples where this contribution might or might not be relevant.

A first open question that would be interesting to address is therefore whether the example of the quartic partition function is special or whether the exactness that we found holds for large classes of examples, either because contributions from infinity are absent or because we can pinpoint such contributions and correctly take them into account. This question is intimately related to the question whether our techniques (and in particular the Stirling transform) can lead to numerical gain: while from the computations that we have performed the use of the Stirling transform does not seem to lead to much faster numerics for large values of g, it may lead to improvements for small values of g – but to compute at such values, it is crucial that many contributions to the exact large order relation – including potential contributions from infinity – are properly taken into account.

The results of this chapter can most likely be generalized to broader settings, and it would be interesting to explore some of those. Here, one can think of transseries with multiple Stokes lines, transseries with logarithmic terms (such as resonant transseries), transseries that have additional parameters and display the higher order Stokes phenomenon of [74], etc. While we do not expect major qualitative differences in such cases, it would still be good to extend the large order toolbox that we have developed to these settings.

The geometry of the Borel cylinder also begs to be explored further. While the $t \sim t + 2\pi\mathrm{i}$ symmetry in the Borel plane of the large order transseries is exact when we explore positive integer g, in more general cases our expressions involved factors of $e^{-2\pi\mathrm{i}g}$ for each shift in the imaginary direction. This seems to hint at a structure where the quantities that we compute, rather than functions on the Borel cylinder, are sections of a bundle over this cylinder. Exploring this possibility may lead to an even better, more geometric understanding of large order relations. Another geometric question arises from the fact that the locations of the singularities on the Borel cylinder are the logarithms of the locations of the singularities of the original transseries. This may suggest that we should not only think of sectors $\hat{\varphi}^{(k)}$ associated to singularities at $\log(k)$, but that one can also think of a sector $\hat{\varphi}^{(0)}$ that encodes the original perturbative series and that has been shifted to the end of the Borel cylinder at $-\infty$.

Chapter 4.

From renormalons to resurgence

This chapter is based on Secs. 2 and 5 of [1].

The perturbative description of gauge theory quantities in terms of a coupling constant is of central importance to our understanding of such theories, and thereby our ability to use them for phenomenology. A full description of these quantities in fact should include non-perturbative contributions, usually in the form of power corrections, themselves multiplied by associated perturbative series in the coupling constant. The direct calculation of such non-perturbative corrections is in many cases very challenging, and often not even fully understood.

From the previous two chapters we know that access to non-perturbative corrections can be gained via the perturbative series itself. Being an asymptotic series, the series sum must be properly defined. The intrinsic ambiguities of such a definition take the form of non-perturbative power corrections. This interesting aspect of perturbative series was first explored in [75, 76] and in particular in [11], where the factorial growth of the perturbative series due to fermion loop diagrams was discussed, and termed *renormalon divergence*. In this chapter – and in more depth in the next chapter, using the mathematical techniques of resurgence – we shall explore such aspects for the Adler function [77]. The application of resurgence to renormalon physics was first studied in [35, 78–80] and investigated in followup-works by these authors. Other interesting recent developments are e.g. in [81] and in a series of papers starting with [37] and summarized in [82]. Excellent reviews on renormalons are [83, 84].

In Sec. 4.1, we briefly discuss the Adler function to introduce the standard renormalon lore. We schematically show how so-called bubble diagrams lead to factorialy growth and explain the distinction between UV and IR renormalons. We next show how bubble diagrams naturally show up in the so-called flavour expansion. In particular, we derive a convolution integral in the Borel plane that is the starting point of Sec. 4.2. In this section we discuss a novel new way to study renormalons by studying the resurgence properties of this convolution integral. We discuss numerous examples that are most relevant for the next chapter, where we study the resurgence properties of the Adler function in more depth. However, the result of Sec. 4.2 can be applied to a broader class of problems.

4.1. Renormalons

We consider the Adler function $D(Q^2)$ [77], which is defined as the logarithmic derivative with respect to Q^2 of the vacuum polarization $\Pi(Q^2)$ in gauge theory:

$$D(Q^2) = 4\pi^2 Q^2 \frac{\mathrm{d}\Pi(Q^2)}{\mathrm{d}Q^2}\,, \tag{4.1}$$

where $\Pi(Q^2)$ is related to the correlator of two vector currents $j^\mu = \bar{\psi}\gamma^\mu\psi$,

$$(-\mathrm{i})\int d^4x\, e^{-\mathrm{i}qx}\,\langle 0|T\left\{j^\mu(x)j^\nu(0)\right\}|0\rangle = (q^\mu q^\nu - \eta^{\mu\nu}q^2)\Pi(Q^2)\,, \qquad Q^2 = -q^2\,. \tag{4.2}$$

The Adler function has long featured as an object to study asymptotic behaviour of perturbative series and renormalons, see e.g. [85–87]. This is because, as a self-energy, it depends on only one scale, and because its imaginary part, for timelike Q^2, is directly related to the so-called R-ratio of the inclusive e^+e^- cross section to hadrons and muons.

The perturbative expansion of the Adler function is typically expressed in terms of Feynman diagrams. A class of diagrams that by itself lead to factorial coefficient growth, and are typical for renormalons, are bubble-chain diagrams, in which n fermionic self energies are inserted in the photon or gluon propagator, see Fig. 4.1. For QED and QCD, the type of (renormalon) singularity in the Borel plane depends on the loop-momentum regions of these diagram, specifically the ultraviolet (UV) and infrared (IR) ones. We review this in the next subsection.

4.1.1. UV and IR renormalons

Consider the one-loop vacuum-polarization graph ("bubble") in Fig. 4.1a. Its expression in $d = 4 - 2\epsilon$ dimensions reads

$$\Pi_{\mu\nu} = (k_\mu k_\nu - k^2\eta_{\mu\nu})\pi(k,\mu) \tag{4.3}$$

with

$$\pi(k,\mu) = \frac{-2\mathrm{i}N_f e^2\mu^{2\epsilon}}{(2\pi)^d}\left(\frac{2-d}{1-d}\right)\int d^dq \frac{1}{(q+\frac{1}{2}k)^2(q-\frac{1}{2}k)^2}\,. \tag{4.4}$$

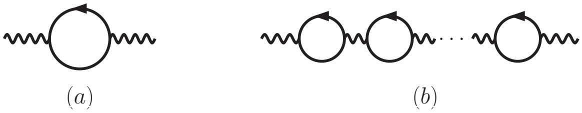

Figure 4.1.: (a) One fermion bubble, (b) chain of fermion bubbles.

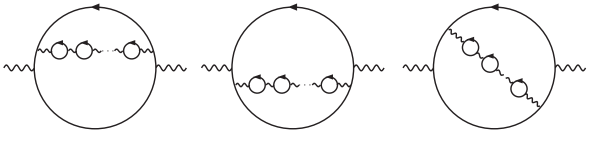

Figure 4.2.: Bubble chain inserted into Adler function.

This integral can be readily carried out using a Feynman parameter, leading to

$$\begin{aligned}\pi(k,\mu) &= \frac{2N_f e^2}{(4\pi)^2}\left(\frac{4\pi\mu^2}{-k^2}\right)^{\epsilon}\frac{(2-2\epsilon)\Gamma(1+\epsilon)\Gamma(1-\epsilon)^2}{\epsilon\,(3-2\epsilon)\Gamma(2-2\epsilon)}\\ &= \frac{\alpha N_f}{3\pi}\left[\frac{1}{\epsilon}-\gamma_E+\log 4\pi-\log\left(\frac{-k^2}{\mu^2}\right)+\frac{5}{3}\right]+\mathcal{O}(\epsilon)\,. \end{aligned}\tag{4.5}$$

To remove the ultraviolet divergence in Eq. (4.5) one includes an $\overline{\mathrm{MS}}$ counterterm, which leads to

$$\pi(k,\mu) = -\alpha\beta_{0f}\log\left(\frac{-k^2e^{-5/3}}{\mu^2}\right)\,, \tag{4.6}$$

where $\beta_{0f} = T\,N_f/3\pi$, with $T=1$ for QED and $T=1/2$ for QCD. For the Adler function, we consider the diagrams in Fig. 4.2, where a fermion bubble chain with n bubbles is inserted. The diagrams, summed over the number of bubbles, yield the expression

$$D = \alpha\int_0^\infty\frac{d\hat{k}^2}{\hat{k}^2}\,F(\hat{k}^2)\sum_n\left[\alpha\beta_{0f}\log\left(\frac{\hat{k}^2Q^2e^{-5/3}}{\mu^2}\right)\right]^n\,, \tag{4.7}$$

where $\hat{k}^2 = -k^2/Q^2$, and F represents the rest of the diagram (see [87]). We can examine the n-dependence of the integral separately for small and large $\hat{k}^2$ (the separation being defined by the argument in the logarithm in Eq. (4.7) being unity), using the small and large $\hat{k}^2$ dependence of F. Up to subleading corrections in n the result [83, 87] reads

$$D = \frac{C_F}{\pi}\sum_{n=0}^{\infty}\alpha_s^{n+1}\left[\frac{3}{4}\left(\frac{Q^2 e^{-5/3}}{\mu^2}\right)^{-2}\left(\frac{-\beta_{0f}}{2}\right)^2 n! + \frac{1}{3}\frac{Q^2 e^{-5/3}}{\mu^2}\beta_{0f}^n\, n!\left(n+\frac{11}{6}\right)\right], \quad (4.8)$$

where the first part is due to the IR behavior and the second to the UV behavior of the integrand in Eq. (4.7). We see that bubble-chain diagrams produce factorial growth at leading power in N_f, i.e. the n-bubble contribution is proportional to $(\alpha N_f)^n$.

To see what this implies for the Borel transform of the Adler function, we use (2.3). For the IR case one finds ($u \equiv -\beta_{0f} t$)

$$\mathcal{B}[D]_{\mathrm{IR}}(u) \sim \frac{1}{u-2}, \qquad \mathcal{B}[D]_{\mathrm{UV}}(u) \sim \frac{1}{(u+1)^2}, \quad (4.9)$$

where we only exhibit the leading u-poles and suppress prefactors. As is known, these poles become logarithmic branch cuts when two or more bubble chains are present [88]. We will show this explicitly in Sec. 5.2. The IR renormalon pole in Eq. (4.9) for QED lies on the negative Borel parameter axis, and vice versa for the UV renormalon pole. As we will discuss in section 4.1.2, for QCD one changes $\beta_{0f} \to \beta_0 = -(11 - 2N_f/3)/(4\pi)$, which also implies a change of sign for u, so that IR (UV) renormalon poles are on the positive (negative) real t axis.

As shown in Eqs. (2.4) and (2.8), the poles on the positive u-axis imply ambiguities in the Borel-resummed perturbative series. In fact, they imply non-perturbative corrections; the QCD version of the ambiguity in equation (2.8), due the pole at $u = 2$ in (4.9), is proportional to

$$e^{\frac{2}{\beta_0 \alpha}} \sim \left(\frac{\Lambda}{Q}\right)^4, \quad (4.10)$$

with Λ the QCD scale parameter, and Q the scale of the Adler function. Non-perturbative effects in QCD are proportional to this typically very small ratio, and are often also referred to as power corrections. Our goal in the next chapter, then, is to learn more about power corrections for the Adler function, using the methods of resurgence introduced in chapters 2 and 3.

4.1.2. Flavour expansion

In the previous subsection, we discussed how bubble-chain diagrams cause perturbative series to show factorial growth. To formalize this, let us consider the flavour expansion of QED/QCD with N_f massless fermions. We can write an observable in perturbation theory as

$$F(\alpha) = \sum_{n=0}^{\infty} c_n\, \alpha^n, \tag{4.11}$$

where, in general, the coefficients c_n can be written as an expansion in N_f,

$$c_n = c_n^{(0)} + ... + c_n^{(n-1)} N_f^{n-1}. \tag{4.12}$$

In this flavour expansion, we take the large N_f limit while keeping the 't Hooft coupling $N_f\,\alpha$ fixed. In this limit, the dominant contribution to c_n is given by $c_n^{(n-1)}$ and we therefore reorder the perturbative expansion as an expansion in $1/N_f$:

$$F = \frac{1}{N_f} \sum_{n=0}^{\infty} c_n^{(n-1)} (N_f \alpha)^n \left(1 + \mathcal{O}\Big(\frac{1}{N_f}\Big)\right). \tag{4.13}$$

To see what diagrams go into each order of $1/N_f$, recall the one-loop vacuum-polarization graph (fermion bubble)

$$\Pi_{\mu\nu}(k) =$$

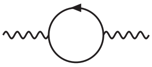

$$= (k_\mu k_\nu - \eta_{\mu\nu} k^2)\ \pi(k^2), \tag{4.14}$$

which we already calculated in Eqs. (4.4) and (4.6), where we found

$$\pi(k^2) = -\alpha\beta_{0f}\left[\log\left(\frac{-k^2}{\mu^2}\right) + C\right], \tag{4.15}$$

with C a scheme dependent constant – e.g. $C = -\frac{5}{3}$ in the $\overline{\text{MS}}$-scheme, as in Eq. (4.6). We notice that such a fermion bubble counts as $N_f\alpha = \mathcal{O}(1)$ in the flavour expansion. Including the external lines, the effective photon propagator with n such fermion bubbles reads

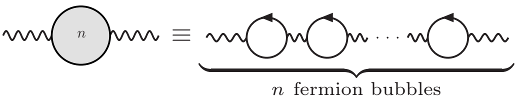

$$= -\frac{\mathrm{i}}{k^2}\left(\eta_{\mu\nu} - \frac{k_\mu k_\nu}{k^2}\right)\Big[-\pi(k^2)\Big]^n, \tag{4.16}$$

so that a bubble chain counts as $(N_f\alpha)^n = \mathcal{O}(1)$ in the flavour expansion as well. In other words, the coefficients $c_n^{(n-1)}$ in Eq. (4.13), and also the coefficients at higher orders in the flavour expansion, can be computed by replacing virtual photons/gluons by the bubble chain Eq. (4.16). From Eq. (4.15) it then follows that this leads to the inclusion of logarithms in the Feynman integral. As already explained in Sec. 4.1.1, integrating over such logarithms in a Feynman integral leads to factorial growth.

Diagrams including the sum over bubble chains can be computed using the effective (Dyson summed) propagator of such a bubble chain:

$$D_{\mu\nu}(k) = -\frac{\mathrm{i}}{k^2}\Big(\eta_{\mu\nu} - \frac{k_\mu k_\nu}{k^2}\Big)\frac{1}{1+\pi(k^2)} - \mathrm{i}\xi\frac{k_\mu k_\nu}{k^4}, \tag{4.17}$$

with ξ the gauge fixing parameter. However, instead of working with this Dyson-summed effective propagator, it will be more convenient to work with its Borel transform with respect to α (which appears in $\pi(k^2)$), which reads [85]

$$\mathcal{B}\big[\alpha D_{\mu\nu}(k)\big](u) = -\frac{\mathrm{i}}{k^2}\left(\eta_{\mu\nu} - \frac{k_\mu k_\nu}{k^2}\right)\left(-\frac{\mu^2}{k^2}e^{-C}\right)^u - \mathrm{i}\xi\frac{k_\mu k_\nu}{k^4}, \tag{4.18}$$

where we again rescaled the usual variable t in the Borel plane to $u = -\beta_{0f}t$. Furthermore, before Borel transforming we inserted an overall factor of α that will be convenient later, when we perform the actual diagram calculations. When we have $n_c > 1$ bubble chains in a diagram, we can use the fact that the Borel transform of a product of series is obtained by taking the convolution of the individual Borel transforms:

$$\begin{aligned}&\mathcal{B}\left[\prod_{j=1}^{n_c}\alpha D_{\mu_j\nu_j}(k_j)\right](u)\\ &\quad= \frac{1}{(-\beta_{0f})^{n_c-1}}\int_0^u\left[\prod_{j=1}^{n_c}du_j\right]\delta\Big(u-\sum_{j=1}^{n_c}u_j\Big)\prod_{j=1}^{n_c}\mathcal{B}\big[\alpha D_{\mu_j\nu_j}(k_j)\big](u_j).\end{aligned} \tag{4.19}$$

This can be verified by taking the Laplace transform of both sides of the equation with respect to t. In Sec. 4.2 we give more details on the effect of the convolution integral on the resurgence structure in the case of general n_c. In Sec. 5.2, where we discuss the Adler function at order $1/N_f^2$, we will only need the case $n_c = 2$.

For the case of QED we notice that positive t corresponds to negative u, since β_{0f} is positive. For QCD one completes β_{0f} to the full first coefficient of the β-function $\beta_0 = -(11-2N_f/3)/(4\pi)$ [83, 88, 89], so that now positive t corresponds to positive u (thus, infrared renormalons appear on the positive u axis for QCD, and on the negative axis for QED). In practice this implies that one can perform a QED calculation to obtain the non-abelian counterpart in QCD by replacing β_{0f} with β_0 and by adding the appropriate $SU(3)$ color factors. In the literature, this procedure is also known as "naive non-abelianization" [90–92]. We should mention here that for the large N_f limit, β_0 changes sign (this happens for $N_f > 16$) after which QCD is no longer asymptotically free. Hence, for QCD, instead of a large N_f expansion one uses a large β_0 expansion, and we rewrite Eq. (4.12) as an expansion in β_0

$$c_n = \tilde{c}_n^{(0)} + ... + \tilde{c}_n^{(n-1)} \beta_0^{n-1}. \tag{4.20}$$

Thus, in the large β_0 expansion for QCD, the expansion of a generic observable Eq. (4.13) becomes

$$F = \frac{1}{\beta_0} \sum_{L=0}^{\infty} \tilde{c}_n^{(n-1)} \, (\beta_0 \alpha)^n \left(1 + \mathcal{O}\left(\frac{1}{\beta_0}\right)\right). \tag{4.21}$$

where we now define the 't Hooft coupling as $\beta_0 \, \alpha$ for the QCD case. In what follows, we refer to the large N_f expansion for both QED and QCD, even though we use the large β_0 expansion in QCD. We perform our calculations in QED and in the end use the procedure of naive non-abelianization to convert our results to obtain the QCD result.

4.2. Using Borel convolution integrals for resurgence

We saw in the previous section that the flavour expansion is a useful framework to isolate perturbative series that show factorial growth due to individual diagrams, i.e. renormalons. At higher orders in $1/N_f$, an important ingredient of the flavour expansion is the convolution integral Eq. (4.19). In section 5.2, we shall apply this integral to go beyond the leading order in the flavour expansion for the Adler function. In this section, we discuss what the effect is of the convolution integral on the resurgence structure. In particular, we will see momentarily that one does not need to know the particular exact Borel transforms, but that the structure of the alien derivatives and their calculus can be used instead. Although the techniques are a straightforward application of the framework outlined in Sec. 2, in physics applications this is, as far as we are aware, a novel way to study renormalon effects.

The results we present in this section have twofold use. First, they set up the calculation of particular $\mathcal{O}(1/N_f^2)$ diagrams that we shall encounter in the next chapter. The results, however, are more general and also apply to more complicated convolution integrals which one would encounter at higher orders in $1/N_f$. We explain, by means of examples that are relevant for the next chapter, how the convolution integral 'builds' resurgent functions. The results will also show glimpses of the full resurgent structure that would emerge upon including all orders in $1/N_f$.

4.2.1. Resurgence of the convolution integral

Given two asymptotic formal power series $F^{(0)}(\alpha)$ and $G^{(0)}(\alpha)$, we can define a new power series $\Psi^{(0)}(\alpha)$, which in general is again asymptotic, by taking the product:

$$\Psi^{(0)}(\alpha) \equiv F^{(0)}(\alpha)\, G^{(0)}(\alpha)\,. \tag{4.22}$$

As explained in more detail in chapters 2 and 3, the resurgence properties of $\Psi^{(0)}$ can be recovered from the singularities of the Borel transform. Here, the convolution integral appears as the Borel transform of $\Psi^{(0)}$ is computed as

$$\mathcal{B}[\Psi^{(0)}](u) = \int_0^u du_1\, \mathcal{B}[F^{(0)}](u)\mathcal{B}[G^{(0)}](u-u_1)\,, \tag{4.23}$$

and the resurgence structure can be found using the relation Eq. (2.26) between the different non-perturbative sectors $\mathcal{B}[\Psi^{(n)}](u)$. However, except for simple examples, performing the convolution integral might be a difficult task. We can study instead the resurgence properties of $\Psi^{(0)}$ by using the alien derivatives. Acting with an arbitrary alien derivative Δ_ω yields

$$\Delta_\omega \Psi^{(0)} = \Delta_\omega \left(F^{(0)}(\alpha)\right) G^{(0)}(\alpha) + F^{(0)}(\alpha)\Delta_\omega \left(G^{(0)}(\alpha)\right), \tag{4.24}$$

since the alien derivative satisfies the Leibniz rule. Thus, the calculation of $\Delta_\omega \Psi^{(0)}$ has shifted to the calculation of $\Delta_\omega F^{(0)}$ and $\Delta_\omega G^{(0)}$. Consequently, if the resurgence structure of $F^{(0)}$ and $G^{(0)}$ is known, one can compute the resurgence structure of $\Psi^{(0)}$. As alluded to above, we will see in Sec. 5.2 that, with one exception, the convolution integral Eq. (4.23) cannot be computed exactly. It will be easier to obtain the resurgence properties of $F^{(0)}$ and $G^{(0)}$ instead of that of $\Psi^{(0)}$. Therefore, to prepare our discussion in Sec. 5.2, and to show how Eq. (4.24) can be employed in practice, we discuss in this section a few relevant examples. In these examples the convolution integral can be computed exactly and therefore these computations act as a check on the method of alien derivatives.

4.2.2. Convolution of pure factorial growth

Let us begin with the simplest possible model. Consider an asymptotic formal power series where the perturbative coefficients show pure factorial growth:

$$F^{(0)}(\alpha) = \sum_{n=0}^{\infty} \Gamma(n+1)\alpha^{n+1} \qquad \Longrightarrow \qquad \mathcal{B}[F^{(0)}](u) = \frac{1}{1-u}\,. \tag{4.25}$$

As the complete asymptotics of $F^{(0)}$ is determined by the pole of $\mathcal{B}[F^{(0)}](u)$ in the Borel plane, we know that in the full transseries there is just one possible non-perturbative sector, $F^{(1)}$, which consists of only a single term $S_1^F f_0^{(1)}(\alpha) = 2\pi \mathrm{i}$. As we will encounter many different Stokes constants for different resurgent functions, we adopt the notation in which we put the function name as a superscript on the Stokes constants, e.g. S_1^F.

Although the resurgence of $F^{(0)}$ is relatively simple, i.e.

$$\Delta_1 F^{(0)} = 2\pi \mathrm{i}\,, \tag{4.26}$$

with all other alien derivatives vanishing, we show in this section that $F^{(0)}$ can be used as a building block to build more complicated resurgent functions. By taking powers of $F^{(0)}$, we will show schematically how such a resurgence structure builds up.

Consider the formal power series

$$\Psi^{(0)}(\alpha) = \Big(F^{(0)}(\alpha)\Big)^2, \tag{4.27}$$

where its Borel transform is computed as

$$\mathcal{B}\Big[\Psi^{(0)}\Big](u) = \int_0^u du_1 \; \frac{1}{1-u_1}\frac{1}{1-u+u_1} = -2\frac{\log(1-u)}{2-u}. \tag{4.28}$$

Having the exact Borel transform, we obtain the resurgence structure using Eq. (2.26). Since we know that

$$\mathcal{B}\Big[\Psi^{(0)}\Big](u) = -S_1^{\Psi}\mathcal{B}\Big[\Psi^{(1)}\Big](u-1)\frac{\log(1-u)}{2\pi \mathrm{i}}\,, \tag{4.29}$$

we can read off the result

$$S_1^{\Psi}\mathcal{B}\Big[\Psi^{(1)}\Big](u-1) = \frac{4\pi \mathrm{i}}{1-(u-1)}\,. \tag{4.30}$$

Transforming back to the α-plane, this corresponds to the formal power series

$$S_1^{\Psi}\Psi^{(1)}(\alpha) = 4\pi \mathrm{i}\sum_{n=0}^{\infty}\Gamma(n+1)\alpha^{n+1}\,. \tag{4.31}$$

We see that in this ‘squared model’, the leading non-perturbative sector $\Psi^{(1)}$ is no longer a single term but now shows pure factorial growth itself.

Though we were able to perform the convolution integral exactly and therefore immediately read off the resurgence structure, it is instructive to obtain the same result using alien derivatives. On the one hand, the bridge equation, Eq. (2.25), tells us that $\Delta_1\Psi^{(0)} = S_1^\Psi \Psi^{(1)}$. On the other hand, we have by direct calculation

$$\Delta_1\Psi^{(0)} = 2F^{(0)}\Delta_1 F^{(0)} = 2\sum_{n=0}^{\infty} 2\pi\mathrm{i}\,\Gamma(n+1)\alpha^{n+1}, \tag{4.32}$$

where we used Eq. (4.26). We observe the same result as obtained from the exact Borel transform in Eq. (4.31). Likewise, for the second non-perturbative sector $\Psi^{(2)}$ we get

$$2\Big(S_1^\Psi\Big)^2\Psi^{(2)} = \Delta_1^2\Psi^{(0)} = 2\Delta_1 F^{(0)}\Delta_1 F^{(0)} = 2(2\pi\mathrm{i})^2\,, \tag{4.33}$$

which is a sector with a single coefficient. Notice that this can also be related to the expansion of Eq. (4.28) around $u = 2$ which reads

$$\mathcal{B}[\Psi^{(0)}(u)\Big|_{u=2} = \pm 2\frac{\pi\mathrm{i}}{2-u} + \dots\,, \tag{4.34}$$

where the ellipsis denotes regular terms. Up to a sign ambiguity this agrees with Eq. (4.33). This ambiguity originates in the ambiguous expansion of the logarithm $\log(1-u)$ in Eq. (4.28) around $u = 2$. We come back to this point extensively in Sec. 5.2.4, where we shall see how to resolve such ambiguities.

This simple example easily generalizes to higher powers of $F^{(0)}(\alpha)$. For example, consider

$$\Phi^{(0)}(\alpha) \equiv \Big(F^{(0)}(\alpha)\Big)^3. \tag{4.35}$$

The convolution integral to get the Borel transform $\mathcal{B}[F^{(0)}(\alpha)^3]$ can still be done exactly, but we stay in the α-plane and follow the second method we just used for $\big(F^{(0)}(\alpha)\big)^2$. Acting once with Δ_1 yields

$$S_1^\Phi\Phi^{(1)} = \Delta_1\Phi^{(0)} = 3\Big(F^{(0)}\Big)^2\Delta_1 F^{(0)} = 6\pi\mathrm{i}\sum_{n=0}^{\infty}\alpha^{n+2}\sum_{h=0}^{n}\Gamma(n-h+1)\Gamma(h+1)\,. \tag{4.36}$$

Acting twice with Δ_1 yields

$$2\left(S_1^\Phi\right)^2\Phi^{(2)} = \Delta_1^2\Phi^{(0)} = 6F^{(0)}\Big(\Delta_1 F^{(0)}\Big)^2 = 6(2\pi\mathrm{i})^2\sum_{n=0}^{\infty}\Gamma(n+1)\alpha^{n+1}\,. \tag{4.37}$$

Finally we have

$$6\left(S_1^\Phi\right)^3\Phi^{(3)} = \Delta_1^3\Phi^{(0)} = 6\Big(\Delta_1 F^{(0)}\Big)^3 = 6(2\pi\mathrm{i})^3\,. \tag{4.38}$$

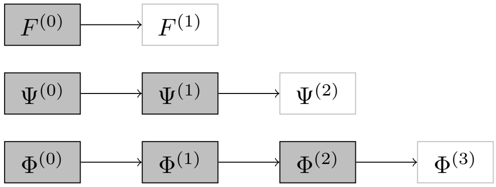

Figure 4.3.: Alien chains for the convolution of an asymptotic power series where the perturbative coefficients show pure factorial growth. The sectors with a filled box are true asymptotic sectors, whereas the white boxes are not and consist of a finite number of terms.

In Fig. 4.3, we show the alien chain built up with more sectors, more of which are now asymptotic.

4.2.3. Convolution of power series with a double pole

In the next chapter we shall consider diagrams at order $1/N_f^2$ in the flavour expansion. We will encounter two generalizations of the above convolution integral of power series with pure factorial growth, which we introduce and discuss already in this section. The first generalization is the case that the large order relation of the formal power series that we convolute with itself is determined by a double pole, treated in this subsection. In the next subsection we address the convolution of a power series with (infinitely many) evenly separated poles in the Borel plane.

Consider a power series $F^{(0)}(\alpha)$ where the large order growth of the coefficients is determined by a double pole in the Borel plane at $u = 1$, e.g.

$$F^{(0)}(\alpha) = \sum_{n=0}^{\infty} \Gamma(n+2)\left(a + \frac{b}{n+1}\right)\alpha^{n+1} \quad \Longrightarrow \quad \mathcal{B}[F^{(0)}](u) = \frac{a}{(1-u)^2} + \frac{b}{1-u}. \tag{4.39}$$

Notice that we keep the option open for subleading growth coming from a $(1-u)^{-1}$ term. We use a and b as a compact notation for $f_0^{(1)}$ and $f_1^{(1)}$ respectively. We are again interested in the resurgence properties of

$$\Psi^{(0)}(\alpha) \equiv \Big(F^{(0)}(\alpha)\Big)^2. \tag{4.40}$$

The Borel transform of this power series is given by the convolution integral

$$\begin{aligned}\mathcal{B}[\big(F^{(0)}\big)^2](u) &= \int_0^u du_1 \left(\frac{a}{(1-u_1)^2}+\frac{b}{1-u_1}\right)\left(\frac{a}{(1-u+u_1)^2}+\frac{b}{1-u+u_1}\right)\\ &= 2\frac{a^2+ab}{1-u} - S_1^{\Psi}\mathcal{B}\Big[\Psi^{(1)}\Big](u-1)\frac{\log(1-u)}{2\pi\mathrm{i}}\\ &\quad - 2\left(\frac{2a^2}{(2-u)^2}+\frac{a^2+2ab}{2-u}\right)\,, \end{aligned} \tag{4.41}$$

where in the second equality we emphasized the resurgence of the non-perturbative sector $\Psi^{(1)}$, which has the explicit form

$$S_1^{\Psi}\mathcal{B}\Big[\Psi^{(1)}\Big](u-1) = 4\pi\mathrm{i}\left(\frac{2a^2}{(2-u)^3}+\frac{2ab}{(2-u)^2}+\frac{b^2}{2-u}\right). \tag{4.42}$$

Notice that, studying the singularities of these expressions around $u=2$, it might look like the second non-perturbative sector $\Psi^{(2)}$ gets contributions from both the $\Psi^{(1)}$ sector and the last line in Eq. (4.41). However, as

$$\log(1-u)\Big|_{u=2} = \pm\pi\mathrm{i} - (2-u) - \frac{1}{2}(2-u)^2 + \ldots\,, \tag{4.43}$$

the last line cancels against the (real part of the) expansion of the logarithm and $\mathcal{B}[\Psi^{(1)}]$ around $u=2$.

The inverse Borel transforms of Eq. (4.42), together with the residue of the simple pole at $u=1$ in Eq. (4.41), yield the coefficients of the first non-perturbative sector

$$S_1^{\Psi}\Psi^{(1)}(\alpha) = 4\pi\mathrm{i}(a^2+ab)+4\pi\mathrm{i}\sum_{n=0}^{\infty}2\Gamma(n+3)\left(a^2+\frac{2ab}{n+2}+\frac{b^2}{(n+2)(n+1)}\right)\alpha^{n+1}. \tag{4.44}$$

where, in the sum, we factored out the leading order growth $\Gamma(n+3)$ coming from the fact that Eq. (4.42) has a cubic pole in the Borel plane (recall Eq. (2.55)).

Instead of performing the convolution integral as in Eq. (4.41), we can again use alien derivatives. Since

$$\Delta_1 F^{(0)} = 2\pi\mathrm{i}\left(\frac{a}{\alpha}+b\right)\,, \tag{4.45}$$

we find

$$\begin{aligned} S_1^{\Psi}\Psi^{(1)} &= 2F^{(0)}\Delta_1 F^{(0)} = 4\pi\mathrm{i}\left(\frac{a}{\alpha}+b\right)\sum_{n=0}^{\infty}\Gamma(n+2)\left(a+\frac{b}{n+1}\right)\alpha^{n+1} \qquad (4.46)\\ &= 4\pi\mathrm{i}(a^2+ab)+4\pi\mathrm{i}\sum_{n=0}^{\infty}2\Gamma(n+3)\left(a^2+\frac{2ab}{n+2}+\frac{b^2}{(n+2)(n+1)}\right)\alpha^{n+1}\,, \end{aligned}$$

which is indeed the same as in Eq. (4.44).

For this specific example there is another way to think about Eq. (4.46). Instead of identifying the coefficients $f_n^{(0)}$, we rewrite Eq. (4.46) as

$$\begin{aligned} S_1^{\Psi}\Psi^{(1)} &= 4\pi\mathrm{i}\left(\frac{a}{\alpha}+b\right)\sum_{n=0}^{\infty}F_n^{(0)}\alpha^{n+1}\\ &= 4\pi\mathrm{i}\,a\,F_0^{(0)}+4\pi\mathrm{i}\,a\sum_{n=0}^{\infty}f_{n+1}^{(0)}\alpha^{n+1}+4\pi\mathrm{i}\,b\sum_{n=0}^{\infty}f_n^{(0)}\alpha^{n+1} \qquad (4.47) \end{aligned}$$

Next, consider a generic series and its Borel transform

$$G(\alpha)=\sum_{n=0}^{\infty}g_n\alpha^{n+1} \qquad \Longrightarrow \qquad \mathcal{B}[G](u)=\sum_{n=0}^{\infty}\frac{g_n}{\Gamma(n+1)}u^n. \qquad (4.48)$$

The derivative of the Borel transform yields

$$\mathcal{B}[G]'(u)=\sum_{n=0}^{\infty}\frac{g_{n+1}}{\Gamma(n+1)}u^n \qquad \Longrightarrow \qquad H(\alpha)=\sum_{n=0}^{\infty}g_{n+1}\alpha^{n+1}, \qquad (4.49)$$

where in the last step we applied an inverse Borel transform. In other words, the newly constructed series $H(\alpha)$, with coefficients those of $G(\alpha)$ but shifted: $g_n \to g_{n+1}$, corresponds to taking the derivative in the Borel plane. Applied to Eq. (4.47), this implies

$$S_1^{\Psi}\mathcal{B}[\Psi^{(1)}](u)=4\pi\mathrm{i}\,a\,\mathcal{B}[F^{(0)}]'(u)+4\pi\mathrm{i}\,b\,\mathcal{B}[F^{(0)}](u). \qquad (4.50)$$

We shall employ this observation in Sec. 5.2.

4.2.4. Convolution with equidistant singularities

A final case we need is where we take the convolution of perturbative series $F^{(0)}$ and $G^{(0)}$, where the large order behaviour of their coefficients, $f_n^{(0)}$ and $g_n^{(0)}$, come from singularities at $u = 1, 2, 3, ...$ in the Borel plane. Furthermore, we assume that we know both the resurgence properties of $F^{(0)}$ and $G^{(0)}$, i.e. we know the action of the alien derivative Δ_1:

$$\Delta_1 F^{(0)} = S_1^F F^{(1)}\,, \qquad \Delta_1^2 F^{(0)} = 2(S_1^F)^2 F^{(2)}\,, \qquad \Delta_1^3 F^{(0)} = 6(S_1^F)^3 F^{(3)}\,, \quad (4.51)$$

etc., and similar for $G^{(0)}$, but now with the Stokes constant S_1^F replaced by S_1^G. This is the standard structure of alien derivatives if one assumes that $F^{(0)}$ and $G^{(0)}$ are one parameter transseries for which one can derive a bridge equation as we did in Sec. 2.3. However, in the next chapter we will argue that the Adler function does not necessarily has such a bridge equation – see in particular the discussion in Sec. 5.1.5). Therefore, we also allow for non-vanishing actions of Δ_2, Δ_3, Δ_4 etc. In fact, when we apply the machinery of this section to the Adler function at order $1/N_f^2$, we see that such 'multiple steps forward' alien derivatives indeed occur.

Using the Leibniz rule repeatedly, we may now also obtain the resurgence structure of the product

$$\Psi^{(0)} \equiv F^{(0)} G^{(0)}\,. \qquad (4.52)$$

In particular, to obtain the first non-perturbative sector $\Psi^{(1)}$, we can act with Δ_1. This yields

$$S_1^\Psi \Psi^{(1)} = \left(\Delta_1 F^{(0)}\right) G^{(0)} + F^{(0)} \left(\Delta_1 G^{(0)}\right)\,. \qquad (4.53)$$

In order to obtain the sector $\Psi^{(2)}$, we can act with Δ_1^2, for which $\Psi^{(2)}$ gets contributions from

$$\frac{1}{2}\Delta_1^2\Big(F^{(0)}G^{(0)}\Big) = \frac{1}{2}\Big(\Delta_1^2 F^{(0)}\Big)G^{(0)} + \Big(\Delta_1 F^{(0)}\Big)\Big(\Delta_1 G^{(0)}\Big) + \frac{1}{2}F^{(0)}\Big(\Delta_1^2 G^{(0)}\Big)\,, \quad (4.54)$$

and potentially also with a nonzero Δ_2, for which the contributions come from

$$\Delta_2\left(F^{(0)}G^{(0)}\right) = \left(\Delta_2 F^{(0)}\right) G^{(0)} + F^{(0)}\left(\Delta_2 G^{(0)}\right)\,. \qquad (4.55)$$

Likewise, an arbitrary sector $\Psi^{(n)}$ could get contributions from products of alien derivatives of the form Δ_1^n, $\Delta_1^{n-2}\Delta_2$, $\Delta_1^{n-3}\Delta_3$, ..., Δ_n.

4.2.5. Prefactor singularities

A final subtlety that we need to address is one that we will encounter at several points in our computations. The Borel transforms in the convolution integral, Eq. (4.19), may contain singular factors – in practice: poles – that only depend on the overall

Borel plane variable u, not on the integration variables u_i. Such singular factors can therefore be taken outside the integral; see Eq. (5.45) and the expressions below it for examples that we will encounter.

In the case of a transseries with non-perturbative exponentials $A_1 = -A_2$, these overall singularities can be somewhat difficult to interpret. Clearly, singular prefactors play a role in the singularity structure of the final Borel transform, and therefore they will determine some of the structure of the full transseries solution that we are after. However, since the singularities are not obtained by acting with a specific alien derivative on one of the factors in the integrand, it is not always immediately clear to which transseries sectors the expansions around them belong.

For example, an expansion in the Borel plane around $u = A_1$ could describe a $(1, 0)$ sector, but also other $(1 + n, n)$ sectors. When such an expansion comes from actions of alien derivatives on factors in the convolution integrand, one can simply read off which alien derivatives play a role and therefore which sectors appear. When an expansion comes from a prefactor singularity, this is not the case. As a result, in these cases one needs other arguments (e.g. comparing different expansions that involve the same higher nonperturbative sectors) to determine the precise transseries structure.

Some of our results on the transseries structure will therefore be conjectural, depending on such additional arguments, though in many cases we can also fully pin down the structure. We will even encounter situations where the extra singularities are a virtue rather than a nuissance – occasionally, they help us to read off transseries coefficients that would otherwise have remained hidden in a regular expansion, but that now become part of the singular structure.

To summarize what we learned in this section, it is clear that the resurgence structure of the convolution integral, Eq. (4.19), can be obtained in two ways: either directly via the singularity structure of the Borel transform, or by applying alien derivatives acting on the constituents of the convolution integral. The examples discussed in this section were relatively simple and we were able to compute the convolution integral exactly. However, generally, in harder problems it is difficult (if not impossible), to compute the convolution integral exactly. In fact, as we see in the next section, this is indeed the case for the Adler function at order $1/N_f^2$ in the flavour expansion, so that there we have to turn to the second method using alien derivatives. Let us emphasize that this method is quite general, and certainly not only applicable to the resurgence properties of the Adler function. It may further open the door to study renormalons in physics in general.

Chapter 5.

Resurgence analysis of the Adler function at $\mathcal{O}(1/N_f^2)$

This chapter is based on Secs. 4 and 6 of [1]. Compared to [1], new here is the discussion on Stokes' automorphism for the Adler function with one bubble-chain and the natural choice of the two transseries parameters.

As discussed in the previous chapters, resurgence provides tools to systematically decode non-perturbative information directly from the perturbative data. The techniques usually require a substantial number of perturbative terms (of order 10 at least, and for precision numerics of order 100), which explains why resurgence has not been widely applied to particle physics and phenomenology yet. Let us note that more broadly in quantum field theory, resurgence techniques have been introduced in e.g. [35, 54, 93, 94] and follow-up works by the same authors. The time seems ripe for applications to more phenomenologically relevant quantities, since for many observables in particle physics a substantial number of perturbative terms can be computed. The Adler function – already briefly introduced in the previous chapter – is a good starting point. In fact, in this chapter, we shall be able to extract new non-perturbative results for the Adler function at $\mathcal{O}(1/N_f)$ and $\mathcal{O}(1/N_f^2)$, where N_f is the number of flavours in the fermion loop diagram. The description of both perturbative and non-perturbative contributions is conveniently summarized in a transseries [53] and here we will do the same.

There has been much earlier work on renormalon contributions to the Adler function [85–87, 91, 95–99], as well as their connection to its operator product expansion [88, 100]. The Adler function appears in more recent renormalon studies [101–105], including a study whether field theories can have renormalons beyond the usual Borel plane [106]. The Adler function has recently been studied using resurgence techniques [107, 108], based on renormalization group considerations [109, 110].[1]

---

[1] Note that in these works, assumptions are used that reproduce the expectations by Parisi and 't Hooft [11, 89, 100] that renormalons occur at half-integer multiples of $1/\beta_0$, the inverse of the leading beta function coefficient. It was found recently [111] that in several examples, this pattern is in fact *not* present – even though the breaking of the pattern only shows up at finite N_f and not in a perturbative expansion in the reciprocal of that parameter.

To obtain our perturbative data, we compute two- and three-loop skeleton diagrams for the Adler function for gauge theory, using Eq. (4.18), the Borel transform of the gauge field propagator with fermion loop insertions. For the two-loop case ($\mathcal{O}(1/N_f)$) we find, using our resurgence techniques, the complete transseries of the Adler function due to renormalon contributions, including subleading effects, which reproduces and extends earlier results in [85–87, 107].

Sec. 5.1 discusses how renormalons are usually studied for the Adler function: by introducing a single bubble chain in the Feynman diagrams. This section contains many known results, but we try to present these in a way that is most suitable for a resurgent analysis. We give the exact expression of the Adler function at leading order in the flavour expansion. Subsequently we perform the resurgence analysis of the Adler function at this order, showing how resurgence and large order relations can be used to extract all non-perturbative sectors in the corresponding transseries. We give many details and checks on the resurgence analysis, to set up a solid framework that can be used at higher orders in the flavour expansion as well. We finish this section with a discussion on some of the more subtle issues encountered at this order.

Our aim is then to explore higher orders in the flavour expansion and investigate which aspects of the leading order analysis persist, and which ones may even show a richer structure. To accommodate the computations at next to leading order, we developed in Sec. 4.2 a powerful convolution method that facilitates the calculation of renormalon contributions due to adding new fermion-loop-summed propagators. In Sec. 5.2 we then compute a set of planar diagrams present at next to leading order in the flavour expansion of the Adler function. Although not all master integrals of the ($\mathcal{O}(1/N_f^2)$) diagrams are known, we can investigate much of the resurgent structure that occurs at order $1/N_f^2$. We discuss the non-perturbative sectors for individual diagrams as well as the alien lattice structure, which is considerably richer than at order $1/N_f$. We find non-perturbative asymptotic sectors, and alien derivative operators that establish relations between these sectors. Moreover, we find a new logarithmic type of non-perturbative power correction in the coupling constant plane. When we put all ingredients together, an intricate transseries structure emerges. Our results derive from thorough analytical and numerical analyses, which were already described extensively in previous chapters.

We summarize our findings in Sec. 5.3 and discuss some open questions. We refer to App. B for further background on the calculation of the diagrams.

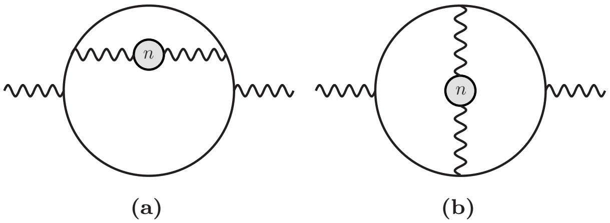

Figure 5.1.: Diagrams at $\mathcal{O}(1/N_f)$ in the flavour expansion. Diagram (a) contributes with a factor of 2 to account for the similar diagram where the bubble chain connects below the vertices.

5.1. Adler function with one bubble chain ($\mathcal{O}(1/N_f)$)

We briefly discussed, in Sec. 4.1, how bubble chain diagrams cause the perturbative series of the Adler function to show factorial growth. For clarity, let us recall the definition of the Adler function. We consider the Fourier transform of the correlation function of two vector currents $j_\mu = \bar{\psi}\gamma_\mu\psi$ of massless quarks, which can be written as

$$(-i)\int d^4x\, e^{-iqx}\langle 0|T\{j_\mu(x)j_\nu(0)\}|0\rangle = (q_\mu q_\nu - \eta_{\mu\nu}q^2)\Pi(Q^2)\,, \tag{5.1}$$

with $Q^2 = -q^2$. The Adler function is defined as

$$D(Q^2) = 4\pi^2 Q^2 \frac{\mathrm{d}\Pi(Q^2)}{\mathrm{d}Q^2}\,. \tag{5.2}$$

Understanding its asymptotic behaviour in perturbation theory and how this is related to non-perturbative expansions will be the main focus for the rest of this chapter. We use the flavour expansion to isolate the relevant Feynman diagrams that lead to asymptotic series. In this section we focus on the diagrams in Fig. 5.1 that contribute to the Adler function at leading order in the flavour expansion. In Sec. 5.2, we will then discuss (a subset of) the diagrams at next-to-leading order in $1/N_f$ for the Adler function.

Instead of calculating diagrams directly, we shall calculate their Borel transform, as the bubble chain then simplifies to an analytic, regularized photon propagator – recall Eq. (4.18). In what follows, we will work in Landau gauge, i.e. $\xi = 0$, and in $d = 4$ dimensions since the Adler function is UV finite after counterterms for the fermion bubbles are included. As we will explain in the next subsection, the perturbative coefficients of the Adler function itself can then be easily extracted by applying an inverse Borel transform.

The calculation of the diagram in Fig. 5.1a is relatively straightforward. Using results of App. B.1 and B.2 one can show that the two-loop integral factorizes into one-loop ones. With the one-loop master integral Eq. (B.1) we find

$$\mathcal{B}[\Pi_a(Q^2)](u) = \frac{1}{2\pi^2}\left(\frac{Q^2}{\mu^2}e^C\right)^{-u}\frac{1}{u(u+1)(u-1)^2(u-2)^2}\,, \tag{5.3}$$

where for notational simplicity we ignored an overall factor of the colour Casimir factor C_F that we will reinstate in our final expressions. In order to calculate the diagram of Fig. 5.1b, one needs the two-loop scalar master integral given in Eq. (B.4). By similar methods as for the diagram in Fig. 5.1a we derive

$$\begin{aligned}\mathcal{B}[\Pi_b(Q^2)](u) = -\frac{1}{6\pi^2}\left(\frac{Q^2}{\mu^2}e^C\right)^{-u}\Bigg[&\frac{6}{u(u+1)(u-1)^2(u-2)^2}\\ &+\frac{\psi^{(1)}(\frac{4-u}{2})-\psi^{(1)}(\frac{3-u}{2})+\psi^{(1)}(\frac{u+1}{2})-\psi^{(1)}(\frac{2+u}{2})}{u(u-1)(u-2)}\Bigg]\,,\end{aligned} \tag{5.4}$$

with $\psi^{(1)}(z) = \frac{\mathrm{d}^2}{\mathrm{d}z^2}\log\Gamma(z)$ the trigamma function. Taking the two diagrams together and using Eq. (5.2) to translate the result for $\Pi(Q^2)$ to that of the Adler function $D(Q^2)$, we obtain the Borel transform of the Adler function at leading order (LO) in the flavour expansion (which has also recently been derived in [112]):

$$\begin{aligned}\mathcal{B}[D_{\mathrm{LO}}](u) &= 4\pi^2 Q^2\frac{\mathrm{d}}{\mathrm{d}Q^2}\Big[\mathcal{B}[\Pi_b(Q^2)](u)+2\mathcal{B}[\Pi_a(Q^2)](u)\Big]\\ &= \frac{2}{3}\left(\frac{Q^2}{\mu^2}e^C\right)^{-u}\frac{\psi^{(1)}\left(\frac{4-u}{2}\right)-\psi^{(1)}\left(\frac{3-u}{2}\right)+\psi^{(1)}\left(\frac{1+u}{2}\right)-\psi^{(1)}\left(\frac{2+u}{2}\right)}{(u-1)(u-2)}\,.\end{aligned} \tag{5.5}$$

In the next subsection we use this result to perform the resurgence analysis, as the expression allows for a straightforward expansion around $u = 0$. Note that this result was already known in the equivalent forms [86]

$$\mathcal{B}[D_{\mathrm{LO}}](u) = \frac{32}{3}\left(\frac{Q^2}{\mu^2}e^C\right)^{-u}\frac{1}{2-u}\sum_{n=2}^{\infty}\frac{(-1)^n n}{(n^2-(1-u)^2)^2} \tag{5.6}$$

$$= \frac{32}{3}\left(\frac{Q^2}{\mu^2}e^c\right)^{-u}\frac{1}{2-u}\sum_{n=2}^{\infty}\frac{(-1)^n}{4(1-u)}\left[\frac{1}{(n-1+u)^2}-\frac{1}{(n+1-u)^2}\right], \tag{5.7}$$

where the second form of this equation allows one to easily read off the pole structure. We see that there exists an infinite set of both UV ($u < 0$) and IR ($u > 0$) singularities at integer values of u, all of which are double poles, except for the singularity at $u = 2$

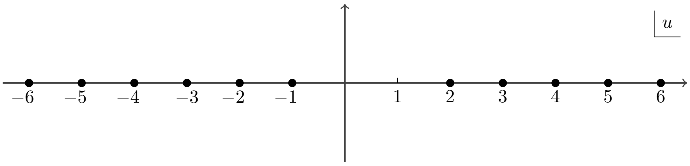

Figure 5.2.: Singularities of $\mathcal{B}[D_{\mathrm{LO}}](u)$. The UV-renormalons lie at $u = -1, -2, -3, ...$ and the IR-renormalons at $u = 2, 3, 4, ...$ Characteristic for the Adler function is that the singularity at $u = 1$ is missing (see the discussion below Eq. (5.7)).

which is a single pole and the singularity at $u = 1$ which is absent,[2] see also Fig. 5.2. This also agrees with the calculation that led to Eq. (4.9), which presented the leading IR and UV poles in the Borel plane. We should mention here that the singularity at $u = 1$ really is absent: it is present in Eq. (5.3) and Eq. (5.4) separately, but cancels when we take the two diagrams together. The fact that the IR renormalon at $u = 1$ is absent is characteristic for the Adler function and is already expected on physical grounds, as there is no dimension-2 operator in the OPE for the Adler function with massless fermions [88, 100].

5.1.1. Transseries Ansatz

Our goal is to construct the transseries for the Adler function. For the associated resurgence analysis we need the perturbative coefficients of the leading order Adler function $D_{\mathrm{LO}}(Q^2)$ itself, i.e. we need to do an inverse Borel transform on the results obtained in the previous subsection. In this section, and the sections hereafter, we will work mostly with the variable $u = -\beta_0 t$ as the actual Borel parameter instead of t, so that singularities in the Borel plane are conveniently placed at integer positions. Therefore, we expand the Borel transform Eq. (5.5) around $u = 0$ and write the result as

$$\mathcal{B}[D_{\mathrm{LO}}(Q^2)](u) = \sum_{n=0}^{\infty} \frac{d_n}{\Gamma(n+1)} u^n, \tag{5.8}$$

after which the perturbative coefficients d_n of D_{LO} can be read off:

$$\begin{aligned}\hat{D}_{\mathrm{LO}}(\alpha) &= \sum_{n=0}^{\infty} d_n \hat{\alpha}^{n+1} \qquad (5.9)\\ &= \hat{\alpha} + \left(\frac{23}{6} - 4\zeta_3\right)\hat{\alpha}^2 + (18 - 12\zeta_3)\,\hat{\alpha}^3 + \left(\frac{201}{2} - 42\zeta_3 - 60\zeta_5\right)\hat{\alpha}^4 + ...\end{aligned}$$

---

[2] Note that although there appears to be a pole at $u = 1$ in Eq. (5.7), it vanishes because the expansion around $u = 1$ of the terms in square brackets starts at order $\mathcal{O}(u - 1)$.

Here $\hat{\alpha} = -\beta_0 \alpha$ is the variable conjugate to the Borel variable u. As the inverse Borel transform gives an additional factor of $\hat{\alpha}$, we also defined $\hat{D}(Q^2) = -\beta_0 D(Q^2)$, to compensate for the additional factor of $-\beta_0$. Furthermore, to avoid logarithms of $\frac{Q^2}{\mu^2}e^C$ that will make the analysis needlessly complicated, we choose $\mu^2 = Q^2 e^C$. For notational convenience, we will drop the hats on $\hat{D}$ and $\hat{\alpha}$ in what follows. When we give the full transseries expression in the end of this section, we will reinstate the factors of β_0.

With the exact Borel transform Eq. (5.5) one can easily compute the first, say $n = 1000$, perturbative coefficients. (However, for the resurgence analysis we perform below, we found that 200 coefficients was enough.) With these coefficients at our disposal, we can start thinking about what we may expect the transseries to look like. As explained near Eq. (2.46), for a k-parameter transseries the Borel singularities of the transseries sector lie at positions $u = \boldsymbol{\ell} \cdot \boldsymbol{A}$ with $\ell \in \mathbb{N}^k$ and $\boldsymbol{A} = (A_1, ..., A_k)$ the non-perturbative exponents. As the poles of $\mathcal{B}[D_{\rm LO}](u)$ lie at both positive and negative integer values of u, a minimal Ansatz for the transseries is a transseries with two non-perturbative exponents $A_1 = 1$ and $A_2 = -1$. Therefore, we write the perturbative sector as

$$D_{\rm LO}^{(0,0)}(\alpha) \equiv \sum_{n=0}^{\infty} d_n^{(0,0)} \alpha^{n+1}, \tag{5.10}$$

with $d_n^{(0,0)} \equiv d_n$ the perturbative coefficients of Eq. (5.9). This will now be the $(0,0)$-sector of the following transseries

$$D_{\rm LO}(\alpha) = \sum_{n=0}^{\infty} \sum_{m=0}^{\infty} \sigma_{n,m} e^{-n\frac{A_1}{\alpha}} e^{-m\frac{A_2}{\alpha}} D_{\rm LO}^{(n,m)}(\alpha)\,, \tag{5.11}$$

with $\sigma_{n,m}$ the transseries parameters. Two remarks are in order.

First, we should emphasize here that this is a *minimal* transseries Ansatz and, recalling our discussion in Sec. 2.6, it might be the case that one needs additional non-perturbative exponents on top of A_1 and A_2, e.g. one needs a new exponent A_3 which is an integer multiple of A_1 or A_2 as was the case in [54]. Furthermore, one might need additional transmonomials – as is the case at order $1/N_f^2$ in the flavour expansion where we find logarithmic transmonomials, see Sec. 5.2.

Secondly, in the case that the Adler function indeed has two non-perturbative exponents A_1 and A_2, one might wonder if the Adler function satisfies a bridge equation of a two-parameter transseries as discussed in chapter 2. In this case, we can write

$$\sigma_{n,m} = \sigma_1^n \sigma_2^m\,, \tag{5.12}$$

where the infinitely many transseries parameters $\sigma_{n,m}$ are expressed in just two free parameters σ_1 and σ_2. However, since e.g. a differential equation for the Adler function as needed for the procedure in Sec. 2.3 is not known, we cannot derive a bridge equation that would allow us to read off the number of parameters. Therefore, we will be more general for now and work with the generic transseries parameters $\sigma_{n,m}$. We shall discuss the interpretation of the transseries parameters in Sec. 5.1.4.

In order to test the Ansatz Eq. (5.11), and construct the non-perturbative sectors[3]

$$D_{\mathrm{LO}}^{(n,m)}(\alpha) = \alpha^{\beta_{nm}} \sum_{h=0}^{\infty} d_h^{(n,m)} \alpha^h\,, \tag{5.13}$$

we will use resurgent large order relations. Of course, we know the exact Borel transform Eq. (5.5) and can therefore read off the non-perturbative sectors from the singularity structure in the Borel plane. We emphasize that this is a rather unique situation. In many resurgence examples one does not have the luxury of knowing the exact Borel transform. Often, one can only compute (a few) perturbative coefficients and thus large order relations are the only way to proceed. In fact, in Sec. 5.2 when we study the Adler function at the next order in the flavour expansion, we cannot compute the Borel transform exactly anymore. To prepare for that, we will therefore mainly focus on the large order analysis and show how this is sufficient to extract the non-perturbative sectors from perturbative data only.

5.1.2. Resurgence analysis: first two non-perturbative sectors

From the transseries ansatz, Eq, (5.11), we can readily write a large order relation for the perturbative coefficients

$$\begin{aligned} d_k^{(0,0)} \sim &- \sum_{\ell=1}^{\infty} \frac{\mathsf{S}_{(0,0)\to(\ell,0)}}{2\pi\mathrm{i}} \sum_{h=0}^{\infty} d_h^{(\ell,0)} \frac{\Gamma(k-h-\beta_{\ell,0})}{(\ell A_1)^{k-h-\beta_{\ell,0}}} \\ &- \sum_{\ell=1}^{\infty} \frac{\mathsf{S}_{(0,0)\to(0,\ell)}}{2\pi\mathrm{i}} \sum_{h=0}^{\infty} d_h^{(0,\ell)} \frac{\Gamma(k-h-\beta_{0,\ell})}{(\ell A_2)^{k-h-\beta_{0,\ell}}}\,, \end{aligned} \tag{5.14}$$

---

[3] We use the conventional notation β_{nm} (and sometimes for readability $\beta_{n,m}$) for the starting orders in the non-perturbative sectors; of course these orders (that always have two indices) should not be confused with the β-function and its coefficients.

which is a relation between the perturbative coefficients $d_k^{(0,0)}$ and the non-perturbative coefficients $d_h^{(\ell,0)}$ and $d_h^{(0,\ell)}$, i.e. only the $(\ell,0)$ and $(0,\ell)$ sectors will play a role. Notice that following chapter 3 and the discussion below Eq, (5.11), we wrote the large order relation in terms of Borel residues and not in terms of Stokes constants since a bridge equation for the Adler function is not known.[4] In order to avoid clogging up our equations with the lengthy notation of the Borel residues, and to avoid writing down ubiquitous minus signs and factors of $2\pi\mathrm{i}$, we will absorb these factors in the non-perturbative coefficients. Therefore we write

$$\tilde{d}_h^{(\ell,0)} \equiv -\frac{\mathsf{S}_{(0,0)\to(\ell,0)}}{2\pi\mathrm{i}} d_h^{(\ell,0)} \qquad \text{and} \qquad \tilde{d}_h^{(0,\ell)} \equiv -\frac{\mathsf{S}_{(0,0)\to(0,\ell)}}{2\pi\mathrm{i}} d_h^{(0,\ell)} \,. \tag{5.15}$$

From the previous chapters, we know that ordering the elements of Eq. (5.14) by their size gives us a way to extract the non-perturbative coefficients, keeping in mind that this relation is valid in the large k limit.

First, we observe that nodes in the alien lattice that are further away from the $(0,0)$-node, i.e. with larger ℓ, have a more exponentially suppressed contribution to the large order growth of $d_k^{(0,0)}$. As $A_1 = 1$ and $A_2 = -1$ are equal in size, the leading order growth comes from the $(1,0)$ and $(0,1)$ sectors. However, we saw above that the pole in the Borel plane at $u = 1$ is missing, meaning that the $(1,0)$-contribution is actually absent, so hence the leading growth will be coming from the $(0,1)$ sector:

$$\begin{aligned} d_k^{(0,0)} &\sim \sum_{h=0}^{\infty} \tilde{d}_h^{(0,1)} \frac{\Gamma(k-h-\beta_{0,1})}{A_2^{k-h-\beta_{0,1}}} + \mathcal{O}(2^{-k}) \qquad\qquad (5.16) \\ &= \frac{\Gamma(k-\beta_{0,1})}{A_2^{k-\beta_{0,1}}} \left[\tilde{d}_0^{(0,1)} + \frac{A_2\, \tilde{d}_1^{(0,1)}}{k} + \frac{A_2(\beta_{0,1}+1)\tilde{d}_1^{(0,1)} + A_2^2\, \tilde{d}_2^{(0,1)}}{k^2} + \ldots \right] + \mathcal{O}(2^{-k})\,, \end{aligned}$$

where $\mathcal{O}(2^{-k})$ refers to contributions from the $(\ell,0)$ and $(0,\ell)$ non-perturbative sectors with $\ell \geq 2$. In the second line we factored out the leading order growth in k and explicitly wrote the first two corrections in $1/k$. To show that this expression indeed captures the large order behaviour of the perturbative coefficients, and in order to find the various as yet unknown coefficients that appear in this large order relation, we can perform *ratio tests* on the known perturbative coefficients $d_k^{(0,0)}$. Recall also examples 3.2.1 and 3.2.4 of the previous chapter where we already performed such

---

[4] In the case of Eq. (5.12), the Borel residues can be written as $\mathsf{S}_{(0,0)\to(\ell,0)} = -S_{1,0}^{\ell}$ and $\mathsf{S}_{(0,0)\to(0,\ell)} = -S_{0,1}^{\ell}$ for some Stokes constants $S_{1,0}$ and $S_{0,1}$.

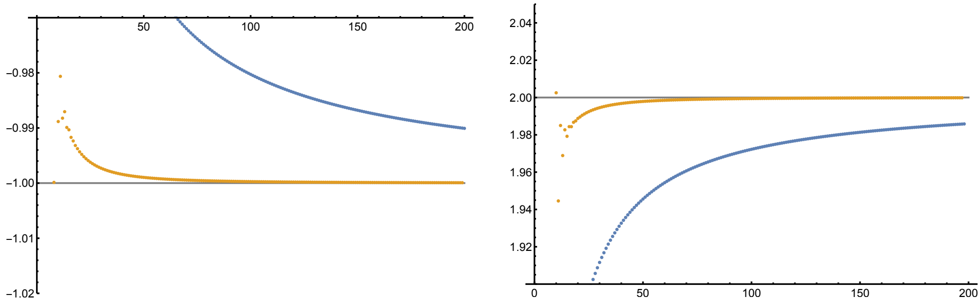

(a) **(b)**

Figure 5.3.: Fig. (a) shows the sequence $\mathbb{A}(k)$, Eq. (5.17) (top curve, blue), together with its first Richardson transform (bottom curve, orange) to accelerate the convergence. Similar, (b) shows the sequence $\mathbb{B}(k)$ (bottom curve, blue), Eq. (5.18), and its first Richardson transform (top curve, orange). We observe that already the first Richardson transform significantly accelerates the convergence. Higher order Richardson transforms converge even faster and become indistinguishable from the gray, horizontal lines denoting the expected values $A_2 = -1$ and $\beta_{0,1} = -2$.

ratio tests. We start with A_2 and $\beta_{0,1}$, and consider

$$\mathbb{A}(k) \equiv k\, \frac{d_k^{(0,0)}}{d_{k+1}^{(0,0)}} \sim A_2 + \mathcal{O}\Big(\frac{1}{k}\Big) \tag{5.17}$$

and

$$\mathbb{B}(k) \equiv k \log\left[\frac{f_{k+1}}{f_k}\right] \sim -\beta_{0,1} + \mathcal{O}\Big(\frac{1}{k}\Big) \qquad \text{with} \qquad f_k = \frac{d_k^{(0,0)} A_2^k}{\Gamma(k)}, \tag{5.18}$$

which should converge to A_2 and $-\beta_{0,1}$ in the large k-limit, respectively. In Figs. 5.3a and 5.3b we have plotted these two sequences together with their first Richardson transform for the first 200 perturbative coefficients. Recall from Sec. 2.7.1 that the Richardson transform method accelerates convergence of sequences of the form

$$s_0 = \lim_{k\to\infty} \mathbb{S}(k) \qquad \text{with} \qquad \mathbb{S}(k) = s_0 + \frac{s_1}{k} + \frac{s_2}{k^2} + \ldots \tag{5.19}$$

where the coefficients s_n are not known explicitly, and the Nth Richardson transform of $\mathbb{S}(k)$ is denoted by $\mathrm{RT}[\mathbb{S}](k, N)$.

Above Eq. (5.10) we expressed the expectation that the non-perturbative exponent A_2 is equal to -1. Recalling our discussion around Eq. (2.55), also the value $\beta_{0,1} = -2$ for the characteristic exponent was expected since the leading singularity in the Borel

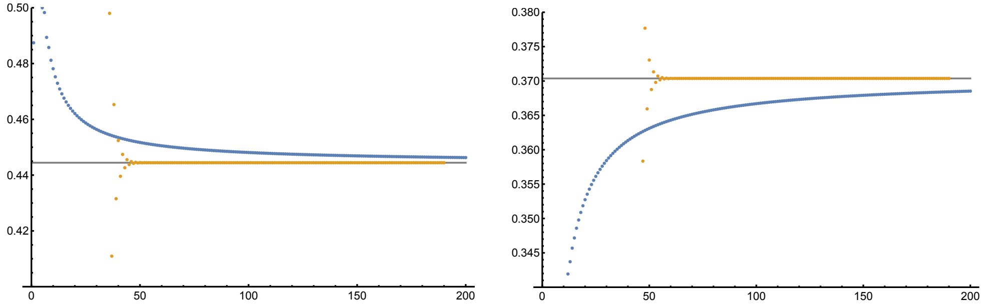

(a) **(b)**

Figure 5.4.: Fig. (a) and (b) show the sequence $\mathbb{D}_0(k)$ (top curve left, blue), Eq. (5.20), and $\mathbb{D}_1(k)$ (bottom curve right, blue), Eq. (5.22), respectively. To accelerate the rate of convergence, the other curves show the 10th Richardson transform in orange, which shows good convergence to the exact values $\frac{4}{9}$ and $\frac{10}{27}$, respectively, denoted by the gray horizontal lines.

plane at $u = -1$ is a double pole. Using Richardson transforms, we confirm these expectations to good numerical precision. For example, $\mathrm{RT}[\mathbb{A}](190, 10)$ agrees to 23 decimal places with $A_2 = -1$, and we obtain similar precision for $\beta_{(0,1)} = -2$.

We can now systematically extract the non-perturbative coefficients $d_h^{(0,1)}$ in Eq. (5.16). First, we rewrite that equation in the form

$$\mathbb{D}_0(k) \equiv \frac{d_k^{(0,0)} A_2^{k-\beta_{0,1}}}{\Gamma(k-\beta_{0,1})} \sim \tilde{d}_0^{(0,1)} + \mathcal{O}\left(\frac{1}{k}\right). \tag{5.20}$$

In Fig. 5.4a we have plotted the sequence together with its 10th Richardson transform, and we conclude that

$$\tilde{d}_0^{(0,1)} = \frac{4}{9} \tag{5.21}$$

to great precision, e.g. $\mathrm{RT}[\mathbb{D}_0](190, 10)$ agrees with 4/9 to 26 decimal places. We should notice here that we determined the value of $\tilde{d}_0^{(0,1)}$, in which the unknown Borel residue $\mathsf{S}_{(0,0)\to(0,1)}$ is absorbed. This is actually a generic phenomenon in the resurgence of transseries with free parameters; one can see from Eq. (5.11) that rescaling these parameters will rescale the expansion coefficients in the non-perturbative sectors. Moreover, as $\sigma_{n,m}$ is rescaled, the Borel resdiues are similarly rescaled. As a result, only 'scale invariant' combinations of the expansion coefficients and the Borel residues have a physical meaning. In Sec. 5.1.4, we use this scale invariance to give a natural interpretation to the transseries parameters.

Next, we can plot the sequence

$$\mathbb{D}_1(k) \equiv k\left[\mathbb{D}_0(k) - \frac{4}{9}\right] \sim A_2\, \tilde{d}_1^{(0,1)} + \mathcal{O}\Big(\frac{1}{k}\Big) \tag{5.22}$$

and from Fig. 5.4b we deduce that this sequence converges to

$$A_2\, \tilde{d}_1^{(0,1)} = \frac{10}{27}. \tag{5.23}$$

which can again be verified up to 26 decimal places by doing 10 Richardson transforms. We can repeat this process and find a closed form for all of the $1/k$ contributions in the large order relation:

$$\begin{aligned} d_k^{(0,0)} &\sim \frac{\Gamma(k+2)}{(-1)^k}\left[\frac{4}{9} + \frac{10}{27}\frac{1}{k}\sum_{n=0}^{\infty}\left(\frac{-1}{k}\right)^n\right] + \mathcal{O}(2^{-k}) \\ &= \frac{\Gamma(k+2)}{(-1)^k}\left[\frac{4}{9} + \frac{10}{27}\frac{1}{k+1}\right] + \mathcal{O}(2^{-k}). \end{aligned} \tag{5.24}$$

Using Eq. (5.16), we can also rewrite this in terms of the non-perturbative coefficients $d_h^{(0,1)}$, which are seen to be

$$\tilde{d}_0^{(0,1)} = \frac{4}{9}, \qquad \tilde{d}_1^{(0,1)} = -\frac{10}{27}, \qquad \tilde{d}_{h\geq 2}^{(0,1)} = 0. \tag{5.25}$$

Most of the coefficients vanish and as a result, the $(1,0)$ sector is not an asymptotic series but a finite one. We will revisit this point more extensively later.

So far, from the first 200 perturbative coefficients that we computed numerically and analyzed, we have extracted the complete first non-perturbative sector $D_{\mathrm{LO}}^{(0,1)}$. For the leading order Adler function, we know the exact Borel transform Eq. (5.5) and can therefore check our large order relations. That is, we have that

$$\mathcal{B}[D_{\mathrm{LO}}^{(0,0)}](u)\Big|_{u=-1} = \frac{4/9}{(u+1)^2} + \frac{10/27}{(u+1)} + \text{regular terms}, \tag{5.26}$$

which indeed agrees with Eq. (5.25). (This is also the reason that we wrote the above numerical estimates with an equal sign.) Note that this leading UV behaviour was already indicated in Eq. (4.9), but here we determined the precise coefficient, as well as the subleading term.

Having obtained the complete first non-perturbative sector, we can now subtract the corresponding leading order growth from the large order expression for the perturbative

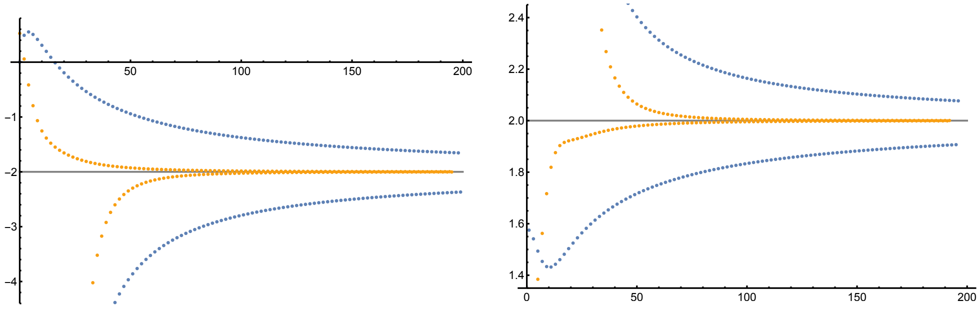

(a) **(b)**

Figure 5.5.: In Fig. (a) and (b), we show the sequences $\mathbb{A}(k)$ of Eq. (5.17) (outer two curves, in blue), and $\mathbb{B}(k)$ of Eq. (5.18), but now constructed from $\delta_k^{(1)}$ given in Eq. (5.27). We also show their 2nd Richardson transforms. (Middle two curves, in orange.) Note that as the parity of k is important, we took the Richardson transforms separately on even and odd k.

sector coefficients. That is, we construct the sequence

$$\delta_k^{(1)} \equiv d_k^{(0,0)} - \frac{\Gamma(k+2)}{(-1)^k}\left[\frac{4}{9} + \frac{10}{27}\frac{1}{k+1}\right] \tag{5.27}$$

where the asymptotic growth should now be dominated by the non-perturbative sectors $(2,0)$ and $(0,2)$, i.e.

$$\delta_k^{(1)} \sim \sum_{h=0}^{\infty} \tilde{d}_h^{(2,0)} \frac{\Gamma(k-h-\beta_{2,0})}{(2A_1)^{k-h-\beta_{2,0}}} + \sum_{h=0}^{\infty} \tilde{d}_h^{(0,2)} \frac{\Gamma(k-h-\beta_{0,2})}{(2A_2)^{k-h-\beta_{0,2}}} + \mathcal{O}(3^{-k}). \tag{5.28}$$

Since the Borel transform has poles at both $u = -2$ and $u = +2$, we now see two sectors appearing in this formula. Note that also $A_1 = -A_2 = 1$, i.e. they are equal but opposite in sign. Even though the rest of the $(\ell, 0)$ and $(0, \ell)$ sectors are quite different from each other, as we shall see later, the parity of k will have an important effect on the right hand side of this expression. In particular, in order to use Richardson transforms to speed up the convergence of series, we have to separate even and odd k and perform Richardson transforms on them separately. In Figs. 5.5a and 5.5b, we show the sequences of Eq. (5.17) and Eq. (5.18), but now constructed from $\delta_k^{(1)}$. Notice that the ratio test Eq. (5.18) can be taken, if we assume that the starting orders $\beta_{2,0} = \beta_{0,2} \equiv \beta_2$ are the same. Even though we find in Eq. (5.29) below that strictly speaking $\beta_{2,0} \neq \beta_{0,2}$, this is not an issue since we can compute with $\beta_2 = \min(\beta_{2,0}, \beta_{0,2})$ and allow for a finite number of vanishing leading coefficients in one of the two series. Here, we conclude that $2A_2 = -2A_1 = -2$ and $\beta_2 = -2$. Following Eqs. (5.20) and (5.22), but now also taking the parity of k into account by using ratio tests for even and odd k separately, we obtain

$$\tilde{d}_0^{(2,0)} = 0, \qquad \tilde{d}_1^{(2,0)} = 2 \qquad \text{and} \qquad \tilde{d}_0^{(0,2)} = -\frac{2}{9}, \qquad \tilde{d}_1^{(0,2)} = \frac{7}{54}, \tag{5.29}$$

with all other coefficients equal to zero. This can be compared to the expansions around $u = 2$ and $u = -2$ respectively, and we find the expected agreement with the exact Borel transform:

$$\begin{aligned} \mathcal{B}[D_{\rm LO}^{(0,0)}](u)\Big|_{u=-2} &= -\frac{2/9}{(2+u)^2} - \frac{7/54}{(2+u)} + \text{regular terms} \\ \mathcal{B}[D_{\rm LO}^{(0,0)}](u)\Big|_{u=2} &= \frac{2}{(2-u)} + \text{regular terms}\,, \end{aligned} \tag{5.30}$$

where this leading IR behaviour was indicated in Eq. (4.9), here given with the precise coefficient. Notice that in the second line the leading singularity around $u = 2$ is a single pole and therefore one should expect $\beta_{2,0} = -1$ instead of -2, as mentioned above. Indeed, we found that $\tilde{d}_0^{(2,0)} = 0$ and one can conclude that the series effectively starts at order -1.

5.1.3. Resurgence analysis: all non-perturbative sectors

Having used resurgence to recover the expressions for the first and second non-perturbative sectors of the Adler function transseries, we can repeat the analysis of the previous subsection to also obtain other sectors. Since the procedure is very similar, we will be more brief here about the techniques and will focus more on the results and on the general structure that emerges.

To find higher sectors, we recursively probe the next sector by subtracting from the large order expression for the perturbative coefficients all sectors we have found so far. Each sector provides two nonzero coefficients, $s_k^{(\ell)}$ and $t_k^{(\ell)}$, whose values for $1 \leq \ell \leq 8$ are given in Tab. 5.1 and we find the following pattern:

$$\delta_k^{(\ell)} \equiv \delta_k^{(\ell-1)} - \frac{\Gamma(k+2)}{(-\ell)^{k+2}}\left(s_k^{(\ell)} + \frac{t_k^{(\ell)}}{k+1}\right), \tag{5.31}$$

where ℓ labels the sectors, and the coefficients $\delta_k^{(\ell)}$ are the ones whose large order behaviour can be used to probe sector $\ell + 1$. As before, we obtained these numbers numerically, using ratio tests. However, for these specific diagrams, we fortunately have an analytic Borel transform result, and as in the previous section our numbers can be directly checked with the expansion of the Borel transform around the poles.

ℓ	$s_k^{(\ell)}$	$t_k^{(\ell)}$
1	$\frac{4}{9}$	$\frac{10}{27}$
2	$-\frac{2}{9}$	$-\frac{7}{27}+4(-1)^k$
3	$\frac{2}{15}-\frac{4}{3}(-1)^k$	$\frac{9}{50}-6(-1)^k$
4	$-\frac{4}{45}+\frac{4}{9}(-1)^k$	$-\frac{88}{675}+\frac{40}{27}(-1)^k$
5	$\frac{4}{63}-\frac{2}{9}(-1)^k$	$\frac{130}{1323}-\frac{35}{54}(-1)^k$
6	$-\frac{1}{21}+\frac{2}{15}(-1)^k$	$-\frac{15}{196}+\frac{9}{25}(-1)^k$
7	$\frac{1}{27}-\frac{4}{45}(-1)^k$	$\frac{119}{1944}-\frac{154}{675}(-1)^k$
8	$-\frac{4}{135}+\frac{4}{63}(-1)^k$	$-\frac{304}{6075}+\frac{208}{1323}(-1)^k$

Table 5.1.: This table gives the values of $s_k^{(\ell)}$ and $t_k^{(\ell)}$ for $1 \leq \ell \leq 8$ contributing to the large order behaviour of the perturbative coefficients via Eq. (5.31). As explained in the text, these values can be extracted numerically from the perturbative coefficients, but as these values can also be extracted from the exact Borel transform, this table is exact.

ℓ	$\tilde{d}_0^{(\ell,0)}$	$\tilde{d}_1^{(\ell,0)}$	$\tilde{d}_0^{(0,\ell)}$	$\tilde{d}_1^{(0,\ell)}$
1	0	0	$\frac{4}{9}$	$-\frac{10}{27}$
2	0	2	$-\frac{2}{9}$	$\frac{7}{54}$
≥ 3	$\frac{8(-1)^\ell}{3(\ell-1)(\ell-2)}$	$\frac{8(-1)^\ell(2\ell-3)}{3(\ell-1)^2(\ell-2)^2}$	$-\frac{8(-1)^\ell}{3(\ell+1)(\ell+2)}$	$\frac{8(-1)^\ell(2\ell+3)}{3(\ell+1)^2(\ell+2)^2}$

Table 5.2.: All non-zero non-perturbative coefficients of the Adler function at leading order $(1/N_f)$ in the flavour expansion.

Thus, our numbers are not only approximately equal to the given fractions, but turn out to be exact.

A closer examination of these numbers reveals the following general pattern:

$$s_k^{(\ell)} = \frac{8}{3}(-1)^\ell \begin{cases} \frac{-1}{(\ell+1)(\ell+2)} & \text{for} \quad \ell < 3 \\ \frac{-1}{(\ell+1)(\ell+2)} + (-1)^k \frac{1}{(\ell-2)(\ell-1)} & \text{for} \quad \ell \geq 3. \end{cases} \tag{5.32}$$

Similarly, we find a closed form for $t_k^{(\ell)}$:

$$t_k^{(\ell)} = \frac{8}{3}(-1)^\ell \begin{cases} -\frac{10}{27} & \text{for} \quad \ell = 1 \\ -\frac{7}{72} + \frac{3}{2}(-1)^k & \text{for} \quad \ell = 2 \\ \frac{-\ell(2\ell+3)}{(\ell+1)^2(\ell+2)^2} + (-1)^k \frac{\ell(2\ell-3)}{(\ell-2)^2(\ell-1)^2} & \text{for} \quad \ell \geq 3. \end{cases} \tag{5.33}$$

Observe that in all these results, there are terms without k-dependent signs as well as terms with $(-1)^k$ factors, respectively probing the coefficients of the $(\ell, 0)$ sectors (with non-perturbative exponent $\ell A_1 = +\ell$) and the $(0,\ell)$ sectors (with non-perturbative exponent $\ell A_2 = -\ell$).

Also notice that we have a closed form with a fixed pattern for all $\ell \geq 3$, while $\ell = 1$ and $\ell = 2$ are different. This can be traced back to the fact that the LO Adler function is the sum of the two diagrams of Fig. 5.1, where the first diagram only contributes singularities at $u = -1$, $u = 1$ and $u = 2$ to the Adler function. Here we recall Eq. (5.3), and note that the singularity at $u = 0$ from that expression vanishes when we take the derivative w.r.t Q^2 to obtain the Adler function.

Combining all results, we arrive at the first main result of this chapter: the complete asymptotic expansion of the perturbative coefficients of the Adler function at LO in the flavour expansion,

$$d_k^{(0,0)} = \frac{\Gamma(k+2)}{(-1)^k} \sum_{\ell=1}^{\infty} \frac{1}{\ell^{k+2}} \left(s_k^{(\ell)} + \frac{t_k^{(\ell)}}{k+1} \right). \tag{5.34}$$

The sum over ℓ converges, and for each term within the sum we only have finitely many coefficients rather than asymptotic expansions, so this is now not a large order formula but an exact form for the coefficients (hence the equal sign). At the next order in $1/N_f$, in Sec. 5.2, we will mostly lack exact expressions, but resurgence will still provide us with very precise large order relations, that involve non-perturbative sectors.

The coefficients of the non-perturbative sectors $(\ell, 0)$ and $(0, \ell)$ are summarised in Tab. 5.2, with the starting orders $\beta_{\ell,0} = \beta_{0,\ell} = -2$. We have seen now that for the Adler function at $\mathcal{O}(1/N_f)$ the non-perturbative sectors consist of only one or two coefficients, i.e. the $1/k$ expansions are not asymptotic. This means that these sectors do not lead to further resurgence. Thus we have now carried out this resurgence analysis to its natural end: there is no resurgence of non-perturbative sectors at any other sector than the $(0,0)$-sector. In other words, the picture of the alien lattice in this case simplifies to that of Fig. 5.6.

This structure implies that the $(\ell, 0)$-sector with $\ell > 1$ is not reached by repeatedly applying Δ_A, i.e. for $\ell > 1$, $\Delta_A^\ell D_{\mathrm{LO}}^{(0,0)} = 0$. Instead one needs non-vanishing alien derivatives for larger steps forward: $\Delta_{\ell A} D_{\mathrm{LO}}^{(0,0)} \sim D_{\mathrm{LO}}^{(\ell,0)}$. Similarly, we have for $\ell > 1$ that $\Delta_{-A}^\ell D_{\mathrm{LO}}^{(0,0)} = 0$, but $\Delta_{-\ell A} D_{\mathrm{LO}}^{(0,0)} \sim D_{\mathrm{LO}}^{(0,\ell)}$. We will comment more on the implications of this in the next subsection.

Finally, observe that at order $1/N_f$, the alien 'lattice' in fact is hardly a lattice: all internal (n, m) sectors with $n \neq 0$ and $m \neq 0$ vanish. In Sec. 5.2, we will see that this is a result of the relative simplicity of the expressions at order $1/N_f$, and that at higher orders such internal sectors *do* appear.

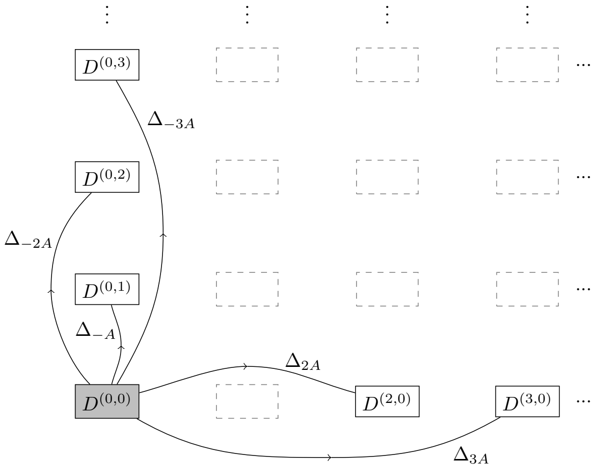

Figure 5.6.: Alien lattice for the LO Adler function. The only asymptotic sector is the $(0,0)$-sector, which we denoted by a filled box to distinquish it from the $(\ell,0)$ and $(0,\ell)$ sectors which are not asymptotic. The dashed boxes are sectors that completely vanish.

5.1.4. Stokes automorphism and transseries

So far, we worked with generic transseries parameters $\sigma_{n,m}$. A natural interpretation of these parameters comes from the Stokes automorphism $\mathfrak{S}_\theta$. In Eqs. (3.12)-(3.14) we saw how Stokes' automorphism acts on the transseries parameters, where in particular, we expressed $\mathfrak{S}_\theta$ in terms of the Borel residues. In other words, the Borel residues describe the jump across every single Stokes line. Recalling example 3.1.1, we saw a case where the Stokes automorphism along the $\theta = 0$ direction can be fully described by one transseries parameters σ and one Stokes constant S_1. For the Adler function, we have now two singular directions in the $\theta = 0$ and $\theta = \pi$ directions. As the only non-vanishing Borel residues are $S_{(0,0)\to(\ell,0)}$ and $S_{(0,0)\to(0,\ell)}$ for $\ell > 0$, the Stokes automorphism as an action on the transseries parameters becomes

$$\mathfrak{S}_0 : \sigma_{n,m} \to \sigma_{n,m} + S_{(0,0)\to(n,0)}\,, \quad \text{and} \quad \mathfrak{S}_\pi : \sigma_{n,m} \to \sigma_{n,m} + S_{(0,0)\to(0,m)}\,. \tag{5.35}$$

First of all, we notice that we can seperate the transseries parameters into two sets of transseries parameters $\sigma_{n,m} = \sigma_n + \tilde{\sigma}_m$. The Stokes automorphism then becomes

$$\begin{aligned}\mathfrak{S}_0 &: (\sigma_n, \tilde{\sigma}_m) \to (\sigma_n + S_{(0,0)\to(n,0)}, \tilde{\sigma}_m)\,,\\ \mathfrak{S}_\pi &: (\sigma_n, \tilde{\sigma}_m) \to (\sigma_n, \tilde{\sigma}_m + S_{(0,0)\to(0,m)})\,.\end{aligned} \tag{5.36}$$

So under the two different Stokes automorphism, only one set of transseries parameters jumps at a time.

We can do even better by exploiting the scale-invariance of the transseries parameters, Borel residues and coefficients. As discussed below Eq. (5.21), we have the freedom to fix the coefficients and Borel residues. A natural choice is to set all the non-zero Borel residues to the same value, such that the Stokes automorphism can be described by a single parameter and a single constant. To be precise, we pick $S_{(0,0)\to(\ell,0)} = -2\pi\mathrm{i}$ and $S_{(0,0)\to(0,\ell)} = -2\pi\mathrm{i}$, such that the factors of $2\pi\mathrm{i}$ in Eq. (5.15) drop out. In other words, $\tilde{d}_h^{(\ell,0)} = d_h^{(\ell,0)}$ and $\tilde{d}_h^{(0,\ell)} = d_h^{(0,\ell)}$, which implies that we can drop the tilde in all the non-perturbative coefficients we wrote down earlier. With this gauge choice of Borel residues and non-perturbative coefficients, we see that the transseries parameters σ_n jump by the same constant $-2\pi\mathrm{i}$ under the action of $\mathfrak{S}_0$. Similarly, the parameters $\tilde{\sigma}_m$ jump by the same constant $-2\pi\mathrm{i}$ under the action of $\mathfrak{S}_\pi$. As a result, two transseries parameters are sufficient to fully describe the Stokes jumps in the $\theta = 0$ and $\theta = \pi$ directions, and we can set $\sigma_n = \sigma_{\mathrm{IR}}$ and $\tilde{\sigma}_m = \sigma_{\mathrm{UV}}$.

Taking the above considerations into account, we can write the complete transseries Eq. (5.11) in the following form:

$$D_{\mathrm{LO}}(\alpha, \sigma_{\mathrm{IR}}, \sigma_{\mathrm{UV}}) = D_{\mathrm{LO}}^{(0,0)}(\alpha) + \sigma_{\mathrm{IR}} D_{\mathrm{LO}}^{\mathrm{IR}}(\alpha) + \sigma_{\mathrm{UV}} D_{\mathrm{LO}}^{\mathrm{UV}}(\alpha), \tag{5.37}$$

where we labeled the different pieces according to their QCD nature. That is, $D_{\mathrm{LO}}^{\mathrm{IR}}$ contains all IR renormalons in QCD, meaning that these are the UV renormalons in QED. Likewise, $D_{\mathrm{LO}}^{\mathrm{UV}}$ contains all UV (IR) renormalons in QCD (QED). With this choice for the transseries parameters, the Stokes automorphism is then described by

$$\begin{aligned}
\mathfrak{S}_0\, D_{\mathrm{LO}}(\alpha, \sigma_1, \sigma_2) &= D_{\mathrm{LO}}(\alpha, \sigma_1 - 2\pi\mathrm{i}, \sigma_2)\,, \\
\mathfrak{S}_\pi\, D_{\mathrm{LO}}(\alpha, \sigma_1, \sigma_2) &= D_{\mathrm{LO}}(\alpha, \sigma_1, \sigma_2 - 2\pi\mathrm{i})\,.
\end{aligned} \tag{5.38}$$

In other words, the Stokes jump in the $\theta = 0$ direction is fully sensitive to the IR sectors

$$D_{\mathrm{LO}}^{\mathrm{IR}}(\alpha) = -\frac{C_F}{\beta_0}\left[2\, e^{\frac{2}{\beta_0\alpha}} + \sum_{\ell=3}^{\infty} e^{\frac{\ell}{\beta_0\alpha}} \left(\frac{\frac{8}{3}(-1)^\ell}{(\ell-1)(\ell-2)}\frac{-1}{\beta_0\alpha} + \frac{\frac{8}{3}(-1)^\ell(2\ell-3)}{(\ell-1)^2(\ell-2)^2}\right)\right]. \tag{5.39}$$

Likewise, the Stokes jump in the $\theta = \pi$ direction is sensitive to the UV sectors

$$D_{\mathrm{LO}}^{\mathrm{UV}}(\alpha) = -\frac{C_F}{\beta_0}\left[e^{\frac{-1}{\beta_0\alpha}}\left(\frac{4}{9}\frac{-1}{\beta_0\alpha} - \frac{10}{27}\right) + e^{\frac{-2}{\beta_0\alpha}}\left(-\frac{2}{9}\frac{-1}{\beta_0\alpha} + \frac{7}{54}\right)\right.$$
$$\left. + \sum_{\ell=3}^{\infty} e^{\frac{-\ell}{\beta_0\alpha}}\left(\frac{-\frac{8}{3}(-1)^\ell}{(\ell+1)(\ell+2)}\frac{-1}{\beta_0\alpha} + \frac{\frac{8}{3}(-1)^\ell(2\ell+3)}{(\ell+1)^2(\ell+2)^2}\right)\right]. \tag{5.40}$$

In these expressions, we switched back to the original coupling constant α – recall the discussion below Eq. (5.9), where we switched to the variable $\hat{\alpha} = -\beta_0\alpha$ – and reinstated all factors of $\beta_0 = -(11 - 2N_f/3)/(4\pi)$, again expressed in QCD variables. We observe the overall factor $1/\beta_0$, and that the coupling constant α always comes with a factor β_0. Recalling Eq. (4.21), this was to be expected as the flavour expansion is an expansion in $1/\beta_0$.

The sums over the sector number ℓ converge and can be carried out explicitly. Defining

$$x_{\mathrm{IR}} = e^{\frac{1}{\beta_0\alpha}} \qquad \text{and} \qquad x_{\mathrm{UV}} = e^{-\frac{1}{\beta_0\alpha}}\,, \tag{5.41}$$

and performing the sums in Eq. (5.39) yields

$$D_{\mathrm{LO}}^{\mathrm{IR}}(\alpha,\sigma_1) = \frac{8\,C_F}{3\beta_0}\left[x_{\mathrm{IR}}^2\left(\frac{1}{\beta_0\alpha} - \frac{7}{4}\right)\right.$$
$$\left. - x_{\mathrm{IR}}(1+x_{\mathrm{IR}})\left(\frac{\log(1+x_{\mathrm{IR}})}{\beta_0\alpha} + \mathrm{Li}_2(-x_{\mathrm{IR}})\right)\right], \tag{5.42}$$

where Li_2 is the dilogarithm. For Eq. (5.40) we get

$$D_{\mathrm{LO}}^{\mathrm{UV}}(\alpha,\sigma_2) = \frac{C_F}{\beta_0}\left[x_{\mathrm{UV}}\left(\frac{4}{9}\frac{1}{\beta_0\alpha} + \frac{10}{27}\right) - x_{\mathrm{UV}}^2\left(\frac{8}{9}\frac{1}{\beta_0\alpha} + \frac{8}{27}\right)\right. \tag{5.43}$$
$$\left. - \frac{8}{3}\frac{1}{x_{\mathrm{UV}}}\left(1+\frac{1}{x_{\mathrm{UV}}}\right)\left(\frac{\log^{(>3)}(1+x_{\mathrm{UV}})}{\beta_0\alpha} - \mathrm{Li}_2^{(>3)}(-x_{\mathrm{UV}})\right)\right],$$

where we defined

$$\log^{(>n)}(1+x) \equiv \log(1+x) + \sum_{j=1}^{n}\frac{(-x)^j}{j} \quad \text{and} \quad \mathrm{Li}_2^{(>n)}(x) \equiv \mathrm{Li}_2(x) - \sum_{j=1}^{n}\frac{x^j}{j^2} \tag{5.44}$$

as the logarithm and polylogarithm with the first n terms of their Taylor expansion removed. Although Eq. (5.43) appears to generate factors such as $1/x_2$, these in fact cancel as the first three coefficients of the Taylor expansion of the log and Li_2 are subtracted.

5.1.5. Discussion

At this point, we have studied the full single bubble-chain part of the Adler function. Before moving on to the main goal of our investigation, the multi-bubble chain contributions, let us discuss some finer details of the structure that has appeared.

In Sec. 5.1.4 we argued by studying Stokes' automorphism that two transseries parameters are sufficient to describe the two different Stokes jumps in the $\theta = 0$ and $\theta = \pi$ directions. We notice that the resulting transseries is different from that of the two-parameter transseries structure known from many toy models and discussed in chapter 2. This difference was to be expected: e.g. $\Delta^2_{A_1} D^{(0,0)}_{\mathrm{LO}} = 0$, but $\Delta_{2A_1} D^{(0,0)}_{\mathrm{LO}} \sim D^{(2,0)}_{\mathrm{LO}}$. Compared to chapter 2, where we had $\Delta_{2A_1} D^{(0,0)}_{\mathrm{LO}} = 0$, this means that the Adler function at least has a bridge equation beyond that of such simple toy models. Unfortunately, since e.g. a differential equation for the Adler function as needed for the procedure in Sec. 2.3 is not known, we cannot derive a bridge equation which would allow us to read off the number of parameters and the transseries structure. The fact that we are able to describe the Stokes jumps for the Adler function at order $1/N_f$ with only two transseries parameters, might be an artifact of the flavour expansion and could break down at higher orders in the flavour expansion.

One may wonder how many free parameters the transseries structure of the Adler function really has. This is not a question that can be answered from the Borel plane alone; once one finds a singularity at a location A it is natural to include a free parameter σ in front of the $e^{-A/\alpha}$ transmonomial, but it is then not clear whether the $e^{-nA/\alpha}$ sectors should come with the same parameter σ, powers σ^n, or with new parameters. (See e.g. [54] where, as we discussed below Eq. (2.51) the latter is the case.) Thus, our transseries may be a many-parameter one, but on physical grounds we still expect the number of 'true' parameters to be two. The reason is that there are only two Stokes automorphisms that play a role – and as we shall see, this continues to be the case when we include further bubble chains – an IR one along the positive real u-axis and a UV one along the negative real u-axis. A single parameter could in principle suffice to describe the jump across a single Stokes line, and there is no known additional physical effect that would lead to singularities on other rays in the u-plane, so we conjecture that two parameters is in fact enough. Interestingly, this is similar to the recent work of [113] where in a different setting a transseries was found with many degrees of freedom (parameterized by variables τ_k there) but with only a single transseries parameter for each Stokes line.

When it comes to the *values* of the transseries parameters, these are difficult to determine and require further physics input. This is beyond the scope of this thesis, where we are mainly interested in the underlying structure. In principle, one would need to numerically sum non-perturbative sectors of the Adler function transseries and compare these to experimental data to read off values for σ_{IR} and σ_{UV}. See [107] for an effort in this direction for the IR Stokes automorphism.

Recall that in Eq. (5.43), a variable x_{UV} appears which comes from the UV singularities and grows exponentially large when $\alpha \to 0$. This is a common feature for transseries that have instanton actions of opposite sign, $\pm A$. An expansion in such a large variable x_{UV} may not seem very physically meaningful. One possible solution to this is of course that the parameter σ_{UV} vanishes or is small. Even if this were not the case, x_{UV} still has a definite value at any given energy scale, and so an expression like Eq. (5.43) still makes sense, even though its small α expansion may not. In fact, often a sum over different powers of x_2 is itself not asymptotic but *converges*, as in our examples above (see also [114] for recent progress on this topic). Also note that part of the large order growth of the original perturbative series is still determined by σ_{UV}-dependent sectors, so even when they have coefficient zero, these sectors do play a role.

As a final remark, let us address the fact that many of the non-perturbative sectors we have found only have a finite number of terms – and therefore, these sectors in particular have no asymptotic growth of their own. This may seem to limit the use of resurgence techniques to only the perturbative sector, but we expect this to be an artifact of the simplicity of the single bubble chain approximation. In fact, in the next sections we shall see that many non-perturbative sectors do become true asymptotic expansions when further bubble chains are included. This is reminiscent of the 'Cheshire cat resurgence' of [115] where asymptotic growth of sectors can disappear in particular parameter limits[5]. This may also happen in $1/N_f$ expansions – see for example the interesting approach of [38] where it was found that in the Gross-Neveu model, only at finite N_f the full resurgent structure and asymptotic growth of sectors becomes visible.

5.2. Adler function with two bubble chains ($\mathcal{O}(1/N_f^2)$)

In Sec. 5.1 we discussed how the minimal two-parameter transseries Ansatz for the Adler function could be obtained using the resurgence relations described in chapters 2 and 3. From a resurgence point of view, the structure of this transseries at order $1/N_f$

---

[5] We quote the authors of [115]: "All of the characteristics of resurgence remains even when its role seems to vanish, much like the lingering grin of the Cheshire Cat".

was surprisingly simple as the only asymptotic sector is the perturbative $(0,0)$-sector. In particular, we saw that most of the non-perturbative sectors are in fact vanishing (recall Fig. 5.6), and those sectors that were not vanishing only consist of one or two terms. As a result, we were even able to sum the whole non-perturbative part of the transseries, leading to the closed form expressions given in Eqs. (5.42) and (5.43).

From our discussion in Sec. 4.2, we do not expect that this relatively simple transseries structure is still present at higher orders in the flavour expansion, i.e. after adding more bubble chains. (See e.g. [97–99, 116] for earlier work including two or more bubble chains.) Recalling Fig. 4.3, we observed that the convolution integral leads to asymptotic non-perturbative sectors, and found that the alien chain or lattice gradually builds up by taking more and more convolution integrals. We therefore expect that already at the next order in the flavour expansion, i.e. at order $1/N_f^2$, the transseries for the Adler function will contain asymptotic non-perturbative sectors.

In order to test these expectations, and to get a first view of the resurgence structure at higher orders in the flavour expansion, we discuss in this section the Adler function at order $1/N_f^2$ (NLO). Unfortunately, a complete calculation of the Adler function at this order is not possible yet, because for some diagrams the master integrals for the Feynman integrals appearing at this order are not yet known. Therefore, we focus in this section on the set of planar diagrams shown in Fig. 5.7, which we are able to compute. (These diagrams are leading in the $SU(3)$ color structure.) A brief review of the complete set of diagrams at order $1/N_f^2$ can be found in App. B.3.

Note that the subset of diagrams of Fig. 5.7 is not gauge invariant, and our resurgence analysis in this section is only on a diagram by diagram basis. Unless very specific cancellations occur between diagrams, however, one may expect most of the resurgence features that appear in individual diagrams to also appear in the sum of the full set of diagrams – as indeed occurred at order $1/N_f$ – and it is those resurgence features that we are after. Our assumption in the present work is that such cancellations do not occur unless there is a clear physical reason for them, as is the case for the absence of a singularity at $u = 1$ in the Borel plane.

In particular, we discuss the resurgence of the complete first two non-perturbative sectors, i.e. the $(1,0)$, $(0,1)$, $(2,0)$ and $(0,2)$ sectors. Using large order relations, we show how these results can be extracted numerically from the perturbative coefficients only. To supplement these results, we use the techniques of Sec. 4.2 to get one of the key results of this section: the exact Borel transforms of these sectors. Using the same techniques, we even find that there are further (n,m) sectors with both n and m nonzero, contary to what was the case at leading order in $1/N_f$. At the end of the section, we briefly discuss the remaining transseries sectors and summarize the structures we have found in Tab. 5.3.

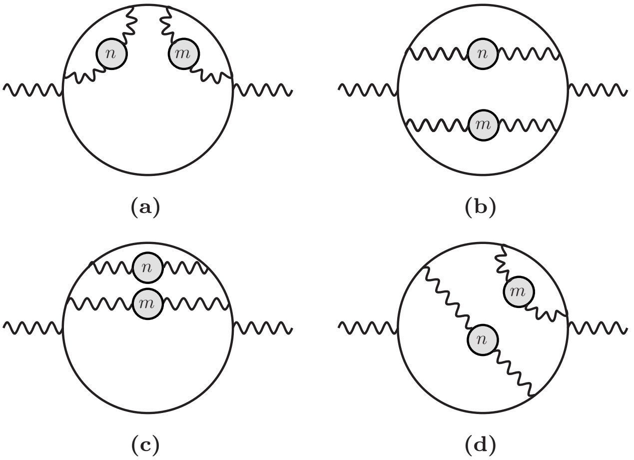

(a) (b) (c) (d)

Figure 5.7.: Subset of diagrams at $\mathcal{O}(1/N_f^2)$ that are computed in this section.

5.2.1. Four diagrams at $\mathcal{O}(1/N_f^2)$

Using the convolution integral Eq. (4.19), the Borel transform of the diagrams shown in Fig. 5.7 can be computed using an analytic regularized propagator for each of the bubble chains, Eq. (4.18). In terms of the convolution integral, the Borel transform for each diagram is given by

$$\mathcal{B}[\Pi(Q^2)](u) = \frac{-1}{\beta_{0f}} \left(\frac{Q^2}{\mu^2} e^C \right)^{-u} \int_0^u du_1 \, du_2 \, \delta\big(u - u_1 - u_2\big) \Pi(u_1, u_2) \,, \tag{5.45}$$

where $\Pi(u_1, u_2)$ is the Q^2-independent part of these diagrams in terms of the two Borel parameters u_1 and u_2 of the bubble chains. Here and in the expressions that follow, we again ignore an overall colour factor C_F^2. For diagrams (a)-(c) in Fig. 5.7, we managed to compute the Q^2-independent part $\Pi(u_1, u_2)$ exactly to all orders in u_1 and u_2, see App. B.1 and B.2 for more details, and the result reads:

$$\begin{aligned}
\Pi_a(u_1, u_2) &= -\frac{3}{2\pi^2} \frac{1}{u(1-u)(2-u)} \frac{1}{(u_1-2)(u_1-1)(u_1+1)} \frac{1}{(u_2-2)(u_2-1)(u_2+1)} \,, \\
\Pi_b(u_1, u_2) &= -\frac{3}{2\pi^2} \frac{\Gamma(u)}{(1-u)\Gamma(3-u)} \frac{\Gamma(1-u_1)}{(u_1-2)\Gamma(2+u_1)} \frac{\Gamma(1-u_2)}{(u_2-2)\Gamma(2+u_2)} \,, \\
\Pi_c(u_1, u_2) &= \frac{3}{2\pi^2} \frac{1}{u(1-u)(2-u)} \frac{\Gamma(u)}{\Gamma(3-u)} \frac{u_1 \Gamma(1-u_1)}{\Gamma(2+u_1)} \frac{\Gamma(1-u_2)}{(u_2-2)\Gamma(2+u_2)} \,,
\end{aligned} \tag{5.46}$$

where, after taking the δ-function in the convolution integral (5.45) into account, we have $u = u_1 + u_2$. For diagram (d) we do not have a such a closed form, but instead computed the expansion in u_1 and u_2, for which the first few terms read

$$\begin{aligned}\Pi_d(u_1,u_2) = {} & \frac{201}{4} - 36\zeta_3 + \Big(\frac{315}{4} - 54\zeta_3\Big)u_1 + \Big(\frac{3123}{16} - 63\zeta_3 - 90\zeta_5\Big)u_1^2 \\ & + \Big(\frac{873}{8} - 54\zeta_3\Big)u_2 + \Big(\frac{747}{4} - 93\zeta_3 - 60\zeta_5\Big)u_2^2 + \frac{1}{u}\Big(18 + \frac{9u_1}{4} + 36u_1^2\Big) \\ & + \Big(\frac{4539}{16} - 144\zeta_3 - 90\zeta_5\Big)u_1u_2 + \ldots \end{aligned} \tag{5.47}$$

In App. B.1 we give additional details for the computation of the perturbative coefficients for this diagram.

In order to get the contributions to (Borel transform of the) Adler function, we can perform the convolution integral (5.45) and take the derivative with respect to Q^2 (recall Eq. (5.2)). The convolution integral (5.45) for diagram (a) can be computed exactly, and we obtain

$$\mathcal{B}[D(Q^2)](u) = \frac{1}{\beta_{0f}}\left(\frac{Q^2}{\mu^2}e^C\right)^{-u}\mathcal{B}[D](u)\,, \tag{5.48}$$

with the closed form expression

$$\begin{aligned}\mathcal{B}[D_a](u) = \frac{6}{(1-u)(2-u)}\Bigg[& \frac{\log(1+u)}{3(1-u)u(2+u)} + \frac{\log(1-u)}{(3-u)(2-u)u} \\ & + \frac{2\log(1-\frac{u}{2})}{3(4-u)(3-u)(1-u)}\Bigg].\end{aligned} \tag{5.49}$$

However, for the other three diagrams we do not have the benefit of a closed form. Instead, one can expand the $\Pi(u_1,u_2)$ for these diagrams in u_1 and u_2 and perform the convolution integral order by order. In this way we find

$$\mathcal{B}[D_a](u) = -\frac{3u}{4} - \frac{3u^2}{2} - \frac{81u^3}{32} - \frac{215u^4}{64} - \frac{2707u^5}{640} + \mathcal{O}(u^6) \tag{5.50}$$

$$\mathcal{B}[D_b](u) = -\frac{3u}{4} - \frac{3u^2}{2} - \frac{85u^3}{32} - \left(\frac{239}{64} - \frac{\zeta_3}{4}\right)u^4 - \left(\frac{3211}{640} - \frac{\zeta_3}{2}\right)u^5 + \mathcal{O}(u^6) \tag{5.51}$$

$$\mathcal{B}[D_c](u) = -\frac{3u}{8} - \frac{13u^2}{16} - \frac{95u^3}{64} - \left(\frac{277}{128} - \frac{\zeta_3}{8}\right)u^4 - \left(\frac{759}{256} - \frac{11\zeta_3}{40}\right)u^5 + \mathcal{O}(u^6) \tag{5.52}$$

$$\begin{aligned}\mathcal{B}[D_d](u) = 3u + \left(\frac{137}{16} - 6\zeta_3\right)u^2 + \left(\frac{565}{32} - 9\zeta_3\right)u^3 + \left(\frac{11219}{384} - \frac{38\zeta_3}{3} - \frac{65\zeta_5}{6}\right)u^4 \\ + \left(\frac{27787}{640} - \frac{703\zeta_3}{48} + \zeta_3^2 - \frac{65\zeta_5}{4}\right)u^5 + \mathcal{O}(u^6)\,,\end{aligned} \tag{5.53}$$

where, even though we have the closed form in Eq. (5.49), we added the first few coefficients for $\mathcal{B}[D_a](u)$. For diagrams (a)-(c), we computed the coefficients up to order u^{150}. Diagram (d) is computationally more involved and we managed to compute up to order u^{18}.[6]

Before we enter the detailed resurgence analysis, we can already have a closer look at the singularities of each of those expressions in the Borel plane. The singularities of diagram (a) can be read off immediately from its closed form, Eq. (5.49): branch cuts starting at $u = -1$, $u = 1$ and $u = 2$ and poles at $u = -2$, $u = 1$, $u = 2$, $u = 3$, and $u = 4$. For the other diagrams, for which we only have a finite number of perturbative coefficients, we cannot read off the singularities in this way. Instead, we use Padé approximants – already explained in Sec. 2.7.2. The poles of these Padé approximants give a good indication of where the 'true' singularities in the Borel plane are located. In order to see the type of singularities that we can expect in the Borel plane of the different diagrams, we plot the poles of the diagonal Padé approximants in Fig. 5.8.

For diagrams (b) and (c), we see essentially the same pattern arising as for diagram (a): the emergence of poles in the UV direction and a branch cut starting at $u = 1$ and at $u = 2$. We also expect the emergence of branch cuts beyond $u = 2$ for diagrams (b) and (c), but more on this in a moment. As we do not have many terms for diagram (d) it is hard to tell if the Padé poles near $u = -1$ and $u = 1$ are the start of a branch cut, or are Borel plane poles instead. We also observe some 'spurious' poles that have an imaginary component. A closer look reveals that these poles always come in pairs: they are the complex conjugate of each other. This is a common phenomenon for Padé approximants, and often reveals the fact that these mimic one pole without an imaginary component.

It is interesting to note that in the Borel transforms of the individual diagrams, the singularity at $u = 1$ does not disappear. This was also the case for the LO ($\mathcal{O}(1/N_f)$) Adler function: when the diagrams were taken separately they did have a singularity at $u = 1$. However, these singularities at $u = 1$ cancelled when we added the diagrams. On physical grounds, we expect that this will still happen when we take all diagrams together at every given order in the flavour expansion – recall the discussion on the OPE below Eq. (5.7). Nevertheless we do *not* expect singularities at other values of u to cancel. This also did not happen in the case of the LO Adler function where the singularities on a diagram by diagram basis indeed gave a realistic picture of the singularities for the sum of the diagrams.

5.2.2. Transseries Ansatz

Our discussion of resurgence in chapter 2 was mainly focused on the case where the singularities of the Borel transform are simple poles or logarithmic branch cuts. In

---

[6] Our calculation exhausts the current datamine [117], which we used to compute these coefficients.

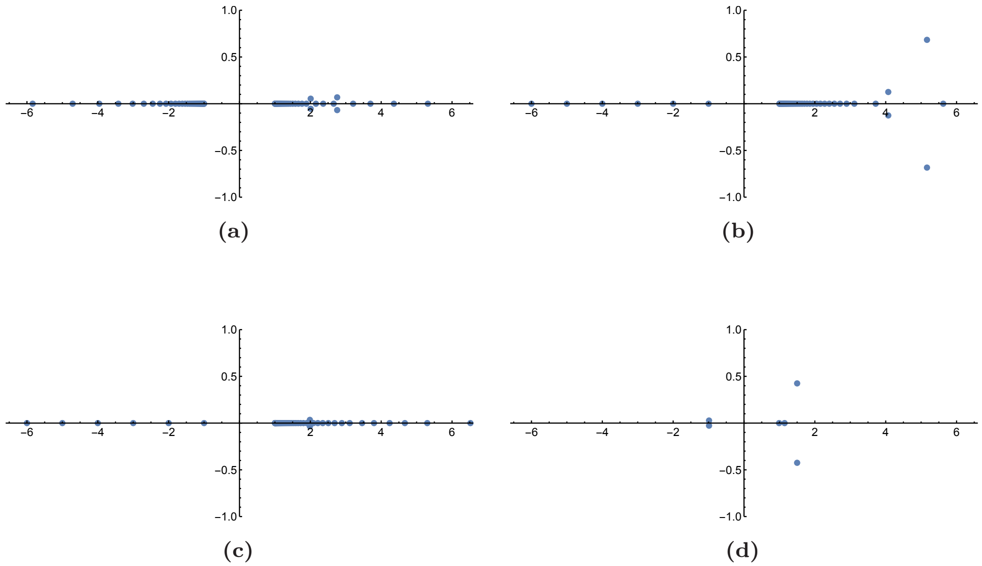

(a) (b)

(c) (d)

Figure 5.8.: Plot (a)-(c) show the singularities of the diagonal order 75 Padé approximants of the diagrams (a)-(c) respectively. Branch cuts are mimicked by an accumulation of poles. As we only have 18 coefficients for diagram (d), we show the Padé poles of the diagonal order 9 Padé approximant in plot (d).

many examples studied so far in the literature these are indeed the only singularities that occur, but in the case of the Adler function several other types of singularity are present. We already encountered double poles in Sec. 5.1, and if we look at the exact Borel transform for diagram (a), we observe another type of singularity:

$$\mathcal{B}[D_a](u)\Big|_{u=1} = -3\frac{\log(1-u)}{u-1} + ... \tag{5.54}$$

where the ellipsis denotes other singularities (poles and logarithmic branch cuts) as well as regular terms. At the end of Sec. 2.6 we saw that a singularity of the form in Eq. (5.54) follows from perturbative coefficients that grow as $\Gamma(k+1)\psi(k+1)$, where $\psi(z)$ is the digamma function. Dividing by $\Gamma(k+1)$, this means that the leading growth of the coefficients of the Borel transform $\mathcal{B}[D_a](u)$ is given by $-3\log(k)$, where we read off the -3 from Eq. (5.54) and used $\psi(k) = \log(k) + \mathcal{O}(1/k)$.

In Fig. 5.9, we show the perturbative coefficients of $\mathcal{B}[D_a]$ together with the function $-3\log(k)$, and indeed this function matches the leading growth of these coefficients quite well. We observe similar logarithmic growth for the coefficients $\mathcal{B}[D_b](u)$ and $\mathcal{B}[D_c](u)$. Notice that the plotted points for the coefficients of $\mathcal{B}[D_b](u)$ nearly overlap with those for $\mathcal{B}[D_a](u)$, implying that the leading growths of D_b and

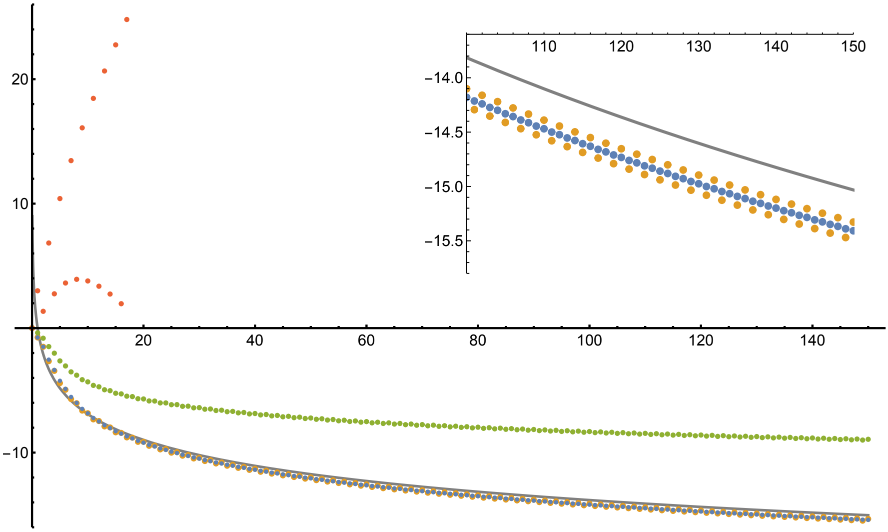

Figure 5.9.: Plot of the first 150 perturbative coefficients of $\mathcal{B}[D_a]$ (blue), $\mathcal{B}[D_b]$ (orange), $\mathcal{B}[D_c]$ (green). As the solid gray line we also show the function $-3\log(k)$ to highlight the fact that the coefficients for (a) and (b) and (c) show logarithmic growth. Similarly, we observe logarithmic growth for the coefficients for (c). Since the points denoting the coefficients for (a) and (b) practically overlap, we included a subfigure zooming in at part of those sequences. In red, above the horizontal axis, we show the 18 coefficients for $\mathcal{B}[D_d]$ we have calculated. As the even and odd coefficients seem to follow different curves it is unclear if these coefficients also show logarithmic growth.

D_a are equal. For the coefficients of $\mathcal{B}[D_d](u)$ it is more difficult to tell if the coefficients show logarithmic growth, as we only have 18 coefficients where the even and odd coefficients seem to follow notably different curves, so that we only have 9 coefficients to determine the trend for each curve. This makes determining the large order behaviour unrewarding. Nevertheless it is a pleasant surprise to see from Fig. 5.8d how well the Padé approximation already estimates the location of the poles in u near ± 1. Comparing the logarithmic growth $\sim \Gamma(k+1)\psi(k+1)$ with Eq. (2.54), which describes the large order relation for a transseries Ansatz of the type Eq. (2.52) with logarithms, we see that at the level of the transseries this implies that logarithmic terms are included in the expansion in α. As discussed in Sec. 5.1 for the Adler function at LO in the flavour expansion, the form of the complete transseries is further determined by the fact that the Borel transforms of the diagrams have singularities at both negative and positive integer values of u. Taking these considerations into account, we make the following minimal transseries Ansatz for diagrams (a), (b) and (c):

$$D_{\text{NLO}}(\alpha) = \sum_{n=0}^{\infty}\sum_{m=0}^{\infty} \sigma_{n,m} e^{-n\frac{A_1}{\alpha}} e^{-m\frac{A_2}{\alpha}} \left[D_{\text{NLO}}^{(n,m)[0]}(\alpha) + \log(\alpha) D_{\text{NLO}}^{(n,m)[1]}(\alpha) \right], \quad (5.55)$$

where as in the LO case $A_1 = -A_2 = 1$.[7] Two remarks are in order.

First of all, we note that diagram (a) does not have an infinite number of singularities in the Borel plane, hence in that case the sums over n and m truncate. Furthermore, note that as the sectors with logarithms lead to singularities of the form Eq. (5.54), we expect that the sectors $D_{\text{NLO}}^{(0,m)[1]}$ vanish as diagram (a) does not contain such a singularity at $u = -1$ and because the Padé plots for diagram (b) and (c) do not show branch cuts starting from negative integers. We will have more to say about diagram (d) at the end of the next subsection.

As a second remark, notice that we use generic transseries parameters $\sigma_{n,m}$. Similar to our analysis in Sec. 5.1.4, we can study Stokes' automorphism to see how many parameters are actually necessary to describe the relevant Stokes jumps. However, as we will see in the rest of this section, the non-perturbative sectors themselves show asymptotic growth and therefore have further resurgence to other non-perturbative sectors. This makes the analysis much more intricate and substantial to carry out. We therefore plan to come back to this in future work [118].

5.2.3. Resurgence analysis: non-perturbative sectors $(1,0)$ and $(0,1)$

Following what we did in Sec. 5.1 for the LO Adler function, we can translate the transseries Ansatz into large order relations for the perturbative coefficients and study these numerically. This will then lead to the extraction of non-perturbative sectors. Taking into account that some coefficients grow logarithmically, this yields the following natural form for the large order relation for the perturbative coefficients:

$$\begin{aligned} d_k^{(0,0)} \sim \; & \frac{\mathsf{S}_{(0,0)\to(1,0)}}{2\pi \mathrm{i}} \sum_{h=0}^{\infty} \frac{\Gamma(k-h-\beta)}{A_1^{k-h-\beta}} \Big(d_h^{(1,0)[0]} + d_h^{(1,0)[1]} (\log(A_1) - \psi(k-h-\beta)) \Big) \\ & + \frac{\mathsf{S}_{(0,0)\to(0,1)}}{2\pi \mathrm{i}} \sum_{h=0}^{\infty} \frac{\Gamma(k-h-\beta)}{A_2^{k-h-\beta}} d_h^{(0,1)[0]} + \mathcal{O}(2^{-k}) \,, \end{aligned} \quad (5.56)$$

---

[7] One often encounters the phenomenon of resonance – see also the discussion on page 24 – in transseries with logarithms and when multiple A_i add up to 0. Although the latter is the case for the diagrams considered in this section, their transseries do not show resonance. See [54] for another example of this behaviour.

where, since we can allow a finite number of the leading coefficients to vanish, we assumed $\beta^{[0]}_{1,0} = \beta^{[0]}_{0,1} = \beta^{[1]}_{1,0} = \beta^{[1]}_{0,1} \equiv \beta$ with no loss of generality (see also the discussion below Eq. (5.28)). As we did in Sec. 5.1, we absorb the Borel residues and factors of $2\pi\mathrm{i}$ into the non-perturbative coefficients:

$$\tilde{d}_h^{(\ell,0)[p]} \equiv -\frac{\mathsf{S}_{(0,0)\to(\ell,0)}}{2\pi\mathrm{i}} d_h^{(\ell,0)[p]}\,, \qquad \tilde{d}_h^{(0,\ell)[p]} \equiv -\frac{\mathsf{S}_{(0,0)\to(0,\ell)}}{2\pi\mathrm{i}} d_h^{(0,\ell)[p]}\,. \tag{5.57}$$

Non-perturbative sectors with these coefficients are denoted with a similarly notation $\tilde{D}^{(\ell,0)[p]}$ and $\tilde{D}^{(0,\ell)[p]}$ respectively.

Diagram (a)

For explicit results, let us first focus on diagram (a) as the closed form of the Borel transform, Eq. (5.49), allows us to read off the resurgence structure using Eqs. (2.26) and (2.57). We extract the dominant growth

$$\tilde{d}_0^{(1,0)[1]} \frac{\Gamma(k-\beta)\psi(k-\beta)}{A_1^{k-\beta}} \sim \tilde{d}_0^{(1,0)[1]} \frac{\Gamma(k-\beta)\log(k-\beta)}{A_1^{k-\beta}} + \mathcal{O}\Big(\frac{1}{k}\Big)\,, \tag{5.58}$$

from the expansion around Eq. (5.54), which yields the exact values

$$\beta = -1\,, \qquad \tilde{d}_0^{(1,0)[1]} = -3\,, \qquad \text{and} \qquad \tilde{d}_{h>0}^{(1,0)[1]} = 0\,. \tag{5.59}$$

Subtracting the leading growth from the large order formula yields

$$\begin{aligned}\delta_k^{(0)} &\equiv \frac{A_1^{k-\beta}}{\Gamma(k-\beta)}\Big(\tilde{d}_k^{(0,0)} - \tilde{d}_0^{(1,0)[1]}\frac{\Gamma(k-\beta)\psi(k-\beta)}{A_1^{k-\beta}}\Big) \\ &\sim \sum_{h=0}^{\infty} \frac{\Gamma(k-\beta-h)}{\Gamma(k-\beta)} A_1^h \Big[\tilde{d}_h^{(1,0)[0]} + (-1)^{h+\beta-k}\tilde{d}_h^{(0,1)[0]}\Big] + \ldots\,,\end{aligned} \tag{5.60}$$

a type of growth that we already encountered in Sec. 5.1. Taking similar ratio tests as we did there, and taking the parity of k into account, we find full asymptotic expansions:

$$\tilde{d}_h^{(1,0)[0]} = \begin{cases} \frac{1}{3} - 3\gamma_E + \frac{13}{9}\log(2) & h=0 \\ \Gamma(h)\Big(\big(3h+\frac{3}{2}\big) + (-1)^h\frac{1}{2} + \frac{1}{2^h}\Big) & h>0 \end{cases} \tag{5.61}$$

for the $(1,0)$ sector, and

$$\tilde{d}_h^{(0,1)[0]} = \begin{cases} 0 & h = 0 \\ \Gamma(h)\Big(\frac{1}{2} - (-1)^h \frac{1}{36} - \frac{1}{2^{h+1}}\big(\frac{2}{3}h + \frac{4}{9}\big) - \frac{1}{3^h}\frac{1}{4}\Big) & h > 0 \end{cases} \tag{5.62}$$

for the $(0,1)$ sector. We have checked Eqs. (5.61) and (5.62) numerically up to 20 decimal places for the first 15 coefficients by using Richardson transforms. Note the gamma-functions $\Gamma(h)$ in these expressions, implying that the first non-perturbative sectors are now indeed asymptotic series, just like the perturbative sector. As an additional check, we can read off the resurgence structure from the exact Borel transform Eq. (5.49) using Eq. (2.46). For example, near the singularity positioned at $u = 1$ we get

$$\begin{aligned} \mathcal{B}[D_a^{(0,0)}](u)\Big|_{u=1} &= 3\frac{\log(1-u) - \psi(1)}{1-u} + \frac{\frac{1}{3} + 3\psi(1) + \frac{13}{9}\log(2)}{1-u} \\ &\quad - \mathcal{B}[\tilde{D}^{(1,0)[0]}](u-1)\log(1-u) + \ldots, \end{aligned} \tag{5.63}$$

where the ellipsis denote regular terms, and with

$$\mathcal{B}[\tilde{D}^{(1,0)[0]}](u-1) = \frac{3}{(2-u)^2} + \frac{\frac{3}{2}}{2-u} - \frac{1}{2u} + \frac{1}{3-u}\,. \tag{5.64}$$

As already discussed above, the first term in Eq. (5.63) can be compared with Eqs. (2.56) and (2.57) and yields the coefficients of Eq. (5.59). This is the reason why we included the $\psi(1)$ term there, and then subtracted it again in the next term. Using $\psi(1) = -\gamma_E$ in the second term in Eq. (5.63) yields the coefficient in the first line in Eq. (5.61). Finally, an inverse Borel transform of Eq. (5.64) gives the second line in Eq. (5.61). In a similar way, one can read off the resurgence of the $\tilde{D}^{(0,1)[0]}$ sector, i.e. Eq. (5.62), by expanding $\mathcal{B}[D_a^{(0,0)}](u)$ around $u = -1$.

We discussed a diagram for which it was possible to find a closed form Borel transform, but the true power of resurgence analysis emerges when we study the diagrams for which we do *not* have such an exact expression. To be precise, for diagrams (b) and (c), we can study the large order behaviour of the perturbative coefficients for these diagrams, compute coefficients in the transseries numerically and can then usually infer their exact values. Furthermore, we can use the discussion of Sec. 4.2 on convolution integrals and their resurgence as a cross check. The interested reader can apply the methods of Sec. 4.2 to obtain the same results for diagram (a).

Diagram (b)

Turning to diagram (*b*), we find, by studying the large order behaviour of the perturbative coefficients, that $\beta_{1,0} = \beta_{0,1} = -1$ and that the non-zero coefficients are

$$\tilde{d}_0^{(1,0)[1]} = -3 \tag{5.65}$$

$$\tilde{d}_h^{(1,0)[0]} = \begin{cases} \frac{1}{3} - 3\gamma_E + \frac{13}{9}\log(2) & h = 0 \\ \Gamma(h)\Big(6 - \frac{3}{2^h}\Big) & h > 0 \end{cases} \tag{5.66}$$

$$\tilde{d}_0^{(0,1)[0]} = \frac{1}{5}\Big(\log(2) - \log(3)\Big)\,. \tag{5.67}$$

We have checked these numbers numerically up to 12 decimal places for the first 15 coefficients for $\tilde{d}_h^{(1,0)[0]}$, after which we inferred the exact expression – an expression that we shall argue to be correct in a different way in a moment. From the coefficients, we deduce the following information. The leading order growth of this diagram is given by a log-sector with a single coefficient $\tilde{d}_0^{(1,0)[1]}$. Furthermore, the non-perturbative $(1,0)$ sector is now an asymptotic sector, while the $(0,1)$ sector only contains just a single non-zero coefficient corresponding to a simple pole in the Borel plane (we already observed this in Fig. 5.8b).

Using the results of Sec. 4.2, we can check these numerical results using the method of alien derivatives acting on the convolution integral. We therefore rewrite the convolution integral for $D_b^{(0,0)}$ (recall Eqs. (5.45) and (5.46)) as

$$\mathcal{B}[D_b^{(0,0)}](u) = \frac{-6\Gamma(1+u)}{(1-u)\Gamma(3-u)}\mathcal{B}[\Psi^{(0)}](u)\,, \tag{5.68}$$

where we defined

$$\mathcal{B}[\Psi^{(0)}](u) = \int_0^u du_1\, \mathcal{B}[F](u_1)\mathcal{B}[F](u-u_1), \quad \mathcal{B}[F](u) = \frac{\Gamma(1-u)}{(2-u)\Gamma(2+u)}\,. \tag{5.69}$$

The singularities of the Borel transform $\mathcal{B}[F](u)$ are simple poles at positive integers, except at $u = 2$ which is a double pole. Therefore, the resurgence structure of F can be easily read off from the expansions around these poles and we find

$$\Delta_1 F = \frac{1}{2}(2\pi \mathrm{i})\,, \quad \Delta_2 F = -\frac{1}{6}(2\pi\mathrm{i})\left(\frac{1}{\alpha} + \frac{17-12\gamma_E}{6}\right), \ldots \tag{5.70}$$

Using the procedure as outlined in Sec. 4.2, we obtain

$$S_1^{\Psi}\Psi^{(1)} = \Delta_1\Psi^{(0)} = 2F\Delta_1 F = (2\pi\mathrm{i})F(\alpha). \tag{5.71}$$

In other words, in a neighborhood around $u = 1$, the Borel transform of $\Psi^{(0)}$ looks like

$$\begin{aligned}\mathcal{B}[\Psi^{(0)}](u)\Big|_{u=1} &= -S_1^{\Psi}\mathcal{B}[\Psi^{(1)}](u-1)\frac{\log(1-u)}{2\pi \mathrm{i}} + \ldots \\ &= -\mathcal{B}[F](u-1)\log(1-u) + \ldots \\ &= -\frac{\Gamma(2-u)}{(3-u)\Gamma(1+u)}\log(1-u) + \ldots\,,\end{aligned} \tag{5.72}$$

where the ellipsis denotes regular terms around $u = 1$. By adding back in the prefactor for $\mathcal{B}[D_b^{(0,0)}](u)$, close to $u = 1$ Eq. (5.68) becomes

$$\begin{aligned}\mathcal{B}[D_b^{(0,0)}](u)\Big|_{u=1} &= \frac{-6\Gamma(1+u)}{(1-u)\Gamma(3-u)}\left[\mathcal{B}[\Psi^{(0)}](u)\Big|_{u=1} + \ldots\right] \\ &= \frac{6\log(1-u)}{(1-u)(2-u)(3-u)} + \ldots \\ &\equiv -\tilde{d}_0^{(1,0)[1]}\frac{\log(1-u)}{1-u} - \mathcal{B}[\tilde{D}_b^{(1,0)[0]}](u-1)\log(1-u) + \ldots\,,\end{aligned} \tag{5.73}$$

with $\tilde{d}_0^{(1,0)[1]} = -3$ already given in Eq. (5.65) and where

$$\mathcal{B}[\tilde{D}_b^{(1,0)[0]}](u) = \frac{6}{1-u} - \frac{3}{2-u}\,. \tag{5.74}$$

Indeed, by performing an inverse Borel transform, we can now directly read off the coefficients $\tilde{d}_h^{(1,0)[0]}$ for $h > 0$ already given in Eq. (5.66).

Note however that the prefactor in the first line of Eq. (5.73) itself has a pole at $u = 1$ – see also our discussion in Sec. 4.2.5. As a result, a constant term from the regular part between square brackets (indicated by the dots) also contributes to the singular terms in the last line. Therefore, the coefficient $\tilde{d}_0^{(1,0)[0]}$, which should correspond to a simple pole at $u = 1$ in the Borel plane, is not determined yet by studying the convolution integral. Furthermore, $\mathcal{B}[F](u)$ in Eq. (5.69) does not have singularities at negative integers, meaning that $\Delta_{-1}F = 0$. Therefore it does not seem possible to compute $\mathcal{B}[D_b^{(0,0)}](u)$ locally near $u = -1$, and thus we can also not extract $\tilde{d}_0^{(0,1)[0]}$ using the method of convolution. We come back to this point in the next subsection, where we will see that by including further non-perturbative sectors in the analysis, some of these undetermined coefficients can still be found.

Diagram (c)

In a similar manner, for diagram (c), a large order analysis of the perturbative coefficients yields $\beta_{1,0} = \beta_{0,1} = -1$ as well as the following non-zero expansion coefficients for the non-perturbative sectors:

$$\tilde{d}_0^{(1,0)[1]} = -\frac{3}{2} \tag{5.75}$$

$$\tilde{d}_h^{(1,0)[0]} = \begin{cases} -\frac{1}{2} - \frac{3}{2}\gamma_E - \frac{1}{6}\log(2) & h=0 \\ \Gamma(h)\Big(\left(3h+\frac{3}{2}\right) - (-1)^h\frac{1}{2} + \frac{1}{2^h}\frac{1}{2}\Big) & h>0 \end{cases} \tag{5.76}$$

$$\tilde{d}_0^{(0,1)[0]} = \frac{1}{6} + \frac{1}{2}\Big(\log(2) - \log(3)\Big), \tag{5.77}$$

which we have checked numerically up to at least 13 decimal places for the first 15 coefficients for $\tilde{d}_h^{(1,0)[0]}$. We observe a similar pattern as for diagram (*b*): a log-sector with a single coefficient $\tilde{d}_0^{(1,0)[1]}$, an asymptotic $(1,0)[0]$ sector, and a $(0,1)$ sector which contains only a single non-perturbative coefficient.

Once again, we can also determine these coefficients by studying the convolution integral more closely. Therefore, we write the convolution integral of diagram (*c*) as

$$\mathcal{B}[D_c^{(0,0)}](u) = \frac{-6\Gamma(u)}{(1-u)(2-u)\Gamma(3-u)}\mathcal{B}[\Phi^{(0)}](u)\,, \tag{5.78}$$

where we defined

$$\mathcal{B}[\Phi^{(0)}](u) = \int_0^u du_1\, \mathcal{B}[F](u_1)\mathcal{B}[G](u-u_1)\,, \qquad \mathcal{B}[G](u) = \frac{u\Gamma(1-u)}{\Gamma(2+u)}\,, \tag{5.79}$$

and with $\mathcal{B}[F]$ the same as in Eq. (5.69). Using that both $\Delta_1 F = \Delta_1 G = \frac{1}{2}(2\pi\mathrm{i})$ we obtain

$$S_1^{\Phi}\Phi^{(1)} = \Delta_1\Phi^{(0)} = F\Delta_1 G + G\Delta_1 F = \frac{1}{2}(2\pi\mathrm{i})(F(\alpha)+G(\alpha)). \tag{5.80}$$

A brief calculation now yields

$$\begin{aligned} \mathcal{B}[D_c^{(0,0)}](u)\Big|_{u=1} &= \frac{-6\Gamma(u)}{(1-u)(2-u)\Gamma(3-u)}\mathcal{B}[\Phi^{(0)}](u)\Big|_{u=1} + \dots \\ &= -\frac{\log(1-u)}{1-u}\,\frac{6-3u(4-u)}{u(2-u)^2(3-u)} + \dots \\ &\equiv -\tilde{d}_0^{(1,0)[1]}\frac{\log(1-u)}{1-u} - \mathcal{B}[\tilde{D}_c^{(1,0)[0]}](u-1)\log(1-u) + \dots\,, \end{aligned} \tag{5.81}$$

with $\tilde{d}_0^{(1,0)[1]} = -\frac{3}{2}$ as given above in Eq. (5.75), and where

$$\mathcal{B}[\tilde{D}_c^{(1,0)[0]}](u) = \frac{\frac{1}{2}}{1+u} + \frac{3}{(1-u)^2} + \frac{\frac{3}{2}}{1-u} + \frac{\frac{1}{2}}{2-u}\,. \tag{5.82}$$

It is straightforward to show that the inverse Borel transform of this indeed yields the coefficients $\tilde{d}_h^{(1,0)[0]}$ given in Eq. (5.76) for $h > 0$. In the next subsection we see how the convolution integral method also allows us to obtain information about the coefficients $\tilde{d}_0^{(1,0)[0]}$ and $\tilde{d}_0^{(0,1)[0]}$.

To summarize the results so far (see also Tab. 5.3): although the convolution integral for diagram (a) was the only one we could compute exactly, our resurgence large order analysis, together with the power of the convolution analysis, allowed us to make a transseries Ansatz and extract the whole first non-perturbative $(1,0)$ and $(0,1)$ sectors for the diagrams (a), (b) and (c). For all three diagrams, the leading order growth of the perturbative coefficients is governed by the non-perturbative coefficient $\tilde{d}_0^{(1,0)[1]}$. In particular, we found for diagram (c) that $\tilde{d}_0^{(1,0)[1]} = -\frac{3}{2}$, while for both diagrams (a) and (b) the growth is twice as strong, i.e. $\tilde{d}_0^{(1,0)[1]} = -3$. We already observed this qualitatively in Fig. 5.9, where we saw that the growth of perturbative coefficients for diagram (c) is indeed less than for the diagrams (a) and (b), which were more or less overlapping. However, at closer inspection, one sees that the points do not overlap exactly – an artifact of the subleading growth dictated by the coefficients $\tilde{d}_h^{(1,0)[0]}$ and $\tilde{d}_h^{(0,1)[0]}$ that we have now also computed. For all three diagrams, the $(1,0)$ sector is asymptotic while only for diagram (a) the $(0,1)$ sector is asymptotic.

Diagram (d)

Finally, we want to offer some observations on diagram (d). A numerical resurgence analysis on this diagram is challenging as we only have 18 coefficients, and we already observed that the even and odd coefficients behave differently. In Fig. 5.9, we see that the growth of the upper curve is much stronger than that of the other three diagrams (a), (b) and (c). Although it looks like the curve bends slightly, there are not enough coefficients to tell if this is the beginning of logarithmic growth. It might as well be the case that the large order growth of the coefficients is different. Furthermore, the coefficients that we displayed have opposite sign to the coefficients of the other diagrams, though the lower curve clearly bends downwards towards negative coefficients.

5.2.4. Resurgence analysis: non-perturbative sectors $(2,0)$ and $(0,2)$

In the previous subsection we determined the non-perturbative $(1,0)$ and $(0,1)$ sectors for diagrams (a)-(c), using both numerical results and the method of alien derivatives acting on the convolution integral. In order to probe the second non-perturbative sectors $(2,0)$ and $(0,2)$, we must subtract the first sectors from the large order expressions. This is not as straightforward as in the LO case (see Eq. (5.27)), since now the coefficients $\tilde{d}_k^{(1,0)[0]}$ and $\tilde{d}_k^{(0,1)[0]}$ grow factorially themselves, implying that we need to subtract an entire (divergent) asymptotic series. To make this possible, we have to apply Borel summation on the first non-perturbative sector before subtracting it, as was discussed in great length in chapter 3.

To prepare for this we rewrite Eq. (5.60) as

$$\begin{aligned}\delta_k^{(0)} &\sim \frac{\Gamma(k-\beta)}{A^{k-\beta}} \sum_{\ell=1}^{\infty} \frac{1}{\ell^{k-\beta}} \sum_{h=0}^{\infty} \frac{\Gamma(k-\beta-h)}{\Gamma(k-\beta)} (\ell A)^h \tilde{d}_h^{(\ell,0)[0]} + (0,\ell)\text{-sectors} \\ &= \frac{\Gamma(k-\beta)}{A^{k-\beta}} e^{\beta \log(\ell)} \sum_{\ell=1}^{\infty} e^{-k\log(\ell)} P^{(\ell,0)}\left(\frac{1}{k}\right) + (0,\ell)\text{-sectors} \qquad (5.83)\end{aligned}$$

where we defined

$$P^{(\ell,0)}(x) \equiv \sum_{h=0}^{\infty} p_h^{(1,0)} x^h \qquad \text{and} \qquad P^{(0,\ell)}(x) \equiv \sum_{h=0}^{\infty} p_h^{(0,\ell)} x^h\,. \qquad (5.84)$$

The coefficients $p_h^{(\ell,0)}$ and $p_h^{(0,\ell)}$ are the coefficients in the $1/k$ expansion of the first line of Eq. (5.83), obtained from expanding the ratio of gamma functions. Recalling Sec. 3.2.1, notice that the coefficients $P^{(\ell,0)}$ and $P^{(0,\ell)}$ are not exactly the rescaled Stirling transform of $\tilde{D}^{(\ell,0)}$ and $\tilde{D}^{(0,\ell)}$ respectively, as in Sec. 3.2.1 we worked with $\beta = 0$. The coefficients $p_h^{(\ell,0)}$ and $p_h^{(0,\ell)}$ are still easily obtained by doing an expansion in $1/(k-\beta)$ first – for which we can use the rescaled Stirling transform of Sec. 3.2.1 – after which one goes from the $1/(k-\beta)$ expansion to the final $1/k$ expansion. One can show that this last expansion, i.e. the case of non-zero $\beta \neq 0$, only has a minor effect and that the properties of the Stirling transform that were so powerfull in chapter 3 are still applicable to our situation.

Recalling the procedure outlined in chapter 3, in the large order expressions we replace these series with the Borel-summed version[8]

$$\mathcal{S}[P^{(1,0)}](x) = p_0^{(1,0)} + \int_0^{\infty} dt\, \mathcal{B}[P^{(1,0)}](t) e^{-t/x}\,, \qquad (5.85)$$

and similarly for $\mathcal{S}[P^{(0,1)}](x)$ with $x = 1/k$. Unfortunately, this expression cannot be taken at face value, as the asymptotic expansion of $P^{(0,1)}$ and $P^{(1,0)}$ is not Borel summable. More precisely, there are singularities on the integration contours, as we can see in Fig. 5.10, where we show the singularities of the Padé approximants of the

---

[8] Recall that the constant term is not included in our definition of $\mathcal{B}[p^{(1,0)}](t)$, which is why we have to add it separately.

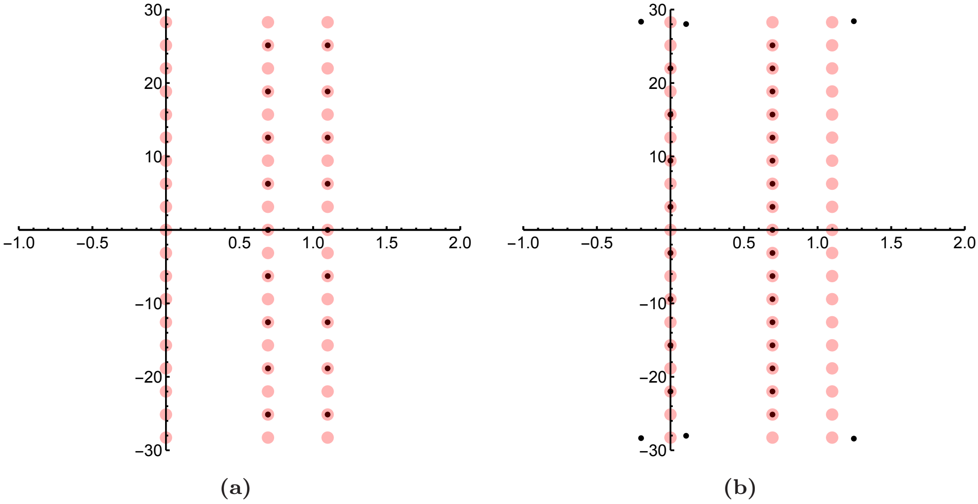

Figure 5.10.: For diagram (a), Figs. (a) and (b) show the Padé poles (small black dots) of the 75th diagonal Padé approximant of $\mathcal{B}[P^{(1,0)}]$ and $\mathcal{B}[P^{(0,1)}]$ respectively. The larger red transparant points are positioned at $\log(\ell)+\pi i m$, with $\ell = 1,2,3$ and $m \in \mathbb{Z}$. At large imaginary values, some 'spurious' poles appear due to numerical inaccuracies.

Borel transforms of Eq. (5.84) for diagram (a). These are the same figures as already shown in Fig. 3.1 and is historically the inspiration for [3], i.e. chapter 3.

From chapter 3, we recall that the singularities of $\mathcal{B}[P^{(1,0)}]$ and $\mathcal{B}[P^{(0,1)}]$ can be traced back to the singularities of $\mathcal{B}[D_a^{(0,0)}](u)$. To be precise, the expansion of $\mathcal{B}[D_a^{(0,0)}](u)$ around $u=1$ and $u=2$ read

$$\left(\frac{6}{(3-u)(2-u)^2u}-1\right)\cdot\frac{\log(1-u)}{(1-u)}\,, \qquad \text{and} \qquad \frac{2\log(1+u)}{(1-u)^2(2-u)u(2+u)}\,, \tag{5.86}$$

where in the first expression we subtracted the $\frac{\log(1-u)}{1-u}$ term from Eq. (5.49) as its contribution, i.e. the large order growth initiated by the coefficient $\tilde{d}_0^{(1,0)[1]}$, is already subtracted in Eq. (5.83). The expansions of (5.86) have singularities at $u=1,2,3$ and $u=-2,1,2$ respectively.[9] Because of the symmetries of the (rescaled) Stirling transform, the singularities of $\mathcal{B}[P^{(1,0)}]$ can be found at $\log(2)+2\pi i m$ and $\log(3)+2\pi i m$ and for $\mathcal{B}[P^{(0,1)}]$ we should observe singularities at $\log(1)+(2m+1)\pi\mathrm{i}$ and $\log(2)+\pi i m$. This is indeed the observed pattern in Fig. 5.10.

For both diagrams (b) and (c), we have simple $(0,1)$-sectors with only a single coefficient, so we do not need to perform a Borel-Padé summation on these sectors to

---

[9] The pole around $u=0$ cancels against the first term in the expansion of the logarithms.

be able to subtract them. For the $(1,0)$ sector, we obtain a similar plot as in Fig. 5.10a, where the positions of the singularities are traced back to locations of the poles in the expansions around $\log(1-u)$, given in Eqs. (5.73) and (5.81). To be precise, for both diagram (b) and (c), we observe singularities at $\log(2)+2\pi i m$ and $\log(3)+2\pi i m$.

Since the Borel transforms in particular have singularities on the real positive axis, we need to deal with the ambiguity of the Laplace contour. In order to do so, we performed a numerical integration under a small negative angle just above the real axis of Fig. 5.10b. See Sec. 2.7.2 for details about the numerical integration. This choice for the 'upper contour' implies that the Borel sums also get an imaginary part. However, as we will see in a moment, this imaginary part does not play a role in determining the perturbative coefficients through large order formulas, because of a similar and corresponding ambiguity in the choice of logarithm branch cuts in the Borel plane. The convention in the original publication [1] – and therefore also in this chapter – is opposite of the one in chosen in chapter 3 and [3]. Of course, we also could have chosen the 'lower contour' in this chapter; the imaginary contribution will then have opposite sign, but will still be 'canceled' leading to the same large order results.

Diagram (a)

With the Borel summed $(1,0)$ and $(0,1)$ sectors at our disposal, we can now turn our attention to the resurgence of the second non-perturbative $(2,0)$ and $(0,2)$ sectors. As in the previous subsection, we start with a discussion of diagram (a). We can now subtract the numerically performed integral from the perturbative coefficients. Recalling that $\beta=-1$ and $A_1=-A_2=1$, we obtain the new sequence

$$\begin{aligned}\delta_k^{(1)} = d_k^{(0,0)} - \tilde{d}_0^{(1,0)[1]}\frac{\Gamma(k-\beta)\psi(k-\beta)}{A_1^{k-\beta}}\\ -\frac{\Gamma(k-\beta)}{A_1^{k-\beta}}\mathcal{S}[P^{(1,0)}]\left(\frac{1}{k}\right) - \frac{\Gamma(k-\beta)}{A_2^{k-\beta}}\mathcal{S}[P^{(0,1)}]\left(\frac{1}{k}\right),\end{aligned} \tag{5.87}$$

which probes the contribution of the $(2,0)$ and $(0,2)$ sectors to the large order behaviour of the perturbative coefficients. In Fig. 5.11 we show $d_k^{(0,0)}$ together with $\delta_k^{(1)}$ for $20 \le k \le 100$ for diagram (a). We clearly observe that the (real) perturbative coefficients $d_k^{(0,0)}$ diverge faster than both $\mathrm{Re}[\delta_k^{(1)}]$ and $\mathrm{Im}[\delta_k^{(1)}]$. This is already a good sign that these coefficients probe the subleading non-perturbative $(2,0)$ and $(0,2)$ sectors.

Let us now discuss the fact that $\delta_k^{(1)}$ for diagram (a) appears to have an imaginary part. This may seem at odds with the fact that we are describing the large order

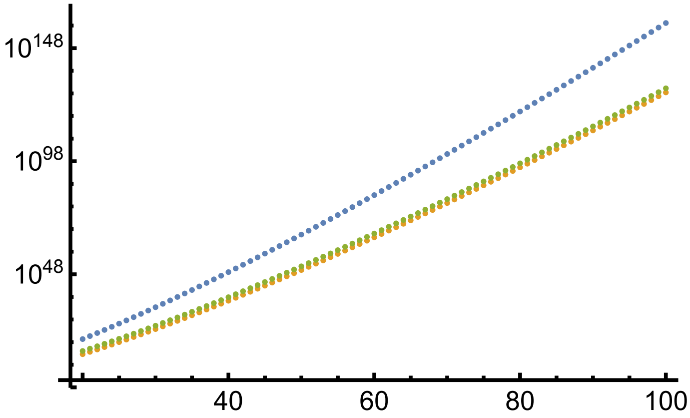

Figure 5.11.: Plot of the coefficients $d_k^{(0,0)}$ (top, blue) and $\mathrm{Re}[\delta_k^{(1)}]$ (bottom, orange), $\mathrm{Im}[\delta_k^{(1)}]$ (middle, green) for $20 \le k \le 100$ for diagram (a). We clearly observe that the coefficients $\delta_k^{(1)}$ are 'less asymptotic' compared to the perturbative coefficients $d_k^{(0,0)}$, a sign that this new sequence probes the subleading non-perturbative $(2,0)$ and $(0,2)$ sectors.

behaviour of a *real* expansion of the Adler function, but in fact it is not. Our numerical resurgence analysis yields

$$\mathrm{i}\,\mathrm{Im}\left[\delta_k^{(1)}\right] \sim \pm\pi\mathrm{i}\left[-\frac{\Gamma(k+2)}{2^{k+2}}\cdot 3-\frac{\Gamma(k+1)}{2^{k+1}}\cdot\frac{3}{2}+\frac{\Gamma(k+1)}{(-2)^{k+1}}\cdot\frac{1}{36}-\frac{\Gamma(k+1)}{3^{k+1}}\right], \tag{5.88}$$

where the overall sign ambiguity comes from a choice of contour in the Borel-Padé evaluation of Eq. (5.87), either above or below the singularities on the positive real axis in the Borel plane. Note that this imaginary contribution can itself be Borel transformed into

$$\pm\mathrm{i}\pi\left[-3\frac{1}{(2-u)^2}-\frac{3}{2}\frac{1}{2-u}-\frac{1}{36}\frac{1}{2+u}-\frac{1}{3-u}\right]. \tag{5.89}$$

Now, these same imaginary and ambiguous contributions will also appear in the Borel transform of diagram (a) itself, Eq. (5.49). For example, an ambiguity is present in the expansion of the logarithm $\log(1-u)$ in that expression around $u=2$. This expansion takes the form

$$\left.\frac{6\log(1-u)}{(3-u)(2-u)^2(1-u)u}\right|_{u=2} = -\frac{\pm 3\pi\mathrm{i}}{(2-u)^2}-\frac{\pm\frac{3}{2}\pi\mathrm{i}+3}{2-u}+\ldots \tag{5.90}$$

where we see the exact same imaginary ambiguity as in the first and second term of Eq. (5.89). As a result, the coefficients of the (2, 0) sector that can be read off from either Eq. (5.88) or Eq. (5.89) will *not* be ambiguous and moreover will be purely real.

A similar reasoning can be applied to the third ambiguous term in Eq. (5.89) which will reappear in the expansion around log(1 + u) of Eq. (5.49):

$$\left.\frac{2\log(1+u)}{(1-u)^2(2-u)u(2+u)}\right|_{u=-2} = -\frac{1}{36}\cdot\frac{\pm\pi\mathrm{i}}{2+u} + \ldots\,. \tag{5.91}$$

For the fourth ambiguous term in Eq. (5.89), which will determine a (3, 0) sector coefficient, we expand around $u = 3$:

$$\left.\frac{6\log(1-u)}{(3-u)(2-u)^2(1-u)u}\right|_{u=3} = -\frac{\pm\pi\mathrm{i}-\log(2)}{3-u} + \ldots\,. \tag{5.92}$$

Taking the same steps as we did for the (1, 0) and (0, 1) sectors, we can now determine the coefficients in the (2, 0) and (0, 2) sectors by doing a large order analysis on the $\delta_k^{(1)}$. Above, we have already analysed the imaginary part of $\delta_k^{(1)}$. The real part does not have a contribution to the (0, 2) sector, but is does affect the (2, 0) sector. From it, we extract $\beta_{2,0} = -1$ and the (2, 0) coefficients

$$\tilde{d}_0^{(2,0)[1]} = -2 \tag{5.93}$$

$$\tilde{d}_h^{(2,0)[0]} = \begin{cases} 3 - 2\gamma_E + \frac{1}{4}\log(3) & h = 0 \\ \Gamma(h)\Big(\left(\frac{2}{3}h + \frac{11}{9}\right)(-1)^h + 1 - \frac{2}{9}\frac{1}{2^h}\Big) & h > 0\,. \end{cases} \tag{5.94}$$

As we see, the (2, 0) sector contains again a log(α) contribution in the transseries, given by the coefficient $\tilde{d}_0^{(2,0)[1]}$. We were able to extract the first 15 coefficients in Eq. (5.94) (as well as those of the simpler imaginary part, Eq. (5.88)) numerically from Eq. (5.87) up to 9 decimal places, after which we inferred the exact expressions. Once again – recall how we did this for the (1, 0) and (0, 1) sectors in Eqs. (5.63) and (5.64) – we know that this is exact to all orders, because we can compare with the exact Borel transform.

Diagram (b)

Similar to diagram (a), before we can probe the second non-perturbative (2, 0) and (0, 2) sectors of diagram (b), we want to subtract the (1, 0) and (0, 1) sectors. As both the (0, 1) sector and the log part of the (1, 0) sector (i.e. the (1, 0)[1] sector) contain just one coefficient, we can directly subtract these parts. The (1, 0)[0] coefficients however grow asymptotically, and therefore we have to perform a Borel-Padé summation on this part. This leads to the new sequence

$$\delta_k^{(1)} = d_k^{(0,0)} - \frac{\Gamma(k-\beta)}{A_2^{k-\beta}} \tilde{d}_0^{(0,1)[1]} - \frac{\Gamma(k-\beta)}{A_1^{k-\beta}} \left[\tilde{d}_0^{(1,0)[1]} \psi(k-\beta) + \mathcal{S}[P^{(1,0)}] \left(\frac{1}{k} \right) \right], \quad (5.95)$$

with $\beta = -1$ and $A_1 = -A_2 = 1$ and the coefficients $\tilde{d}_0^{(1,0)[1]}$ and $\tilde{d}_0^{(1,0)[0]}$ given in Eqs. (5.65) and (5.67) respectively. A numerical analysis on the imaginary part of $\delta_k^{(1)}$ yields a contribution to the $(2,0)$ sector:

$$\mathrm{i}\,\mathrm{Im}\left[\delta_k^{(1)}\right] \sim \pm 6\pi\mathrm{i} \frac{\Gamma(k+1)}{2^{k+1}} + \mathcal{O}(3^{-k}) \,. \quad (5.96)$$

From the real part of $\delta_k^{(1)}$ we extract for both sectors $\beta_{2,0} = \beta_{0,2} = -1$. Furthermore, we extract a single non-perturbative coefficient for the $(0,2)$ sector,

$$\tilde{d}_0^{(0,2)[0]} = -\frac{1}{6} + \frac{2}{9} \log(2) \,, \quad (5.97)$$

and the first few coefficients of the $(2,0)$ sectors. We list the first four:

$$\tilde{d}_0^{(2,0)[0]} = -2 \,, \quad \tilde{d}_1^{(2,0)[0]} = -\frac{14}{3} \,, \quad \tilde{d}_2^{(2,0)[0]} = -\frac{5}{2} \,, \quad \tilde{d}_3^{(2,0)[0]} = -\frac{7}{6} - 8\zeta_3 \,. \quad (5.98)$$

We have obtained these coefficients numerically up to at least 9 decimal places, as well as seven further ones not displayed here, after which we inferred the analytic expression. Furthermore, notice that the $(2,0)$ sector of this diagram does not have a log sector, i.e. all the coefficients $\tilde{d}_h^{(2,0)[1]}$ vanish.

We can improve on these results using again the method of alien derivatives acting on the convolution integral to find all $\tilde{d}_h^{(2,0)[0]}$ exactly. We repeat Eqs. (5.68) and (5.69), for this diagram:

$$\mathcal{B}[D_b^{(0,0)}](u) = \frac{-6\Gamma(1+u)}{(1-u)\Gamma(3-u)} \mathcal{B}[\Psi^{(0)}](u), \quad (5.99)$$

with the convolution integral

$$\mathcal{B}[\Psi^{(0)}](u) = \int_0^u du_1\, \mathcal{B}[F](u_1)\mathcal{B}[F](u-u_1), \quad \mathcal{B}[F](u) = \frac{\Gamma(1-u)}{(2-u)\Gamma(2+u)} \,. \quad (5.100)$$

In order to extract the $(2,0)$ sector, we need the expansion of $\mathcal{B}[\Psi^{(0)}]$ around $u = 2$, i.e. we need the second non-perturbative sector $\Psi^{(2)}$. As discussed in Sec. 4.2, this implies we need

$$\Delta_1 F = \frac{1}{2}(2\pi\mathrm{i}), \qquad \text{and} \qquad \Delta_2 F = -\frac{1}{6}(2\pi\mathrm{i})\left(\frac{1}{\alpha} + \frac{17-12\gamma_E}{6}\right), \tag{5.101}$$

which are read off from the expansions around the poles of $\mathcal{B}[F]$ positioned at $u = 1$ and $u = 2$. We notice that, similar to the LO Adler function, $\Delta_1^2 F = 0$. However, $\Delta_2 F$ is now non-vanishing. This yields

$$\begin{aligned}
\left(S_1^\Psi\right)^2 \Psi^{(2)} &= 2 \cdot \frac{1}{2}(\Delta_1 F)^2 + 2 \cdot F \Delta_2 F \qquad\qquad (5.102)\\
&= \frac{1}{4}(2\pi\mathrm{i})^2 - \frac{1}{3}(2\pi\mathrm{i})\left(\frac{1}{\alpha} + \frac{17-12\gamma_E}{6}\right)\sum_{n=0}^{\infty} F_n \alpha^{n+1}\\
&= 2\pi\mathrm{i}\left(\frac{1}{2}\pi\mathrm{i} - \frac{1}{3}F_0\right) - \frac{1}{3}(2\pi\mathrm{i})\sum_{n=0}^{\infty}\left(F_{n+1} + \frac{17-12\gamma_E}{6}\sum_{n=0}^{\infty} F_n\right)\alpha^{n+1}.
\end{aligned}$$

Recalling the discussion at the end of Sec. 4.2.3, in particular Eqs. (4.47) and (4.50), we can write the Borel transform of $\Psi^{(2)}$ in terms of $\mathcal{B}[F](u)$ and its derivative $\mathcal{B}[F]'(u)$ w.r.t. u. Therefore, the Borel transform $\mathcal{B}[\Psi^{(0)}]$ around $u = 2$ reads

$$\begin{aligned}
\mathcal{B}[\Psi^{(0)}](u)\Big|_{u=2} &= \frac{\frac{1}{2}\pi\mathrm{i} - \frac{1}{3}F_0}{u-2} - \left(S_1^\Psi\right)^2 \mathcal{B}[\Psi^{(2)}](u-2)\frac{\log(1-\frac{u}{2})}{2\pi\mathrm{i}} + \ldots \qquad (5.103)\\
&= \frac{\frac{1}{2}\pi\mathrm{i} - \frac{1}{3}F_0}{u-2} + \frac{1}{3}\left(\mathcal{B}[F]'(u-2) + \frac{17-12\gamma_E}{6}\mathcal{B}[F](u-2)\right)\log\left(1-\frac{u}{2}\right) + \ldots
\end{aligned}$$

Adding back in the prefactor to get $\mathcal{B}[D_b](u)$ and $F_0 = \frac{1}{2}$ yields, after a brief calculation[10],

$$\begin{aligned}
\mathcal{B}[D_b^{(0,0)}](u)\Big|_{u=2} &= \frac{-6\Gamma(1+u)}{(1-u)\Gamma(3-u)}\mathcal{B}[\Psi^{(0)}](u)\Big|_{u=2} + \ldots\\
&= \frac{6\pi\mathrm{i} - 2}{2-u} - \mathcal{B}[\tilde{D}_b^{(2,0)}](u-2)\log(1-\frac{u}{2}) + \ldots, \qquad (5.104)
\end{aligned}$$

with

$$\mathcal{B}[\tilde{D}_b^{(2,0)}](u-2) = \frac{2u}{(1-u)(4-u)}\left(\frac{1}{4-u} + \frac{17-12\gamma_E}{6} - \psi(3-u) - \psi(u)\right). \tag{5.105}$$

---

[10] Note that in Eq. (5.96) the factor $6\pi\mathrm{i}$ appears with an ambiguous sign. As usual, in large order formulas this imaginary ambiguity should not contribute to the perturbative coefficients; it will be 'canceled' by the $6\pi i$ terms in the present equation. One may be worried that here, no ambiguous sign appears in front of the $6\pi\mathrm{i}$, but this is a result of the fact that we have implicitly chosen the 'lower contour' by applying a particular form of the Stokes automorphism and the resulting alien derivatives.

The exact coefficients $\tilde{d}_h^{(2,0)[0]}$ are obtained from the residue of the simple pole around $u = 2$ in Eq. (5.104), and after applying an inverse Borel transform on Eq. (5.105).

At this point, we want to come back to a left over point of the previous subsection: the resurgence of the $\tilde{d}_0^{(1,0)[0]}$ and $\tilde{d}_0^{(0,1)[0]}$ coefficients – which we were not yet able to determine there – from the convolution integral. (We shall see momentarily how the same reasoning also leads to the resurgence of the $\tilde{d}_0^{(0,2)[0]}$ coefficient.) In principle, as $\mathcal{B}[F](u)$ only has singularities at positive integers of u, also its convolution integral $\mathcal{B}[\Psi^{(0)}](u)$ only has possible singularities at positive integers of u. Therefore, with the techniques of studying the convolution integral with alien derivatives, it seems we can only make statements about the local expansions of $\mathcal{B}[\Psi^{(0)}](u)$ around these values. However, the prefactor

$$\frac{-6\Gamma(1+u)}{(1-u)\Gamma(3-u)} \tag{5.106}$$

in front of this convolution integral has singularities at $u = 1$ and the negative integers of u. Therefore, these singularities pick up regular terms of $\mathcal{B}[\Psi^{(0)}](u)$ at these points. In particular, the prefactor also leads to the pattern of singularities at negative integers in u of $\mathcal{B}[D_b^{(2,0)}](u-2)$. Furthermore, there is also a singularity at $u = 1$ and therefore we notice that this sector contributes to the coefficients $\tilde{d}_0^{(1,0)[0]}$, $\tilde{d}_0^{(0,1)[0]}$ and $\tilde{d}_0^{(0,2)[0]}$. For example, expanding the Borel transform of the $(0, 2)$ sector around $u = 1$ yields

$$\mathcal{B}[\tilde{D}_b^{(2,0)}](u-2)\log(1-\frac{u}{2})\Big|_{u=1} = \frac{13\log(2)}{9(u-1)} + ... \tag{5.107}$$

with the ellipsis denoting regular terms around $u = 1$. We notice that this indeed corresponds with part of the coefficient $\tilde{d}_0^{(1,0)[0]}$ already obtained numerically in Eq. (5.66). The remaining part of this coefficient follows from the fact that we multiplied a pole at $u = 1$ of the prefactor with the expansion of $\mathcal{B}[\Psi^{(0)}[u]$ around $u = 1$. Similarly, we can expand the same expression around $u = -1$ and $u = -2$ to find (parts of) the coefficients $\tilde{d}_0^{(0,1)[0]}$ and $\tilde{d}_0^{(0,2)[0]}$ as given above. In conclusion, we see in particular that knowing the subleading $(2, 0)$ and $(0, 2)$ sectors actually teaches us a bit more about the leading $(1, 0)$ and $(0, 1)$ sectors that we were not able to deduce from the perturbative $(0, 0)$ sector alone.

Diagram (c)

Finally, we discuss the resurgence of the $(2, 0)$ and $(0, 2)$ sectors of diagram (c). For this, we can use the same sequence as in Eq. (5.95), but now using the coefficients of the $(1, 0)$ and $(0, 1)$ sectors of diagram (c) given in Eqs. (5.75)-(5.77). A numerical analysis yields

$$\mathrm{i}\,\mathrm{Im}\left[\delta_k^{(1)}\right] \sim \pm 3\pi\mathrm{i}\frac{\Gamma(k+2)}{2^{k+2}}\left(1-\frac{1}{k+1}\right) + \mathcal{O}(3^{-k}) \tag{5.108}$$

for the imaginary part. Similar to diagram (b), there is only a single non-vanishing non-perturbative coefficient in the $(0,2)$ sector:

$$\tilde{d}_0^{(0,2)[0]} = -\frac{17}{72} + \frac{1}{3}\log(2)\,. \tag{5.109}$$

However, the $(2,0)$ sector of diagram (c) has a log contributing in the transseries, given by the non-perturbative coefficient

$$\tilde{d}_0^{(1,0)[1]} = -2\,. \tag{5.110}$$

Again we list the first four coefficients of the $(2,0)[0]$ sector and we show in a moment how higher coefficients are obtained using the convolution method:

$$\begin{aligned} \tilde{d}_0^{(2,0)[0]} &= 4 - 2\gamma_E + \frac{\log(3)}{4}\,, & \tilde{d}_1^{(2,0)[0]} &= \frac{1}{3}\,, \\ \tilde{d}_2^{(2,0)[0]} &= \frac{11}{12}\,, & \tilde{d}_3^{(2,0)[0]} &= -\frac{43}{12} + 4\zeta_3\,. \end{aligned} \tag{5.111}$$

The numerical analysis on $\delta_k^{(1)}$ agrees with Eqs. (5.108)-(5.111) up to at least 11 decimal places.

These same results are obtained using the convolution integral method. We repeat Eqs. (5.78) and (5.79),

$$\mathcal{B}[D_c^{(0,0)}](u) = \frac{-6\Gamma(u)}{(1-u)(2-u)\Gamma(3-u)}\mathcal{B}[\Phi^{(0)}](u), \tag{5.112}$$

with

$$\mathcal{B}[\Phi^{(0)}](u) = \int_0^u du_1\,\mathcal{B}[F](u_1)\mathcal{B}[G](u-u_1)\,, \qquad \mathcal{B}[G](u) = \frac{u\Gamma(1-u)}{\Gamma(2+u)}\,, \tag{5.113}$$

and $\mathcal{B}[F]$ the same as for diagram (b) given in Eq. (5.69). Again, for the resurgence of the $(2,0)$ and $(0,2)$ sectors of diagram (c), we need access the second non-perturbative sector of Φ. To compute this this, we use $\Delta_1 F$ and $\Delta_2 F$ already given in Eq. (5.101), and also

$$\Delta_1 G = \frac{1}{2}(2\pi\mathrm{i}), \qquad \text{and} \qquad \Delta_2 G = -\frac{1}{3}(2\pi\mathrm{i})\,. \tag{5.114}$$

As $\Delta_1^2 F = \Delta_1^2 G = 0$, we get

$$\begin{aligned}\left(S_1^\Phi\right)^2\Phi^{(2)} &= 2\cdot\frac{1}{2}\Delta_1 F\Delta_1 G + F\Delta_2 G + G\Delta_2 F \\ &= \frac{1}{4}(2\pi\mathrm{i})^2 - \frac{1}{3}(2\pi\mathrm{i})\sum_{n=0}^{\infty}F_n\alpha^{n+1} - \frac{1}{6}(2\pi\mathrm{i})\left(\frac{1}{\alpha}+\frac{17-12\gamma_E}{6}\right)\sum_{n=0}^{\infty}G_n\alpha^{n+1} \\ &= (2\pi\mathrm{i})\left(\frac{1}{2}\pi\mathrm{i}-\frac{1}{6}G_0\right) - \frac{1}{6}(2\pi\mathrm{i})\sum_{n=0}^{\infty}\left(2F_n + G_{n+1} + \frac{17-12\gamma_E}{6}G_n\right)\alpha^{n+1}.\end{aligned}\tag{5.115}$$

We can write the Borel transform $\mathcal{B}[\Phi^{(2)}](u)$ in terms of $\mathcal{B}[F](u)$, $\mathcal{B}[G](u)$, and $\mathcal{B}[G]'(u)$. This yields

$$\begin{aligned}\mathcal{B}[\Phi^{(0)}](u)\Big|_{u=2} &= \frac{\frac{1}{2}\pi\mathrm{i}-\frac{1}{6}G_0}{u-2} - \left(S_1^\Phi\right)^2\mathcal{B}[\Phi^{(2)}](u-2)\frac{\log(1-\frac{u}{2})}{2\pi\mathrm{i}} + \ldots \\ &= \frac{\frac{1}{2}\pi\mathrm{i}-\frac{1}{6}G_0}{u-2} + \frac{1}{6}\Bigg(2\mathcal{B}[F](u-2) + \mathcal{B}[G]'(u-2) \\ &\qquad + \frac{17-12\gamma_E}{6}\mathcal{B}[G](u-2)\Bigg)\log\left(1-\frac{u}{2}\right) + \ldots .\end{aligned}\tag{5.116}$$

Adding back in the prefactor to get $\mathcal{B}[D_c](u)$ and $G_0 = 0$ yields

$$\begin{aligned}\mathcal{B}[D_c^{(0,0)}](u)\Big|_{u=2} &= \frac{-6\Gamma(u)}{(1-u)(2-u)\Gamma(3-u)}\left[\mathcal{B}[\Phi^{(0)}](u)\Big|_{u=2} + \ldots\right] \\ &= -\frac{3\pi\mathrm{i}}{(2-u)^2} - \frac{3\pi\mathrm{i}}{2-u} - \mathcal{B}[\tilde{D}_c^{(2,0)}](u-2)\log(1-\frac{u}{2}) + \ldots ,\end{aligned}\tag{5.117}$$

with

$$\mathcal{B}[\tilde{D}_c^{(2,0)}](u-2) = -\frac{1}{1-u}\left(\frac{1}{4-u} - \frac{2}{2-u} + \frac{17-12\gamma_E}{6} - \psi(3-u) - \psi(u)\right).\tag{5.118}$$

An inverse Borel transform indeed yields the coefficients $\tilde{d}_h^{(2,0)[0]}$ given above. Note that the prefactor in the first line of Eq. (5.117) has a pole at $u = 2$, and therefore a constant term from the regular part between square brackets also contributes to the singular terms in the last line. This corresponds to the coefficient $\tilde{d}_0^{(2,0)[0]}$. With the same reasoning as for diagram (b), we can get parts of the coefficients of $\tilde{d}_0^{(1,0)[0]}$, $\tilde{d}_0^{(0,1)[0]}$ and $\tilde{d}_0^{(0,2)[0]}$ by expanding the sector $\mathcal{B}[D_c^{(2,0)}]$ around the singular points $u = 1$, $u = -1$ and $u = -2$ respectively.

This finishes the analysis and discussion of the resurgence of the $(2,0)$ and $(0,2)$ sectors. In our analysis, we saw that for diagram (b) and (c) the $(2,0)$ sector was more interesting from a resurgence point of view, with resurgence relations that involve multiple non-perturbative sectors. In the next two subsections, we study some further non-perturbative sectors and draw the alien lattices for these diagrams.

5.2.5. Further non-perturbative sectors and alien derivative structure

In the previous two subsections, we have focused on the resurgence of the $(1,0)$, $(0,1)$, $(2,0)$ and $(0,2)$ sectors from the perturbative $(0,0)$ sector. As already observed in these sections, the coefficients of (some of) these non-perturbative sectors show asymptotic growth, so these sectors themselves have resurgence relations to other non-perturbative sectors. We will see momentarily that non-perturbative sectors like (n,m) with $n \neq 0$ and $m \neq 0$ will appear, something we have not observed before.

Diagram (a)

Let us once again start our discussion with diagram (a). In Eqs. (5.63) and (5.64), we saw how in the Borel plane of $\mathcal{B}[D_a^{(0,0)}](u)$, the $(1,0)$ sector resurges in the form

$$\mathcal{B}[\tilde{D}^{(1,0)[0]}](u-1) = \frac{3}{(2-u)^2} + \frac{3}{2(2-u)} - \frac{1}{2u} + \frac{1}{3-u}\,. \tag{5.119}$$

Likewise, one finds the Borel transform of the $(0,1)$ sector:

$$\mathcal{B}[\tilde{D}^{(0,1)[0]}](u+1) = -\frac{1}{4(2-u)} - \frac{2}{3(1-u)^2} + \frac{2}{9(1-u)} - \frac{1}{2u} + \frac{1}{36(2+u)}\,. \tag{5.120}$$

In particular, we notice that these expressions have a singularity at $u=0$. One can wonder why the perturbative $(0,0)$ sector does not contain this singularity in its own Borel transform. The reason is that, to get the $(0,0)$ sector, one has to include the logarithms:

$$\mathcal{B}[\tilde{D}^{(1,0)[0]}](u-1)\log(1-u)\Big|_{u=0} = \frac{1}{2} + \mathcal{O}(u) \tag{5.121}$$

and

$$\mathcal{B}[\tilde{D}^{(0,1)[0]}](u+1)\log(1+u)\Big|_{u=0} = -\frac{1}{2} + \mathcal{O}(u)\,. \tag{5.122}$$

That is, as seen from the point of view of the $(0,0)$ sector, the two constant terms that would contribute to a singularity at $u=0$ cancel. However, from the perspective of the $(1,0)$ and $(0,1)$ sectors, the individual singularities contribute to the large order growth of these sectors. Note that what these sectors see is *not* the $(0,0)$ sector again, as that sector has a vanishing constant term (see Eq. (5.50)) and moreover, as in examples with bridge equations, one would not expect a sector like $(1,0)$ to be able to detect the $(0,0)$ sector. Thus, we conclude that what we find here is the contribution of a $(1,1)$ sector, i.e. we get

$$D^{(1,1)[0]} = \frac{1}{2}\,, \tag{5.123}$$

which is a sector containing only a single non-perturbative coefficient. This relation is best viewed in the alien lattice, for which we now learn that it must contain the following arrows:

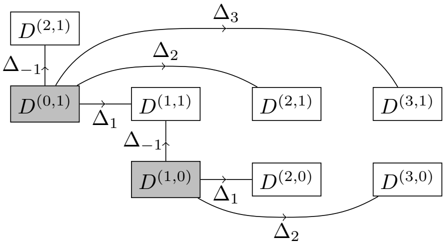

Here we also included the motions towards other non-perturbative sectors. Let us make two more remarks about this diagram.

First of all, observe that from the $(0,1)$ sector we have also drawn alien derivative arrows towards a $(2,1)$ and a $(3,1)$ sector. The existence of a $(2,1)$ sector can be argued in a similar way as above and we will show this explicitly in a moment, by looking at the singularities in the relevant Borel transforms and observing that these do not correspond to sectors that are already known. The same argument for a $(3,1)$ sector is on less solid ground, as the coefficient we find for that sector is also contained in the relevant perturbative coefficient in the $(2,0)$ sector, and so we cannot be certain that it is indeed the former sector that the $(1,0)$ sector detects. Thus, for now the existence of a $(3,1)$ sector is a conjecture, which we hope to come back to in future work.

Secondly, notice the alien derivative Δ_1 pointing from the $(1,0)$ sector to the $(2,0)$ sector; this alien derivative was discussed and explained around Eq. (5.89). In this diagram, we drew the $(2,0)$ sector with a white, solid box, which would imply that it is not an asymptotic series, contrary to the fact that we already know from the previous subsection that this *is* an asymptotic sector. The reason for this representation here is that the $(1,0)$ sector only sees a small, non-asymptotic part of the $(2,0)$ sector.

Similarly, we observe that the Borel transform of the $(0,1)$ sector has a double pole at $u = 1$, whereas this does not resurge from the $(0,0)$ sector directly, i.e. in our analysis we only found a single pole given by the coefficient $\tilde{d}_0^{(1,0)[0]} = \frac{1}{3} - 3\gamma_E + \frac{13}{9}\log(2)$. A closer inspection of the $(2,0)$ sector reveals the same double pole at $u=1$, i.e. we have

$$\mathcal{B}[\tilde{D}^{(2,0)[0]}](u-1) = -\frac{2}{3(1-u)^2} + \frac{11}{9(1-u)} + \frac{1}{3-u} - \frac{2}{9(4-u)}\,, \tag{5.124}$$

with the same coefficient $\frac{2}{3}$ as in Eq. (5.120). Again, from the point of view of the $(0,0)$ sector, one has to include the logarithms:

$$\mathcal{B}[\tilde{D}^{(2,0)[0]}](u-1)\log\left(1-\frac{u}{2}\right)\Big|_{u=1} = \frac{2\log(2)}{3(1-u)^2} + \frac{\frac{2}{3}+\frac{11}{9}\log(2)}{1-u} + \ldots \tag{5.125}$$

and

$$\mathcal{B}[\tilde{D}^{(0,1)[0]}](u+1)\log(1+u)\Big|_{u=1} = -\frac{2\log(2)}{3(1-u)^2} + \frac{-\frac{1}{3}+\frac{2}{9}\log(2)}{1-u} + \ldots\,. \tag{5.126}$$

This means that the $(0,0)$ sector does not see the double pole, but the $(2,0)$ and $(0,1)$ sectors independently do. Furthermore, we observe that the $(2,0)$ and the $(0,1)$ sectors see the same double pole, and we thus conclude that this is part of the $(2,1)$ sector.

We notice however that the single pole, as seen from the point of view of the $(2,0)$ and $(0,1)$ sectors has a different residue in the two cases, i.e. 11/9 and 2/9 respectively. This is a result of the fact that both sectors have resurgence relations towards both the $(1,0)$ sector and the $(2,1)$ sector. As the $(2,0)$ sector sees the $(2,1)$ and $(1,0)$ sectors with different weights compared to the $(0,1)$ sector (which depend on different Stokes constants), we conclude that it is hard to distinguish which part of the single pole at $u=1$ is part of the $(2,1)$ sector and which part corresponds to the $(1,0)$ sector. Being able to distinguish between the two would allow one to extract an interesting relation between the Stokes constants of the Adler function. This is another point that we hope to come back to in future work.

Again, these relations are best viewed in terms of the alien lattice, which as we now have learned also contains the following ingredients:

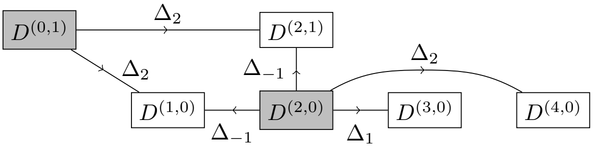

The full alien lattice for diagram (a) can now be obtained by combining the previous two diagrams with the similar diagram for the $(0,0)$ sector:

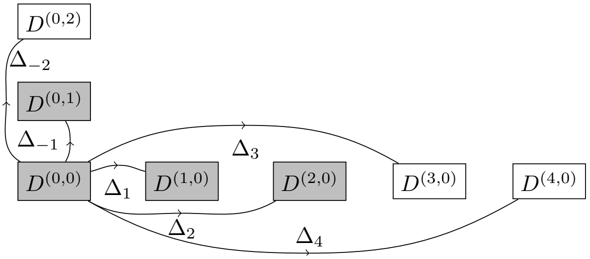

where we also inlcuded motions from the perturbative $(0,0)$ sector towards a $(3,0)$ and $(4,0)$ sector (see also the discussion in the next subsection).

Diagrams (b) and (c)

For diagrams (b) and (c), we have seen that only the $(1,0)$ and $(2,0)$ sectors are asymptotic. To be precise, we derived for diagram (b) the following Borel transform of the $(1,0)$ sector:

$$\mathcal{B}[\tilde{D}_b^{(1,0)[0]}](u-1) = \frac{6}{2-u} - \frac{3}{3-u}\,. \tag{5.127}$$

The singularities at $u=2$ and $u=3$ can be seen as part of the $(2,0)$ and $(3,0)$ sectors, i.e. in terms of alien lattices:

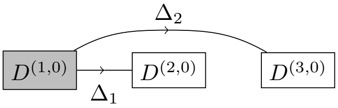

(5.128)

Diagram (c) on the other hand is slightly different. The Borel transform of its $(1,0)$ sector reads

$$\mathcal{B}[\tilde{D}_c^{(1,0)[0]}](u-1) = \frac{1}{2u} + \frac{3}{(2-u)^2} + \frac{3}{2(2-u)} + \frac{1}{2(3-u)}\,. \tag{5.129}$$

Again we notice a singularity at $u=0$ which is not seen by the perturbative $(0,0)$ sector. We therefore conclude that this is the effect of a non-zero $(1,1)$ sector. As before, this new sector is not an asymptotic sector, but it only contains one non-perturbative coefficient. This yields the following part of the alien lattice:

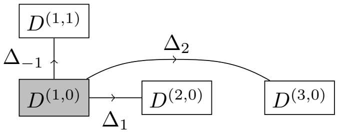

We already observed earlier that the $(2,0)$ sector of both diagram (b) and (c) has an infinite number of singularities in u at both positive and negative integers. Coming back to our discussion in Sec. 4.2.5, we want to mention here that from the convolution integral alone, Eq. (5.79), we would not have expected singularities at $u = 0$ or negative values of u. However the prefactor in front of the convolution integral, Eq. (5.79) adds singularities at non-positive u. It is therefore hard to distinguish which part of the pole at $u = 1$ for diagram (c) is related to the $(0,1)$ sector or the $(1,2)$ sector. First of all, the singularities at positive integers of u follow mainly from the convolution integral, but they also arise from the prefactors in front of the convolution integral since these add a pole at $u = 1$ for diagram (b) and a pole at $u = 1, 2$ for diagram (c). We therefore expect that this contributes to both a $(1,0)$ and a $(2,1)$ sector as seen from the $(2,0)$ sector. Likewise, the prefactor adds an infinite number of singularities at negative u, leading to both $(0,n)$ as well as $(2,2+n)$ sectors, for $n \geq 1$, or in terms of motions on the alien lattice:

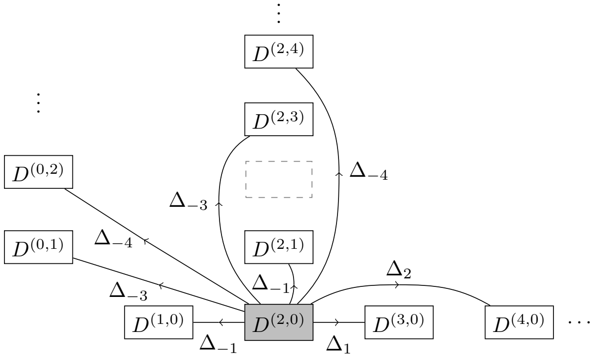

All in all, we see that at order $1/N_f^2$ in the number of flavours, the Adler function displays many more interesting resurgence features than were present at order $1/N_f$.

5.2.6. Overview: transseries sectors and relations

We have discussed the resurgence of the first non-perturbative sectors ($(1,0)$ and $(0,1)$) as well as the second non-perturbative sectors ($(2,0)$ and $(0,2)$) of diagrams

(a)-(c), plus how further sectors resurge from these sectors. We now briefly sketch the resurgence structure of higher sectors for these diagrams.

Looking at the closed form expression for diagram (a) in Eq. (5.49), we notice from the singularity structure that the only remaining non-vanishing sectors are the $(3,0)$ and $(4,0)$ sectors. Furthermore, as these singularities are not branch cuts but just simple poles, we conclude that they describe non-asymptotic sectors containing just a single non-vanishing non-perturbative coefficient.

From our discussion in Sec. 4.2.4, it might seem that we need to act with many alien derivatives to get access to the higher sectors of diagrams (b) and (c). However, the constituents F and G of the convolution integral of diagram (b) and (c) (recall Eqs. (5.68) and (5.78) respectively), have $\Delta_\omega^n F = \Delta_\omega^n G = 0$ for $n > 1$. This implies that we only get non-vanishing contributions by acting with at most two alien derivatives – one for each factor in the convolution product. Still, that leaves us with quite a few options to consider, but as we see momentarily, we can categorise all remaining options into a few classes. We discuss each of these classes case by case.

Let us first discuss the higher non-perturbative asymptotic sectors of diagram (b). The non-vanishing alien derivatives acting on F of that diagram are given by

$$\Delta_1 F = \frac{1}{2}(2\pi \mathrm{i})\,, \qquad \Delta_2 F = -\frac{1}{6}(2\pi \mathrm{i})\left(\frac{1}{\alpha} + \frac{17-12\gamma_E}{6}\right)\,, \tag{5.130}$$

and

$$\Delta_n F = \frac{(-1)^n}{(2-n)(n+1)!(n-1)!}(2\pi \mathrm{i})\,, \qquad n \geq 3\,. \tag{5.131}$$

First of all, using the convolution method we get an asymptotic contribution to the $(n,0)$, $n \geq 3$, sector via:

$$F\Delta_n F\,. \tag{5.132}$$

One can show that this gives a contribution to $\mathcal{B}[D_b^{(0,0)}](u)$ around $u = n$ proportional to

$$\begin{aligned}\frac{-6\Gamma(1+u)}{(1-u)\Gamma(3-u)}&\mathcal{B}[F](u-n)\log\left(1-\frac{u}{n}\right)\\ &= \frac{-6\Gamma(1+u)}{(1-u)\Gamma(3-u)}\,\frac{\Gamma(n+1-u)}{(n+2-u)\Gamma(2+u-n)}\log\left(1-\frac{u}{n}\right)\,.\end{aligned} \tag{5.133}$$

The ratio of gamma functions is regular for $n \geq 3$ and furthermore it cancels the pole at $u = 1$. We therefore see that this asymptotic part of the $(n, 0)$ sector is completely determined by the singularity at $u = n + 2$, i.e., by the sector $(n + 2, 0)$.

Secondly, one gets contributions from acting with two alien derivatives:

$$\Delta_k \, F \Delta_{(n-k)} F \,. \tag{5.134}$$

However, many of these cases do not lead to a contribution to the resurgence of diagram (b) due to the prefactor in front of the convolution integral. That is, the contributions of Eq. (5.134) that lead to a simple pole do not contribute as the prefactor contains a term $1/\Gamma(3-u)$ which has zeros at $u = n$ for $n \geq 3$. As a result, the only non-vanishing contribution follows from the case $k = 2$ as this leads to a double pole at $u = n$. In particular, this results in a contribution to $\mathcal{B}[D_b^{(0,0)}](u)$ at $u = n$ proportional to:

$$\frac{-6\Gamma(1+u)}{(1-u)\Gamma(3-u)} \frac{1}{(n-u)^2} \,. \tag{5.135}$$

Combining the above observations leads to the contributions to the alien lattices shown in the second column of Tab. 5.3.

The structure of higher sectors of diagram (c) is similar to that of diagram (b). The non-vanishing alien derivatives acting on G are

$$\Delta_n G = \frac{n(-1)^n (2\pi \mathrm{i})}{(n+1)!(n-1)!} \,, \qquad n \geq 1 \,. \tag{5.136}$$

Acting with a single alien derivative on the product FG, we get asymptotic contributions to the $(n, 0)$ sectors $(n \geq 3)$ from

$$F \Delta_n G + G \Delta_n F \,. \tag{5.137}$$

First, we consider $n = 3$, where $G\Delta_3 F$ yields a contribution to $\mathcal{B}[D_c^{(0,0)}](u)$ proportional to

$$\frac{\log(1 - \frac{u}{3})}{8(2-u)} \,. \tag{5.138}$$

Likewise, $F\Delta_3 G$ yields a contribution proportional to

$$\left(\frac{1}{8(2-u)} + \frac{1}{4(5-u)}\right) \log(1 - \frac{u}{3}) \,. \tag{5.139}$$

<table>
<tr><td></td><td>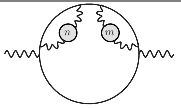 </td><td>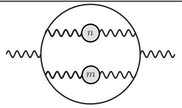 </td><td>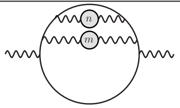 </td></tr>
<tr><td>$(0,0)$</td><td>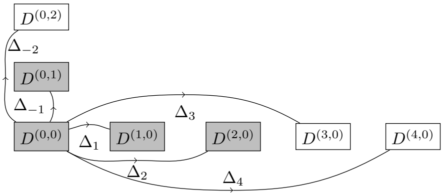 </td><td colspan="2">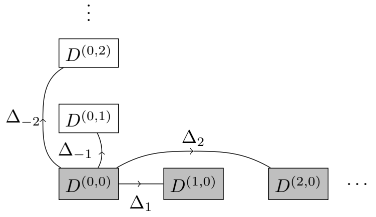 </td></tr>
<tr><td>$(1,0)$</td><td>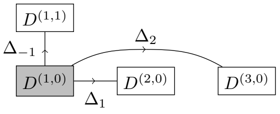 </td><td>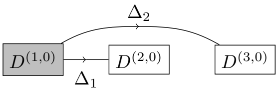 </td><td>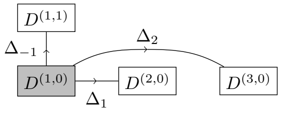 </td></tr>
<tr><td>$(0,1)$</td><td>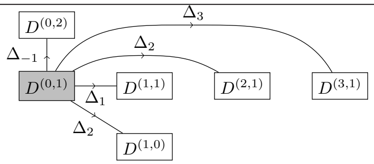 </td><td colspan="2">$D^{(0,1)}$</td></tr>
<tr><td>$(2,0)$</td><td>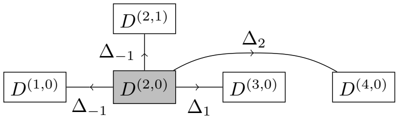 </td><td colspan="2">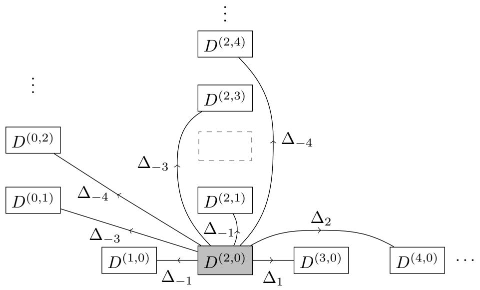 </td></tr>
<tr><td>$(0,2)$</td><td>$D^{(0,2)}$</td><td colspan="2">$D^{(0,2)}$</td></tr>
<tr><td>$(3,0)$</td><td>$D^{(3,0)}$</td><td>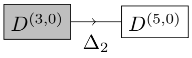 </td><td>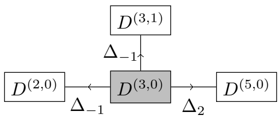 </td></tr>
<tr><td>$(0,3)$</td><td>-</td><td colspan="2">$D^{(0,3)}$</td></tr>
<tr><td>$(n,0)$</td><td>$D^{(4,0)}$</td><td colspan="2">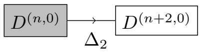 </td></tr>
<tr><td>$(0,n)$</td><td>-</td><td colspan="2">$D^{(0,n)}$</td></tr>
</table>

Table 5.3.: Final summary of the relations between non-perturbative sectors at order $1/N_f^2$.

Notice in particular that the expansion of this around $u = 2$ leads to part of the coefficient $\tilde{d}_0^{(2,0)[0]}$.

For $n > 3$, the only non-vanishing contribution of the convolution integral to the resurgence of diagram (c) coming from a single alien derivative is given by $F\Delta_n G$. This yields a contribution proportional to

$$\frac{\log(1-\frac{u}{n})}{(2+n-u)}\,. \tag{5.140}$$

Similar to diagram (b), when acting with two alien derivatives, one can show that only a double pole coming from the convolution integral contributes to the resurgence of diagram (c). This means that the contribution has to come from $\Delta_2 F\Delta_{n-2}G$, and we get a term proportional to

$$\frac{-6\Gamma(u)}{(1-u)(2-u)\Gamma(3-u)}\frac{1}{(n-u)^2} \tag{5.141}$$

We have added the resulting motions on the alien lattice in Tab. 5.3.

This brings us to the end of our resurgence analysis of diagrams (a), (b) and (c). The results are summarized in Tab. 5.3. Compared to the LO Adler function, at order $1/N_f^2$ the $(n,0)$ sectors (and also the $(0,1)$ sector for diagram (a)) are asymptotic sectors with their own resurgence relations towards further non-perturbative sectors. In particular we find sectors like (n,m) with $n \neq 0$ and $m \neq 0$. We notice however that the asymptotic non-perturbative sectors only have resurgence relations to sectors that contain only one or two coefficients, quite similar to asymptotic perturbative series of the LO Adler function. We expect that at higher order in the flavour expansion, the asymptotic non-perturbative sectors will have resurgence towards full asymptotic sectors, thus yielding an alien lattice with more motions between sectors.

5.3. Conclusion and outlook

In this chapter we have analyzed the transseries of the Adler function, which includes non-perturbative effects, to order $1/N_f^2$. Let us summarize our main findings.

First, while the exact Borel transform of the $\mathcal{O}(1/N_f)$ Adler function and its singularities has been known for a long time [85, 86] (reviewed and rederived in Sec. 5.1), we constructed a complete resummed *two-parameter* transseries expression – recall Eqs. (5.42) and (5.43) – for the Adler function at order $1/N_f$ in the original α variable. At this order in $1/N_f$ there are only poles in the Borel plane: UV double poles at negative integer values of the (rescaled) Borel plane parameter u, and IR double poles at positive integer values with the exceptions of an absent pole at $u = +1$ and the occurence of a single pole at $u = +2$.

Second, we found that resurgent properties of the Adler function are best expressed using the calculus and lattice structure based on the alien derivative (as advocated in [47]). In particular, applying the techniques developed in Sec. 4.2, we saw in Sec. 5.2 a way to extract resurgence properties without having immediate access to the exact Borel transform of a given asymptotic expansion. Furthermore, from this technique we were able to extract locally the form of the Borel transformed result.

Our third finding is a more intricate singularity structure in the Borel plan at order $1/N_f^2$, involving logarithmic branch cuts. In particular, using the Borel-Padé technique and a large order analysis of the coefficients that we computed, we found many of these branch cuts at IR singularities and a few at UV singularities. Of course, since we have only computed a limited number of diagrams, we cannot state with full certainty which singularities have branch cuts (and therefore which sectors have asymptotic expansions) in the full Adler function at all orders in $1/N_f$. However, we conjecture that all singularities in fact become of this sort - except of course a potential IR singularity at $u = +1$ which on physical grounds (due to the absence of a corresponding operator in the OPE [88, 100]) we expect to remain absent.

A fourth finding for the order $1/N_f^2$ transseries is that overlapping poles and branch point singularities in the Borel plane lead to $\log(\alpha)$ transmonomials in the transseries and indicate a new type of power correction. These factors were already anticipated in [98]; we indeed find that they occur. Furthermore, at this order in the flavour expansion – summarised in Tab. 5.3 – we found non-perturbative sectors (n, m) with both $n \neq 0$ and $m \neq 0$. These sectors come with both the IR transmonomial $e^{1/\beta_0 \alpha}$ and the UV transmonomial $e^{-1/\beta_0 \alpha}$. We expect all of this structure to persist at higher orders in $1/N_f$.

The picture that emerges from these findings is that the structure of our transseries, displayed in detail for order $1/N_f^2$ in Tab. 5.3, is interestingly different from that occurring in many models studied in the literature. In particular, we have seen that for the Adler function, ‘multiple forward alien derivatives’ such as Δ_2 give nonzero results, whereas in most simple models that have a bridge equation, only Δ_1 provides a nonvanishing ‘forward motion’. Furthermore, even though opposite non-perturbative exponentials $\pm A$ as well as logarithmic transmonomials appear in the Adler function transseries, the transseries turns out *not* to be resonant.

With our analysis, many open questions and opportunities for further research suggest themselves. Let us mention a few interesting directions.

To start verifying further the conjecture that for the full Adler function all non-perturbative sectors are asymptotic, one could take a closer look at specific diagrams at higher orders in $1/N_f$ and study their resurgence properties using the techniques developed in this thesis. Ultimately, it would be interesting to also be able to perform a sum over all orders in $1/N_f$. For example, this may allow one to see if the interesting shift in renormalon pole locations of [111] also occurs for the Adler function.

A second interesting area for further research concerns the structure of the Adler transseries. One way to answer this question would be using a bridge equation; however, no such equation is currently available. Despite this limitation, we have demonstrated that the absence of a bridge equation did not hinder our analysis at order $1/N_f$. By studying the Stokes automorphism, we concluded that two transseries parameters at this order suffice. Our findings suggest that the $1/N_f^2$ diagrams discussed in this section also feature two Stokes lines and, consequently, two Stokes automorphisms. Nevertheless, it remains possible that one would in fact require more parameters. A related observation is that our Adler transseries has a nonvanishing 'two steps forward' alien derivative Δ_2; a 'three-steps forward' Δ_3 etc. This may indicate a situation where sectors like the $e^{-2A/\alpha}$ sector introduce their own independent transseries parameters. It will therefore be interesting to study the Stokes automorphism for the $1/N_f^2$ diagrams, following an approach similar to that employed in Sec. 5.1.4 for the $1/N_f$ diagrams.

In conclusion, the Adler function remains an interesting object to study using resurgence techniques. It is sufficiently complicated to show features not displayed by many simpler models, but is also amenable to further perturbative studies that might uncover some of the subtleties mentioned. We expect many more lessons and surprises to lie ahead.

Chapter 6.

From power counting to factorization

And now for something completely different: in this and the next two chapters, we shift our focus to the topic of *factorization*.

The importance of factorization theorems and their impact on precision physics – particularly through resummation – was already highlighted in Sec. 1.2. The goal of this chapter is to review some key aspects of factorization and establish the necessary notation for the discussions ahead. Specifically, we will focus on the diagrammatic derivation of the leading power factorization theorem, Eq. (1.5), already given in the introduction of this thesis. Subsequently, we will review how a next-to-leading power factorization theorem can be derived along similar lines, as detailed in [25] (see also [119–121]).

The structure of this chapter is as follows. In Sec. 6.1, we start by discussing how infrared (IR) singularities of Feynman integrals can be classified and represented in a diagrammatic way. We then discuss how IR power counting can be used as a mechanism to isolate the dominant contribution of a Feynman integral. In particular, we review the QED power counting analysis of [25] and discuss how the diagrammatic representation can be cast into a factorization formula. The leading power contribution to this factorization formula is well established (see e.g. [23, 24] for more details). In [25], also the ingredients necessary to extend the factorization formula to next-to-leading power for both parametrically small and zero fermion masses was derived. In chapters 7 and 8, we will discuss this subleading power factorization formula in great detail in the case of massive fermions. Before we do so, we review the leading power factorization formula in Sec. 6.2. This gives us the chance to set up the notation and explain the ingredients to verify the factorization formulas, as we will follow a similar strategy in the next two chapters at subleading power.

6.1. Factorization in a diagrammatic language

From the previous chapters, it should be clear that the singularity structure of a complex function encodes important information. For a generic Feynman integral, this is not any different and in this section we review how IR singularities can be classified.

In particular, we discuss how factorization was first derived at the diagrammatic level from a systematic study of these IR singularities in terms of collinear and soft singularities.

6.1.1. Reduced diagrams

An arbitrary Feynman diagram $G(p_1, ..., p_E)$ with E external legs, L loops and I internal lines can be written as

$$G(p_1, \ldots, p_E) = \prod_{j=1}^{L} \int \frac{d^d k_j}{(2\pi)^d} N(p_r, k_s) \prod_{i=1}^{I} \frac{1}{l_i^2 - m_i^2 + \mathrm{i}\epsilon}\,, \tag{6.1}$$

with $N(p_r, k_j)$ some numerator factor and m_i and l_i the mass and momentum of the i-th propagator, where the latter may depend on the external momenta p_r, $1 \leq r \leq E$, and loop momenta k_s, $1 \leq s \leq L$. For every line we introduce a Feynman parameter α_i resulting in the Feynman-parametrized form

$$G(p_1, \ldots, p_E) = \Gamma(I) \prod_{i=1}^{I} \int_0^1 d\alpha_i \delta\Big(1 - \sum_{k=1}^{I} \alpha_k\Big) \prod_{j=1}^{L} \int \frac{d^d k_j}{(2\pi)^d} \frac{\tilde{N}(p_r, k_j, \alpha_i)}{D(p_r, k_j, \alpha_i)^I}\,, \tag{6.2}$$

where $\tilde{N}(p_r, k_j, \alpha_i)$ gathers all numerator factors after the parametrization. Potential IR singularities of this integral correspond to roots of the denominator

$$D(p_r, k_j, \alpha_i) = \sum_{i=1}^{I} \alpha_i \Big(l_i^2 - m_i^2\Big) + \mathrm{i}\epsilon\,. \tag{6.3}$$

As the integral in Eq. (6.2) is a contour integral in the complex variables k_j and α_i, the condition $D = 0$ alone is not enough to produce a singularity of G. By Cauchy's theorem, we may deform the integration contours to stay away from singularities. However, if $D = 0$ is the result of a fixed endpoint of the α_i contour, deforming the contour away from the singularity is not possible. Another way in which the singularity cannot be avoided is if two coalescing poles in l_i pinch the contour in between them. We call these singularities endpoint and pinch singularities respectively. These necessary conditions for such a singularity are summarised by the Landau equations [122]

$$\begin{cases} l_i^2 - m_i^2 = 0 \quad \text{or} \quad \alpha_i = 0 \\ \frac{\partial D}{\partial l_i^\mu} = 0\,, \quad \forall i, \mu\,. \end{cases} \tag{6.4}$$

Example 6.1.1. *As an example of the Landau equations, consider the massless triangle*

$$G(p_1,p_2) = \int \frac{d^dk}{(2\pi)^d} \frac{1}{k^2(k+p_1)^2(k-p_2)^2}$$
$$= 2\int \prod_i d\alpha_i \delta(1-\alpha_1-\alpha_2-\alpha_3) \int \frac{d^dk}{(2\pi)^d} \frac{1}{D^3}\,, \tag{6.5}$$

with $p_1^2 = p_2^2 = 0$ *and*

$$D = \alpha_1 k^2 + \alpha_2 (k+p_1)^2 + \alpha_3 (k-p_2)^2\,. \tag{6.6}$$

There are two collinear solutions to the Landau equations, Eq. (6.4)*, which read*

$$k^\mu = y p_1^\mu\,, \quad \alpha_3 = 0\,, \quad \alpha_1 y + \alpha_2(1+y) = 0\,, \tag{6.7}$$

and

$$k^\mu = z p_2^\mu\,, \quad \alpha_2 = 0\,, \quad \alpha_1 z - \alpha_3(1-z) = 0\,. \tag{6.8}$$

Furthermore, there is one soft solution which reads

$$k^\mu = 0, \quad \frac{\alpha_2}{\alpha_1} = \frac{\alpha_3}{\alpha_1} = 0\,. \tag{6.9}$$

Notice that the soft solution overlaps with the collinear solution in the limit $y \to 0$ *or* $z \to 0$*.*

Although solving the Landau equations is not too difficult in the above example, it may become cumbersome for more complicated Feynman integrals. A more intuitive picture is offered by the graphical analysis of Coleman and Norton [123]. They define a space-time separation

$$\Delta x_i^\mu \equiv \alpha_i l_i^\mu\,, \tag{6.10}$$

which can be interpreted as the displacement done in proper time $\alpha_i l_i^0$ of a classical particle with four-velocity $v^\mu = (1, l_i/l_i^0)$. In terms of Δx_i^μ, the Landau equations, Eq. (6.4), become

$$\begin{cases} \Delta x_i^\mu = 0, & \text{if } l_i^2 \neq m_i^2 \\ \sum_{i\in \text{loop } j} \Delta x_i^\mu \, \eta_{i,j} & \text{if } l_i^2 = m_i^2 \end{cases} \tag{6.11}$$

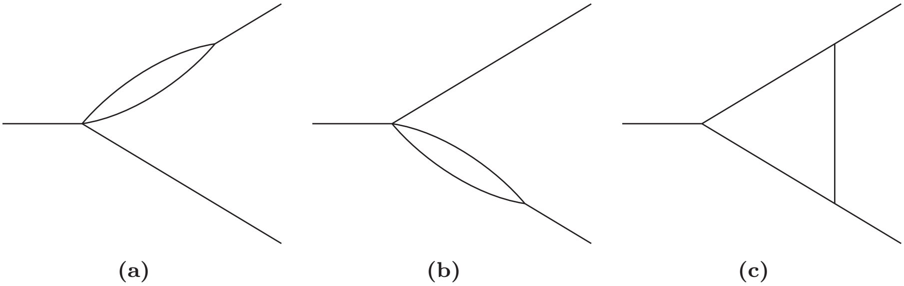

Figure 6.1.: Reduced diagrams for the one loop massles triangle as discussed in examples 6.1.1 and 6.1.2.

where the sum runs over the propagators in a certain loop j and $\eta_{i,j}$ is $+1$ (-1) if l_i is in the same (opposite) direction as the loop momentum k_j. As the following example shows, the solutions to the Landau equation can be represented by so called *reduced diagrams* made up of the displacement vectors Δx_j^μ.

Example 6.1.2. *The collinear solutions of example 6.1.1 now become respectively*

$$\Delta x_k^\mu = -\Delta x_{k+p_1}^\mu \,, \quad \Delta x_{k-p_2} = 0 \,, \tag{6.12}$$

and

$$\Delta x_k^\mu = -\Delta x_{k-p_2}^\mu \,, \quad \Delta x_{k+p_1} = 0 \,. \tag{6.13}$$

The reduced diagrams corresponding to these two solutions are shown in Fig. 6.1 (a) and (b). For the soft solution, we write

$$\Delta x_k^\mu = \lambda \alpha_1 \left(\frac{k^\mu}{\lambda} \right) \,, \tag{6.14}$$

and think of $k^\mu = 0$ as the limit $\lambda \to \infty$. This agrees with the physical picture of Coleman and Norton where vanishing momentum corresponds with an infinite wavelength. The reduced diagram is shown in Fig. 6.1 (c).

Hence, the task of finding solutions to the Landau equations now boils down to drawing all the possible reduced diagrams, obtained by contracting off-shell lines to points (the first condition in Eq. (6.11)). They form the vertices of the reduced diagram, whereas the on-shell lines form the lines of the reduced diagram (the second condition in Eq. (6.11)). The general reduced diagram for a QED process where a photon decays into N fermions is shown in Fig. 6.2. The following terminology is standard. We call a set of lines collinear to each other a *jet subdiagram*, which is

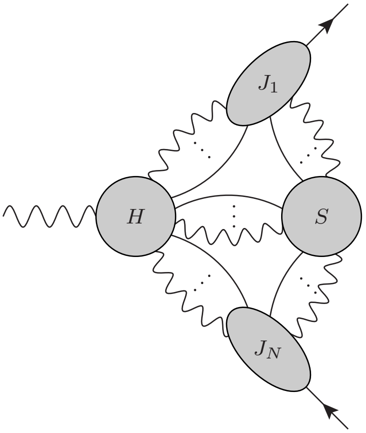

Figure 6.2.: General reduced diagram for a QED proces where a photon decays into N fermions.

abbreviated by J_i in the reduced diagram. The vertex H where lines from different jet subdiagrams meet is called the *hard vertex*. The lines with vanishing momenta can be gathered in a so-called *soft subdiagram*, denoted by S.

6.1.2. Power counting of QED amplitudes

The Landau equations – and therefore the reduced diagrams in the Coleman-Norton picture – give the necessary conditions for a Feynman integral to have IR singularities. However, these are not sufficient conditions for a Feynman integral to be singular as the integration measure or numerator factors might supress the singularity. In order to understand what configurations actually diverge, one introduces *IR power counting*.

The solutions to the Landau equations form a so-called *pinch surface* in the multi-dimensional (k_j, α_i)-space. These hypersurfaces can be parameterized using a set of *intrinsic coordinates* $\{v_a\}$. The remaining variables are called *normal coordinates* $\{n_b\}$ and they describe the perturbations around the singular pinch surfaces. By rescaling the normal coordinates with a power counting variable λ, we have a way to measure the degree of divergence of the pinch surfaces. We rescale

$$n_b \to \lambda^{\omega_b} n_b \tag{6.15}$$

for some power ω_b after which we can perform a so-called *power expansion* in λ. Eq. (6.2) becomes

$$\begin{aligned} G(p_1,\dots,p_E) &= \frac{\Gamma(I)}{(2\pi)^{Ld}} \prod_{i=1}^{I} \int_0^1 d\alpha_i \, \delta\Big(1-\sum_{k=1}^{I}\alpha_k\Big) \\ &\qquad \prod_{a,b} \int dv_a \lambda^{\omega_b} \int dn_b \frac{\tilde{N}(p_r,v_a,n_b,\alpha_i,\lambda)}{D(p_r,v_a,n_b,\alpha_i,\lambda)^I} \\ &= \lambda^{\gamma_G}\big(I+\mathcal{O}(\lambda)\big)\,, \end{aligned} \tag{6.16}$$

where I is the homogeneous integral obtained after expanding the Feynman integral G to leading power in λ, and γ_G denotes the IR degree of divergence of this integral. We conclude that $\gamma_G \le 0$ denotes diagrams which really do have singularities, whereas diagrams with $\gamma_G > 0$ are finite and vanish in the limit $\lambda \to 0$.

We notice that the power counting analysis not only gives the *leading power* (LP) in λ. One can also expand further and extract subleading powers in λ. In [25], this power counting analysis has been caried out for the reduced diagrams shown in Fig. 6.2, by carefully counting how many powers of λ each vertex and each line gives, and simplifying the overall expression with certain graph identities. The analysis was done for QED in the case of massless fermions, as well as the case of fermions with a parametrically small mass $m \sim \lambda Q$. In the rest of the thesis we are interested in the latter case and the power counting result of [25] reads

$$\gamma_G = I_f + 2m_\gamma + 4m_f + \sum_{i=1}^{N}\Big(N_\gamma^{(i)} + N_f^{(i)} + 2n_f^{(i)} - 1\Big)\,, \tag{6.17}$$

with I_f the total number of internal fermion lines in the amputated soft subdiagram and m_f (m_γ) denote the number of soft fermion (photon) connections with the hard part. Similarly, $N_f^{(i)}$ ($N_\gamma^{(i)}$) is the number of collinear fermion (photon) connections of jet i to the hard part and $n_f^{(i)}$ is the number of soft fermion connections to jet i. Notice that Eq. (6.17) is independent of $n_\gamma^{(i)}$ – the number of soft photon connections to jet i. A similar formula in [25] can be found for the power counting in the case of QED with massless fermions.

Similar to [25], as a specific case of the power counting formula Eq. (6.17), we consider the decay of an off-shell photon into two massive fermions $\gamma^* \to f\bar{f}$. The LP configuration is $\gamma_G = 0$, which is obtained for $N_f^{(i)} = 1$ and all other variables vanishing. The corresponding reduced graph is shown in Fig. 6.3 (a). We denoted the jet and soft subdiagrams by J_f, $J_{\bar{f}}$ and S respectively and the hard vertex by $H_{f\bar{f}}$. The next order in the power expansion $\gamma_G = 1$ has one additional photon connection

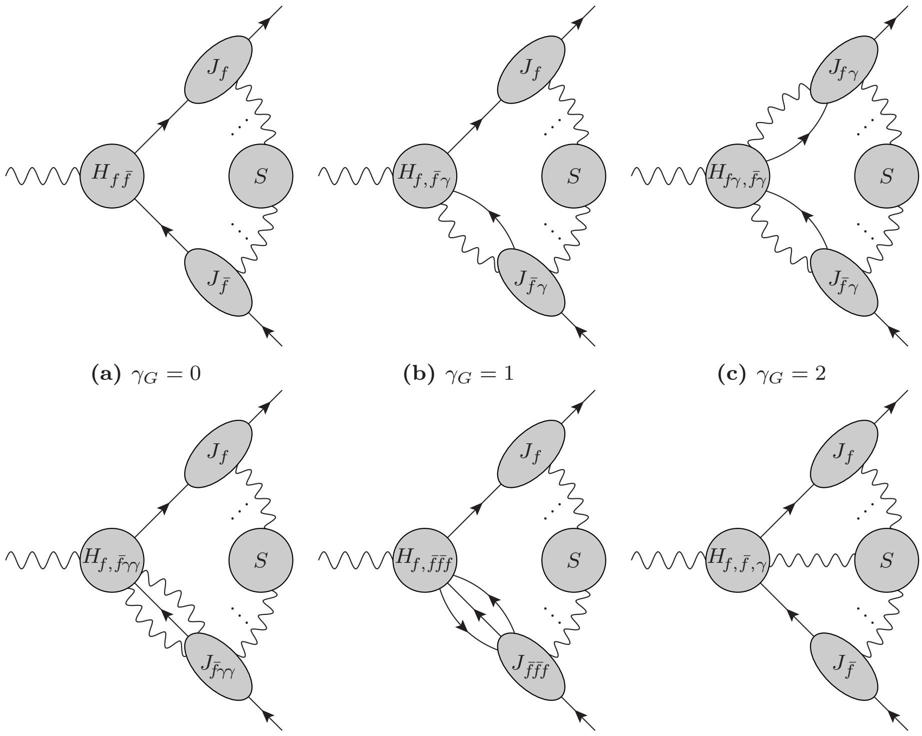

(a) $\gamma_G = 0$ **(b)** $\gamma_G = 1$ **(c)** $\gamma_G = 2$

(d) $\gamma_G = 2$ **(e)** $\gamma_G = 2$ **(f)** $\gamma_G = 2$

Figure 6.3.: Reduced diagrams for fermions with a parametrically small mass $m \sim \lambda Q$ contributing up to NLP [25]. Diagram (a) is the LP reduced diagram whereas diagram (b) is the first subleading contribution of order λ. Diagrams (c)-(f) contribute at order λ^2. We labeled the different jet sub diagrams by their connection to the hard vertex, which has a similar notation.

between a jet subdiagram and the hard vertex. One of the two configurations is shown in Fig. 6.3 (b), where a similar diagram can be drawn with the upper jet subdiagram connected to the hard vertex by both a fermion and a photon. We denoted this new jet subdiagram by $J_{\bar{f}\gamma}$ where again the subscript indicates the connection of the jet subdiagram to the hard vertex. Ultimately, we are also interested in $\gamma_G = 2$ and we call both the orders λ and λ^2 *next-to-leading power* (NLP). At order λ^2, more configurations exist and their reduced diagrams are shown in Fig. 6.3 (c)-(f).

The reduced diagrams of Fig. 6.3 encode all relevant soft and collinear configurations up to NLP. If one can find functional forms for the jet and soft subdiagrams as well as for the hard vertex, we would have a way to *factorize* the amplitude (in anticipation of such a factorization formula, we will therefore call these *jet, soft* and *hard functions* from now on). It is known for a long time that such a factorization formula indeed exist at LP, see e.g. [23, 24] for details, and it reads

$$\mathcal{M}^{\mathrm{LP}} = J_f \otimes H_{f,\bar{f}} \otimes J_{\bar{f}} \otimes S \tag{6.18}$$

where the symbol $\otimes$ denotes a contraction of spinor and Lorentz indices, which are neglected for notational simplicity (we will be more precise later on). We will review this well known factorization formula Eq. (6.18) in the next section.

Following the same reasoning, we may assume that a similar factorization formula holds at NLP:

$$\begin{aligned}\mathcal{M}^{\mathrm{NLP}} &= J_f \otimes H_{f,\bar{f}\gamma} \otimes J_{\bar{f}\gamma} \otimes S + J_{f\gamma} \otimes H_{f\gamma,\bar{f}} \otimes J_{\bar{f}} \otimes S + J_{f\gamma} \otimes H_{f\gamma,\bar{f}\gamma} \otimes J_{\bar{f}\gamma} \otimes S \\ &\quad + J_f \otimes H_{f,\bar{f}\gamma\gamma} \otimes J_{\bar{f}\gamma\gamma} \otimes S + J_{f\gamma\gamma} \otimes H_{f\gamma\gamma,\bar{f}} \otimes J_{\bar{f}} \otimes S \\ &\quad + J_f \otimes H_{f,\bar{f}\bar{f}f} \otimes J_{\bar{f}\bar{f}f} \otimes S + J_{ff\bar{f}} \otimes H_{ff\bar{f},\bar{f}} \otimes J_{\bar{f}} \otimes S\,,\end{aligned} \tag{6.19}$$

where we included the new NLP jet functions $J_{\bar{f}\gamma}$, $J_{\bar{f}\gamma\gamma}$ and $J_{\bar{f}\bar{f}f}$ shown in Fig. 6.3 (b)-(e), as well as the similar jet functions $J_{f\gamma}$, $J_{f\gamma\gamma}$ and $J_{ff\bar{f}}$. A few remarks are in order. First of all, the first two terms start at order λ and to be accurate to order λ^2, we also need their subleading terms. Similarly, we also need the subleading λ and λ^2 contributions of Eq. (6.18). We discuss both subtleties further in chapter 8. Second, we expect the soft function to be the same for all diagrams – including the LP factorization formula Eq. (6.18) – except for diagram (f) of Fig. 6.3 where the soft function has a direct connection to the hard function. However, this reduced diagram only contributes at the three loop order, which is beyond the scope of this thesis, and we therefore excluded this from the factorization formula. Finally, we want to note that [25] gives a more general factorization formula with N jets in the final state. However, the jet functions we will derive with two final state jets should be universal. That is, they can also be used for amplitudes with more than two final state jets and the difference would only be in the hard function. We come back to this in chapter 8.

6.2. LP factorization

In this section, we review the LP factorization formula Eq. (6.18) by discussing the decay of an off-shell photon of invariant mass Q into a massive fermion anti-fermion pair of mass m

$$\gamma^*(q) \to q(p_1) + \bar{q}(p_2)\,, \tag{6.20}$$

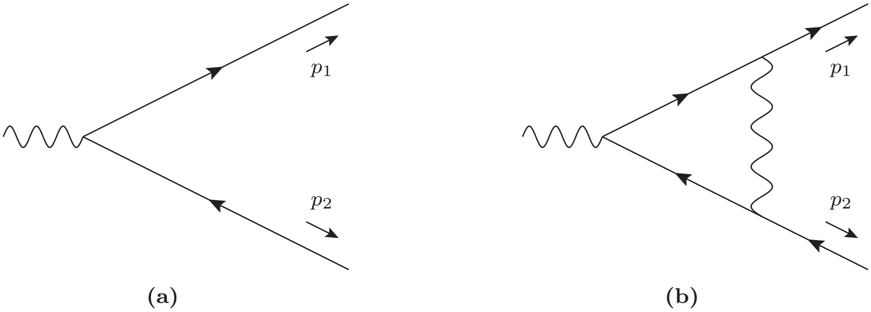

Figure 6.4.: Tree and one loop diagrams contributing to the massive form factors in QED.

whose tree and one loop contribution in QED is given respectively in Fig. 6.4 (a) and (b). The LP factorization is well known [23, 24], and we review it here to set up notation and explain the strategy we will utilize in checking the NLP factoriztation formula, Eq. (6.19), in chapters 7 and 8.

6.2.1. Massive form factors

Following [124], the vertex function $V^\mu(p_1,p_2)$ corresponding to the process, Eq. (6.20), is expressed in terms of two form factors, F_1 and F_2, as follows:

$$\begin{aligned} V^\mu(p_1,p_2) &= \bar{u}(p_1)\,\Gamma^\mu(p_1,p_2)\,v(p_2), && (6.21)\\ \Gamma^\mu(p_1,p_2) &= -i\,e\,e_q\left[F_1\big(s,m^2\big)\gamma^\mu + \frac{1}{2m}F_2\big(s,m^2\big)\,i\,\sigma^{\mu\nu}q_\nu\right], && (6.22)\end{aligned}$$

where $\sigma^{\mu\nu} = \frac{i}{2}[\gamma^\mu,\gamma^\nu]$; furthermore, $s = (p_1+p_2)^2$ represents the center of mass energy, and m en e_q are the fermion mass and charge fraction respectively. The form factors F_i, $i = 1,2$ can be extracted by applying projection operators:

$$F_i\big(s,m^2\big) = \mathrm{Tr}\big[P_i^\mu(m,p_1,p_2)\,\Gamma_\mu(p_1,p_2)\big], \qquad (6.23)$$

where

$$P_i^\mu(m,p_1,p_2) = \frac{\not{p}_2 - m}{m}\left[i\,g_1^{(i)}\gamma^\mu + \frac{i}{2m}g_2^{(i)}\big(p_2^\mu - p_1^\mu\big)\right]\frac{\not{p}_1 + m}{m}, \qquad (6.24)$$

and[1]

$$
\begin{aligned}
g_1^{(1)} &= -\frac{1}{e}\frac{1}{4(1-\epsilon)}\frac{1}{(s/m^2-4)}, \\
g_2^{(1)} &= \frac{1}{e}\frac{3-2\epsilon}{(1-\epsilon)}\frac{1}{(s/m^2-4)^2}, \\
g_1^{(2)} &= \frac{1}{e}\frac{1}{(1-\epsilon)}\frac{1}{s/m^2(s/m^2-4)}, \\
g_2^{(2)} &= -\frac{1}{e}\frac{1}{(1-\epsilon)}\frac{1}{(s/m^2-4)^2}\left[\frac{4m^2}{s}+2-2\epsilon\right].
\end{aligned}
\tag{6.25}
$$

Here and in the next chapters, we work in $d = 4-2\epsilon$ dimensions and compute the unsubtracted form factor at one and two loops respectively. We therefore omit counterterm insertions, which makes the mass m the unrenormalized mass. The form factors have the perturbative expansion

$$
\begin{aligned}
F_i\left(s,m^2,\mu^2\right) = F_i^{(0)}\left(s,m^2\right) + \frac{e_q^2\,\alpha_{\rm EM}}{4\pi}\,F_i^{(1)}\left(s,m^2,\mu^2\right) \\
+\left(\frac{e_q^2\,\alpha_{\rm EM}}{4\pi}\right)^2 F_i^{(2)}\left(s,m^2,\mu^2\right) + \mathcal{O}\left(\alpha_{\rm EM}^3\right)\,,
\end{aligned}
\tag{6.26}
$$

with $\alpha_{\rm EM} = e^2/(4\pi)$ and where

$$
F_1^{(0)}\left(s,m^2\right) = 1, \qquad F_2^{(0)}\left(s,m^2\right) = 0. \tag{6.27}
$$

We are interested in computing the higher order corrections in the small mass (or high-energy) limit $m^2/s \sim \lambda^2 \ll 1$. We assume the center of mass frame, with the incoming quark moving along the positive z-axis. The momenta of the quark and anti-quark can then be decomposed along two light-like directions, $n_\pm = (1,0,0,\mp 1)$ as follows:

$$
\begin{aligned}
p_1^\mu &= \left(\sqrt{p^2+m^2},0,0,p\right) = p_1^+\frac{n_-^\mu}{2} + p_1^-\frac{n_+^\mu}{2}, \\
p_2^\mu &= \left(\sqrt{p^2+m^2},0,0,-p\right) = p_2^+\frac{n_-^\mu}{2} + p_2^-\frac{n_+^\mu}{2}.
\end{aligned}
\tag{6.28}
$$

In the small mass limit the $p_i^\pm$ components have the scaling properties

$$
\begin{aligned}
p_1^+ = n_+\cdot p_1 = p_2^- = n_-\cdot p_2 = \sqrt{p^2+m^2}+p \sim \sqrt{s}, \\
p_1^- = n_-\cdot p_1 = p_2^+ = n_+\cdot p_2 = \sqrt{p^2+m^2}-p \sim \lambda^2\sqrt{s}.
\end{aligned}
\tag{6.29}
$$

---

[1] The definition of $g_2^{(2)}$ in [124] has a typo; here we follow the definition given in Eq. (2.7) of [125].

In what follows it will prove useful to define a variable

$$\hat{s} \equiv p_1^+ p_2^- = \left(\sqrt{m^2+p^2}+p\right)^2 , \tag{6.30}$$

such that

$$s = 2m^2 + p_1^+ p_2^- + p_1^- p_2^+ = 2m^2 + \hat{s} + \frac{m^4}{\hat{s}}. \tag{6.31}$$

Throughout the remainder of this thesis, we define the loop integration measure in dimensional regularization as follows:

$$\int [dk] \equiv \left(\frac{\mu^2 e^{\gamma_E}}{4\pi}\right)^{\epsilon} \int \frac{d^{4-2\epsilon}k}{(2\pi)^{4-2\epsilon}}. \tag{6.32}$$

We will next compute the one loop massive form factor using the method of regions.

6.2.2. Method of regions

In order to test the factorization formulas, Eqs (6.18) and (6.19), we need some data to compare with. For the purpose of checking the LP factorization formula Eq. (6.18) – which we do in this section – we need at least the one loop small mass expansion of the form factors, i.e. $m \ll Q$. In [25] some explicit checks have been provided at one loop for the NLP factorization formula, Eq. (6.19). However, a more thorough test of the factorization formula requires at least a two-loop computation, since the functions in the second and third line of Eq. (6.19) appear for the first time at NNLO. The analysis is much more extensive and we therefore dedicate the next two chapters to this.

The small mass expansion alone does not provide enough information to compare with the corresponding factorized expression given in Eq. (6.18). Indeed, in the small mass limit it is possible to calculate the form factors with the *method of expansion by momentum regions* [126–128], often also simply called the method of regions. Within this approach, one assigns to the loop momentum a specific scaling, which can be hard, collinear, soft, etc, with respect to the scaling of the external particle momenta. Each term defines a momentum region, and it is then possible to expand the form factors directly at the level of the integrand in the small parameters appearing in each region. The full result is recovered by summing over all regions. This approach is particularly useful because we expect the jet functions in Eq. (6.19) to be directly related to the collinear and anti-collinear region contributions. (See [129, 130] for previous applications of the method of regions to study the correspondence between collinear regions and jet functions.)

Let us explain the method of regions in more detail by discussing the one loop form factor in the limit $m^2 \ll s$ and calculating the first two terms in the expansion. Notice that for now we are just interested in the first term of this expansion, i.e. the LP term, but we need the subleading term as well when we discuss the NLP factorization in the next two chapters. At one loop only the single diagram of Fig. 6.4(b) contributes to the form factors and the amplitude in Feynman gauge reads

$$-e_q^3 e^3 \int [dk] \frac{\bar{u}(p_1)\gamma^\rho(\not{k}+\not{p}_1+m)\gamma^\mu(\not{k}-\not{p}_2+m)\gamma_\rho v(p_2)}{[k^2+i0^+][(k+p_1)^2-m^2+i0^+][(k-p_2)^2-m^2+i0^+]} \tag{6.33}$$

The first step in the method of regions is then to decompose k along the light-like directions $n_\pm$:

$$k^\mu = k^+\frac{n_-^\mu}{2} + k^-\frac{n_+^\mu}{2} + k_\perp^\mu, \qquad\qquad k^\mu = (k^+, k^-, k_\perp), \tag{6.34}$$

where $k_\pm = n_\pm \cdot k$. The second identity in the equation above provides a compact notation to indicate scaling relations similar to the scaling we assigned to the external momenta in Eq. (6.29). As we will see below, up to one loop the following loop momentum modes contribute:

$$\begin{aligned} \text{Hard } (h)\text{:} \qquad & k \sim \sqrt{\hat{s}}\,(\lambda^0, \lambda^0, \lambda^0)\,, \\ \text{Collinear } (c)\text{:} \qquad & k \sim \sqrt{\hat{s}}\,(\lambda^0, \lambda^2, \lambda^1)\,, \\ \text{anti-Collinear } (\bar{c})\text{:} \qquad & k \sim \sqrt{\hat{s}}\,(\lambda^2, \lambda^0, \lambda^1)\,. \end{aligned} \tag{6.35}$$

Beyond one loop – see chapter 7 – we find that two additional momentum modes are necessary, which scale as

$$\begin{aligned} \text{Ultra-Collinear } (uc)\text{:} \qquad & k \sim \sqrt{\hat{s}}\,(\lambda^2, \lambda^4, \lambda^3)\,, \\ \text{Ultra-anti-Collinear } (u\bar{c})\text{:} \qquad & k \sim \sqrt{\hat{s}}\,(\lambda^4, \lambda^2, \lambda^3)\,. \end{aligned} \tag{6.36}$$

One might also expect the following modes to contribute:[2]

$$\begin{aligned} \text{Semi-Hard } (sh)\text{:} \qquad & k \sim \sqrt{\hat{s}}\,(\lambda^1, \lambda^1, \lambda^1)\,, \\ \text{Soft } (s)\text{:} \qquad & k \sim \sqrt{\hat{s}}\,(\lambda^2, \lambda^2, \lambda^2)\,, \end{aligned} \tag{6.37}$$

however, these turn out to give rise to scaleless loop integrals and therefore do not contribute up to two-loop level.[3]

---

[2] In literature the modes of Eq. (6.37) are sometimes referred to as *soft* and *ultra-soft* respectively [21].

[3] In the presence of rapidity divergences this depends on the type of rapidity regulator, which we discuss in detail in Sec. 7.2 and App. C.

	k^2	$k^+p_1^-$	$k^-p_1^+$	$k^+p_2^-$	$k^-p_2^+$	$[dk]$
(h)	1	λ^2	1	1	λ^2	1
(c)	λ^2	λ^2	λ^2	1	λ^4	λ^4
$(\bar{c})$	λ^2	λ^4	1	λ^2	λ^2	λ^4
(uc)	λ^6	λ^4	λ^4	λ^2	λ^6	λ^{12}
$(\overline{uc})$	λ^6	λ^6	λ^2	λ^4	λ^4	λ^{12}

Table 6.1.: Scaling associated to the different momentum regions.

The next step is to perform the power expansion of the integrand in Eq. (6.33) in each momentum region. For example, for the collinear region, it is straightforward to do this power expansion by expanding in λ using the scalings of the third row of Tab. 6.1 – which is obtained using the scalings of Eq. (6.29) for the external momenta and the collinear scaling of Eq. (6.35) for the loop momenta. That is, the third denominator in Eq. (6.33) is expanded as

$$\left.\frac{1}{k^2 - k^- p_2^+ - k^+ p_2^- + i0^+}\right|_c = \frac{1}{-k^+ p_2^- + i0^+}\left[1 - \frac{k^2}{-k^+ p_2^- + i0^+} + \mathcal{O}(\lambda^4)\right] \qquad (6.38)$$

and one can perform a similar expansion for the rest of the integrand. Here and in the rest of this thesis, to denote that k has collinear scaling, we introduced the notation $|_c$, with a similar notation for the other momentum scalings. After the integrand in Eq. (6.33) is expanded up to the order in λ in which we are interested, we can perform the loop integration using standard techniques. (We will be brief for now on the one loop calculation as we will give many more details when we turn to the two loop calculation in the next chapter.) The procedure for the other momentum regions is the same.

Finally, the form factor is given as a sum over the contributing regions. For instance, at one loop we have:

$$F_i^{(1)}\left(\frac{\mu^2}{\hat{s}}, \frac{\mu^2}{m^2}, \epsilon\right) = \left.F_i^{(1)}\right|_h\left(\frac{\mu^2}{\hat{s}}, \epsilon\right) + \left.F_i^{(1)}\right|_c\left(\frac{\mu^2}{m^2}, \epsilon\right) + \left.F_i^{(1)}\right|_{\bar{c}}\left(\frac{\mu^2}{m^2}, \epsilon\right), \qquad (6.39)$$

and all other regions vanishing as they lead to scaleless integrals which vanishes in dimensional regularization. Each region is expected to depend non-analytically (logarithmically) on a single scale, which is dictated by the kinematics of the process. We find that the non-analytic dependence of the hard region is conveniently given in terms of the factor $\hat{s}$, while the non-analytic structure of the collinear and anti-collinear regions is given in terms of the mass m.

It is important to emphasize that we are integrating over the whole loop integration domain. This may seem disturbing as we are expanding the integrand in a specific limit of this domain, so one might expect that we should limit the integration domain as well to avoid a possible overcounting with other momentum regions. This overlap is often called the zero-bin contribution [131]. However, since each individual region depends on a single scale, the overlap with another region would be given by a scaleless integral. Indeed, the region results we show below and in the next chapter do not have such overlap. We refer to App. C.4 for an example of a zero-bin contribution.

For the form factor F_1 we have

$$F_1^{(1)}\Big|_h = \left(\frac{\mu^2}{-\hat{s}-i0^+}\right)^\epsilon \Bigg\{-\frac{2}{\epsilon^2}-\frac{3}{\epsilon}-8+\zeta_2+\epsilon\left(-16+\frac{3\zeta_2}{2}+\frac{14\zeta_3}{3}\right) + \frac{m^2}{\hat{s}}\left[-\frac{2}{\epsilon}-6+\epsilon\big(-16+\zeta_2\big)\right]+\mathcal{O}(\epsilon^2)+\mathcal{O}(\lambda^4)\Bigg\}, \tag{6.40}$$

for the hard region, and

$$F_1^{(1)}\Big|_c = \left(\frac{\mu^2}{m^2-i0^+}\right)^\epsilon \Bigg\{\frac{1}{\epsilon^2}+\frac{2}{\epsilon}+4+\frac{\zeta_2}{2}+\epsilon\left(8+\zeta_2-\frac{\zeta_3}{3}\right) + \frac{m^2}{\hat{s}}\left[\frac{1}{\epsilon}+5+\epsilon\left(13+\frac{\zeta_2}{2}\right)\right]+\mathcal{O}(\epsilon^2)+\mathcal{O}(\lambda^4)\Bigg\}, \tag{6.41}$$

for the collinear region, and

$$F_1^{(1)}\Big|_{\bar{c}} = F_1^{(1)}\Big|_c. \tag{6.42}$$

In the prefactors in Eqs. (6.40) and (6.41), we have explicitly written the Feynman prescription $i0^+$, which upon expanding in ϵ give logarithms $\log(\mu^2/(-\hat{s}-i0^+))$ and $\log(\mu^2/(m^2-i0^+))$. For $\mu^2>0, m^2>0$ and $\hat{s}>0$ these can be rewritten using $\log(\mu^2/(-\hat{s}-i0^+)) \to \log(\mu^2/\hat{s})+i\pi$ and $\log(\mu^2/(m^2-i0^+)) \to \log(\mu^2/m^2)$ to obtain the imaginary parts. For notational convenience, we will drop the Feynman prescription in what follows and note that this can always be reinstated by $\hat{s}\to\hat{s}+i0^+$ and $m^2\to m^2-i0^+$ after which the imaginary parts can be retrieved adopting the rule described above.

The form factor F_2 starts at NLP. We have

$$F_2^{(1)}\Big|_h = \left(\frac{\mu^2}{-\hat{s}}\right)^\epsilon \left\{\frac{m^2}{\hat{s}}\left[\frac{4}{\epsilon}+16+\epsilon\big(32-2\zeta_2\big)\right]+\mathcal{O}(\epsilon^2)+\mathcal{O}(\lambda^4)\right\}, \tag{6.43}$$

and

$$F_2^{(1)}\Big|_c = \left(\frac{\mu^2}{m^2}\right)^{\epsilon}\left\{\frac{m^2}{\hat{s}}\left[-\frac{2}{\epsilon}-8+\epsilon\big(-16-\zeta_2\big)\right]+\mathcal{O}(\epsilon^2)+\mathcal{O}(\lambda^4)\right\}, \quad (6.44)$$

and

$$F_2^{(1)}\Big|_{\bar{c}} = F_2^{(1)}\Big|_c. \quad (6.45)$$

These results can be compared directly with [124] by extracting the coefficients $\mathcal{F}_i^{(1)}(s,\mu)$ as defined in Eq. (18) there, as follows:

$$\mathcal{F}_i^{(1)}(s,\mu) = \frac{e^{-\epsilon\gamma_E}}{\Gamma(1+\epsilon)}\left(\frac{\mu^2}{m^2}\right)^{-\epsilon}F_i^{(1)}(s,\mu). \quad (6.46)$$

Summing over the regions and expanding also the scale factors in powers of ϵ we find

$$\begin{aligned}\mathcal{F}_1^{(1)}(s,\mu) &= \left\{\frac{1}{\epsilon}\left[1-2\ln\left(-\frac{m^2}{\hat{s}}\right)\right]-3\ln\left(-\frac{m^2}{\hat{s}}\right)-\ln^2\left(-\frac{m^2}{\hat{s}}\right)+2\zeta_2\right.\\ &\qquad\left.+\frac{m^2}{\hat{s}}\left[4-2\ln\left(-\frac{m^2}{\hat{s}}\right)\right]+\mathcal{O}(\epsilon)+\mathcal{O}(\lambda^4)\right\}, \quad (6.47)\end{aligned}$$

and

$$\mathcal{F}_2^{(1)}(s,\mu) = 4\frac{m^2}{\hat{s}}\ln\left(-\frac{m^2}{\hat{s}}\right)+\mathcal{O}(\epsilon)+\mathcal{O}(\lambda^4),$$

in agreement with the high-energy expansion $\hat{s} \gg m^2$ of Eqs. (19) and (20) of [124].

6.2.3. LP jet function

To one loop accuracy, the LP factorization formula Eq. (6.18) can be expanded as

$$\begin{aligned}V^\mu(p_1,p_2) = {}& J_f^{(0)}\otimes H_{f,\bar{f}}^{(0),\mu}\otimes J_{\bar{f}}^{(0)}\otimes S^{(0)}\\ &+J_f^{(1)}\otimes H_{f,\bar{f}}^{(0),\mu}\otimes J_{\bar{f}}^{(0)}\otimes S^{(0)}+J_f^{(0)}\otimes H_{f,\bar{f}}^{(0),\mu}\otimes J_{\bar{f}}^{(1)}\otimes S^{(0)}\\ &+J_f^{(0)}\otimes H_{f,\bar{f}}^{(1),\mu}\otimes J_{\bar{f}}^{(0)}\otimes S^{(0)}+J_f^{(0)}\otimes H_{f,\bar{f}}^{(0),\mu}\otimes J_{\bar{f}}^{(0)}\otimes S^{(1)}, \quad (6.48)\end{aligned}$$

where, similar to Eq. (6.26), we assummed that the jet functions have the perturbative expansion

$$J_i = J_i^{(0)}+\frac{e_q^2\,\alpha_{\rm EM}}{4\pi}J_i^{(1)}+\left(\frac{e_q^2\,\alpha_{\rm EM}}{4\pi}\right)^2 J_i^{(2)}+\mathcal{O}\left(\alpha_{\rm EM}^3\right), \quad (6.49)$$

and with a similar expansion for the hard and soft functions.

The jet functions can be defined in terms of the matrix elements

$$J_f(p_1, n_1) = \big\langle p_1 \big| \bar{\psi}(0)\, W_{n_1}(0,\infty) \big| 0 \big\rangle\,, \tag{6.50}$$

and

$$J_{\bar{f}}(p_2, n_2) = \big\langle p_2 \big| W_{n_2}(\infty,0)\, \psi(0) \big| 0 \big\rangle\,, \tag{6.51}$$

where $W_n(x,y)$ represents a Wilson line defined by

$$W_n(x,y) = \exp\bigg[-i\, e\, e_q \int_x^y ds\, n\cdot A(s\, n) \bigg]. \tag{6.52}$$

The choice of the gauge-link vectors n_1 and n_2 is free. Given that their function is to mimic the coupling of photons collinear to the outgoing fermion to the opposite moving hard fermion, we will make for computational convenience the choice $n_1 = n^+$, $n_2 = n^-$ and drop the second argument in Eqs (6.50) and (6.51) from now on. At lowest order in perturbation theory, the jet function is given by

$$J_f^{(0)}(p_1) = \bar{u}(p_1) \quad \text{and} \quad J_{\bar{f}}^{(0)}(p_2) = v(p_2)\,. \tag{6.53}$$

The one loop contribution to $J_f(p_1)$ is given by

$$\begin{aligned}(-ie\, e_q \mu^\epsilon)^2 \int_\infty^0 d\lambda \int dx\, \langle p_1 | \bar{\psi}(0) n_+ A(\lambda n_+) \bar{\psi}(x) \not{A}(x) \psi(x) | 0 \rangle \\ = i e^2 e_q^2 \bar{u}(p_1) \int [dk] \frac{\not{n}_+ (\not{p}_1 - \not{k} + m)}{k^2[(p_1-k)^2 - m^2][n_+ k]}\,,\end{aligned} \tag{6.54}$$

where we considered the vertex correction, which is the only 1PI contribution. Furthermore, we work in Feynman gauge as this was also the choice of gauge in the previous subsection. The corresponding diagram is shown in Fig. 6.5 (a), where the double line represents the linear Wilson line propagator

$$\frac{n_+^\mu}{[n_+ k]}\,. \tag{6.55}$$

The little hook at the end of the outgoing fermion line indicates that we have to include the spinor $\bar{u}(p_1)$. A small calculation yields

$$J_f^{(1)}(p_1) = \left(\frac{\mu^2}{m^2}\right)^\epsilon \bar{u}(p_1) \frac{\Gamma(\epsilon) e^{\epsilon \gamma_E}}{\epsilon(1-2\epsilon)} \left(1 - \frac{2m\epsilon}{\hat{s}} \not{p}_2^-\right), \tag{6.56}$$

(a) **(b)**

Figure 6.5.: Figures (a) and (b) show the diagrammatic representation of the one loop LP jet functions $J_f^{(1)}(p_1)$ and $J_{\bar{f}}^{(1)}(p_2)$ respectively.

where we used the identity

$$\not{n}_+ = \frac{2}{p_2^-}\left(p_2^- \frac{\not{n}_+}{2}\right) \equiv \frac{2}{p_2^-}\not{p}_2^- \tag{6.57}$$

to put the result in a familiar form.

Similarly, the one loop contribution to $J_{\bar{f}}(p_2)$ is shown in Fig. 6.5 (b), where the Wilson line propagator is now given by

$$\frac{n_-^\mu}{[-n_- k]} \,. \tag{6.58}$$

The result reads

$$J_{\bar{f}}^{(1)}(p_2) = \left(\frac{\mu^2}{m^2}\right)^\epsilon \frac{\Gamma(\epsilon)e^{\epsilon\gamma_E}}{\epsilon(1-2\epsilon)}\left(1 + \frac{2m\epsilon}{\hat{s}}\not{p}_1^+\right)v(p_2) \,. \tag{6.59}$$

Comparing the jet functions in the two directions, one observes the symmetry $p_1^\mu \leftrightarrow -p_2^\mu$, and hence also the symmetry $n_+^\mu \leftrightarrow -n_-^\mu$. The origin of the minus sign is related to the fact that the momentum p_2 along the anti-fermion leg is taken outgoing, thus against the fermion flow, while for the quark leg the (outgoing) momentum p_1 goes in the same direction as the fermion flow.

Before we can verify the above jet functions, we need the soft and hard functions. Their tree level expressions can be easily matched to the full tree level diagram – shown in Fig. 6.4 (a) – which reads

$$\bar{u}(p_1)\,(-ie\gamma^\mu)\,v(p_2) \,. \tag{6.60}$$

This can be compared to the factorized expression

$$J_f^{(0)} \otimes H_{f,\bar{f}}^{(0),\mu} \otimes J_{\bar{f}}^{(0)} \otimes S^{(0)} \,. \tag{6.61}$$

Given that the tree level expressions for J_f and $J_{\bar{f}}$ are just the spinors, we obtain the following:

$$H_{f,\bar{f}}^{(0),\mu} = -\mathrm{i}e\, e_q\, \gamma^\mu \,, \qquad\qquad S^{(0)} = 1 \,. \tag{6.62}$$

We now have the ingredients to verify the jet functions J_f and $J_{\bar{f}}$ up to one loop by comparing with the results obtained with the method of regions. That is, we can compare the factorized expression

$$J_f^{(1)} \otimes H_{f,\bar{f}}^{(0),\mu} \otimes J_{\bar{f}}^{(0)} \otimes S^{(0)} \tag{6.63}$$

with the c-region of the vertex function $V^\mu(p_1,p_2)$. Substituting the results calculated above, we get

$$\begin{aligned} J_f^{(1)} \otimes & H_{f,\bar{f}}^{(0),\mu} \otimes J_{\bar{f}}^{(0)} \otimes S^{(0)} \\ &= \left(\frac{\mu^2}{m^2}\right)^{\epsilon} \frac{\Gamma(\epsilon) e^{\epsilon\gamma_E}}{\epsilon(1-2\epsilon)} \bar{u}(p_1) \left(1 - \frac{2m\epsilon}{\hat{s}} \not{p}_2^{-}\right) \Big[-ie\gamma^\mu\Big] v(p_2) \\ &= -ie\, e_q\, \bar{u}(p_1)\, \gamma^\mu\, v(p_2) \left(\frac{\mu^2}{m^2}\right)^{\epsilon} \left[\frac{1}{\epsilon^2} + \frac{2}{\epsilon} + 4 + \frac{\zeta_2}{2} + \mathcal{O}(\epsilon)\right] + \mathcal{O}(\lambda) \,, \end{aligned} \tag{6.64}$$

where in the last line, we only kept the LP term and performed the expansion in ϵ. Recalling the relation Eq. (6.22) between the vertex function $V^\mu(p_1,p_2)$ and the form factors, we indeed find agreement with the collinear expansion of the form factor F_1 at LP given in Eq. (6.41). Similarly, one finds agreement with the LP term of the factorized expression

$$J_f^{(0)} \otimes H_{f,\bar{f}}^{(0),\mu} \otimes J_{\bar{f}}^{(1)} \otimes S^{(0)} \tag{6.65}$$

and the LP terms of the $\bar{c}$-region of $V^\mu(p_1,p_2)$.

Finally, we give the LP one loop hard function

$$H_{f,\bar{f}}^{(1),\mu} = -\mathrm{i}e\, e_q\, \gamma^\mu \left(\frac{\mu^2}{-\hat{s}}\right)^{\epsilon} \left[-\frac{2}{\epsilon^2} - \frac{3}{\epsilon} - 8 + \zeta_2\right] + \mathcal{O}(\lambda) \,, \tag{6.66}$$

which is just equal to the one loop hard region. As discussed in more detail in the next subsection, we are mainly interested in the hard-collinear part of the factorization and we therefore work with bare form factors. As a result, we saw that the soft momentum region vanishes, so we can assume that the soft function is trivial, i.e. $S^{(0)} = 1$ and $S^{(1)} = 0$.

6.2.4. Discussion

In view of verifying the NLP factorization formula Eq. (6.19), it may be useful to elaborate on the results given in this section for the LP factorization formula. As said before, the factorization of the amplitude at leading power is well known, and often presented in the following form in the literature:

$$V^{\mu}_{\mathrm{LP}}(p_1, p_2) = \frac{J_f(p_1, n^+)}{\mathcal{J}_f(n^-, n^+)} \otimes H^{\mu}_{f\bar{f}}(p_1^+, p_2^-) \otimes \frac{J_{\bar{f}}(p_2, n^-)}{\mathcal{J}_{\bar{f}}(n^+, n^-)} \otimes S(n^+ \cdot n^-)\,. \tag{6.67}$$

A few words of explanation are in order. The hard function $H^{\mu}(p_1^+, p_2^-)$ represents the virtual hard modes contributing to the amplitude, and thus it depends on the large momentum components p_1^+ and p_2^-. Next, we have the contribution due to the jet functions, which reproduce virtual collinear and anti-collinear modes. Their operator matrix definitions were already given in Eqs. (6.50) and (6.51). Lastly, Eq. (6.67) contains the soft function $S(n^+ \cdot \bar{n}^-)$, as well as the eikonal approximation of the two jet functions, all defined in terms of the vacuum expectation value of Wilson lines. That is:

$$S(\beta_1 \cdot \beta_2) = \big\langle 0 \big| W_{\beta_1}(0, -\infty)\, W_{\beta_2}(\infty, 0) \big| 0 \big\rangle\,, \tag{6.68}$$

for the soft function, and

$$\begin{aligned} \mathcal{J}_f(\beta_1, n^+, \mu) &= \big\langle 0 \big| W_{\beta_1}(0, -\infty)\, W_{n^+}(\infty, 0) \big| 0 \big\rangle\,, \\ \mathcal{J}_{\bar{f}}(\beta_2, n^-, \mu) &= \big\langle 0 \big| W_{n^-}(0, -\infty)\, W_{\beta_2}(\infty, 0) \big| 0 \big\rangle\,, \end{aligned} \tag{6.69}$$

for the two eikonal jet functions. Again, one has the freedom to choose $\beta_1 = n^-$ and $\beta_2 = n^+$.

It is important to notice that Eq. (6.67) describes the factorization of the form factor *after* soft and collinear singularities have been removed from the hard function, and they appear explicitly in the jet and soft functions. Let us clarify this relevant point. Loop corrections to the amplitude $V^{\mu}(p_1, p_2)$ in general contain soft and collinear divergences, in case of massless fermions, and just soft divergences, in case of massive fermions, as considered here. Calculating $V^{\mu}(p_1, p_2)$ by means of the method of regions generates spurious singularities within each region, such that the original singularities are reproduced only after the sum of all regions has been taken. At one loop – and as we will see in the next chapter also for two-loops – the massive form factors receive contributions from the hard, collinear and anticollinear regions. We would like soft singularities to be associated to the soft function $S(\beta_1 \cdot \beta_2)$, however, the latter corresponds to the contribution one would obtain from the soft regions, which is known to be scaleless. The standard interpretation of scaleless regions in dimensional regularization is that one has soft and ultraviolet divergences cancelling each other, such that $1/\epsilon_{\rm IR} - 1/\epsilon_{\rm UV} = 0$. Conventionally, UV poles are removed from the soft function, and inserted back into the hard function which becomes finite. The soft function then contains the leftover infrared divergence, and it is a pure counterterm. Given the definitions for the soft function S and the jet functions J_f and $J_{\bar{f}}$, soft and collinear poles appear in all three functions and are double-counted. For this reason they need to be removed from either the soft function or the jet functions. This is achieved in Eq. (6.67) by dividing with $\mathcal{J}_f$ and $\mathcal{J}_{\bar{f}}$.

Now, in this thesis we are mostly interested to check that the jet functions appearing at subleading power are able to reproduce the contribution given by the collinear and anti-collinear regions. We aim to reproduce the factorization theorem in Eq. (6.67) (and its generalization at subleading power, to be discussed) in its "bare" form, i.e., before soft (and collinear) singularities are reshuffled into pure-counterterm soft and eikonal jet functions. For the leading power contribution this implies that we can write the factorization formula as

$$V_\mu^{\rm LP}(p_1, p_2) = J_f^b(p_1) \otimes H_\mu^b(p_1^+, p_2^-) \otimes J_{\bar{f}}^b(p_2), \tag{6.70}$$

where the index b, for "bare", means that no reshuffling of soft and collinear singularities has been considered. In what follows we will always intend a factorization theorem as written in Eq. (6.70), and drop the index b for simplicity.

This concludes the discussion of the LP factorization formula, Eq. (6.18). Before we turn to the NLP factorization formula, Eq. (6.19), let us summarize the strategy we used in this section to verify the LP factorization formula:

1. First expand the form factors in momentum regions. As said before, some of the jet functions appearing in the NLP factorization formula start at two loops. We will therefore consider the two loop form factors and discuss their region analysis in chapter 7.
2. Next, we construct operator matrix elements for the jet functions. We already gave the definitions for the LP jet functions J_f and $J_{\bar{f}}$ in Eqs. (6.50) and (6.51) respectively. In chapter 8, we will propose operator matrix elements for the NLP jet functions.

3. Before we can verify these jet functions, we need to match with the appropriate hard functions. We will also discuss this in chapter 8.
4. Finally, we can compare the resulting factorized expression with the momentum regions. In particular the regions with collinear scaling (c and $\bar{c}$) are a good cross-check for the jet functions.

Chapter 7.

Region analysis of QED massive fermion form factor

This chapter is based on [2].

In the previous chapter, we discussed how IR singularities of Feynman integrals can be analysed. Together with IR power counting, the leading (LP) and subleading contributions to an amplitude can be categorized, with the result up to next-to-leading order in the power counting (NLP) summarised in Fig. 6.3. These diagrams can be cast into the factorization formulas given in Eq. (6.18) for the LP contribution, and Eq. (6.19) for NLP. We then considered the simplest QED process that gives non-trivial contributions to all the jet functions appearing in Eqs. (6.18) and (6.19), namely, the decay of an off-shell photon of invariant mass Q into a massive fermion anti-fermion pair of mass m. We reviewed the LP factorization formula and in particular how this can be varified using the method of regions.

The purpose of this chapter is to provide data that can be used to validate the NLP factorization formula Eq. (6.19). Since some of the jet functions at NLP appear for the first time at NNLO, we consider the two-loop calculation of the massive form factors evaluated within the method of regions. The two-loop result is known [124, 132], and in recent years a lot of effort has been devoted to the calculation of the three loop correction [125, 133–143], although no complete analytic result as yet exists.

It is possible to use geometric methods (see e.g. [144–146]) to reveal all regions contributing to an integral. In the case of the problem at hand we find it is still possible to find all regions contributing up to two loops by straightforward inspection of the propagators in the loops. One advantage of this method is that the regions are directly associated to the scaling of the loop momenta, rather than to the scaling of Feynman parameters, as when geometric methods are used. This will allow us to relate more easily to the factorization formula.

Besides providing more data for the comparison with Eq. (6.19), the calculation carried out in this chapter has intrinsic value of its own. For instance, one feature of the region expansion, which was found in [127, 147, 148], is that, at the level of single integrals, more regions appear at two loops, that were not present in the calculation at one loop. This is problematic for the derivation of factorization theorems valid at all orders in perturbation theory. It is clear that if new momentum modes appear at each order in perturbation theory, no factorization theorem can be expected to be valid to all orders in perturbation theory. However, it was already observed in [149] that, although new regions appear in single integrals at two loops, their contributions cancels when summing all diagrams, i.e., at the level of the form factors. The analysis in [149] considered only the LP terms in the small mass expansion; our calculation shows that the ultra-collinear regions cancel also at NLP, at the level of the form factors. This result gives confidence in the all-order validity of factorization formulae such as Eq. (6.19), whose derivation is based on power counting arguments [25] using the momentum modes appearing at one loop.

Another well-known feature of the method of regions is that expansion of the integrand in certain regions may render the integral divergent, even in dimensional regularization, so that additional analytic regulators are necessary in order to make the integral calculable. We check that this is indeed the case for the massive form factor, starting at two loops. Analytic regulators were already applied in the past to the calculation of single integrals. Here, we need to apply analytic regulators to the calculation of different diagrams, which gives us the opportunity to discuss a few different regulators in detail and verify their consistency by checking that the dependence on the analytic regulator cancels at the level of single integrals, given that the full result does not require analytic regulators.

This chapter is structured as follows. Sec. 7.1 describes the general approach we adopt for the expansion by regions, while Sec. 7.2 presents the corresponding technical details. As will be discussed there, we compute diagrams categorized into three different topologies depending on the flow of the internal momenta, which we denote by A, B and X.[1] The main results are provided in Sec. 7.3, where we list explicit expressions of the form factor specified per region, up to NLP. We conclude and discuss our results in Sec. 7.4, pointing to several interesting subtleties we encountered, which can be relevant for chapter 8 where we discuss the NLP jet functions in more detail.

In App. C and D, we present further technical details related to the use of rapidity regulators and the regional analysis performed in topology X, which is the most challenging of the three topologies.

---

[1] We adopt the definition of topology as given in [150] in the context of IBP reductions for Feynman integrals.

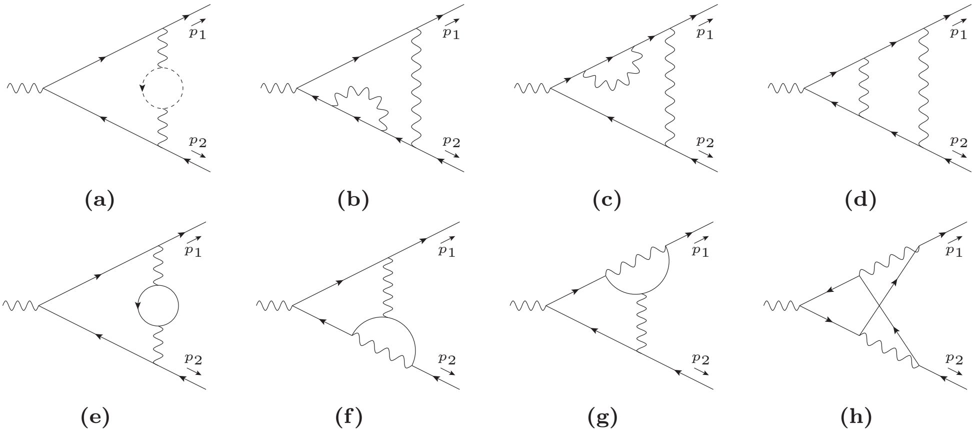

Figure 7.1.: Diagrams that contribute to the massive form factor at two-loop in QED. The dashed lines in diagram (a) represent massless fermions.

Figure 7.2.: Diagrams with a closed fermion loop that cancel in QED by Furry's theorem [151].

7.1. Calculational steps

Here we describe the general approach that we adopt throughout the rest of this chapter, deferring a discussion of technical details to Sec. 7.2.

7.1.1. Diagrams contributing to the two-loop form factor

The diagrams that contribute to the massive form factors, Eq. (6.22), at two-loop are displayed in Fig. 7.1. There are eight diagrams in total, labeled (a) - (h), with p_1 and p_2 denoting the external momenta of the outgoing fermion and anti-fermion respectively. Solid and dashed lines are used to represent massive and massless fermions respectively. Fig. 7.2 suggests there are two additional diagrams, but these diagrams cancel by Furry's theorem [151]. Concerning diagram (e), note that the fermion running inside the loop does not need to correspond to those on the external lines, but here we ignore this possibility for simplicity as it would introduce an additional hierarchy of scales that makes the power counting much more involved. Diagrams (b) and (c), as well as

(f) and (g), are related by exchanging p_1 and p_2 and therefore we expect this symmetry to be present also during an expansion by regions.

In anticipation of our regional analysis, it is convenient to classify diagrams (a) to (h) into three different topologies labeled A, B and X which are distinguished by the flow of their internal momenta.

7.1.2. Topology classification

Starting with diagrams (a)-(d), we note that the Feynman integrals contributing to these diagrams share the following parameterization

$$\begin{aligned} I_{A;\{n_i\}} \equiv \int [dk_1][dk_2] \frac{1}{k_1^{2n_1}} \frac{1}{k_2^{2n_2}} \frac{1}{[(k_1-k_2)^2]^{n_3}} \frac{1}{[(k_1+p_1)^2-m^2]^{n_4}} \frac{1}{[(k_2+p_1)^2-m^2]^{n_5}} \\ \times \frac{1}{[(k_1-p_2)^2-m^2]^{n_6}} \frac{1}{[(k_2-p_2)^2-m^2]^{n_7}} \,, \end{aligned} \tag{7.1}$$

which we define as topology A. In Eq. (7.1), k_1 and k_2 denote the internal loop momenta and the integer n_i represents the generic power associated to the ith propagator.

In a similar way, the integrals associated to diagrams (e), (f) and (g) in Fig. 7.1 can be parameterized by

$$\begin{aligned} I_{B;\{n_i\}}^{b_3,b_4,b_5,b_6} \equiv \int [dk_1][dk_2] \frac{1}{[k_1^2-m^2]^{n_1}} \frac{1}{[k_2^2-m^2]^{n_2}} \frac{\mu_3^{2b_3}}{[(k_1-p_1)^2]^{n_3+b_3}} \\ \times \frac{\mu_4^{2b_4}}{[(k_1+k_2-p_1)^2-m^2]^{n_4+b_4}} \frac{\mu_5^{2b_5}}{[(k_1+p_2)^2]^{n_5+b_5}} \frac{\mu_6^{2b_6}}{[(k_1+k_2+p_2)^2-m^2]^{n_6+b_6}} \frac{1}{[(k_1+k_2)^2]^{n_7}} \,, \end{aligned} \tag{7.2}$$

and this defines topology B. An important distinction compared to topology A is the appearance of the complex numbers b_i associated to propagators $3, 4, 5$ and 6 in Eq. (7.2), where artificial scales μ_i with unit mass dimensions have been introduced on dimensional grounds. The need for the powers b_i can be seen as follows. When expanding in momentum regions, one finds eikonal propagators that contain only the k_i^+ or k_i^- momentum components. As a result, additional divergences may arise from the k_i^+ and k_i^- integrals because the dimensional parameter ϵ regulates only the transverse momentum components $k_{i,\perp}$. Various regulators have been introduced in the literature to tame these rapidity divergences, e.g. space-like Wilson-lines [152], δ regulators [153–157], η regulators [158, 159], exponential regulators [160], analytic regulators [161–164] and pure rapidity regulators [165]. In this thesis, we adopt the analytic regulator [161], meaning that we raise the relevant propagators to complex powers b_i. The rapidity divergences then manifest themselves as poles in b_i, similar to poles in ϵ that one encounters in dimensional regularization. As will be described in greater detail in Sec. 7.2.2, one does not need to add all four regulators b_i simultaneously to regulate the rapidity divergences present in diagrams (e), (f) and (g). However, we do need to make different choices per diagram, and therefore the parameterization in Eq. (7.2) captures all three diagrams at once. Furthermore, we point out that the b_i's do not need to be different; in fact, we will see that only a single regulator is sufficient in topology B. We refer to App. C for more details, as well as for a study on the use of other rapidity regulators. Note that the rapidity divergences show up only as a result of the expansion by regions, since the corresponding full Feynman integral gets fully regularized by the dimensional regulator ϵ alone. This observation provides us with a valuable cross-check: all dependence on b_i must cancel once all regions are combined.

Finally, we come to topology X, which corresponds to diagram (h) and is characterized by the parameterization

$$\begin{aligned} I^{b_3,b_4,b_5,b_6}_{X;\{n_i\}} &= \int [dk_1][dk_2] \frac{1}{k_1^{2n_1}} \frac{1}{k_2^{2n_2}} \frac{\mu_3^{2b_3}}{[(k_2-p_1)^2-m^2]^{n_3+b_3}} \frac{\mu_4^{2b_4}}{[(k_1+k_2-p_1)^2-m^2]^{n_4+b_4}} \\ &\times \frac{\mu_5^{2b_5}}{[(k_1+p_2)^2-m^2]^{n_5+b_5}} \frac{\mu_6^{2b_6}}{[(k_1+k_2+p_2)^2-m^2]^{n_6+b_6}} \frac{1}{[(k_1+k_2)^2]^{n_7}}\,, \end{aligned} \tag{7.3}$$

where again we need $b_i \neq 0$ in order to regulate rapidity divergences that show up once we expand by region.

7.1.3. Summary of technical details

A common approach in the computation of higher order loop diagrams is to reduce the many Feynman integrals to master integrals using integration by parts (IBP) identities. When it comes to calculating these integrals following the method of regions one has two options. Either one first reduces the large number of integrals in each topology, Eqs. (7.1)-(7.3), to master integrals before expanding by regions. However, as we are interested in an expansion up to NLP, the expansion of a master integral into its momentum regions might lead to many additional integrals, so that again a new reduction to master integrals is recommended per momentum region. Or, one might as well first expand by regions and only perform an IBP reduction at the very end of the calculational steps. Ultimately, these two ways are equivalent and cannot lead to different final results. We will discuss these alternative approaches further in Sec. 7.2.1, where we also point out the subtleties that enter while expanding the topologies in different momentum regions.

Another difficulty we encountered concerns the analytic regulators that we added to topologies B and X, Eqs. (7.2) and (7.3). Although the analytic regulator is a convenient regulator when computing Feynman integrals, it has the downside that the usual IBP reduction programs cannot handle non-integer powers of the propagators. To the best of our knowledge, only `Kira` [166] is suitable for this, which we therefore adopt as our standard IBP reduction program. In topology A, which does not require rapidity regulators, we also use `LiteRed` [167] as an independent crosscheck of our results.

As discussed in Sec. 6.2.1, the one-loop form factor contains just three momentum regions: hard, collinear and anti-collinear. However, the number of momentum regions is much larger at the two-loop level. First, the two loop momenta k_1 and k_2 can have different scalings, which already gives nine possibilities that combine the hard, collinear and anti-collinear momentum regions. Second, we find the appearance of two new momenta scalings: ultra-collinear and ultra-anti-collinear; the contribution from such regions was already observed in [148]. Finally for topology B and X, new regions might appear when one shifts the loop momenta *before* expanding in regions. Although such a shift leaves the full integral invariant, it can lead to additional regions when expanding.

A summary of our work flow is given in Fig. 7.3, which shows the steps we have discussed so far. Not shown is the final step, which consists of verifying whether the small mass limit as given in [124, 168] is reproduced after collecting all regions.

7.2. Region expansions

Having presented the computational scheme in Sec. 7.1, we now move to the technical details of the calculation of the integrals in topology A, B and X using the method of regions. An important remark from the outset concerns the distinction between the regions present at the level of the diagrams in Fig. 7.1 on the one hand, and the integral level on the other hand; these do not necessarily coincide as non-vanishing regions at the integral level can cancel when combined to constitute the diagrams. The results presented in this section should be understood at the integral level.

We shall now discuss topology A, B and X in turn. For each topology, we analyze first the associated regions (at the integral level), followed by a discussion of its IBP relations. At the end of each topology subsection, we provide a brief summary of the aspects that enter the computation of the momentum regions.

7.2.1. Region expansion of topology *A*

As explained in Sec. 6.2.1, it is convenient to use light-cone coordinates, Eq. (6.34), to identify the various momentum regions that lead to non-vanishing contributions. At one-loop we found that only momentum modes h, c and $\bar{c}$ contributed. This

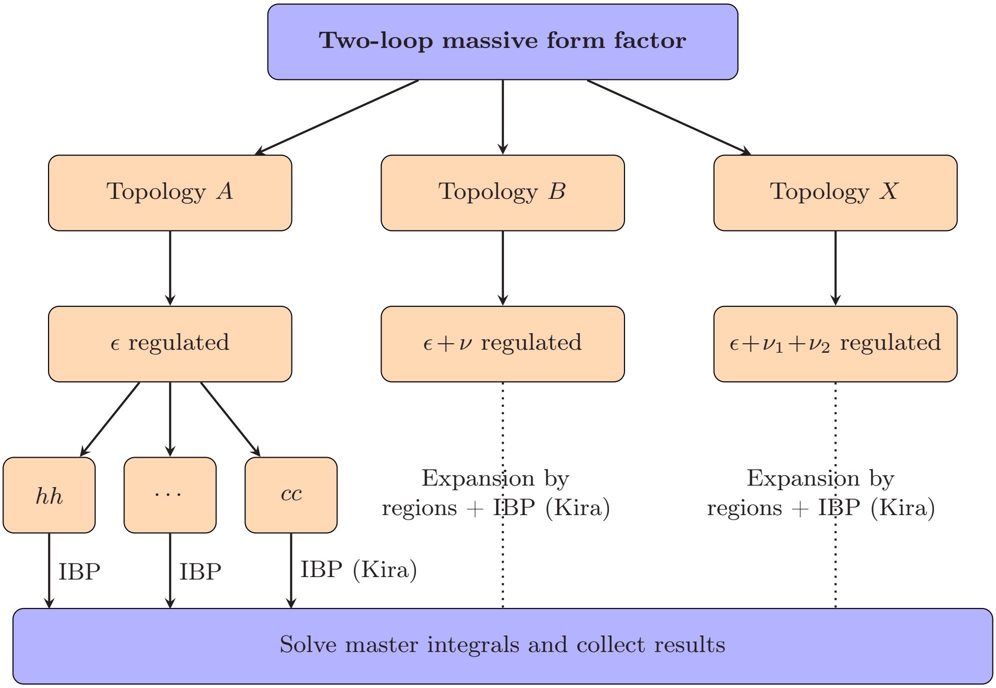

Figure 7.3.: Flow diagram displaying the pipeline of our NLP region analysis of the QED massive form factor. The diagrams in Fig. 7.1 are classified into either topology A, B or X depending on their momentum flow. We regulate each topology using dimensional regularization, denoted by ϵ, plus additional rapidity regulators, denoted ν, in case of topology B, and ν_1, ν_2 in case of topology X, as it turns out to need two rapidity regulators. For each topology, we expand the relevant integrals by regions and then reduce the result into a simpler set of master integrals with IBP reduction using `Kira` [166].

picture changes as soon as we move to the two-loop level where we receive additional contributions coming from momentum modes such as uc and $\overline{uc}$, as defined in Eq. (6.36). In total, there are 25 possible combinations of momentum modes at the two-loop level. However, many combinations vanish because they lead to scaleless integrals. For the Feynman integrals contributing to diagrams (a)-(d) we find 11 non-vanishing regions: hh, cc, $\bar{c}\bar{c}$, $c\bar{c}$, $\bar{c}c$, ch, hc, $\bar{c}h$, $h\bar{c}$, $uc\bar{c}$ and $\overline{uc}c$, with the momentum flow as indicated in Tab. 7.1 on page 186. Even though the power expansion for the momentum modes is straightforward using e.g. Tab. 6.1, the resulting integrals can in general become quite involved. Let us illustrate this by highlighting several subtleties that enter here.

The first subtlety we want to discuss concerns the interplay between the usual IBP reduction and the region expansion. To this end, we consider as an example the

hh region of topology A, Eq. (7.1), which up to LP reads

$$I_A\Big|_{hh} = \int [dk_1][dk_2] \frac{1}{k_1^{2n_1}} \frac{1}{k_2^{2n_2}} \frac{1}{[(k_1-k_2)^2]^{n_3}} \frac{1}{[k_1^2+k_1^- p_1^+]^{n_4}} \frac{1}{[k_2^2+k_2^- p_1^+]^{n_5}} \\ \frac{1}{[k_1^2-k_1^+ p_2^-]^{n_6}} \frac{1}{[k_2^2-k_2^+ p_2^-]^{n_7}} + \mathcal{O}\left(\lambda^2\right) , \tag{7.4}$$

while many additional terms occur beyond LP. To see this, we expand the fourth propagator of Eq. (7.1) in the hh-region up to NLP

$$\begin{aligned} \frac{1}{(k_1+p_1)-m^2} &= \frac{1}{k_1^2+k_1^- p_1^+} - \frac{k_1^+ p_1^-}{[k_1^2+k_1^- p_1^+]^2} + \mathcal{O}\left(\lambda^4\right) \\ &= \frac{1}{k_1^2+k_1^- p_1^+} - \frac{m^2}{\hat{s}} \frac{k_1^2 - [k_1^2 - k_1^+ p_2^-]}{[k_1^2+k_1^- p_1^+]^2} + \mathcal{O}\left(\lambda^4\right) . \end{aligned} \tag{7.5}$$

In the second line of Eq. (7.5) we used the identity $p_1^- = \left(m^2/\hat{s}\right) p_2^-$ to rewrite the power expansion in terms of the first, fourth and sixth LP (inverse) propagators appearing in Eq. (7.4). Typically, one can perform an IBP reduction on the full integrals for a given diagram and then expand by regions. However, Eq. (7.5) shows that after the regions expansion, the number of integrals increases considerably again beyond LP. Therefore, a new IBP reduction applied to the hh-region is called for. Instead, one might just as well expand the full integrals in the momentum region, and perform a single IBP-reduction on region integrals at the end.

As a second subtlety, note that in order to set up the IBP reduction for the expanded topology, the LP propagators of Eq. (7.4) appear in the last line of Eq. (7.5). Similarly, as shown for the fourth propagator in Eq. (7.5), we can rewrite the power expansion of the fifth, sixth and seventh propagator in terms of the corresponding LP propagators, where we can use the identity $p_2^+ = \left(m^2/\hat{s}\right) p_1^+$ for the sixth and seventh propagator. This implies that Eq. (7.4) defines a closed topology for the hh-region up to arbitrary order in the power expansion. This is particularly useful when applying IBP relations, because it leads to the smallest number of master integrals to solve. Along similar lines, the full power expansion of the cc and $\bar{c}\bar{c}$ region can also be written in terms LP propagators only.

Another subtlety concerns regions where the loop momenta k_1 and k_2 scale according to different momentum modes, which requires extending the expanded topology by an additional propagator. For example, consider the expansion of the denominator of the third propagator in Eq. (7.1) in the $\bar{c}c$ region

$$(k_1 - k_2)^2 = \underbrace{k_1^2 - 2k_{1,\perp} \cdot k_{2,\perp} + k_2^2}_{\sim\lambda^2} - \underbrace{k_1^- k_2^+}_{\sim 1} - \underbrace{k_1^+ k_2^-}_{\sim\lambda^4} \,. \tag{7.6}$$

The perpendicular components in Eq. (7.6) cannot be rewritten in terms of the LP propagators from Eq. (7.1). Rather than adding $-2k_{1,\perp} \cdot k_{2,\perp}$ to the $\bar{c}c$ topology, we instead rewrite this as

$$-2k_{1,\perp} \cdot k_{2,\perp} = -2k_1 \cdot k_2 + k_1^+ k_2^- + k_1^- k_2^+ \,, \tag{7.7}$$

and add $[-2k_1 \cdot k_2]^{-n_8}$ as an additional propagator to the $\bar{c}c$ topology. The same logic can be applied to other regions where k_1 and k_2 scale differently. Eq. (7.7) shows that standard propagators may turn into non-standard propagators of the form $k_1^- k_2^+$ which cannot be given directly as input to the IBP programs that are currently on the market. We treat these in the following way, which we will refer to as a loop-by-loop approach. First, we rewrite $k_1^- k_2^+$ as $k_1 \cdot (k_2^+ n^-)$ and perform an IBP reduction over k_1 while considering k_2 and $k_2^+ n^-$ as external momenta similar to p_1 and p_2. By doing so, the integrals over k_1 get reduced to a smaller set of integrals. Next, we repeat the first step but now switching the roles of k_2 and k_1, i.e. we perform IBP over k_2 rewriting $k_1^- k_2^+$ as $(k_1^- n^+) \cdot k_2$, while considering k_1 and $k_1^- n^+$ as external momentum. Again, the number of integrals over k_2 gets reduced. The combination of both IBP reductions over k_1 and k_2 leaves us with a smaller set of (two-loop) integrals to solve.

Finally, one must be careful when dealing with regions where one of the loop momenta has hard scaling and the other has (anti-)collinear scaling. As discussed above, one can define a closed topology containing the LP propagators and the addition of an eighth propagator $[-2k_1 \cdot k_2]^{-n_8}$. However, because a loop-by-loop IBP reduction may lead to new propagators that are not part of the expanded topology, adding these propagators to the topology does not work as this leads to an over-determined topology. A possible solution, which we used for topology A, is to perform the IBP reduction over the loop with hard loop momentum and then compute the master integrals. After that, the left-over one-loop integrals with (anti-)collinear loop momentum will be simple enough to calculate directly.

Let us summarize our strategy for topology A:

1. Expand Eq. (7.1) in a given momentum region and rewrite subleading corrections in terms of the LP propagators.

2. Use IBP relations that can either handle both loops over k_1 and k_2 at the same time or adopt a loop-by-loop approach by introducing a non-standard additional propagator $[-2k_1 \cdot k_2]^{-n_8}$.
3. Solve the resulting master integrals and repeat steps 1-3 for the remaining momentum regions.

7.2.2. Region expansion of topology *B*

As we already stated in Sec. 7.1, the Feynman integrals needed to calculate diagrams (e), (f) and (g) in Fig. 7.1 can be classified as part of topology B, defined in Eq. (7.2). More specifically, all integrals obtained from diagram (e) have the form $I^{b_3,b_4,b_5,b_6}_{B;\{n_i\}}$ with both $n_3 \leq 0$ and $n_5 \leq 0$, the integrals of diagrams (f) satisfy $n_3 \leq 0$, while the integrals of diagrams (g) correspond to $n_5 \leq 0$. The integrals of diagrams (e) thus belong to a subclass of the integrals associated to diagrams (f) and (g). Consequently, the regions contributing to diagram (e) form a subset of those contributing to diagram (f) and (g). In addition, the integrals of diagram (f) and diagram (g) can be related to each other by the transformation $p_1 \leftrightarrow p_2$, $k_1 \leftrightarrow -k_1$ and $k_2 \leftrightarrow -k_2$. In the following we will discuss the regions obtained in diagrams (e), (f) and (g).

Diagram (e)

Starting with the integrals of diagram (e), we find that the regions hh, hc, $\bar{c}h$, cc and $\bar{c}\bar{c}$ contribute.[2] Of these, the first three regions are free of rapidity divergences, so that we can set the analytic regulators $b_i = 0$ in Eq. (7.2) either at the beginning or at the end of the calculation (both giving to the same results). Taking $b_i = 0$ from the start, we can treat these three regions similarly to the corresponding regions in topology A, as we discussed in Sec. 7.2.1. However, there are two other regions, the cc and $\bar{c}\bar{c}$ regions, that do have rapidity divergences, so that here the regulators b_i must be kept. fortunately, we do not need to include four regulators b_i in the calculation. Because $n_3 \leq 0$ and $n_5 \leq 0$ we can safely take $b_3 = 0$ and $b_5 = 0$ at the beginning of the calculation. Interestingly, we find that we cannot take $b_4 = b_6$ to regulate the rapidity divergences of all integrals[3], although taking either $b_4 = 0$ or $b_6 = 0$ is possible. We therefore call $b_6 = \nu$ and $b_3 = b_4 = b_5 = 0$ with corresponding scale $\mu_6 = \tilde{\mu}$ as our scheme to regulate the rapidity divergences in both the cc and $\bar{c}\bar{c}$ regions

---

[2] Note that the $h\bar{c}$-region and hc-region, as well as the $\bar{c}h$-region and ch-region are equivalent for this diagram. Furthermore, these two regions only appear at the Feynman integral level, but cancel at the diagram level as will become clear in Sec. 7.3. Similar cancellations occur for diagrams (f), (g) and (h).

[3] Indeed if we take $b_4 \neq b_6$, the integrals are proportional to $\Gamma(b_4 - b_6)$. A similar situation was encountered in Ref. [169].

of diagram (e). Note that this particular choice breaks the symmetry between the cc and $\bar{c}\bar{c}$ regions. Nevertheless, after combining all of the above five regions, our result up to NLP for each integral, has no rapidity divergence. Moreover we find agreement with the corresponding result obtained by expanding the full result in Ref. [132, 170] in the small mass limit.

Diagram (f)

The regions needed to calculate the integrals of diagram (f) are more complicated. First, the integrals of diagram (f) satisfy $n_3 \leq 0$. Similar to diagram (e), we encounter rapidity divergences in the cc and $\bar{c}\bar{c}$ regions, and in order to handle those we take $b_3 = b_4 = 0$ and $b_5 = b_6 = \nu$ with corresponding scale $\mu_5 = \mu_6 = \tilde{\mu}$. However, we find that the rapidity divergences do not cancel after summing the cc and $\bar{c}\bar{c}$ regions. We therefore expect that there is at least one more region with rapidity divergences.

Indeed, in addition to the five regions for diagram (e) (hh, hc, $\bar{c}h$, cc and $\bar{c}\bar{c}$), we find three additional contributing regions, although it is not straightforward to define these three regions in momentum space using the definition for $I^{b_3,b_4,b_5,b_6}_{B;\{n_i\}}$ in Eq. (7.2). We exploit the freedom to shift $k_2 \to -k_1 - k_2$ to so that topology B can be written as:

$$I'^{\,b_3,b_4,b_5,b_6}_{B;\{n_i\}} = \int [dk_1][dk_2] \frac{1}{[k_1^2 - m^2]^{n_1}} \frac{1}{[(k_1+k_2)^2 - m^2]^{n_2}} \frac{\mu_3^{2b_3}}{[(k_1-p_1)^2]^{n_3+b_3}} \times \frac{\mu_4^{2b_4}}{[(k_2+p_1)^2 - m^2]^{n_4+b_4}} \frac{\mu_5^{2b_5}}{[(k_1+p_2)^2]^{n_5+b_5}} \frac{\mu_6^{2b_6}}{[(k_2-p_2)^2 - m^2]^{n_6+b_6}} \frac{1}{k_2^{2n_7}} . \tag{7.8}$$

We stress that $I^{b_3,b_4,b_5,b_6}_{B;\{n_i\}}$ and $I'^{\,b_3,b_4,b_5,b_6}_{B;\{n_i\}}$ are equivalent *before* region expansion due to the Lorentz invariance, but this is not always the case for a given region, i.e. after expansion. For example, in the cc-region, the loop momenta k_1 and k_2 have the same momentum scaling and as a result, the shift $k_2 \to -k_1 - k_2$ does not change the scale of the propagators nor the results of the integrals. However, in the hc-region, the shift $k_2 \to -k_1 - k_2$ changes the leading behavior of the second, fourth, sixth and seventh propagator of $I^{b_3,b_4,b_5,b_6}_{B;\{n_i\}}$ and as a result we find a different hc-region through this shift. In general, one must be aware that different momentum flows can lead to a different scaling of the leading term in the propagator and uncover additional regions as a result. This illustrates the alternative viewpoint that regions correspond to the scaling of the leading term in the propagators rather than the loop momenta itself, a reasoning which connects also to the geometric approach in parameter space. However, in view of factorization, it is more convenient to still think about the scaling of the

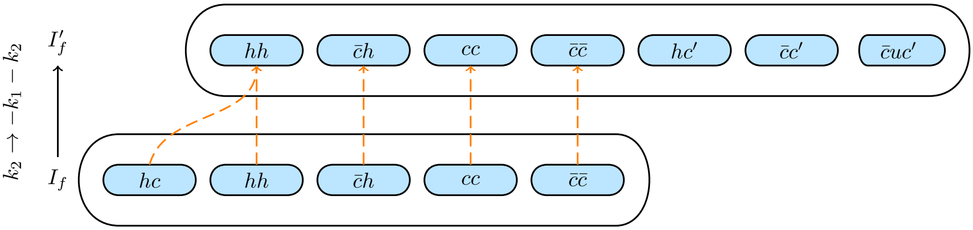

Figure 7.4.: Momentum regions that contribute to the integrals of diagram (f) before and after applying the transformation $k_2 \to -k_1 - k_2$, corresponding to I_f and I'_f respectively. The dashed arrows represent how the regions in I_f transform accordingly, e.g. the original hc-region maps onto a new hh-region after the collinear mode k_2 mixes with the dominant hard scale associated to k_1. Note how two previously uncovered regions, $\bar{c}c'$ and $\bar{c}uc'$, and a different hc-region appear after the shift, where the $\bar{c}c'$-region removes the rapidity divergences present in the cc and $\bar{c}\bar{c}$ regions. Regions that remain invariant are displayed on top of each other, while additional regions are shifted outwards so that all regions are found by collapsing the top row onto its base I_f.

momentum modes of the loop momenta, rather than the scaling of the leading term in the propagators.

Based on the new definition ${I'}^{b_3,b_4,b_5,b_6}_{B;\{n_i\}}$, we find three additional regions: $\bar{c}c'$, hc' and $\bar{c}uc'$, as illustrated in Fig. 7.4. Besides a modified hc-region, we also find $\bar{c}c'$ and $\bar{c}uc'$ as complete new regions. Apart from these three regions, we do not need other regions based on ${I'}^{b_3,b_4,b_5,b_6}_{B;\{n_i\}}$, as these are the same as the corresponding regions given based on $I^{b_3,b_4,b_5,b_6}_{B;\{n_i\}}$. The appearance of the $\bar{c}uc'$-region for example can be understood as follows (the $\bar{c}c'$-region following similarly). First, note that the last propagator, $1/k_2^2$, in Eq. (7.8) has ultra-collinear scaling in the $\bar{c}uc'$-region. Having found this region in this way, it is also clear that we could not have found it in the original momentum routing. First, it is not possible to select scalings of both loop momenta such that the last momentum factor is ultra-collinear. Second, it is only possible to make the last propagator have an ultra-collinear scaling if one considers the $ucuc$-region, which leads to scaleless integrals. This is because the masses and external momenta in the propagators of Eq. (7.2) have harder scales than the loop momentum with an ultra-(anti-)collinear mode, thus kinematic configurations where one of the loop momenta is ultra-(anti-)collinear are always scaleless. In other words, in the parametrization of Eq. (7.2), the propagator $(k_1 + k_2)^2$ can produce a leading term with uc scaling only if k_1 and k_2 are large and opposite, so that they almost cancel. Thus this ultra-collinear kinematic configuration can only be revealed by the shift leading to the parametrization in Eq. (7.8). A similar circumstance has been discussed in Ref. [130] at one-loop, where a soft region arises in the kinematic configuration in which the loop momentum is large and opposite to an external momentum, such that their sum is soft. In general, revealing such regions by means of momentum shifts in order to find the scaling of the leading term may become ever more intricate at higher loops, due to an increasing number of loop momenta that can conspire to yield new regions. We can still validate our results in another way though. Combining the new $\bar{c}c'$-region with the cc-region and $\bar{c}\bar{c}$-region from before the shift, we remove all the rapidity divergences belonging to the integrals of diagram (f). Furthermore, combining all of the above eight regions, we obtain the result up to NLP for each integral of diagram (f), reproducing the corresponding result found by expanding the exact result in Refs. [132, 170] in the small mass limit.

Diagram (g)

All the Feynman integrals for diagram (g) fall in the category of Eq. (7.2) with $n_5 \leq 0$. Diagram (g) is related to diagram (f) by the transformation $p_1 \leftrightarrow p_2$, $k_1 \leftrightarrow -k_1$ and $k_2 \leftrightarrow -k_2$. Naturally the rapidity regulators should also be exchanged: $b_3 \leftrightarrow b_5$ and $b_4 \leftrightarrow b_6$. Thus we choose as rapidity regulators $b_3 = b_4 = \nu$ and $b_5 = b_6 = 0$ with corresponding scales $\mu_3 = \mu_4 = \tilde{\mu}$. All the regions from diagram (f), corresponding to the hh, $h\bar{c}$, ch, cc and $\bar{c}\bar{c}$, $c\bar{c}'$, $h\bar{c}'$ and $c\overline{uc}'$ regions can then be copied.

Remarks

Above we discussed how one can apply the rapidity regulators and find all the contributing regions per diagram. However, the calculation of the integrals in each region is not always straightforward and we therefore finish the discussion of topology B with a few technical remarks on these calculations.

First, regarding regions without rapidity divergences, such as the hh, hc and $c\overline{uc}'$ regions, we can safely set $\nu = 0$ and calculate the resulting integrals in each region following the same methods as for topology A. We emphasize however that in topology B (and also in topology X below) for the region including a hard loop momentum and a (anti-)collinear momentum, one should be quite careful when calculating the expanded integrals. Specifically, one should first expand the full integral $I_{B;\{n_i\}}^{b_3,b_4,b_5,b_6}$ into regions, e.g. the hc-region, and only then perform IBP reduction on the part with hard loop momentum. Then $I_{B;\{n_i\}}^{b_3,b_4,b_5,b_6}$ will be expressed as a linear combination of one-loop integrals – which we generically denote by I_i^c – that include only the collinear-mode loop momentum. Although in the hc-region $I_{B;\{n_i\}}^{b_3,b_4,b_5,b_6}$ is free of rapidity divergences and the b_i have been set to zero, we find that rapidity divergences reappear in some of these I_i^c. The rapidity divergences are however expected to cancel among different I_i^c leading to a finite $I_{B;\{n_i\}}^{b_3,b_4,b_5,b_6}$. In this particular case, one should choose an auxiliary regulator to regulate I_i^c. The poles in this auxiliary regulator will then cancel to yield a finite $I_{B;\{n_i\}}^{b_3,b_4,b_5,b_6}$. Alternatively, one can rearrange the integrands of I_i^c at the level of Feynman parametrization so that the integrations over the Feynman parameters are well-defined and finite without introducing extra regulators.

We use the first method to calculate the integrals in the region including a hard loop momentum and a (anti-)collinear momentum, which is more convenient than the second one when dealing with a large number of such integrals. We also use the second method to calculate several integrals, always leading to the same results. Note that such complexity does not appear in topology A.

Then, for regions with rapidity divergences, we first expand the integrals with the rapidity regulator ν and perform IBP reduction using `Kira` to obtain a set of master integrals in each region. As a result, we only need to calculate the master integrals with up to 2-fold Mellin-Barnes (MB) representations after expanding in the rapidity regulator ν and the dimensional regulator ϵ to the required order.

Before moving to the last topology, we summarise the subtleties we have encountered in topology B:

1. Shifts in the loop momenta that leave the full integral invariant, can lead to additional regions nonetheless. These are needed to find all regions, and remove all rapidity divergences in a consistent manner.
2. The introduction of rapidity regulators requires detailed inspection on a case by case basis depending on the given diagram.
3. One must expand in ν before ϵ as the rapidity regulator is a secondary regulator.

7.2.3. Region expansion of topology X

The Feynman integrals needed for the last diagram in Fig. 7.1, diagram (h), belong to a new topology we denote as X, reflecting the shape of (h), defined in Eq. (7.3) with $n_7 \leq 0$. Due to a new pattern of rapidity divergences, which we will see when analysing the cc and $\bar{c}\bar{c}$ regions, X is the most complicated of the three topologies.

Focusing on the $\bar{c}\bar{c}$-region first, it suffices to set $b_3 = b_4 = \nu_1$ and $b_5 = b_6 = 0$ in order to regulate the corresponding rapidity divergence, but this choice does not regulate the rapidity divergence in the cc-region. However, we note that the integrand in Eq. (7.3) is invariant under exchanging $p_1 \leftrightarrow p_2$, $k_1 \leftrightarrow -k_1$ and $k_2 \leftrightarrow -k_2$, which leads to a symmetry between the cc and $\bar{c}\bar{c}$-regions. Motivated by this symmetry one may thus set $b_3 = b_4 = 0$ and $b_5 = b_6 = \nu_2$ to regulate the rapidity divergence in the cc-region. So in order to regulate *simultaneously* the rapidity divergences in the cc-region and the $\bar{c}\bar{c}$-region, we choose $b_3 = b_4 = \nu_1$ and $b_5 = b_6 = \nu_2$. The associated

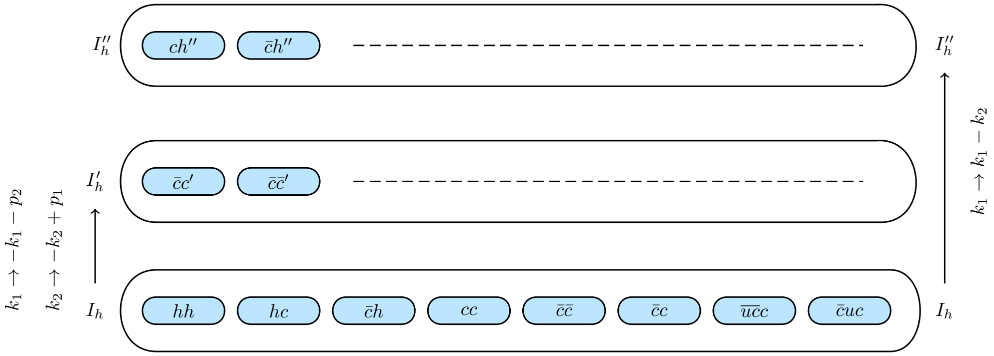

Figure 7.5.: Similar to Fig. 7.4, now displaying the momentum shifts performed in diagram (h) of topology X. Two shifts starting from I_h are needed, to I'_h and I''_h, in order to uncover all regions. In contrast to Fig. 7.4, we only display new regions with respect to parametrization I_h.

scales we shall denote by $\tilde{\mu}_1$ and $\tilde{\mu}_2$ for ν_1 and ν_2 respectively. Note that $\nu_1 = \nu_2$ leads to an unregulated divergence, similar to what we saw in topology B for diagram (e).

According to the definition of topology X as given in Eq. (7.3), together with the choice of rapidity regulators ν_1 and ν_2 as argued above, we find 8 regions in total: hh, hc, $\bar{c}h$, $\overline{uc}c$, $\bar{c}uc$, cc, $\bar{c}\bar{c}$ and $\bar{c}c$. The rapidity divergences only appear in the last three regions. However, their sum does not yet lead to a finite result in the rapidity regulators ν_1 and ν_2, as can for example be checked for the integral with $n_i = 1$ for $i \leq 6$ and $n_7 = 0$, which is discussed in more detail in App. D.1. This requires us to look for other regions with rapidity divergences, and this we do again by redefining the loop momenta. Let us adopt the shifts $k_1 \to -k_1 - p_2$ and $k_2 \to -k_2 + p_1$ to redefine topology X as

$$\begin{aligned} I'^{\,\nu_1,\nu_1,\nu_2,\nu_2}_{X;\{n_i\}} &= \int [dk_1][dk_2] \frac{1}{(k_1+p_2)^{2n_1}} \frac{1}{(k_2-p_1)^{2n_2}} \frac{1}{[k_2^2-m^2]^{n_3+\nu_1}} \\ &\times \frac{\mu_1^{2\nu_1}}{[(k_1+k_2+p_2)^2-m^2]^{n_4+\nu_1}} \frac{\mu_1^{2\nu_1}}{[k_1^2-m^2]^{n_5+\nu_2}} \frac{\mu_2^{2\nu_2}}{[(k_1+k_2-p_1)^2-m^2]^{n_6+\nu_2}} \frac{\mu_2^{2\nu_2}}{[(k_1+k_2)^2]^{n_7}} \,. \end{aligned} \tag{7.9}$$

Note that the momentum in the last propagator should be $(k_1 + k_2 - p_1 + p_2)$ rather than $(k_1 + k_2)$ according to the above shifts $k_1 \to -k_1 - p_2$ and $k_2 \to -k_2 + p_1$. However, this does not affect the analysis of the regions in diagram (h) as all the integrals associated to diagram (h) satisfy $n_7 \leq 0$, meaning that $(k_1 + k_2 - p_1 + p_2)^2$ appears in the numerator. After shifting, the integral $I^{\nu_1,\nu_1,\nu_2,\nu_2}_{X;\{n_i\}}$ with $n_7 < 0$ can always be rewritten as a linear combination of $I'^{\,\nu_1,\nu_1,\nu_2,\nu_2}_{X;\{n'_i\}}$.

Adopting definition ${I'}^{\,\nu_1,\nu_1,\nu_2,\nu_2}_{X;\{n_i\}}$, we find two new regions: the cc'-region and the $\bar{c}\bar{c}'$-region, as shown in Fig. 7.5. In these momentum regions, $(k_1+k_2)^2$ scales homogeneously, while $(k_1+k_2-p_1+p_2)^2$ does not, which provides another reason to choose the last propagator in the form of Eq. (7.9). We have checked that the rapidity divergences cancel after combining the cc $\bar{c}\bar{c}$, $\bar{c}c$, cc' and $\bar{c}\bar{c}'$ regions. However, to obtain the correct result after combining all regions, we find that we need yet another two regions. As it turns out these are the ch''-region and the $\bar{c}h''$-region, without rapidity divergences. These can be revealed by adopting the following parametrization

$$\begin{aligned} {I''}^{\,\nu_1,\nu_1,\nu_2,\nu_2}_{X;\{n_i\}} &= \int [dk_1][dk_2] \frac{1}{(k_1-k_2)^{2n_1}} \frac{1}{k_2^{2n_2}} \frac{\mu_1^{2\nu_1}}{[(k_2-p_1)^2-m^2]^{n_3+\nu_1}} \frac{\mu_1^{2\nu_1}}{[(k_1-p_1)^2-m^2]^{n_4+\nu_1}} \\ &\quad\times \frac{\mu_2^{2\nu_2}}{[(k_1-k_2+p_2)^2-m^2]^{n_5+\nu_2}} \frac{\mu_2^{2\nu_2}}{[(k_1+p_2)^2-m^2]^{n_6+\nu_2}} \frac{1}{k_1^{2n_7}}\,, \end{aligned} \tag{7.10}$$

as obtained from $I^{\nu_1,\nu_1,\nu_2,\nu_2}_{X;\{n_i\}}$ after shifting $k_1 \to k_1 - k_2$, as also shown in Fig. 7.5. Combining all of the above 12 regions (hh, hc, $\bar{c}h$, $u\bar{c}c$, $\bar{c}uc$, cc, $\bar{c}\bar{c}$, $\bar{c}c$, cc', $\bar{c}\bar{c}'$, ch'' and $\bar{c}h''$) we indeed obtain the result up to NLP for each integral of diagram (h), consistent with expanding the full result in Ref. [132, 170] in the small mass limit[4].

Compared to the topology A and B, the calculation of the integrals in topology X is more involved due to the appearance of two different rapidity regulators ν_1 and ν_2. As remarked already at the end of Sec. 7.3.2, one should expand the integrals first in the rapidity regulator(s) followed by the dimensional regulator ϵ, as the ν_i are secondary regulators. However, in the case of more than one rapidity regulator, we need to further fix the expansion order in the ν_i. Here we choose to expand in ν_1 before expanding in ν_2. We emphasize that the expansion order in ν_i does not affect the final results once all regions are combined as the rapidity divergences cancel. Of course, additional rapidity regulators make the IBP reduction more complex. Even though

---

[4] The identification of the missing contribution may depend on the momentum shift considered. In the case at hand, the shift $k_1 \to k_1 - k_2$ applied onto $I^{\nu_1,\nu_1,\nu_2,\nu_2}_{X;\{n_i\}}$ leads to the missing contribution being identified with the ch''- and the $\bar{c}h''$-regions. Note, however, that we always have the freedom to apply two further shifts $k_1 \to k_1 + p_1$ and $k_2 \to k_2 - p_2$ onto ${I''}^{\,\nu_1,\nu_1,\nu_2,\nu_2}_{X;\{n_i\}}$ which make the contribution due to the ch''- and $\bar{c}h''$ region unchanged, respectively. However, in this case, the ch'' and $\bar{c}h''$ can also be regarded as two $sh\,h''$ regions (where by sh we indicate the semi-hard scaling introduced in Eq. (6.37)) without changing the scaling of each propagator and the final results of the integrals. From the point of view of a factorization analysis, the second shift is more meaningful: this is because interpreting the new regions as ch''- and $\bar{c}h''$-regions, one has a momentum configuration in which there is a lightlike edge with both endpoints in the hard subgraph, which does not conform with the Coleman-Norton interpretation, which is instead consistent with the $sh\,h''$ regions interpretation. We refer to section 2.3 of [146] for further discussions. Here we do not explore this issue further, because, as indicated in Table 7.3, these additional regions (either identified as ch''- and $\bar{c}h''$-regions or $sh\,h''$-regions) do not contribute at the form factor level. From the point of view of a factorization analysis, this indicates that the relevant regions at two loops are still just the hard, collinear and anticollinear regions identified at one loop, which is consistent with the power counting analysis discussed in the previous chapter.

the rapidity divergences are fully regularized by ν_1 (ν_2) in the $\bar{c}\bar{c}$-region (cc-region), meaning that we can choose $\nu_2 = 0$ ($\nu_1 = 0$), this is not the case in the cc'-region and $\bar{c}\bar{c}'$-region, where both ν_1 and ν_2 are necessary.[5]

Summarising the subtleties we encountered in topology X, we find that

1. In contrast to topology B, topology X requires two unique rapidity regulators ν_1 and ν_2. One must adopt a consistent order with respect expanding in ν_1 and ν_2.
2. We find altogether 12 regions, some of which only show up after rerouting the internal momenta.

7.3. Results

We now present the main results of this chapter and list the various momentum regions that contribute to the two-loop massive form factors F_1 and F_2. We switch viewpoint from Sec. 7.2 and emphasize that the results here are at the level of the diagrams rather than integrals. Recall that some momentum regions may not contribute at the diagrammatic level even though they contribute at the integral level. An overview of the various regions that contribute to each diagram is provided below in Tables 7.1-7.3 for topologies A, B and X respectively.

As discussed in Sec. 7.2, diagrams belonging to topology B and X may require the introduction of rapidity regulators. Consequently, the corresponding diagrams acquire poles in ν (in case of topology B), and poles in ν_1 and ν_2 (in case of topology X). Because the full form factor is independent of any rapidity divergences, the regulator dependence must cancel after combining all regions; we check this explicitly in the results we provide below. In this respect, two remarks are in order.

First, as we already observed in the one-loop result given by Eqs. (6.40) and (6.41), it is natural to factor out the overall scaling per momentum region, i.e. $\left(-\mu^2/\hat{s}\right)^\epsilon$ and $\left(\mu^2/m^2\right)^\epsilon$ for each hard and (anti-)collinear loop respectively. In contrast to the one-loop case, we now receive an additional contribution coming from the ultra-(anti-)collinear region which appear with a factor $\left(\mu^2\hat{s}^2/m^6\right)^\epsilon$. Note that these scales also appear as powers of ν depending on the specific momentum region and as a result of regulated propagators. For example, in the case of collinear scaling in k_2, one expands

$$[k_2^2 - 2k_2p_2]^\nu = [-2k_2p_2^-]^\nu + \mathcal{O}(\lambda^2),$$

which has hard scaling and thus leads to an overall factor $\left(\tilde{\mu}^2/\hat{s}\right)^\nu$.

---

[5] The integrals in these two regions were among the most challenging to calculate.

topology A		hh	cc	$\overline{cc}$	ch	$\bar{c}h$	$uc\bar{c}$	$\overline{ucc}$
(a)	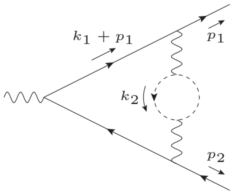	✓	✓	✓				
(b)	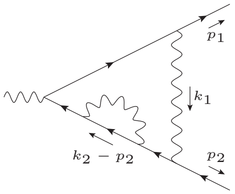	✓		✓	✓		✓	
(c)	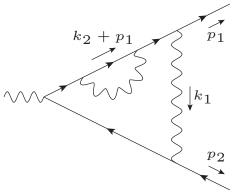	✓	✓			✓		✓
(d)	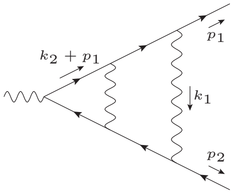	✓	✓	✓	✓	✓	✓	✓

Table 7.1.: Overview of the regions that contribute up to NLP per diagram in topology A.

Secondly, it is important to note that any power of ν that we factor out is irrelevant for carrying out the check whether the rapidity regulators cancel in the full result. This is due to the fact that except for the leading order term, all terms lead to finite terms in ν and thus vanish upon setting ν to zero, e.g.

$$\left(\frac{\tilde{\mu}^2}{\hat{s}}\right)^{\nu}\frac{1}{\nu} - \left(\frac{\tilde{\mu}^2}{-m^2}\right)^{\nu}\frac{1}{\nu} = \ln\left(-\frac{m^2}{\hat{s}}\right) + \mathcal{O}\left(\nu\right), \tag{7.11}$$

which shows how the regulator dependence indeed cancels. A side remark concerns the opposite behavior of the signs associated to the hard and collinear scales in the case of rapidity regulators, i.e. $\left(\mu^2/\hat{s}\right)^{\epsilon}$ and $\left(-\mu^2/m^2\right)^{\epsilon}$, as compared to the scenario in

topology B		hh	cc	$\bar{c}\bar{c}$	$c\bar{c}'$	$\bar{c}c'$	ch	$\bar{c}h$	$h\bar{c}'$	hc'	$c\overline{uc}'$	$\bar{c}uc'$
(e)	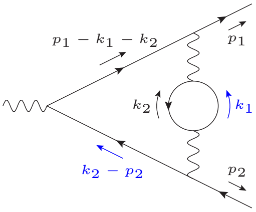	✓	ν	ν								
(f)	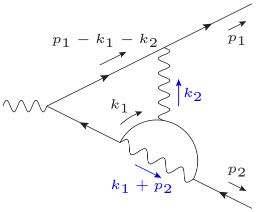	✓	ν	ν		ν		✓		✓		✓
(g)	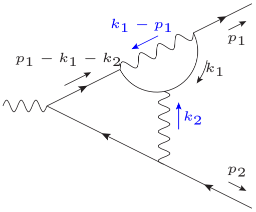	✓	ν	ν	ν		✓		✓		✓	

Table 7.2.: Overview of the regions that contribute up to NLP per diagram in topology B. We denote with ν regions that require a rapidity regulator. In black (blue) we show the flow of loop momenta k_1, k_2 corresponding to the parametrization I_B (I'_B).

which the rapidity regulator is absent, i.e. $\left(-\mu^2/\hat{s}\right)^\epsilon$ and $\left(\mu^2/m^2\right)^\epsilon$. This is purely an automatic consequence of a Wick rotation, as we explain in more detail in App. C.2.

In topology X, we have two independent rapidity regulators, ν_1 and ν_2, and therefore double poles may arise. Similar to the single pole case, these cancel as can for example be seen by considering

$$\left(\frac{\tilde{\mu}_2^2}{-m^2}\right)^{\nu_2}\frac{1}{\nu_2^2} - \left(\frac{\tilde{\mu}_2^2}{\hat{s}}\right)^{\nu_2}\left(\frac{1}{\nu_2^2}\right)$$
$$= -\frac{1}{\nu_2}\ln\left(-\frac{m^2}{\hat{s}}\right) + \frac{1}{2}\ln^2\left(-\frac{m^2}{\hat{s}}\right) - \ln\left(-\frac{m^2}{\hat{s}}\right)\ln\left(\frac{\tilde{\mu}_2^2}{\hat{s}}\right) + \mathcal{O}\left(\nu_2\right) \quad (7.12)$$

topology X		hh	cc	$\bar{c}\bar{c}$	$\bar{c}c$	hc	$\bar{c}h$	$\bar{c}uc$	$\overline{uc}c$	cc'	$\bar{c}\bar{c}'$
(h)	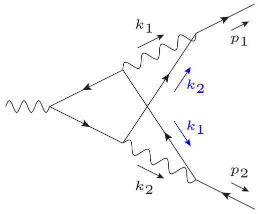	✓	ν_2	ν_1	ν_1,ν_2	✓	✓	✓	✓	ν_1,ν_2	ν_1,ν_2

Table 7.3.: Overview of the regions that contribute up to NLP in the topology X. Note the presence of only one diagram here. As opposed to the topology B, two rapidity regulators are needed to make all regions well-defined. Regions to which this applies are denoted by ν_1 and/or ν_2. In black (blue) we show the flow of loop momenta k_1, k_2 corresponding to the parametrization I_X (I'_X). We omit the momentum flow of I''_X as it does not contribute at the level of the form factor.

where the remaining single pole in ν_2 cancels against terms that have simultaneous poles in ν_1 and ν_2,

$$\left(\frac{\tilde{\mu_1}^2}{\hat{s}}\right)^{\nu_1}\left(\frac{\tilde{\mu}_2^2}{\hat{s}}\right)^{\nu_2}\frac{1}{\nu_1\nu_2}-\left(\frac{\tilde{\mu_1}^2}{-m^2}\right)^{\nu_1}\left(\frac{\tilde{\mu}_2^2}{\hat{s}}\right)^{\nu_2}\frac{1}{\nu_1\nu_2}$$

$$=\frac{1}{\nu_2}\ln\left(-\frac{m^2}{\hat{s}}\right)+\ln\left(-\frac{m^2}{\hat{s}}\right)\ln\left(\frac{\tilde{\mu}_2^2}{\hat{s}}\right)+\mathcal{O}\left(\nu_1,\nu_2\right)\,, \tag{7.13}$$

while the finite terms in Eq. (7.12) and Eq. (7.13) combine to a double logarithm of $(-m^2/\hat{s})$.

We now provide our results for F_1 and F_2, split by the various regions as specified in Tables 7.1-7.3 for topologies A, B and X respectively. For further checks and in anticipation of a QCD generalization, we also list the QCD color factor for each diagram, which would follow if the virtual photons were gluons. We finish this section by commenting on the series of checks we have performed to validate our results against existing results in the literature.

7.3.1. Topology *A*

Diagram (a)

QCD color factor: $C_F T_R N_f$, with N_f the number of light flavors. For the QED massive form factors, we can also allow for multiple light flavors, with different charges, and therefore we add an overall factor to diagram (a)

$$C = \frac{N_f}{e_q^2} \sum_{l=1}^{N_f} e_{q,l}^2 \,, \tag{7.14}$$

with $e_{q,l}$ the fractional charges of the light flavors. We divided out the factor e_q^2 as it was explicitly extracted from the form factors in Eq. (6.26). The results for diagram (a) are:

$$\begin{aligned} F_1^{(2,a)}\Big|_{hh} =& C\left(\frac{\mu^2}{-\hat{s}}\right)^{2\epsilon}\left[\frac{2}{3\epsilon^3}+\frac{28}{9\epsilon^2}+\frac{18\zeta_2+353}{27\epsilon}+\frac{28\zeta_2}{9}-\frac{52\zeta_3}{9}+\frac{7541}{162}\right. \\ &\left.+\frac{m^2}{\hat{s}}\left(\frac{4}{3\epsilon^2}+\frac{110}{9\epsilon}+\frac{4\zeta_2}{3}+\frac{1615}{27}\right)\right], \end{aligned} \tag{7.15}$$

$$\begin{aligned} F_1^{(2,a)}\Big|_{cc} =& C\left(\frac{\mu^2}{m^2}\right)^{2\epsilon}\left[-\frac{1}{3\epsilon^3}-\frac{17}{9\epsilon^2}+\frac{-45\zeta_2-196}{27\epsilon}-\frac{85\zeta_2}{9}-\frac{22\zeta_3}{9}-\frac{2012}{81}\right. \\ &\left.+\frac{m^2}{\hat{s}}\left(-\frac{2}{3\epsilon^2}-\frac{79}{9\epsilon}-\frac{10\zeta_2}{3}-\frac{2575}{54}\right)\right]. \end{aligned} \tag{7.16}$$

By symmetry, we have

$$F_1^{(2,a)}\Big|_{\bar{c}\bar{c}} = F_1^{(2,a)}\Big|_{cc} \,. \tag{7.17}$$

For F_2 we get

$$F_2^{(2,a)}\Big|_{hh} = C\left(\frac{\mu^2}{-\hat{s}}\right)^{2\epsilon}\frac{m^2}{\hat{s}}\left[-\frac{8}{3\epsilon^2}-\frac{196}{9\epsilon}-\frac{8\zeta_2}{3}-\frac{2498}{27}\right], \tag{7.18}$$

$$F_2^{(2,a)}\Big|_{cc} = C\left(\frac{\mu^2}{m^2}\right)^{2\epsilon}\frac{m^2}{\hat{s}}\left[\frac{4}{3\epsilon^2}+\frac{98}{9\epsilon}+\frac{20\zeta_2}{3}+\frac{1249}{27}\right]. \tag{7.19}$$

By symmetry, we have

$$F_2^{(2,a)}\Big|_{\bar{c}\bar{c}} = F_2^{(2,a)}\Big|_{cc} \,. \tag{7.20}$$

Diagram (b)

QCD color factor: C_F^2

$$F_1^{(2,b)}\Big|_{hh} = \left(\frac{\mu^2}{-\hat{s}}\right)^{2\epsilon} \Bigg[\frac{1}{\epsilon^3} + \frac{7}{2\epsilon^2} + \frac{53-4\zeta_2}{4\epsilon} - \frac{7\zeta_2}{2} - \frac{32\zeta_3}{3} + \frac{355}{8} + \frac{m^2}{\hat{s}}\left(\frac{9}{\epsilon^3} + \frac{55}{2\epsilon^2} - \frac{36\zeta_2-513}{4\epsilon} - \frac{55\zeta_2}{2} - 96\zeta_3 + \frac{3171}{8}\right)\Bigg], \tag{7.21}$$

$$F_1^{(2,b)}\Big|_{\bar{c}\bar{c}} = \left(\frac{\mu^2}{m^2}\right)^{2\epsilon} \Bigg[\frac{1}{\epsilon^3} + \frac{6}{\epsilon^2} + \frac{17\zeta_2-6}{\epsilon} + 46\zeta_2 + \frac{94\zeta_3}{3} + 14 + \frac{m^2}{\hat{s}}\left(-\frac{5}{2\epsilon^2} + \frac{144\zeta_2-63}{4\epsilon} + \frac{191\zeta_2}{2} + 72\zeta_3 - \frac{629}{8}\right)\Bigg], \tag{7.22}$$

$$F_1^{(2,b)}\Big|_{ch} = \left(\frac{\mu^2}{m^2}\right)^{\epsilon}\left(\frac{\mu^2}{-\hat{s}}\right)^{\epsilon} \Bigg[-\frac{2}{3\epsilon^3} - \frac{8}{3\epsilon^2} - \frac{28}{3\epsilon} + \frac{16\zeta_3}{9} - \frac{92}{3} + \frac{m^2}{\hat{s}}\left(-\frac{6}{\epsilon^3} - \frac{31}{3\epsilon^2} - \frac{575}{6\epsilon} + 16\zeta_3 - \frac{1997}{12}\right)\Bigg], \tag{7.23}$$

$$F_1^{(2,b)}\Big|_{uc\bar{c}} = \left(\frac{\mu^2\hat{s}^2}{m^6}\right)^{\epsilon}\left(\frac{\mu^2}{m^2}\right)^{\epsilon} \Bigg[-\frac{4}{3\epsilon^3} - \frac{4}{3\epsilon^2} - \frac{60\zeta_2+8}{3\epsilon} - 20\zeta_2 - \frac{112\zeta_3}{9} - \frac{16}{3} + \frac{m^2}{\hat{s}}\left(-\frac{3}{\epsilon^3} - \frac{8}{3\epsilon^2} + \frac{-135\zeta_2-14}{3\epsilon} - 40\zeta_2 - 28\zeta_3 - \frac{22}{3}\right)\Bigg]. \tag{7.24}$$

For F_2 we get

$$F_2^{(2,b)}\Big|_{hh} = \left(\frac{\mu^2}{-\hat{s}}\right)^{2\epsilon} \frac{m^2}{\hat{s}}\left[-\frac{6}{\epsilon^3} - \frac{31}{\epsilon^2} + \frac{12\zeta_2-235}{2\epsilon} + 31\zeta_2 + 64\zeta_3 - \frac{1593}{4}\right], \tag{7.25}$$

$$F_2^{(2,b)}\Big|_{\bar{c}\bar{c}} = \left(\frac{\mu^2}{m^2}\right)^{2\epsilon} \frac{m^2}{\hat{s}}\left[-\frac{3}{\epsilon^2} - \frac{48\zeta_2+15}{2\epsilon} - 71\zeta_2 - 48\zeta_3 + \frac{27}{4}\right], \tag{7.26}$$

$$F_2^{(2,b)}\Big|_{ch} = \left(\frac{\mu^2}{m^2}\right)^{\epsilon}\left(\frac{\mu^2}{-\hat{s}}\right)^{\epsilon} \frac{m^2}{\hat{s}}\left[\frac{4}{\epsilon^3} + \frac{62}{3\epsilon^2} + \frac{247}{3\epsilon} + \frac{1705}{6} - \frac{32\zeta_3}{3}\right], \tag{7.27}$$

$$F_2^{(2,b)}\Big|_{uc\bar{c}} = \left(\frac{\mu^2\hat{s}^2}{m^6}\right)^{\epsilon}\left(\frac{\mu^2\hat{s}}{m^2}\right)^{\epsilon} \frac{m^2}{\hat{s}}\left[\frac{2}{\epsilon^3} + \frac{4}{3\epsilon^2} + \frac{90\zeta_2+8}{3\epsilon} + 20\zeta_2 + \frac{56\zeta_3}{3} + \frac{16}{3}\right]. \tag{7.28}$$

Diagram (c)

Diagram (c) is related to diagram (b) via the symmetry $c \leftrightarrow \bar{c}$.

Diagram (d)

QCD color factor: C_F^2

$$F_1^{(2,d)}\Big|_{hh} = \left(\frac{\mu^2}{-\hat{s}}\right)^{2\epsilon}\left[\frac{1}{\epsilon^4}+\frac{2}{\epsilon^3}+\frac{2\zeta_2+17}{2\epsilon^2}+\frac{-24\zeta_2+184\zeta_3+303}{12\epsilon}+\frac{103\zeta_2^2}{10}-\frac{35\zeta_2}{2}\right.$$
$$+\frac{152\zeta_3}{3}+\frac{631}{8}+\frac{m^2}{\hat{s}}\left(\frac{2}{\epsilon^3}-\frac{16\zeta_2-32}{\epsilon^2}+\frac{-6\zeta_2-16\zeta_3+73}{\epsilon}\right.$$
$$\left.\left.-\frac{64\zeta_2^2}{5}-174\zeta_2+\frac{68\zeta_3}{3}+\frac{893}{2}\right)\right], \tag{7.29}$$

$$F_1^{(2,d)}\Big|_{cc} = \left(\frac{\mu^2}{m^2}\right)^{2\epsilon}\left[\frac{2-3\zeta_2}{\epsilon^2}+\frac{-8\zeta_2-13\zeta_3+10}{\epsilon}-\frac{163\zeta_2^2}{5}-22\zeta_2-16\zeta_3+38\right.$$
$$\left.+\frac{m^2}{\hat{s}}\left(\frac{12-8\zeta_2}{\epsilon^2}+\frac{12\zeta_2-72\zeta_3+60}{\epsilon}-\frac{712\zeta_2^2}{5}-44\zeta_2+136\zeta_3+228\right)\right], \tag{7.30}$$

$$F_1^{(2,d)}\Big|_{ch} = \left(\frac{\mu^2}{m^2}\right)^{\epsilon}\left(\frac{\mu^2}{-\hat{s}}\right)^{\epsilon}\left[-\frac{2}{3\epsilon^4}-\frac{5}{3\epsilon^3}-\frac{22}{3\epsilon^2}+\frac{2\,(8\zeta_3-111)}{9\epsilon}+\frac{4\zeta_2^2}{5}+\frac{40\zeta_3}{9}-\frac{238}{3}\right.$$
$$+\frac{m^2}{\hat{s}}\left(-\frac{4}{3\epsilon^3}+\frac{16\zeta_2-31}{\epsilon^2}+\frac{-84\zeta_2+480\zeta_3-613}{6\epsilon}\right.$$
$$\left.\left.+\frac{608\zeta_2^2}{5}+20\zeta_2-\frac{598\zeta_3}{9}-\frac{4411}{12}\right)\right], \tag{7.31}$$

$$F_1^{(2,d)}\Big|_{uc\bar{c}} = \left(\frac{\mu^2\hat{s}^2}{m^6}\right)^{\epsilon}\left(\frac{\mu^2}{m^2}\right)^{\epsilon}\left[\frac{1}{6\epsilon^4}+\frac{2}{3\epsilon^3}+\frac{15\zeta_2+8}{6\epsilon^2}+\frac{90\zeta_2+14\zeta_3+24}{9\epsilon}+\frac{493\zeta_2^2}{20}\right.$$
$$\left.+20\zeta_2+\frac{56\zeta_3}{9}+\frac{16}{3}+\frac{m^2}{\hat{s}}\left(\frac{1}{3\epsilon^3}+\frac{3}{\epsilon^2}+\frac{15\zeta_2+23}{3\epsilon}+45\zeta_2+\frac{28\zeta_3}{9}+\frac{61}{3}\right)\right]. \tag{7.32}$$

By symmetry, we have

$$F_1^{(2,d)}\Big|_{\bar{c}\bar{c}} = F_1^{(2,d)}\Big|_{cc}, \qquad F_1^{(2,d)}\Big|_{\bar{c}h} = F_1^{(2,d)}\Big|_{ch}, \qquad F_1^{(2,d)}\Big|_{\overline{uc}c} = F_1^{(2,d)}\Big|_{uc\bar{c}}. \tag{7.33}$$

For F_2 we get

$$F_2^{(2,d)}\Big|_{hh} = \left(\frac{\mu^2}{-\hat{s}}\right)^{2\epsilon}\frac{m^2}{\hat{s}}\left[-\frac{4}{\epsilon^3}-\frac{20}{\epsilon^2}+\frac{4\zeta_2-70}{\epsilon}+48\zeta_2-\frac{160\zeta_3}{3}-249\right], \tag{7.34}$$

$$F_2^{(2,d)}\Big|_{cc} = \left(\frac{\mu^2}{m^2}\right)^{2\epsilon}\frac{m^2}{\hat{s}}\left[\frac{8\zeta_2-8}{\epsilon}+48\zeta_2+16\zeta_3-40\right], \tag{7.35}$$

$$F_2^{(2,d)}\Big|_{ch} = \left(\frac{\mu^2}{m^2}\right)^{\epsilon}\left(\frac{\mu^2}{-\hat{s}}\right)^{\epsilon}\frac{m^2}{\hat{s}}\left[\frac{8}{3\epsilon^3}+\frac{14}{\epsilon^2}+\frac{51}{\epsilon}+8\zeta_2-\frac{64\zeta_3}{9}+\frac{349}{2}\right], \tag{7.36}$$

$$F_2^{(2,d)}\Big|_{uc\bar{c}} = \left(\frac{\mu^2\hat{s}^2}{m^6}\right)^{\epsilon}\left(\frac{\mu^2}{m^2}\right)^{\epsilon}\frac{m^2}{\hat{s}}\left[-\frac{2}{3\epsilon^3}-\frac{4}{\epsilon^2}-\frac{10\zeta_2+8}{\epsilon}-60\zeta_2-\frac{56\zeta_3}{9}-16\right]. \quad (7.37)$$

By symmetry, we have

$$F_2^{(2,d)}\Big|_{\bar{c}\bar{c}} = F_2^{(2,d)}\Big|_{cc}, \qquad F_2^{(2,d)}\Big|_{\bar{c}h} = F_2^{(2,d)}\Big|_{ch}, \qquad F_2^{(2,d)}\Big|_{\overline{uc}c} = F_2^{(2,d)}\Big|_{uc\bar{c}}. \quad (7.38)$$

7.3.2. Topology *B*

Diagram (e)

QCD color factor: $C_F T_R$

$$\begin{aligned} F_1^{(2,e)}\Big|_{hh} = \left(\frac{\mu^2}{-\hat{s}}\right)^{2\epsilon}\Bigg[&\frac{2}{3\epsilon^3}+\frac{28}{9\epsilon^2}+\frac{18\zeta_2+353}{27\epsilon}+\frac{28\zeta_2}{9}-\frac{52\zeta_3}{9}+\frac{7541}{162} \\ &+\frac{m^2}{\hat{s}}\left(\frac{28}{3\epsilon^2}+\frac{254}{9\epsilon}+\frac{28\zeta_2}{3}+\frac{3775}{27}\right)\Bigg], \end{aligned} \quad (7.39)$$

$$\begin{aligned} F_1^{(2,e)}\Big|_{cc} = \left(\frac{\mu^2}{m^2}\right)^{2\epsilon}\left(\frac{\tilde{\mu}^2}{\hat{s}}\right)^{\nu}\Bigg[&-\frac{4}{3\epsilon^3}+\frac{1}{\epsilon^2}\left(\frac{4}{3\nu}-\frac{4}{3}\right)-\frac{1}{\epsilon}\left(\frac{20}{9\nu}+\frac{8\zeta_2}{3}+\frac{56}{9}\right) \\ &+\frac{36\zeta_2+112}{27\nu}+\frac{32\zeta_2}{3}+\frac{20\zeta_3}{9}-\frac{2144}{81} \\ &+\frac{m^2}{\hat{s}}\left(-\frac{2}{3\epsilon^2}-\frac{1}{\epsilon}\left(\frac{16}{\nu}+\frac{151}{9}\right)+42\zeta_2-\frac{3511}{54}\right)\Bigg], \end{aligned} \quad (7.40)$$

$$\begin{aligned} F_1^{(2,e)}\Big|_{\bar{c}\bar{c}} = \left(\frac{\mu^2}{m^2}\right)^{2\epsilon}\left(\frac{\tilde{\mu}^2}{-m^2}\right)^{\nu}\Bigg[&\frac{2}{3\epsilon^3}-\frac{1}{\epsilon^2}\left(\frac{4}{3\nu}+\frac{28}{9}\right)+\frac{1}{\epsilon}\left(\frac{20}{9\nu}-\frac{2\zeta_2}{3}-\frac{212}{27}\right) \\ &-\frac{36\zeta_2+112}{27\nu}+\frac{80\zeta_2}{9}-\frac{16\zeta_3}{9}-\frac{1292}{81} \\ &+\frac{m^2}{\hat{s}}\left(-\frac{26}{3\epsilon^2}+\frac{1}{\epsilon}\left(\frac{16}{\nu}-\frac{151}{9}\right)+34\zeta_2-\frac{55}{54}\right)\Bigg]. \end{aligned} \quad (7.41)$$

Notice that the LP contribution of the *hh* region is the same as for diagram (a), Eq. (7.15). For F_2 we get

$$F_2^{(2,e)}\Big|_{hh} = \left(\frac{\mu^2}{-\hat{s}}\right)^{2\epsilon}\frac{m^2}{\hat{s}}\left[-\frac{8}{3\epsilon^2}-\frac{196}{9\epsilon}-\frac{8\zeta_2}{3}-\frac{2498}{27}\right], \quad (7.42)$$

$$F_2^{(2,e)}\Big|_{cc} = \left(\frac{\mu^2}{m^2}\right)^{2\epsilon}\frac{m^2}{\hat{s}}\left[\frac{4}{3\epsilon^2}+\frac{98}{9\epsilon}+12\zeta_2+\frac{25}{27}\right]. \quad (7.43)$$

By symmetry, we have

$$F_2^{(2,e)}\Big|_{\bar{c}\bar{c}} = F_2^{(2,e)}\Big|_{cc}\,. \tag{7.44}$$

Diagram (f)

QCD color factor: $C_F^2 - \frac{1}{2}C_F C_A$

$$\begin{aligned} F_1^{(2,f)}\Big|_{hh} = {} & \left(\frac{\mu^2}{-\hat{s}}\right)^{2\epsilon}\Bigg[-\frac{1}{\epsilon^3}+\frac{4\zeta_2-11}{2\epsilon^2}+\frac{40\zeta_2+8\zeta_3-109}{4\epsilon}+\frac{8\zeta_2^2}{5}+\frac{91\zeta_2}{2}+\frac{59\zeta_3}{3}-\frac{911}{8} \\ & +\frac{m^2}{\hat{s}}\left(-\frac{7}{\epsilon^3}-\frac{59}{2\epsilon^2}+\frac{108\zeta_2-695}{4\epsilon}+\frac{231\zeta_2}{2}+\frac{284\zeta_3}{3}-\frac{5129}{8}\right)\Bigg], \end{aligned} \tag{7.45}$$

$$F_1^{(2,f)}\Big|_{cc} = \left(\frac{\mu^2}{m^2}\right)^{2\epsilon}\left(\frac{\tilde{\mu}^2}{\hat{s}}\right)^{2\nu}\frac{m^2}{\hat{s}}\left[\frac{2}{\epsilon^3}+\frac{2-4\nu}{\nu\epsilon^2}+\frac{6}{\epsilon}+\frac{2\zeta_2+6}{\nu}-\frac{10\zeta_3}{3}-20\zeta_2+22\right], \tag{7.46}$$

$$\begin{aligned} F_1^{(2,f)}\Big|_{\bar{c}\bar{c}} = {} & \left(\frac{\mu^2}{m^2}\right)^{2\epsilon}\left(\frac{\tilde{\mu}^2}{-m^2}\right)^{2\nu}\Bigg[-\frac{1}{\epsilon^3}+\frac{2\left(\zeta_2-1\right)}{\epsilon^2}-\frac{2\left(6\zeta_2-5\zeta_3+5\right)}{\epsilon} \\ & +\frac{32\zeta_2^2}{5}+24\zeta_2-\frac{19\zeta_3}{3}-72\zeta_2\log(2)-42+\frac{m^2}{\hat{s}}\Bigg(-\frac{5}{\epsilon^3}-\frac{1}{\epsilon^2}\left(\frac{2}{\nu}+\frac{35}{2}\right) \\ & -\frac{92\zeta_2+279}{4\epsilon}-\frac{2\zeta_2+2}{\nu}+\frac{133\zeta_2}{2}+\frac{16\zeta_3}{3}-144\zeta_2\log(2)-\frac{2281}{8}\Bigg)\Bigg], \end{aligned} \tag{7.47}$$

$$\begin{aligned} F_1^{(2,f)}\Big|_{\bar{c}h} = {} & \left(\frac{\mu^2}{m^2}\right)^{\epsilon}\left(\frac{\mu^2}{-\hat{s}}\right)^{\epsilon}\Bigg[\frac{4-4\zeta_2}{\epsilon^2}-\frac{14\zeta_2+12\zeta_3-26}{\epsilon}-\frac{44\zeta_2^2}{5}-52\zeta_2-42\zeta_3+122 \\ & +\frac{m^2}{\hat{s}}\left(\frac{10}{\epsilon^3}+\frac{50}{\epsilon^2}+\frac{207-40\zeta_2}{\epsilon}-200\zeta_2-\frac{440\zeta_3}{3}+\frac{1633}{2}\right)\Bigg], \end{aligned} \tag{7.48}$$

$$\begin{aligned} F_1^{(2,f)}\Big|_{\bar{c}c'} = {} & \left(\frac{\mu^2}{m^2}\right)^{2\epsilon}\left(\frac{\tilde{\mu}^2}{-m^2}\right)^{\nu}\left(\frac{\tilde{\mu}^2}{\hat{s}}\right)^{\nu}\Bigg[\frac{m^2}{\hat{s}}\Bigg(-\frac{9}{\epsilon^3}-\frac{14}{\epsilon^2}-\frac{3\left(3\zeta_2+22\right)}{\epsilon}-\frac{4}{\nu} \\ & -14\zeta_2+6\zeta_3-82\Bigg)\Bigg], \end{aligned} \tag{7.49}$$

$$\begin{aligned} F_1^{(2,f)}\Big|_{hc'} = {} & \left(\frac{\mu^2}{-\hat{s}}\right)^{\epsilon}\left(\frac{\mu^2}{m^2}\right)^{\epsilon}\Bigg[\frac{2}{3\epsilon^3}+\frac{8}{3\epsilon^2}+\frac{28}{3\epsilon}+\frac{92}{3}-\frac{16\zeta_3}{9} \\ & +\frac{m^2}{\hat{s}}\left(\frac{6}{\epsilon^3}+\frac{37}{3\epsilon^2}+\frac{575}{6\epsilon}+\frac{1637}{12}-16\zeta_3\right)\Bigg], \end{aligned} \tag{7.50}$$

$$F_1^{(2,f)}\Big|_{\bar{c}uc'} = \left(\frac{\mu^2}{m^2}\right)^{\epsilon}\left(\frac{\mu^2\hat{s}^2}{m^6}\right)^{\epsilon}\left[\frac{4}{3\epsilon^3}+\frac{4}{3\epsilon^2}+\frac{60\zeta_2+8}{3\epsilon}+20\zeta_2+\frac{112\zeta_3}{9}+\frac{16}{3}\right.$$
$$\left.+\frac{m^2}{\hat{s}}\left(\frac{3}{\epsilon^3}+\frac{8}{3\epsilon^2}+\frac{135\zeta_2+14}{3\epsilon}+40\zeta_2+28\zeta_3+\frac{22}{3}\right)\right]. \tag{7.51}$$

For F_2 we get

$$F_2^{(2,f)}\Big|_{hh} = \left(\frac{\mu^2}{-\hat{s}}\right)^{2\epsilon}\frac{m^2}{\hat{s}}\left[\frac{6}{\epsilon^3}+\frac{39}{\epsilon^2}+\frac{377-44\zeta_2}{2\epsilon}-151\zeta_2-80\zeta_3+\frac{3075}{4}\right], \tag{7.52}$$

$$F_2^{(2,f)}\Big|_{\bar{c}c} = \left(\frac{\mu^2}{m^2}\right)^{2\epsilon}\frac{m^2}{\hat{s}}\left[\frac{6}{\epsilon^3}+\frac{15}{\epsilon^2}+\frac{133-4\zeta_2}{2\epsilon}-61\zeta_2-68\zeta_3+96\zeta_2\ln(2)+\frac{1135}{4}\right], \tag{7.53}$$

$$F_2^{(2,f)}\Big|_{\bar{c}h} = \left(\frac{\mu^2}{m^2}\right)^{\epsilon}\left(\frac{\mu^2}{-\hat{s}}\right)^{\epsilon}\frac{m^2}{\hat{s}}\left[-\frac{12}{\epsilon^3}-\frac{52}{\epsilon^2}+\frac{48\zeta_2-222}{\epsilon}+232\zeta_2+176\zeta_3-869\right], \tag{7.54}$$

$$F_2^{(2,f)}\Big|_{\bar{c}c'} = \left(\frac{\mu^2}{m^2}\right)^{2\epsilon}\frac{m^2}{\hat{s}}\left[\frac{6}{\epsilon^3}+\frac{24}{\epsilon^2}+\frac{6\zeta_2+64}{\epsilon}+24\zeta_2-4\zeta_3+160\right], \tag{7.55}$$

$$F_2^{(2,f)}\Big|_{hc'} = \left(\frac{\mu^2}{-\hat{s}}\right)^{\epsilon}\left(\frac{\mu^2}{m^2}\right)^{\epsilon}\frac{m^2}{\hat{s}}\left[-\frac{4}{\epsilon^3}-\frac{74}{3\epsilon^2}-\frac{283}{3\epsilon}+\frac{32\zeta_3}{3}-\frac{1873}{6}\right], \tag{7.56}$$

$$F_2^{(2,f)}\Big|_{\bar{c}uc'} = \left(\frac{\mu^2}{m^2}\right)^{\epsilon}\left(\frac{\mu^2\hat{s}^2}{m^6}\right)^{\epsilon}\frac{m^2}{\hat{s}}\left[-\frac{2}{\epsilon^3}-\frac{4}{3\epsilon^2}-\frac{90\zeta_2+8}{3\epsilon}-20\zeta_2-\frac{56\zeta_3}{3}-\frac{16}{3}\right]. \tag{7.57}$$

Diagram (g)

Diagram (g) is related to diagram (f) via the symmetry $c \leftrightarrow \bar{c}$.

7.3.3. Topology *X*

Diagram (h)

QCD color factor: $C_F^2 - \frac{1}{2}C_F C_A$

$$F_1^{(2,h)}\Big|_{hh} = \left(\frac{\mu^2}{-\hat{s}}\right)^{2\epsilon}\left[\frac{1}{\epsilon^4}+\frac{4}{\epsilon^3}+\frac{16-7\zeta_2}{\epsilon^2}-\frac{48\zeta_2+122\zeta_3-174}{3\epsilon}\right.$$
$$-\frac{53\zeta_2^2}{2}-58\zeta_2-\frac{380\zeta_3}{3}+204+\frac{m^2}{\hat{s}}\left(\frac{1}{\epsilon^4}+\frac{5}{\epsilon^3}+\frac{\zeta_2+18}{\epsilon^2}\right.$$
$$\left.\left.-\frac{186\zeta_2+196\zeta_3-843}{6\epsilon}-\frac{201\zeta_2^2}{10}-64\zeta_2-\frac{382\zeta_3}{3}+\frac{1491}{4}\right)\right], \tag{7.58}$$

$$\begin{aligned}
F_1^{(2,h)}\Big|_{hc} = {} & \left(\frac{\mu^2}{-\hat{s}}\right)^{\epsilon}\left(\frac{\mu^2}{m^2}\right)^{\epsilon}\Bigg[-\frac{4}{3\epsilon^4}-\frac{16}{3\epsilon^3}+\frac{12\zeta_2-56}{3\epsilon^2}+\frac{126\zeta_2+140\zeta_3-552}{9\epsilon} \\
& +\frac{52\zeta_2^2}{5}+52\zeta_2+\frac{506\zeta_3}{9}-\frac{584}{3}+\frac{m^2}{\hat{s}}\Bigg(-\frac{4}{\epsilon^4}-\frac{20}{3\epsilon^3}+\frac{4\zeta_2-29}{\epsilon^2} \\
& +\frac{144\zeta_2+88\zeta_3-761}{6\epsilon}-8\zeta_2^2+88\zeta_2+\frac{952\zeta_3}{9}-\frac{4955}{12}\Bigg)\Bigg],
\end{aligned} \tag{7.59}$$

$$\begin{aligned}
F_1^{(2,h)}\Big|_{u\bar{c}c} = {} & \left(\frac{\mu^2\hat{s}^2}{m^6}\right)^{\epsilon}\left(\frac{\mu^2}{m^2}\right)^{\epsilon}\Bigg[-\frac{1}{6\epsilon^4}-\frac{2}{3\epsilon^3}-\frac{15\zeta_2+8}{6\epsilon^2}-\frac{90\zeta_2+14\zeta_3+24}{9\epsilon}-\frac{493\zeta_2^2}{20} \\
& -20\zeta_2-\frac{56\zeta_3}{9}-\frac{16}{3}+\frac{m^2}{\hat{s}}\Bigg(-\frac{1}{3\epsilon^3}-\frac{3}{\epsilon^2}-\frac{15\zeta_2+23}{3\epsilon}-45\zeta_2-\frac{28\zeta_3}{9}-\frac{61}{3}\Bigg)\Bigg],
\end{aligned} \tag{7.60}$$

$$\begin{aligned}
F_1^{(2,h)}\Big|_{cc} = {} & \left(\frac{\mu^2}{m^2}\right)^{2\epsilon}\left(\frac{\tilde{\mu}_2^2}{\hat{s}}\right)^{2\nu_2}\Bigg[\frac{1}{2\epsilon^4}+\frac{2}{\epsilon^3}+\frac{3\zeta_2+12}{2\epsilon^2}+\frac{6\zeta_2+26\zeta_3+54}{3\epsilon}+\frac{363\zeta_2^2}{20}+14\zeta_2 \\
& -\frac{4\zeta_3}{3}+54+\frac{m^2}{\hat{s}}\Bigg(\frac{1}{\epsilon^3}+\frac{8\zeta_2-5}{2\epsilon^2}+\frac{1}{\epsilon}\left(\frac{4}{\nu_2}-3\zeta_2+36\zeta_3-\frac{27}{4}\right) \\
& +\frac{8}{\nu_2}+\frac{356\zeta_2^2}{5}+\frac{7\zeta_2}{2}-\frac{110\zeta_3}{3}-\frac{177}{8}\Bigg)\Bigg],
\end{aligned} \tag{7.61}$$

$$\begin{aligned}
F_1^{(2,h)}\Big|_{\bar{c}c} = {} & \left(\frac{\mu^2}{m^2}\right)^{2\epsilon}\left(\frac{\tilde{\mu}_1^2}{-m^2}\right)^{\nu_1}\left(\frac{\tilde{\mu}_1^2}{\hat{s}}\right)^{\nu_1}\left(\frac{\tilde{\mu}_2^2}{-m^2}\right)^{\nu_2}\left(\frac{\tilde{\mu}_2^2}{\hat{s}}\right)^{\nu_2}\Bigg[\frac{1}{\epsilon^4}+\frac{4}{\epsilon^3}+\frac{\zeta_2+12}{\epsilon^2} \\
& +\frac{12\zeta_2-2\zeta_3+96}{3\epsilon}+\frac{7\zeta_2^2}{10}+12\zeta_2-\frac{8\zeta_3}{3}+80+\frac{m^2}{\hat{s}}\Bigg(\frac{4}{\epsilon^4}-\frac{1}{\epsilon^3}\left(\frac{4}{\nu_2}+\frac{4}{\nu_1}+10\right) \\
& +\frac{1}{\epsilon^2}\left(\frac{8}{\nu_1}+\frac{4}{\nu_1\nu_2}+\frac{8}{\nu_2}+4\zeta_2+30\right)+\frac{1}{\epsilon}\Bigg(\frac{8-8\zeta_2}{\nu_1}+\frac{8-8\zeta_2}{\nu_2}-\frac{4}{\nu_1\nu_2} \\
& -18\zeta_2+\frac{16\zeta_3}{3}+110\Bigg)+\frac{12+36\zeta_2-52\zeta_3}{3\nu_1}+\frac{4\zeta_2-4}{\nu_1\nu_2}+\frac{12+36\zeta_2-52\zeta_3}{3\nu_2} \\
& -\frac{46\zeta_2^2}{5}-\frac{124\zeta_3}{3}+22\zeta_2+278\Bigg)\Bigg],
\end{aligned} \tag{7.62}$$

$$\begin{aligned}
F_1^{(2,h)}\Big|_{cc'} = {} & \left(\frac{\mu^2}{m^2}\right)^{2\epsilon}\left(\frac{\tilde{\mu}_1^2}{-m^2}\right)^{\nu_1}\left(\frac{\tilde{\mu}_1^2}{\hat{s}}\right)^{\nu_1}\left(\frac{\tilde{\mu}_2^2}{-m^2}\right)^{2\nu_2}\Bigg[\frac{m^2}{\hat{s}}\Bigg(\frac{20}{\epsilon^4}-\frac{1}{\epsilon^3}\left(\frac{10}{\nu_2}+10\right) \\
& +\frac{1}{\epsilon^2}\left(\frac{4}{\nu_2^2}+\frac{6}{\nu_2}-8\zeta_2-8\right)+\frac{1}{\epsilon}\left(-\frac{4}{\nu_2^2}+\frac{2\zeta_2+6}{\nu_2}-\frac{4}{\nu_1}+6\zeta_2-\frac{112\zeta_3}{3}+16\right) \\
& +\frac{4\zeta_2-4}{\nu_2^2}+\frac{80\zeta_3-18\zeta_2-12}{3\nu_2}-\frac{8}{\nu_1}-46\zeta_2^2+\frac{32\zeta_3}{3}+4\zeta_2+46\Bigg)\Bigg],
\end{aligned} \tag{7.63}$$

$$
\begin{aligned}
F_1^{(2,h)}\Big|_{\bar{c}\bar{c}'} = {} & \left(\frac{\mu^2}{m^2}\right)^{2\epsilon} \left(\frac{\tilde{\mu}_1^2}{-m^2}\right)^{2\nu_1} \left(\frac{\tilde{\mu}_2^2}{-m^2}\right)^{\nu_2} \left(\frac{\tilde{\mu}_2^2}{\hat{s}}\right)^{\nu_2} \Bigg[\frac{m^2}{\hat{s}} \bigg(-\frac{17}{\epsilon^4}+\frac{1}{\epsilon^3}\left(\frac{14}{\nu_2}+\frac{4}{\nu_1}+27\right) \\
& + \frac{1}{\epsilon^2}\left(-\frac{4}{\nu_2^2}-\frac{14}{\nu_2}-\frac{8}{\nu_1}-\frac{4}{\nu_1\nu_2}-13\zeta_2+29\right) \\
& + \frac{1}{\epsilon}\left(\frac{4}{\nu_2^2}+\frac{6\zeta_2-18}{\nu_2}+\frac{8\zeta_2-8}{\nu_1}+\frac{4}{\nu_1\nu_2}-\frac{110\zeta_3}{3}+11\zeta_2+16\right) \\
& + \frac{4-4\zeta_2}{\nu_2^2}-\frac{28\zeta_3+18+24}{3\nu_2}+\frac{52\zeta_3-36\zeta_2-12}{3\nu_1}+\frac{4-4\zeta_2}{\nu_1\nu_2} \\
& -\frac{223\zeta_2^2}{10}+10\zeta_3+9\zeta_2+46\bigg)\Bigg]\,.
\end{aligned}
\tag{7.64}
$$

By symmetry, we have

$$
\begin{aligned}
& F_1^{(2,h)}\Big|_{\bar{c}h} = F_1^{(2,h)}\Big|_{hc}\,, \qquad F_1^{(2,h)}\Big|_{\bar{c}uc} = F_1^{(2,h)}\Big|_{\overline{uc}c}\,, \\
& F_1^{(2,h)}\Big|_{\bar{c}\bar{c}} = F_1^{(2,h)}\Big|_{cc}(\nu_2 \leftrightarrow \nu_1)\,.
\end{aligned}
\tag{7.65}
$$

For F_2 we get

$$
F_2^{(2,h)}\Big|_{hh} = \left(\frac{\mu^2}{-\hat{s}}\right)^{2\epsilon} \frac{m^2}{\hat{s}} \left[-\frac{4}{\epsilon^3}-\frac{26}{\epsilon^2}+\frac{5\,(4\zeta_2-23)}{\epsilon}+114\zeta_2+\frac{320\zeta_3}{3}-\frac{977}{2}\right], \tag{7.66}
$$

$$
F_2^{(2,h)}\Big|_{hc} = \left(\frac{\mu^2}{-\hat{s}}\right)^{\epsilon} \left(\frac{\mu^2}{m^2}\right)^{\epsilon} \frac{m^2}{\hat{s}} \left[\frac{16}{3\epsilon^3}+\frac{34}{\epsilon^2}+\frac{127-16\zeta_2}{\epsilon}-104\zeta_2-\frac{560\zeta_3}{9}+\frac{885}{2}\right], \tag{7.67}
$$

$$
F_2^{(2,h)}\Big|_{u\bar{c}c} = \left(\frac{\mu^2\hat{s}^2}{m^6}\right)^{\epsilon} \left(\frac{\mu^2}{m^2}\right)^{\epsilon} \frac{m^2}{\hat{s}} \left[\frac{2}{3\epsilon^3}+\frac{4}{\epsilon^2}+\frac{2\,(5\zeta_2+4)}{\epsilon}+60\zeta_2+\frac{56\zeta_3}{9}+16\right], \tag{7.68}
$$

$$
F_2^{(2,h)}\Big|_{cc} = \left(\frac{\mu^2}{m^2}\right)^{2\epsilon} \frac{m^2}{\hat{s}} \left[-\frac{2}{\epsilon^3}-\frac{9}{\epsilon^2}+\frac{-4\zeta_2-59}{2\epsilon}-29\zeta_2+\frac{4\zeta_3}{3}-\frac{369}{4}\right], \tag{7.69}
$$

$$
F_2^{(2,h)}\Big|_{\bar{c}c} = \left(\frac{\mu^2}{m^2}\right)^{2\epsilon} \frac{m^2}{\hat{s}} \left[-\frac{4}{\epsilon^3}-\frac{32}{\epsilon^2}-\frac{4\,(\zeta_2+24)}{\epsilon}-32\zeta_2+\frac{8\zeta_3}{3}-256\right]. \tag{7.70}
$$

By symmetry, we have

$$
F_2^{(2,h)}\Big|_{\bar{c}h} = F_2^{(2,h)}\Big|_{hc}\,, \qquad F_2^{(2,h)}\Big|_{\bar{c}uc} = F_2^{(2,h)}\Big|_{\overline{uc}c}\,, \qquad F_2^{(2,h)}\Big|_{\bar{c}\bar{c}} = F_2^{(2,h)}\Big|_{cc}\,. \tag{7.71}
$$

7.3.4. Cross-checks

We have listed all contributions to the massive form factor at two loop at NLP per momentum region. To validate our results and to make sure no region has been left unaccounted for, we have performed several cross-checks with results presented in [168] and [124]. The former presents the full result of the two-loop QED massive form factor at the level of the individual diagrams, while the latter provides the corresponding QCD result for all diagrams combined, see Eqs. (22) and (23) in [124] for F_1 and F_2 respectively.

In order to compare our results with [168] and [124], one needs to keep the following in mind. To begin with, one must define

$$\mathcal{F}_i^{(2)}(\epsilon, \hat{s}) = \frac{e^{-2\epsilon\gamma_E}}{\Gamma(1+\epsilon)^2} \left(\frac{\mu^2}{m^2}\right)^{-2\epsilon} F_i^{(2)}\left(\epsilon, \frac{m^2}{\hat{s}}\right) , \tag{7.72}$$

as defined in Eq. (21) in [124], and second, expand the variable x as defined in Eq. (14) in [124] in powers of $m^2/\hat{s}$ to match our conventions. Finally, we also remark that one must reinstate the QCD color factors in the QED diagrams in Fig. 7.1 before comparing against Ref. [124]. With these conventions in mind, we now compare the sum of the momentum regions as given in Sec. 7.2.1-7.2.3 to the expansion in $m^2/\hat{s}$ up to NLP of the full result of [168] and [124], where we have made use of the `Mathematica` package `HPL` [171, 172] to expand the polylogarithms.

First, we have checked that diagram (a), which is absent in [168], reproduces the $C_F T_R N_f$ term in [124], while diagram (e) can be checked either directly against the result of [168] or against the $C_F T_R$ term in [124]. Similarly, one can verify the result of the remaining diagrams (b)-(d) and (f)-(h) by checking directly with [168], which we reproduce up to some small verified typos.

In addition to an inspection at the individual diagram level, we have also performed checks at the level of the form factor itself. The sum of our results of diagrams (b)-(d) and (f)-(h) reproduces the term proportional to C_F^2 in [124]. Additional diagrams appearing only in QCD do not contribute at C_F^2.

As a final check we remark that the LP part of the hh region corresponds to the massless limit and we have verified this with the massless form factors at two loops as given in [173, 174].

7.4. Discussion of results

The previous section contains the main results of this chapter, namely, the two-loop massive form factors F_1 and F_2, in the limit $\hat{s} \gg m^2$, written as the sum of contributions arising from all momentum regions. It may be useful to elaborate on this result a bit more, focusing in particular on what can be learnt in light of the computational technique itself, and of factorization.

The first issue one encounters within the expansion by regions is of course identifying all contributing regions. To this end, geometric methods have been developed, which identify the regions by associating them to certain scaling vectors in the parameter representation of a given Feynman graph G [144–146, 175–178]. From the perspective of exploiting the expansion by regions to reveal the underlying factorization structure of a given physical observable, it is important to be able to associate a given region to the (hard, collinear, soft, etc) scaling of the loop momenta, in order to reinterpret a given region as originating from the exchange of a (hard, collinear, soft, etc) particle. Identifying all regions by assigning all possible momentum scalings to the loop momentum is however non-trivial, because loop momenta can be routed in many different ways. As discussed in the literature (see e.g. [126, 130]), starting from a given integral representation it may be necessary to shift the loop momenta one or more times in order to reveal all regions. In case of the two-loop calculation considered here, we found it was necessary to perform such shifts in topologies B and X, as discussed in Sec. 7.2.2 and 7.2.3 respectively. An obvious question is whether loop momentum shifts are sufficient to reveal all regions. The answer is positive for the two-loop problem at hand. In general, finding all regions by means of loop momentum shifts becomes increasingly involved as the loop order grows; it remains an open question whether this approach can be effective at to all loop orders. Let us also mention that shifting the loop momenta does not provide per se a criterion to establish whether all regions have been taken into account. In case the result of the exact integral is unknown, we find it useful to consider other constraints, such as the requirement that rapidity divergences cancel in the sum of all regions, which is a strong constraint on whether all regions have been correctly considered. Another criterion that we have found quite useful is to determine, given a certain loop momentum parametrization, whether all possible scalings of the *leading* term in a given propagator can be obtained, as explained in Sec. 7.2.2. If not, this gives a good indication that some momentum regions are missing, and a momentum shift is needed to reveal them.

Once all regions have been found, the next question concerns their significance for a factorization approach. In this respect, one of the relevant results of our analysis is the observation that new momentum regions appearing at the two-loop level cancel in the physical observable, i.e. the form factors F_1 and F_2 in this case. Indeed, it was observed already some time ago [147, 148] that at higher-loop order new regions may appear, compared to the one already present at lower loops. From a factorization viewpoint this may be problematic, because it could imply that an all-order factorization cannot be obtained. Indeed, one would have to add new contributions to the factorization theorem at each subsequent order in perturbation theory. For our case we find new ultra-(anti-)collinear regions appearing at two loops, both at the level of master integrals and single diagrams, but these cancel in the form factors, so that only the regions already appearing at one loop contribute. More specifically, we find that the sum of the $uc\bar{c}$, $\overline{uc}c$ regions of diagrams (b) and (c) cancels against the sum of the regions $\bar{c}uc'$, $c\overline{uc}'$ in diagrams (f) and (g); similarly, the sum of the $\overline{uc}c$, $uc\bar{c}$ regions in diagrams (d) cancels against the sum of the $\bar{c}uc$, $\overline{uc}c$ regions in diagram (h).

Focusing now on the calculation of the loop integrals in a given region, as usual one has to deal with standard UV and IR singularities, which we regulate in dimensional regularization, as well as rapidity divergences. In this thesis we consider massive form factors, which means that collinear singularities are regulated by the masses on the external legs, and one is left with soft singularities, which give a single pole per loop, proportional to $1/\epsilon$ in dimensional regularization. As is well-known, the expansion into regions generates additional poles in each region. For instance, the hard region at one loop and the hard-hard region at two loop correspond to the massless form factor, because masses are neglected when the momentum is hard and proportional to the large scale $\hat{s}$; as such, in the hard region we find double poles per loop, generated when the loop momentum becomes soft and collinear to one of the external momenta. The double poles cancel against additional UV singularities arising in the collinear momentum regions; indeed, the cancellation of spurious singularities, i.e., the fact that the two loop massive form factors contain at most $1/\epsilon^2$ poles, provides another check that all regions have been correctly taken into account.

As mentioned above, the expansion by regions also generates rapidity singularities, which we observe in topology B and X. We discussed in Sec. 7.1 that the original master integrals do not have rapidity divergences, and when summing all regions of a given integral, we indeed observed the cancellation of rapidity divergences at the integral level (details have been given in Sec. 7.2). In the context of the present discussion, it may be more interesting to note that rapidity divergences cancel *per region* for the form factor F_1 at LP, and at NLP for the form factor F_2 (which is probably a consequence of the fact that F_2 starts at NLP). With the calculation at hand we are however not able to determine whether this is a general feature, valid at arbitrary order. We leave such questions for further research.

Concerning the specific structure of the rapidity divergences per diagram, we saw that for topology B it was enough to use a single rapidity regulator, while for topology X we needed up to two rapidity regulators. In general the addition of a rapidity regulator breaks the symmetry $p_1 \leftrightarrow p_2$: for instance, in case of topology B the cc region ceases to be equal to the $\overline{cc}$ region. In case of more than one rapidity regulator, symmetry between regions can also be broken by expanding the integral in the regulators in a given order. This is what happens in case of topology X: even if we choose the rapidity regulators ν_1 and ν_2 such that the symmetry between the

cc and $\bar{c}\bar{c}$ regions is respected, expanding in ν_1 and ν_2 in a chosen order breaks this symmetry.

To conclude, we found that the calculation of the massive form factors in the limit $\hat{s} \gg m^2$ by means of the method of regions provides useful data in light of developing a factorization framework for scattering amplitudes beyond leading power. It gave us the additional opportunity to test features of the region expansion of complete form factors, giving new perspectives with respect to cases where the method is applied to single integrals.

Chapter 8.

Next-to-leading power jet functions

This chapter is based on forthcoming work [4].

In the previous chapter, we discussed the first step in verifying the NLP factorization formula of Eq. (6.19): the expansion by momentum regions of the two-loop massive QED form factors up to NLP. As discussed at the end of Sec. 6.2.4, we aim to verify the factorization formula in its "bare" form, i.e., before reshuffling soft and collinear singularities into soft and eikonal jet functions. In this form, the factorization formula, accurate up to NLP, can be written as

$$\begin{aligned} V^{\mu}_{\text{NLP}}(p_1,p_2) = {} & J_f \otimes H^{\mu}_{f,\bar f} \otimes J_{\bar f} + J_{f\gamma} \otimes H^{\mu}_{f\gamma,\bar f} \otimes J_{\bar f} + J_{f\gamma} \otimes H^{\mu}_{f\gamma,\bar f\gamma} \otimes J_{\bar f\gamma} \\ & + J_{f\gamma\gamma} \otimes H^{\mu}_{f\gamma\gamma,\bar f} \otimes J_{\bar f} + J_{ff\bar f} \otimes H^{\mu}_{ff\bar f,\bar f} \otimes J_{\bar f} \\ & + J_f \otimes H^{\mu}_{f,\bar f\gamma} \otimes J_{\bar f\gamma} + J_f \otimes H^{\mu}_{f,\bar f\gamma\gamma} \otimes J_{\bar f\gamma\gamma} + J_f \otimes H^{\mu}_{f,\bar f\bar f f} \otimes J_{\bar f\bar f f}\,. \end{aligned} \tag{8.1}$$

where we used that in its bare form, the soft function becomes trivial, i.e. $S = 1$ as corrections consist of scaleless integrals. From another point of view, we can also see that the soft function is trivial up to two loops, as all soft regions for the massive form factors vanish up to this order.

With the results of the previous chapter at hand, we are now ready to propose operator matrix definitions for the jet functions, and in particular verify them by comparing to the various momentum regions as summarised in Sec. 7.3. Note that in this chapter we will mainly consider the first two lines of Eq. (8.1). For the complete factorization at NLP one also needs the jet functions of the last line. However, given the symmetry between the c and $\bar c$ regions of the form factors it is sufficient to check the factorization formula already by focussing on the first two lines of Eq. (8.1). It is straightforward to extend the results of this chapter to include operator matrix definitions for $J_{\bar f\gamma\gamma}$ and $J_{\bar f\bar f f}$ as well. Furthermore, we want to emphasize that although we verify the proposed jet functions with the process $\gamma^* \to f\bar f$, they are in fact universal and can be used for other processes as well. The process dependence resides in the hard functions.

This chapter is structured as follows. In Sec. 8.1, we extend the one loop factorization – already discussed at LP in Sec. 6.2.3 – up to NLP. This affords us the opportunity to set up the necessary notation for this chapter and discuss the first

NLP jet function $J_{f\gamma}$. Next in Sec. 8.2, we propose operator matrix definitions for the various NLP jet functions. In particular, we consider their perturbative expansion up to two loops. Besides the jet functions, we will also give an effective diagrammatic interpretation to the corresponding hard functions. In Sec. 8.3, we verify the proposed jet functions by comparing with the momentum regions obtained in the previous chapter. We will see that there is a strong relation between the jet functions and the different regions on a diagram by diagram basis. As a result, we can often compare results diagram by diagram. We finish in Sec. 8.4 with a discussion of various subtleties we encountered.

8.1. One loop factorization up to NLP

Recall the LP jet functions J_f and $J_{\bar{f}}$, defined in Eqs. (6.50) and (6.51) respectively, and computed in Sec. 6.2.3 up to one loop. We repeat the result for completeness:

$$J_f^{(0)} = \bar{u}(p_1)\,, \qquad J_f^{(1)}(p_1) = \left(\frac{\mu^2}{m^2}\right)^{\epsilon} \bar{u}(p_1) \frac{\Gamma(\epsilon) e^{\epsilon\gamma_E}}{\epsilon(1-2\epsilon)} \left(1 - \frac{2m\epsilon}{\hat{s}} \not{p}_2^-\right). \tag{8.2}$$

and

$$J_{\bar{f}}^{(0)}(p_2) = v(p_2)\,, \qquad J_{\bar{f}}^{(1)}(p_2) = \left(\frac{\mu^2}{m^2}\right)^{\epsilon} \frac{\Gamma(\epsilon) e^{\epsilon\gamma_E}}{\epsilon(1-2\epsilon)} \left(1 + \frac{2m\epsilon}{\hat{s}} \not{p}_1^+\right) v(p_2)\,. \tag{8.3}$$

We already verified these jet functions up to LP by comparing the factorized expression

$$J_f^{(1)} \otimes H_{f,\bar{f}}^{(0),\mu} \otimes J_{\bar{f}}^{(0)} \tag{8.4}$$

with the c-region of the vertex function $V^\mu(p_1,p_2)$, where we used $H_{f,\bar{f}}^{(0),\mu} = -ie\,e_q\,\gamma^\mu$.

In this chapter we are mainly interested in the NLP factorization, i.e. order λ^2 (or equivalently m^2). The projection of Eq. (8.4) onto F_1 up to NLP is given by

$$\left(\frac{\mu^2}{m^2}\right)^{\epsilon} \left\{ \frac{1}{\epsilon^2} + \frac{2}{\epsilon} + 4 + \frac{\zeta_2}{2} + \frac{m^2}{\hat{s}} \left[\frac{2}{\epsilon} + 4\right] + \mathcal{O}(\epsilon) + \mathcal{O}(\lambda^4) \right\}, \tag{8.5}$$

where we performed the expansion in ϵ and λ. Similarly, we can project onto F_2, which yields

$$\left(\frac{\mu^2}{m^2}\right)^{\epsilon} \left\{ \frac{m^2}{\hat{s}} \left[-\frac{4}{\epsilon} - 8 \right] + \mathcal{O}(\epsilon) + \mathcal{O}(\lambda^4) \right\}. \tag{8.6}$$

Comparing to F_1 and F_2 in the c-region, Eqs. (6.41) and (6.44) respectively, we notice that the NLP contributions do not match. This was to be expected as according to Eq. (8.1), we expect new jet functions to appear at this order in the power expansion.

8.1.1. $J_{f\gamma}$ jet function

For the one loop form factors, only the $(f\gamma)$-jet function can contribute at NLP as the other jet functions only start contributing from two-loop onwards. We therefore expect that up to NLP, the one loop c-region of the vertex function $V^\mu(p_1, p_2)$ – or equivalently that of F_1 and F_2 – is reproduced by the factorized expression

$$J_f^{(1)} \otimes H_{f,\bar f}^{(0),\mu} \otimes J_{\bar f}^{(0)} + J_{f\gamma}^{(1)} \otimes \tilde H_{f\gamma,\bar f}^{(0),\mu} \otimes J_{\bar f}^{(0)}\,. \tag{8.7}$$

Let us make the following remarks about the second term. First of all, we can be more specific and write

$$J_{f\gamma} = J_{f\gamma}^{\rho}(p_1-\ell,\ell)\,, \quad \text{and} \quad H_{f\gamma,\bar f} = H_{f\gamma,\bar f}^{\mu,\rho}(p_1-\ell,p_2,\ell)\,, \tag{8.8}$$

where the arguments in the jet function denote the momenta flowing through the fermion and photon leg respectively. In the hard function, the arguments denote the shift in outgoing fermion momenta, as well as the additional momentum ℓ for the collinear photon emission. We want the jet and hard function to depend only on the large momentum component ℓ^+ of ℓ. However, since $J_{f\gamma}$ starts to contribute at order λ, and we want the NLP factorization formula to be accurate up to order λ^2, we need to keep the subleading transverse momentum $\ell_\perp$. Thus, we can Taylor expand the hard function in the transverse momentum

$$\begin{aligned} H_{f\gamma,\bar f}^{\mu,\rho}(p_1-\ell,p_2,\ell) &= H_{f\gamma,\bar f}^{\mu,\rho}(p_1-\ell^+,p_2,\ell^+) + \ell_\perp^\sigma \left[\frac{\partial}{\partial \ell_\perp^\sigma} H_{f\gamma,\bar f,\sigma}^{\mu,\rho}(p_1-\ell,p_2,\ell)\right]_{\ell_\perp=0} + \mathcal{O}(\lambda^2) \\ &\equiv H_{f\gamma,\bar f}^{\mu,\rho}(p_1-\ell^+,p_2,\ell^+) + \ell_\perp^\sigma H_{f\partial\gamma,\bar f,\sigma}^{\mu,\rho}(p_1-\ell^+,p_2,\ell^+)\,. \end{aligned} \tag{8.9}$$

Now, by defining a jet function $J_{f\partial\gamma}$ that absorbs the $\ell_\perp^\sigma$, we can write the second term of Eq. (8.7) as

$$\begin{aligned} &\left[J_{f\gamma}^{(1)} \otimes H_{f\gamma,\bar f}^{(0),\mu} + J_{f\partial\gamma}^{(1)} \otimes H_{f\partial\gamma,\bar f}^{(0),\mu}\right] \otimes J_{\bar f}^{(0)} \\ &\qquad = \int_0^{p_1^+} d\ell^+ \Big[J_{f\gamma,\rho}^{(1)}(p_1-\ell^+,\ell^+) H_{f\gamma,\bar f}^{\mu,\rho}(p_1-\ell^+,p_2,\ell^+) \\ &\qquad\qquad + J_{f\partial\gamma,\rho\sigma}^{(1)}(p_1-\ell^+,\ell^+) H_{f\partial\gamma,\bar f}^{\mu,\rho,\sigma}(p_1-\ell^+,p_2,\ell^+)\Big] J_{\bar f}^{(0)}\,, \end{aligned} \tag{8.10}$$

where we expanded the $\otimes$-product, which besides spinor contractions now also includes contractions of the Lorentz indices carried by the photon leg, as well as a convolution over its large momentum component. Notice that due to the extra factor $\ell_\perp$, the $J_{f\partial\gamma}$ has a power counting that starts at order λ^2.

The jet functions $J_{f\gamma}$ and $J_{f\partial\gamma}$ were already derived in [25] from a generic amplitude, assuming the validity of the factorized picture of above. An operator matrix definition for these jet functions was however not given. Let us do that here and verify that our operator matrix definition both reproduces the result of [25] as well as the c-region of F_1 and F_2 up to NLP. We define the $(f\gamma)$-jet function as

$$J^{\mu}_{f\gamma}(p_1,\ell^+) = \int_{-\infty}^{\infty}\frac{d\xi}{2\pi}\, e^{-i\ell(\xi n_+)}\langle p_1|\left[\bar{\psi}(0)W_{n_+}(0,\infty)\right]\mathcal{A}^{\mu}_{n_+}(\xi n_+)|0\rangle, \tag{8.11}$$

with [179]

$$\mathcal{A}^{\mu}_{n_+}(y) = W_{n_+}(\infty,y)\left(iD^{\mu}W_{n_+}(y,\infty)\right)\,, \tag{8.12}$$

where $D^\mu = \partial^\mu - ie\,e_q\,A^\mu$ is understood to act at the spacetime point y. A few remarks are in order. First of all, we notice that the part in square brackets in Eq. (8.11) is the same as for the jet function J_f defined in Eq. (6.50). This mimicks the fermion coupling of these jet functions with the hard function. Similar, the additional insertion of $\mathcal{A}^{\mu}_{n_+}(\xi n_+)$ in the definition of $J_{f\gamma}$ can be understood as the photon coupling to the hard part. Second, we notice that this definition of $J_{f\gamma}$ is gauge invariant, since both the factor inside the square brackets and $\mathcal{A}^{\mu}_{n_+}(\xi n_+)$ in Eq. (8.11) are individually gauge invariant. Finally, for the complete factorization at NLP we also need the jet function $J_{\bar{f}\gamma}(p_2,\ell^-)$ in opposite direction, which now depends on the momentum p_2 and the large momentum component ℓ^- of the photon which is $\bar{c}$-collinear to $\bar{f}$. We will consider its operator matrix definition in Sec. 8.2.2 and for now only test the factorization of the c-region as the $\bar{c}$-region is exactly the same due to the symmetry of the form factors.

In Feynman gauge, expanding Eq. (8.11) at leading order in perturbation theory, one finds two terms that contribute

$$\begin{aligned} J^{(1)\mu}_{f\gamma}(p_1,\ell^+) = {} & ie^2\bar{u}(p_1)\int[dk]\frac{\gamma^\mu\left(\not{p}_1-\not{k}+m\right)}{k^2[(k-p_1)^2-m^2]}\delta(n_+k-n_+\ell) \\ & - ie^2\bar{u}(p_1)\int[dk]\frac{\not{n}_+\left(\not{p}_1-\not{k}+m\right)k^\mu}{k^2[(k-p_1)^2-m^2][n_+k]}\delta(n_+k-n_+\ell)\,. \end{aligned} \tag{8.13}$$

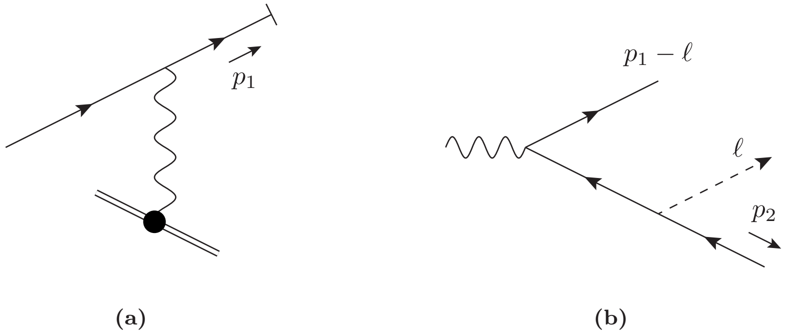

Figure 8.1.: In (a), we show the diagrammatic representation of the jet function $J^{(1)}_{f\gamma}$. Fig. (b) shows the diagram used to calculate the leading order hard function $H^{(0)}_{(f\gamma)}$ and $H^{(0)}_{(f\partial\gamma)}$.

This jet function is shown in Fig. 8.1 (a), where the black dot on the vertex of the photon with the Wilson line is translated into

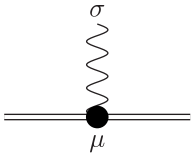

$$= \left(g^{\mu\sigma} - \frac{n_+^\sigma\ k^\mu}{n_+k}\right)\delta(n_+k - n_+\ell)\,. \tag{8.14}$$

The one-loop contribution $J^{(1)\mu}_{f\gamma}(p_1,\ell^+)$ was already calculated in [25] in axial gauge. Here we work in Feynman gauge; the results should of course be the same as the operator matrix definition, Eq. (8.11), is gauge invariant. Indeed, a straightforward calculation yields

$$\begin{aligned} J^{(1)\mu}_{f\gamma}(p_1,x) = {} & \left(\frac{\mu^2\, e^{\gamma_E}}{m^2}\right)^{\epsilon}\Gamma(\epsilon)\bar{u}(p_1)\Bigg\{ m x^{1-2\epsilon}\left(-\gamma^\mu + \frac{2\not{p}_2^{\,-} p_1^\mu}{\hat{s}}\right) \\ & + \frac{m^2}{\hat{s}}\left[\frac{1}{1-\epsilon}\left(\delta(1-x) - (1-2\epsilon)x^{1-2\epsilon}\right)\gamma^\mu \not{p}_2^{\,-} - 4x^{-2\epsilon}(1-x)p_2^{-\mu}\right]\Bigg\}\,, \end{aligned} \tag{8.15}$$

which is in agreement with the result presented in [25]. Two remarks about this result can be made. First, as discussed earlier and made explicit in Eq. (8.10), we still need to perform an integral over the large momentum component ℓ^+, when the jet function is convoluted with the hard function. In calculating Eq. (8.15), we made the change of variables $x \equiv \ell^+/p_1^+$ and subsequently removed a factor of $1/p_1^+$ in the above expression because of the variable change in the measure. We will therefore perform the convolution integral over x, instead of ℓ^+. Second, a priori the x-integration appears to be over the whole range $(-\infty,\infty)$, but in fact it is restricted to $0 < x < 1$.

To see this, consider one of the scalar integrals needed to calculate Eq. (8.15):

$$\int \frac{d\ell^- d^{d-2}\ell_\perp}{(2\pi)^d} \frac{1}{\left[2xp_1^+\ell^- + \ell_\perp^2 + i\eta\right]\left[2(1-x)\ell^- p_1^+ - \ell_\perp^2 + xm^2 - i\eta\right]} \,. \tag{8.16}$$

We notice that if the two poles in ℓ^- lie on the same side of the integration contour the integral over ℓ^- vanishes, as it can be closed at infinity in such a way that no singularities are ecnlosed by the integration contour. A brief analysis shows that only if $0 < x < 1$, the poles in ℓ^- are on different sides of the integration contour.

The jet function $J_{f\partial\gamma}$ at one loop is given by multiplying the integrands in Eq. (8.13) by $k_\perp^\sigma$. The result reads

$$J^{(1)\mu\sigma}_{f\partial\gamma}(p_1,x) = \left(\frac{\mu^2\, e^{\gamma_E}}{m^2}\right)^{\epsilon} m^2 \frac{\Gamma(\epsilon)x^{2-2\epsilon}}{2(1-\epsilon)} \bar{u}(p_1)\left[\frac{2}{x}\eta_\perp^{\mu\sigma} + \gamma_\perp^\sigma\left(\frac{2}{\hat{s}}\not{p}_2^- p_1^\mu - \gamma^\mu\right)\right]. \tag{8.17}$$

In order to find the hard functions we consider the diagram in Fig. 8.1 (b), where the dashed line represents the photon that has to be connected to the $(f\gamma)$-jet function. The full amplitude reads

$$\tilde{H}^{(0)\mu\rho}_{f\gamma,\bar{f}}(p_1,p_2,\ell) = e\,\gamma^\mu \frac{i(-\not{p}_2 - \not{\ell} + m)}{(p_2+\ell)^2 - m^2}\gamma^\rho \,. \tag{8.18}$$

Performing the Taylor expansion as we did in Eq. (8.9), we obtain

$$H^{(0)\mu\rho}_{f\gamma,\bar{f}}(x) = \tilde{H}^{(0)\mu\rho}_{f\gamma,\bar{f}}(p_1,p_2,\ell)\Big|_{\ell_\perp=0} = \frac{-ie}{x\hat{s}}\gamma^\mu\left(\not{p}_2^- + x\not{p}_1^+ - m\right)\gamma^\rho \,, \tag{8.19}$$

and

$$H^{(0)\mu\rho\sigma}_{f\partial\gamma,\bar{f}}(x) = \frac{\partial}{\partial\ell_\perp^\sigma}\tilde{H}^{(0)\mu\rho}_{f\gamma,\bar{f}}(p_1,p_2,\ell)(x,\ell_\perp)\Bigg|_{\ell_\perp=0} = \frac{-ie}{x\hat{s}}\gamma^\mu\gamma_\perp^\sigma\gamma^\rho, \tag{8.20}$$

where we suppressed the arguments of the hard functions, except for their dependence on x.

8.1.2. Verifying the one loop factorization

With the $(f\gamma)$-jet computed, we are now able to verify the factorized expression Eq. (8.7) by comparing to the c-expansion of the one loop form factors. It is straightforward to compute the final x-integral of

$$\int_0^1 dx\, J^{(1)}_{f\gamma,\rho}(p_1,x)\, H^{(0)\mu\rho}_{f\gamma,\bar{f}}(x)\, J^{(0)}_{\bar{f}}(p_2)\,, \tag{8.21}$$

and project onto F_1 and F_2. This yields

$$\left(\frac{\mu^2}{m^2}\right)^{\epsilon}\left\{\frac{m^2}{\hat{s}}\left[-\frac{2}{\epsilon}-2\right]+\mathcal{O}(\epsilon)+\mathcal{O}(\lambda^4)\right\} \tag{8.22}$$

for F_1 and for F_2 we obtain

$$\left(\frac{\mu^2}{m^2}\right)^{\epsilon}\left\{\frac{m^2}{\hat{s}}\left[\frac{2}{\epsilon}\right]+\mathcal{O}(\epsilon)+\mathcal{O}(\lambda^4)\right\}. \tag{8.23}$$

In a similar manner, we compute the convolution integral of

$$\int_0^1 dx\, J^{(1)}_{f\partial\gamma,\rho\sigma}(p_1,x)\, H^{(0)\mu\rho\sigma}_{f\partial\gamma,\bar{f}}(x)\, J^{(0)}_{\bar{f}}(p_2)\,, \tag{8.24}$$

which only contributes to F_1 at NLP:

$$\left(\frac{\mu^2}{m^2}\right)^{\epsilon}\left\{\frac{m^2}{\hat{s}}\left[\frac{1}{\epsilon}+3\right]+\mathcal{O}(\epsilon)+\mathcal{O}(\lambda^4)\right\}. \tag{8.25}$$

Upon summing all contributions Eqs (8.5), (8.22) and (8.25), we obtain for F_1

$$\left(\frac{\mu^2}{m^2}\right)^{\epsilon}\left\{\frac{1}{\epsilon^2}+\frac{2}{\epsilon}+4+\frac{\zeta_2}{2}+\frac{m^2}{\hat{s}}\left[\frac{1}{\epsilon}+5\right]+\mathcal{O}(\epsilon)+\mathcal{O}(\lambda^4)\right\}. \tag{8.26}$$

Similarly, we obtain for F_2

$$\left(\frac{\mu^2}{m^2}\right)^{\epsilon}\left\{\frac{m^2}{\hat{s}}\left[-\frac{2}{\epsilon}-8\right]+\mathcal{O}(\epsilon)+\mathcal{O}(\lambda^4)\right\}, \tag{8.27}$$

where we summed the contributions of Eq. (8.6) and (8.23). This is indeed in agreement with the c-region of the one loop form factors as computed in Eqs. (6.41) and (6.44) respectively.

8.2. Jet functions up to NLP

So far, we gave operator matrix definitions for the jet functions J_f, $J_{\bar{f}}$ and $J_{f\gamma}$ and successfully verified them up to NLP by comparing to the momentum regions of the one loop form factors. We are now ready to discuss the full NLP factorization formula Eq. (8.1) and also define operator matrix definitions for the remaining $(f\gamma\gamma)$- and (fff)-jet functions. As said before, the $(f\gamma\gamma)$- and (fff)-jet functions appear for the first time at two loops, and to verify their operator matrix definitions we can compare with the momentum regions of the two-loop massive form factors. Before we do so, a few remarks are in order.

First of all, the factorization formula Eq. (8.1) can be expanded as

$$
\begin{aligned}
&V^{\mu}_{\mathrm{NLP}}(p_1,p_2) \\
&\quad = J_f(p_1)\, H^{\mu}_{f,\bar f}(p_1,p_2)\, J_{\bar f}(p_2) \\
&\quad + \int_0^{p_1^+} d\ell^+ \Big[J_{f\gamma}(p_1,\ell^+)\, H^{\mu}_{f\gamma,\bar f}(p_1,p_2,\ell^+) + J_{f\partial\gamma}(p_1,\ell^+)\, H^{\mu}_{f\partial\gamma,\bar f}(p_1,p_2,\ell^+)\Big] J_{\bar f}(p_2) \\
&\quad + \int_0^{p_1^+} d\ell_1^+ \int_0^{p_2^-} d\ell_2^-\, J_{f\gamma}(p_1,\ell_1^+)\, H^{\mu}_{f\gamma,\bar f\gamma}(p_1,p_2,\ell_1^+,\ell_2^-)\, J_{\bar f\gamma}(p_2,\ell_2^-) \\
&\quad + \int_0^{p_1^+} d\ell_1^+\, d\ell_2^+ \Big[J_{f\gamma\gamma}(p_1,\ell_1^+,\ell_2^+)\, H^{\mu}_{f\gamma\gamma,\bar f}(p_1,p_2,\ell_1^+,\ell_2^+) \\
&\qquad\qquad\qquad\qquad + J_{ff\bar f}(p_1,\ell_1^+,\ell_2^+)\, H^{\mu}_{ff\bar f,\bar f}(p_1,p_2,\ell_1^+,\ell_2^+)\Big] J_{\bar f}(p_2) \\
&\quad + J_f(p_1) \int_0^{p_2^-} d\ell^- \Big[H^{\mu}_{f,\bar f\gamma}(p_1,p_2,\ell^-)\, J_{f,\bar f\gamma}(p_2,\ell^-) + H^{\mu}_{\bar f\partial\gamma}(p_1,p_2,\ell^-)\, J_{\bar f\partial\gamma}(p_2,\ell^-)\Big] \\
&\quad + J_f(p_1) \int_0^{p_2^-} d\ell_1^-\, d\ell_2^- \Big[H^{\mu}_{f,\bar f\gamma\gamma}(p_1,p_2,\ell_1^-,\ell_2^-)\, J_{\bar f\gamma\gamma}(p_2,\ell_1^-,\ell_2^-) \\
&\qquad\qquad\qquad\qquad + H^{\mu}_{f,\bar f\bar f f}(p_1,p_2,\ell_1^-,\ell_2^-)\, J_{\bar f\bar f f}(p_2,\ell_1^-,\ell_2^-)\Big]\,, \qquad (8.28)
\end{aligned}
$$

where we made the convolution integral over large momentum components between the various jet and hard functions explicit (notice that spinor and Lorentz indices are still suppressed, we make these explicit below). We already saw in Sec. 8.1.1 how the convolution integral over $J_{f\gamma}$ and $H^{\mu}_{f\gamma,\bar f}$ – now the second line in Eq. (8.28) – was derived. The other convolution integrals in Eq. (8.28) can be derived in a similar way. Notice however that for the jet functions $J_{f\gamma\gamma}$ and $J_{ff\bar f}$ the convolution integral is over two large momentum components ℓ_1^+ and ℓ_2^+, which are the large momentum components of the c-collinear photons and fermions respectively. Similarly, we need to integrate over two components ℓ_1^- and ℓ_2^- for the jet functions $J_{\bar f\gamma\gamma}$ and $J_{\bar f\bar f f}$. Finally, we notice that the $(f\gamma\gamma)$- and $(ff f)$-jet functions are already of order λ^2, so there is no need to expand further in transverse momentum, i.e. up to NLP there is need for a jet function $J_{f\partial\gamma\gamma}$ etc.

The second remark we want to make is that altough the two-loop massive form factors have more regions compared to one-loop, we can still compare region per region with the factorization formula. To be precise, the cc-region can be compared with the following factorized expression:

$$\left[J_f^{(2)} \otimes H_{f,\bar{f}}^{(0)} + J_{f\gamma}^{(2)} \otimes H_{f\gamma,\bar{f}}^{(0)} + J_{f\gamma\gamma}^{(2)} \otimes H_{f\gamma\gamma,\bar{f}}^{(0)} + J_{ff\bar{f}}^{(2)} \otimes H_{ff\bar{f},\bar{f}}^{(0)}\right] \otimes J_{\bar{f}}^{(0)}\,, \tag{8.29}$$

where besides the jet functions $J_{f\gamma\gamma}$ and $J_{ff\bar{f}}$ not considered so far, we also need the two-loop expansion of J_f and $J_{f\gamma}$. In Eq. (8.29), and also in what follows below, we keep $J_{f\partial\gamma}$ often implicit as it should be understood as the next order in the expansion of $J_{f\gamma}$. The $\bar{c}\bar{c}$-region can be compared with:

$$J_f^{(0)} \otimes \left[H_{f,\bar{f}}^{(0)} \otimes J_{\bar{f}}^{(2)} + H_{f,\bar{f}\gamma}^{(0)} \otimes J_{\bar{f}\gamma}^{(2)} + H_{f,\bar{f}\gamma\gamma}^{(0)} \otimes J_{\bar{f}\gamma\gamma}^{(2)} + H_{f,\bar{f}\bar{f}f}^{(0)} \otimes J_{\bar{f}\bar{f}f}^{(2)}\right]. \tag{8.30}$$

For the ch and $\bar{c}h$ regions, we need to expand the hard function as well as one of the jet functions to one-loop while keeping the other jet function at tree level. That is, we can compare the ch-region with

$$\left[J_f^{(1)} \otimes H_{f,\bar{f}}^{(1)} + J_{f\gamma}^{(1)} \otimes H_{f\gamma,\bar{f}}^{(1)}\right] \otimes J_{\bar{f}}^{(0)}\,, \tag{8.31}$$

and the $\bar{c}h$-region can be compared with

$$J_f^{(0)} \otimes \left[H_{f,\bar{f}}^{(1)} \otimes J_{\bar{f}}^{(1)} + H_{f,\bar{f}\gamma}^{(1)} \otimes J_{\bar{f}\gamma}^{(1)}\right]. \tag{8.32}$$

For the comparison with the $c\bar{c}$-region, we need the hard functions at tree level and the jet functions expanded up to one-loop:

$$\begin{aligned} J_f^{(1)} \otimes H_{f,\bar{f}}^{(0)} \otimes J_{\bar{f}}^{(1)} + J_{f\gamma}^{(1)} \otimes H_{f\gamma,\bar{f}}^{(0)} \otimes J_{\bar{f}}^{(1)} \\ + J_f^{(1)} \otimes H_{f,\bar{f}\gamma}^{(0)} \otimes J_{\bar{f}\gamma}^{(1)} + J_{f\gamma}^{(1)} \otimes H_{f\gamma,\bar{f}\gamma}^{(0)} \otimes J_{\bar{f}\gamma}^{(1)}\,. \end{aligned} \tag{8.33}$$

We notice that this is another test for the one-loop J_f and $J_{f\gamma}$ functions already computed in Secs. 6.2.3 and 8.1.1 respectively. The final region to compare with is the hh-region, for which we need the hard function expanded up to two loops while keeping the jet functions at tree level. This should therefore be reproduced by

$$J_f^{(0)} \otimes H_{f,\bar{f}}^{(2)} \otimes J_{\bar{f}}^{(0)}\,. \tag{8.34}$$

However, as the hard functions are matching conditions we notice that $H_{f,\bar{f}}^{(2)}$ can be immediately picked to be the hh-region. There is therefore no need to consider this region again in this chapter.

As already remarked in the introduction of this chapter, we can keep our discussion consise due to the symmetry between the c and $\bar{c}$ regions of the form factors. To be precise, if we can show that the factorized expression Eq. (8.29) indeed reproduces the

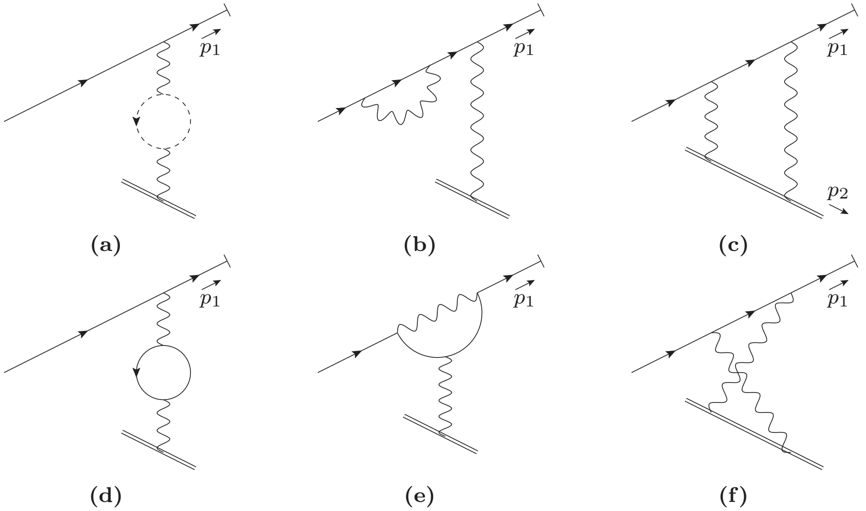

Figure 8.2.: Diagrams contributing to J_f at two-loops.

cc-region, we know that it is also possible to factorize the $\bar{c}\bar{c}$-region.[1] Similarly, it is sufficient to show the factorization of the ch-region. We now consider the jet and hard functions needed for Eqs. (8.29), (8.31) and (8.33). It is straightforward to extend the results to Eqs. (8.30) and (8.32) as well.

8.2.1. J_f jet

In Sec. 6.2.3, we already defined the following operator matrix definitions for the jet functions J_f and $J_{\bar{f}}$:

$$J_f(p_1) = \langle p_1 | \bar{\psi}(0)\, W_{n_+}(0,\infty) | 0 \rangle \,, \qquad J_{\bar{f}}(p_2) = \langle p_2 | W_{n_-}(\infty,0)\, \psi(0) | 0 \rangle \,. \tag{8.35}$$

In particular, we verified their one-loop contribution – shown in Fig. 6.5 – by comparing to the momentum regions of the one-loop form factor. In order to verify that these definitions also work at two loops, we consider the expansion up to $\mathcal{O}(e^4)$. In Fig. 8.2, we show the six 1PI contributions to J_f (one can draw similar diagrams for $J_{\bar{f}}$), where one notices the similarity with the full two-loop diagrams (a), (b), (d), (e), (g) and (h) respectively. As an example, the integral expression of the ladder diagram, Fig. 8.2 (c),

---

[1] In the previous chapter, we saw that the symmetry between cc and $\bar{c}\bar{c}$ is broken due to the needed rapidity regulators. However, as we will discuss in Sec. 8.4 it is still enough to focus on the factorization of the cc-region.

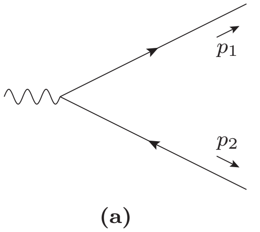

Figure 8.3.: Diagrammatic expressions that correspond with the tree level and one-loop hard functions of $H^{\mu}_{f,\bar{f}}$.

is given by:

$$e^4 e_q^4 \bar{u}(p_1) \int [dk_1][dk_2] \gamma_\mu \frac{i(\not{p}_1 - \not{k}_1 + m)}{(p_1-k_1)^2 - m^2} \gamma_\nu \frac{i(\not{p}_1 - \not{k}_2 + m)}{(p_1-k_2)^2 - m^2} \times \frac{-i}{k_1^2} \frac{-i}{(k_2-k_1)^2} \frac{-in_+^\mu}{[n_+k_1]} \frac{-in_+^\nu}{[n_+k_2]} \,, \tag{8.36}$$

and similar integral expressions can be derived for the other diagrams shown in Fig. 8.2.

Next, we consider the $H^{\mu}_{f,\bar{f}}$ hard function. The tree level hard function was already given in Eq. (6.62). It corresponds with the tree level diagram shown in Fig. 8.3 (a). To verify the factorization formula up to two-loops, i.e. reproduce the *ch*-region, we will also need the hard function at one loop. It can be extracted from the diagram shown in Fig. 8.3 (b), where the one-loop diagram should be computed in the hard momentum limit with the method of regions. Notice that in the computation of these hard functions, we do not include spinors for the external fermions as these are included in J_f and $J_{\bar{f}}$.

8.2.2. $J_{f\gamma}$ jet

We already considered the operator matrix definition for $J_{f\gamma}$ in the previous section, but let us repeat the definition for completeness:

$$J^\mu_{f\gamma}(p_1, \ell^+) = \int_{-\infty}^{\infty} \frac{d\xi}{2\pi}\, e^{-i\ell(\xi n_+)} \langle p_1 | \left[\bar{\psi}(0) W_{n_+}(0,\infty)\right] \mathcal{A}^\mu_{n_+}(\xi n_+) |0\rangle, \tag{8.37}$$

with

$$\mathcal{A}^\mu_{n_+}(y) = W_{n_+}(\infty, y) \left(iD^\mu W_{n_+}(y,\infty) \right) \,. \tag{8.38}$$

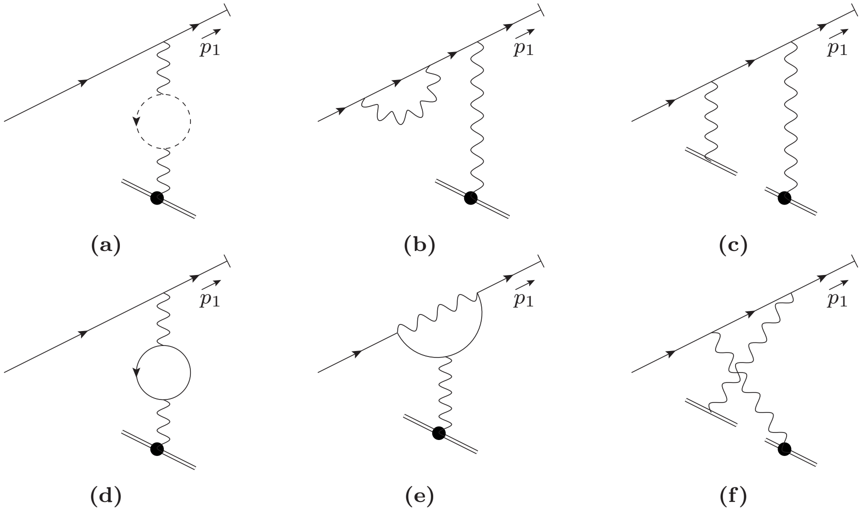

(a) **(b)** **(c)**

(d) **(e)** **(f)**

Figure 8.4.: Two-loop contributions to $J_{f\gamma}$.

Similarly, the jet function $J_{\bar{f}\gamma}$ can be defined as

$$J^{\mu}_{\bar{f}\gamma}(p_2, \ell^-) = \int_{-\infty}^{\infty} \frac{d\xi}{2\pi}\, e^{-i\ell(\xi n_-)} \langle p_2| \left[W_{n_-}(\infty,0)\psi(0)\right] \mathcal{A}^{\mu}_{n_-}(\xi n_-)|0\rangle\,. \tag{8.39}$$

The one-loop contribution to $J_{f\gamma}$ and $J_{f\partial\gamma}$ were already computed in Eq. (8.15) and (8.17) respectively. Similarly, one computes the one-loop contribution to $J_{\bar{f}\gamma}$ which yields

$$\begin{aligned} J^{(1)\mu}_{\bar{f}\gamma}(p_2, \bar{x}) = \left(\frac{\mu^2\, e^{\gamma_E}}{m^2}\right)^{\epsilon} \Gamma(\epsilon) \bigg\{ & m\bar{x}^{1-2\epsilon}\left(-\gamma^\mu + \frac{2\not{p}_1^+ p_2^\mu}{\hat{s}}\right) \\ & - \frac{m^2}{\hat{s}}\left[\frac{1}{1-\epsilon}\left(\delta(1-\bar{x}) - (1-2\epsilon)\bar{x}^{1-2\epsilon}\right)\gamma^\mu \not{p}_1^+ - 4\bar{x}^{-2\epsilon}(1-\bar{x})p_1^{+\mu}\right]\bigg\}\, v(p_2)\,, \end{aligned} \tag{8.40}$$

and

$$J^{(1)\mu\sigma}_{f\partial\gamma}(p_2, \bar{x}) = \left(\frac{\mu^2\, e^{\gamma_E}}{m^2}\right)^{\epsilon} m^2 \frac{\Gamma(\epsilon)\bar{x}^{2-2\epsilon}}{2(1-\epsilon)} \left[\frac{2}{\bar{x}}\eta_\perp^{\mu\sigma} + \gamma_\perp^\sigma\left(\frac{2}{\hat{s}}\not{p}_1^+ p_2^\mu - \gamma^\mu\right)\right] v(p_2). \tag{8.41}$$

where we defined the momentum fraction $\bar{x} = \ell^-/p_2^-$.

In Fig. 8.4, we show the two-loop contributions to $J_{f\gamma}$ (one can draw similar diagrams for $J_{\bar{f}\gamma}$), where we used the Feynman rule defined in Eq. (8.14) to draw the diagrams. For example, the integral expression for the diagram shown in Fig. 8.4 (c)

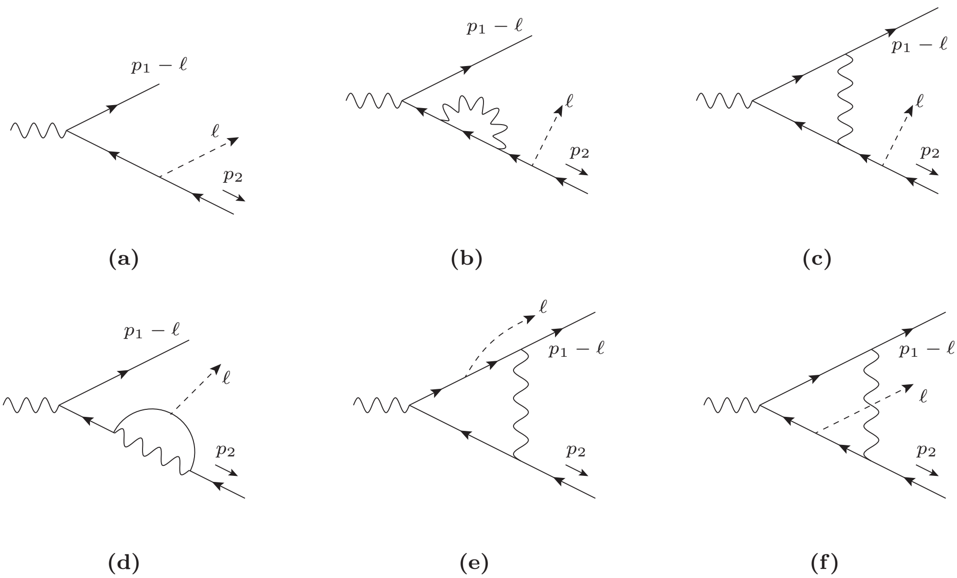

(a) **(b)** **(c)**

(d) **(e)** **(f)**

Figure 8.5.: In (a), we show the diagram that correspond with the tree-level hard function $H^{(0)}_{f\gamma,\bar{f}}$. In (b)-(f), we show the diagrams that corresponds to the hard function $H^{(1)}_{f\gamma,\bar{f}}$.

is given by

$$\begin{aligned} e^4 e_q^4 \bar{u}(p_1) \int [dk_1][dk_2]\gamma_\rho \frac{i(\not{p}_1 - \not{k}_1 + m)}{(p_1 - k_1)^2 - m^2}\frac{-i}{k_1^2}\left(g^{\rho\mu} - \frac{n_+^\rho k_1^\mu}{n_+ k}\right)\delta(n_+k_1 - n_+\ell) \\ \gamma_\sigma \frac{i(\not{p}_1 - \not{k}_2 + m)}{(p_1 - k_2)^2 - m^2}\frac{-i}{k_2^2}\frac{-in_+^\sigma}{n_+ k_2}\,. \end{aligned} \tag{8.42}$$

Again, we notice the strong correspondence with the full two-loop diagrams (a), (b), (d), (e), (g) and (h) respectively.

The tree level hard function $H^{(0)\mu\rho}_{f\gamma,\bar{f}}$ was derived in Eq. (8.19), as well as the hard function $H^{(0)\mu\rho\sigma}_{f\partial\gamma,\bar{f}}$ in Eq. (8.20). Similarly to the case of the (f)-jet function, in order to be accurate up to two loop and reproduce the ch-region up to NLP, we also need the one-loop hard functions $H^{(1)\mu\rho}_{f\gamma,\bar{f}}$ and $H^{(1)\mu\rho\sigma}_{f\partial\gamma,\bar{f}}$. Due to the additional emission of a photon from the hard function, the one loop hard function can be extracted from the five diagrams shown in Fig. 8.5. The dashed line represents the c-collinear photon that is to be connected to the $J_{f\gamma}$ jet function. These diagrams are again computed using the method of regions, where the loop momentum has hard scaling and we take the momentum ℓ to be c-collinear. In order to be accurate up to NLP, the diagrams

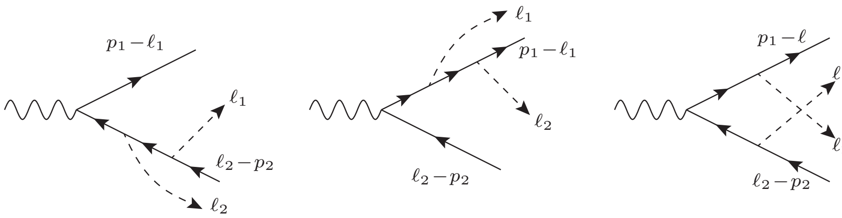

(a) (b) (c)

Figure 8.6.: Diagrammatic expressions that correspond with the tree-level hard function $H^{(0)}_{f\gamma,\bar{f}\gamma}$.

need to be computed up to $\mathcal{O}(\lambda)$, as the jet function $J_{f\gamma}$ starts at order $\mathcal{O}(\lambda)$. For example, consider one of the propagators of the diagram shown in Fig. 8.5 (f):

$$\frac{\slashed{k}-\slashed{\ell}-\slashed{p}_2+m}{(k-\ell-p_2)^2-m^2}=\frac{\slashed{k}-\slashed{\ell}^+-\slashed{\ell}_\perp-\slashed{p}_2^-+m}{(k-\ell^+-p_2^-)^2}\left(1-\frac{2k_\perp\cdot\ell_\perp}{(k-\ell^+-p_2^-)^2}+\mathcal{O}(\lambda^2)\right), \tag{8.43}$$

where we expanded according to hard momentum scaling for k and c-collinear scaling for ℓ. For $H^{(1)\mu\rho}_{f\gamma,\bar{f}}$, one evaluates the relevant propagators at $\ell_\perp=0$, while for $H^{(1)\mu\rho\sigma}_{f\partial\gamma,\bar{f}}$, one takes the derivative with respect to $\ell_\perp$.

Finally, to reproduce the $c\bar{c}$-region, we also need the hard function $H^{(0)}_{f\gamma,\bar{f}\gamma}$. This hard function can be derived from the three diagrams shown in Fig. 8.6. For example, the diagram shown in (a) yields the following part of the hard function:

$$\begin{aligned}&ie\gamma^\mu\frac{i(-\slashed{p}_2-\slashed{\ell}_1+m)}{(p_2+\ell_1)^2-m^2}\gamma^\rho\frac{i(-\slashed{p}_2-\slashed{\ell}_1+\slashed{\ell}_2+m)}{(-p_2-\ell_1+\ell_2)^2-m^2}\gamma^\sigma\bigg|_{\mathcal{O}(\lambda^0)}\\&\qquad\qquad=-ie\gamma^\mu\frac{-\slashed{p}_2^--x\slashed{p}_1^+}{x\hat{s}}\gamma^\rho\frac{-(1-\bar{x})\slashed{p}_2^--x\slashed{p}_1^+}{x(1-\bar{x})\hat{s}}\gamma^\sigma+\mathcal{O}(\lambda)\,,\end{aligned} \tag{8.44}$$

where we expanded according to c-scaling for ℓ_1 and $\bar{c}$-scaling for ℓ_2 and with $x=\ell_1^+/p_1^+$ and $\bar{x}=\ell_2^-/p_2^-$.

8.2.3. $J_{f\gamma\gamma}$ jet

For the $(f\gamma\gamma)$-jet function, we want to have an additional photon going out of the jet, compared to the $(f\gamma)$-jet function. We therefore define $J_{f\gamma\gamma}$ as

$$\begin{aligned}J^{\mu\nu}_{f\gamma\gamma}(p_1,\ell_1^+,\ell_2^+)=&\int\frac{d\xi_1}{2\pi}\int\frac{d\xi_2}{2\pi}e^{-i\ell_1(\xi_1n_+)}e^{-i\ell_2(\xi_2n_+)}\\&\langle p_1|\Big[\bar{\psi}(0)W_{n_+}(0,\infty)\Big]\mathcal{A}^\mu_{n_+}(\xi_1n_+)\mathcal{A}^\nu_{n_+}(\xi_2n_+)|0\rangle\,.\end{aligned} \tag{8.45}$$

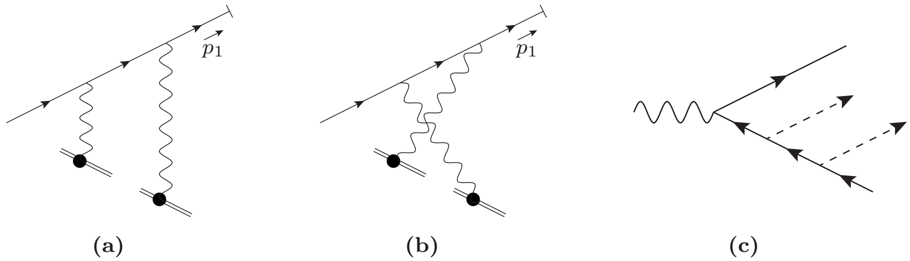

(a) (b) (c)

Figure 8.7.: Diagrams (a) and (b) show the two-loop contributions to $J_{f\gamma\gamma}$. In (c) we show the leading order hard function for $H_{(f\gamma\gamma)}$. All momenta are flowing from left to right.

Notice that this jet function is again made of gauge invariant building blocks and is therefore gauge invariant itself. Furthermore, there are now two large momentum components that are not integrated over, namely ℓ_1^+ and ℓ_2^+. The leading order perturbative contribution to this jet function starts at two loops and the contributing diagrams are shown in Fig. 8.7 (a) and (b). We notice the similarities with diagrams (d) and (h) and, in fact, we will see in the next section that they only contribute to the *cc*-region of these diagrams. This is to be expected, since these are the only diagrams where two photon propagators can connect to the hard vertex.

The lowest order hard function can be derived from the diagram shown in Fig. 8.7 (c). That is, by keeping the hard momentum fractions, we obtain

$$\begin{aligned} H^{(0)\mu\rho\sigma}_{(f\gamma\gamma)}(x_1,x_2) &= ie\gamma^\mu \frac{i(-\slashed{p}_2 - \slashed{\ell}_1 - \slashed{\ell}_2 + m)}{(p_2+\ell_1+\ell_2)^2 - m^2}\gamma^\sigma \frac{i(-\slashed{p}_2 - \slashed{\ell}_1 + m)}{(p_2+\ell_1)^2 - m^2}\gamma^\rho \bigg|_{\mathcal{O}(\lambda^0)} \\ &= -ie\gamma^\mu \frac{\slashed{p}_2^- + (x_1{+}x_2)\slashed{p}_1^+}{(x_1{+}x_2)\hat{s}}\gamma^\rho \frac{\slashed{p}_2^- + x_1\slashed{p}_1^+}{x_1\hat{s}}\gamma^\sigma + \mathcal{O}(\lambda)\,, \end{aligned} \tag{8.46}$$

where $x_j = \ell_j^+/p_1^+$, $j = 1, 2$. Note that we only had to expand the hard function up to order $\mathcal{O}(\lambda^0)$ since the corresponding jet function is already at $\mathcal{O}(\lambda^2)$ accuracy.

8.2.4. J_{fff} jet

The final jet function we consider in this thesis is the (fff)-jet function. The three fermions can attach in two distinct ways to the hard function while conserving the charge flow. As a result, we can consider two different operator matrix definitions for the (fff)-jet function. It turns out that we need both definitions in order to find all

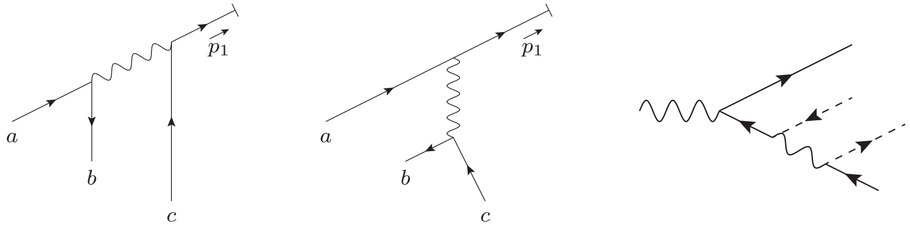

(a) **(b)** **(c)**

Figure 8.8.: Diagrams (a) and (b) show the two-loop contributions to $J^{(I)}_{fff}$. In (c) we show the leading order hard function for $H^{(I)}_{ff\bar{f},\bar{f}}$. All momenta are flowing from left to right.

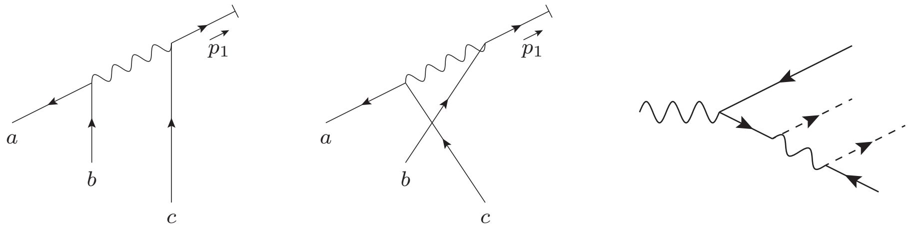

(a) **(b)** **(c)**

Figure 8.9.: Diagrams (a) and (b) show the two-loop contributions to $J^{(II)}_{fff}$. In (c) we show the leading order hard function for $H^{(II)}_{ff\bar{f},\bar{f}}$ (notice the different fermion flow compared to $H^{(I)}_{ff\bar{f},\bar{f}}$ shown in Fig. 8.8 (c)). All momenta are flowing from left to right.

the contributions to the massive form factors. The definitions are

$$
\begin{aligned}
J^{(I)}_{ff\bar{f}}(p_1,\ell_1^+,\ell_2^+) = {}& \int_{-\infty}^{\infty}\frac{d\xi_1}{2\pi}\int_{-\infty}^{\infty}\frac{d\xi_2}{2\pi}e^{-i\ell_1(\xi_1 n_+)}e^{-i\ell_2(\xi_2 n_+)} \\
& \times \langle p_1|\Big[\bar{\psi}(0)W(0,\infty)\Big]\Big[W(\infty,\xi_1 n_+)\psi(\xi_1 n_+)\Big]\Big[\bar{\psi}(\xi_2 n_+)W(\xi_2 n_+,\infty)\Big]|0\rangle,
\end{aligned}
\tag{8.47}
$$

and

$$
\begin{aligned}
J^{(II)}_{ff\bar{f}}(p_1,\ell_1^+,\ell_2^+) = {}& \int_{-\infty}^{\infty}\frac{d\xi_1}{2\pi}\int_{-\infty}^{\infty}\frac{d\xi_2}{2\pi}e^{-i\ell_1(\xi_1 n_+)}e^{-i\ell_2(\xi_2 n_+)} \\
& \times \langle p_1|\Big[W(\infty,0)\psi(0)\Big]\Big[\bar{\psi}(\xi_1 n_+)W(\xi_1 n_+,\infty)\Big]\Big[\bar{\psi}(\xi_2 n_+)W(\xi_2 n_+,\infty)\Big]|0\rangle\,.
\end{aligned}
\tag{8.48}
$$

Note that we will have multiple uncontracted spin indices after calculating these jet functions in perturbation theory. As these spin indices have to be contracted in the right way with the hard function, we take a bit more care and explicitly denote the spin indices below. Both contributions $J^{(I)}_{ff\bar{f}}$ and $J^{(II)}_{ff\bar{f}}$ start at two loops, and their expressions read

$$\begin{aligned}J^{(I)}_{ff\bar{f}}(p_1,\ell_1^+,\ell_2^+) &= e^2\int[dk_1][dk_2]\,\delta(\ell_1^+-k_1^+)\delta(\ell_2^+-k_2^+) \\ &\quad\Bigg\{\left(\bar{u}(p_1)\gamma^\rho\frac{i(\not{k}_1+m)}{k_1^2-m^2}\right)_c\frac{-i}{(p_1-k_1)^2}\left(\frac{i(-\not{k}_2+m)}{k_2^2-m^2}\gamma_\rho\frac{i(\not{p}_1-\not{k}_1-\not{k}_2+m)}{(p_1-k_1-k_2)^2-m^2}\right)_{ba} \\ &\quad-\left(\bar{u}(p_1)\gamma^\rho\frac{i(\not{p}_1-\not{k}_1-\not{k}_2+m)}{(p_1-k_1-k_2)^2-m^2}\right)_a\frac{-i}{(k_1+k_2)^2}\left(\frac{i(-\not{k}_2+m)}{k_2^2-m^2}\gamma_\rho\frac{i(\not{k}_1+m)}{k_1^2-m^2}\right)_{bc}\Bigg\},\end{aligned} \tag{8.49}$$

and

$$\begin{aligned}J^{(II)}_{ff\bar{f}}(p_1,\ell_1^+,\ell_2^+) &= e^2\int[dk_1][dk_2]\delta(\ell_1^+-k_1^+)\delta(\ell_2^+-k_2^+) \\ &\quad\Bigg\{\left(\bar{u}(p_1)\gamma^\rho\frac{i(\not{k}_1+m)}{k_1^2-m^2}\right)_c\left(\frac{i(-\not{p}_1+\not{k}_1+\not{k}_2+m)}{(p_1-k_1-k_2)^2-m^2}\gamma_\rho\frac{i(\not{k}_2+m)}{k_2^2-m^2}\right)_{ab}\frac{-i}{(p_1-k_1)^2} \\ &\quad-\left(\bar{u}(p_1)\gamma^\rho\frac{i(\not{k}_2+m)}{k_2^2-m^2}\right)_b\left(\frac{i(-\not{p}_1+\not{k}_1+\not{k}_2+m)}{(p_1-k_1-k_2)^2-m^2}\gamma_\rho\frac{i(\not{k}_1+m)}{k_1^2-m^2}\right)_{ac}\frac{-i}{(p_1-k_2)^2}\Bigg\},\end{aligned} \tag{8.50}$$

where a, b and c denote the open spin indices.

We also need two hard functions for the different definitions of the $(ff\!f)$-jet. The lowest order hard function for $J^{(I)}_{ff\bar{f}}$ can be derived from the diagram shown in Fig. 8.8 (c) and is given by

$$\begin{aligned}H^{(I)\,(0)\mu}_{ff\bar{f},\bar{f}}(x_1,x_2) &= (-ie)^3\left(\gamma^\mu\frac{-i(\not{p}_2+\not{\ell}_1+\not{\ell}_2-m)}{(p_2+\ell_1+\ell_2)^2-m^2}\gamma_\nu\right)_{ab}\frac{-i}{(p_2+\ell_1)^2}(\gamma^\nu)_{cd}\Bigg|_{\mathcal{O}(\lambda^0)} \\ &= -\frac{ie^3}{\hat{s}(x_1+x_2)}\left(\gamma^\mu\Big[\not{p}_2^- + (x_1+x_2)\not{p}_1^+\Big]\gamma_\nu\right)_{ab}\frac{1}{\hat{s}x_1}\,(\gamma^\nu)_{cd}+\mathcal{O}(\lambda)\,,\end{aligned} \tag{8.51}$$

where $x_j = \ell_j^+/p_1^+$, $j = 1, 2$. The spinor indices a, b and c are contracted with the open indices of the $J^{(I)}_{ff\bar{f}}$. The left over index d will be contracted with the open index of $J_{\bar{f}}$ after convolution of the jet functions with this hard function. For the second jet function, $J^{(II)}_{ff\bar{f}}$, we have a different hard function namely

$$\begin{aligned}H^{(II)\,(0)\mu}_{ff\bar{f},\bar{f}}(x_1,x_2) &= (-ie)^3\left(\gamma_\nu\frac{i(\not{p}_2+\not{\ell}_1+\not{\ell}_2+m)}{(p_2+\ell_1+\ell_2)^2-m^2}\gamma^\mu\right)_{ba}\frac{-i}{(p_2+\ell_1)^2}(\gamma^\nu)_{cd}\Bigg|_{\mathcal{O}(\lambda^0)} \\ &= \frac{ie^3}{\hat{s}(x_1+x_2)}\left(\gamma_\nu\Big[\not{p}_2^- + (x_1+x_2)\not{p}_1^+\Big]\gamma^\mu\right)_{ba}\frac{1}{\hat{s}x_1}\,(\gamma^\nu)_{cd}+\mathcal{O}(\lambda)\,,\end{aligned} \tag{8.52}$$

which one can derive from the diagram shown in Fig. 8.9 (c).

8.3. Verifying results in different regions

The main purpose of this chapter is to check whether the operator matrix definitions for the various NLP jet functions work, and thus that the factorization formula Eq. (8.1) reproduces the results for the process $\gamma^* \to f\bar{f}$ considered in this thesis. We already verified in Secs. 6.2.3 and 8.1 that the one loop contribution indeed can be factorized up to NLP. The recipe to check the NLP factorization formula at two loops is the same: calculate the new jet functions up to two loops and compare with the different momentum regions, presented in the previous chapter. However, calculating the relevant jet functions up to two loops with their general momentum fraction dependence is a task on its own, and with a complexity beyond that of the calculation of the momentum regions of the previous chapter. Luckily, for the purpose of checking the jet definitions, it suffices to do something one could call "reversed factorization". To give an example, we consider the $(f\gamma)$-jet function at one loop. We make the observation that the convolution of the jet function with the hard function schematically takes the form

$$\int d\ell^+ \, J^{(1)}_{f\gamma,\rho}(\ell^+) \, H^{(0)\mu\rho}_{f\gamma,\bar{f}}(\ell^+) = \int d\ell^+ \int [dk] \mathcal{J}^{\rho}(k) \delta(\ell^+ - k^+) \, H^{(0)\mu\rho}_{f\gamma,\bar{f}}(\ell^+) \,, \tag{8.53}$$

where $\mathcal{J}$ denotes the integrand of the jet function with the overall δ-function extracted. Because of the constraint given by the δ-function, integrating over ℓ^+ yields a standard two-loop integral over the full measure $[dk]$. Similarly, we can rewrite the convolution of the other jet functions with their respective hard functions into standard two loop integrals. Moreover, we find that the resulting integrals can be cast into the momentum region expansions of the three topologies A, B and X. In other words, we can thus validate the NLP factorization formula using all the tools developed in the previous chapter, *without* first calculating the specific x-dependence of the jet function. We leave it to future work to calculate all the relevant jet functions up to two loops with a general momentum fraction dependence.

8.3.1. *cc*-region

We will now verify the jet functions by comparing our factorized expression to the various momentum regions obtained in the previous chapter. Let us start with the cc-region, which means we need to compare with

$$\Big[J^{(2)}_{f} \otimes H^{(0)}_{f,\bar{f}} + J^{(2)}_{f\gamma} \otimes H^{(0)}_{f\gamma,\bar{f}} + J^{(2)}_{f\gamma\gamma} \otimes H^{(0)}_{f\gamma\gamma,\bar{f}} + J^{(2)}_{ff\bar{f}} \otimes H^{(0)}_{ff\bar{f},\bar{f}}\Big] \otimes J^{(0)}_{\bar{f}} \,, \tag{8.54}$$

Diagram		J_f	$J_{f\gamma}$	$J_{f\gamma\gamma}$	J_{fff}
(a)	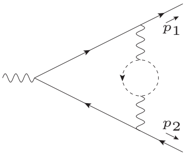	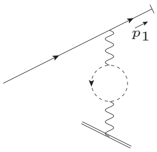	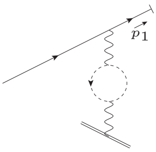		
(c)	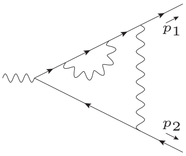	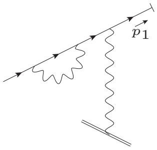	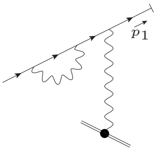		
(e)	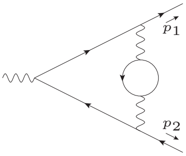	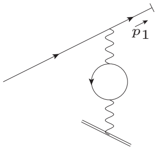	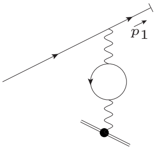		
(f)	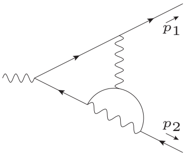				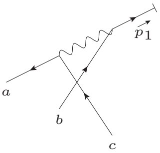
(g)	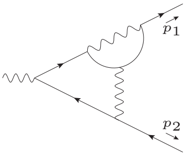	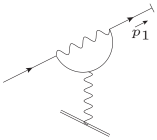	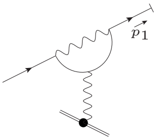		
(d)+(h)	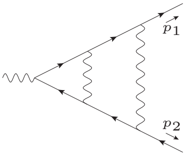	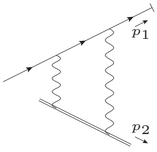	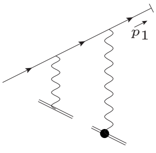	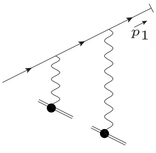	
	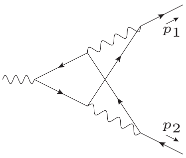	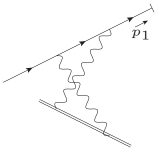	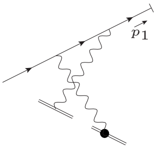	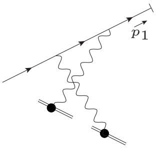	
(h)'	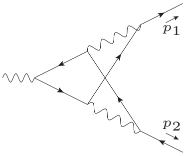				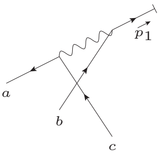

Table 8.1.: Summary of the jet functions contributing to the *cc*-region.

where we suppressed the arguments of the various jet and hard functions. We already noticed that the perturbative expansion of the jet function shows similarities with the full QED diagrams. As a result, it is often not necessary to compare the full factorized expression with the full sum of all *cc*-regions, but we can already compare on a diagram by diagram basis. The results are summarised in Tab. 8.1, where in the first column we listed the full QED diagrams that have a *cc*-region. The last four columns list the diagrams contributing to the factorized expression Eq. (8.54) – i.e. the diagrams in the perturbative expansion of $J_f^{(2)}$, $J_{f\gamma}^{(2)}$, $J_{f\gamma\gamma}^{(2)}$ and $J_{ff\bar{f}}^{(2)}$ – that reproduce the *cc* region of the full QED diagram(s). A few remarks are in order here.

First of all, we want to emphasize that the correct NLP result is only obtained after one also takes the subleading contributions of J_f and $J_{f\gamma}$ into account. This is different compared to SCET, where one defines the jet function in such a way that they have a homogeneous power counting.

Second, we notice that the *cc*-region of diagrams (a), (c), (e) and (g) is reproduced by the jet functions $J_f^{(2)}$ and $J_{f\gamma}^{(2)}$. This can be understood due to the corresponding reduced diagrams only having a fermion, or a fermion plus photon connection between the hard vertex and the collinear subdiagram.

Furthermore, we notice that the *cc*-region of diagrams (d) and (h) is only reproduced when taken together. Besides contributions from $J_f^{(2)}$ and $J_{f\gamma}^{(2)}$ we also get contributions from $J_{f\gamma\gamma}^{(2)}$. Again, we can understand the latter contribution as one is indeed able to draw a reduced diagram with a fermion and two photons connecting between the hard vertex and the collinear subdiagram.

Another subtlety concerns the rapidity divergences. We recall from the previous chapter that rapidity divergences showed up in the *cc*-regions of diagrams (e)-(h). The same divergences also showed up in the calculation of the factorized expression. As the operator matrix definitions given for the various jet functions do not include a rapidity regulator a priori, we added regulators after writing down the loop integrals by reversed factorization. Because these integrals were matched exactly to the *cc*-expansion of one of the three topologies A, B or X, we could pick the regulators in the same way as we did for the region expansion discussed in the previous chapter. We discuss this point further in Sec. 8.4.

Finally, we notice that $J_{ff\bar{f}}^{(2)}$ reproduces the *cc*-region of diagram (f) and the cc'-region of diagram (h), where we recall from the previous chapter that in order to find all regions for diagram (h), we had to define multiple momenta routings. We therefore see that the jet functions give a clear separation between the *cc* and cc'-regions of diagram (h). We come back to this point in Sec. 8.4. There are two more diagrams in the perturbative expansion of $J_{ff\bar{f}}^{(2)}$ not listed in Tab. 8.1. However, they contribute to the triangle diagrams shown in Fig. 7.2. As explained in Sec. 7.1.1, these diagrams cancel each other by Furry's theorem and can therefore be neglected.

8.3.2. *ch*-region

So far, we tested the NLP factorization formula sucessfully in situations where one of the ingredients was expanded up to either one or two loops, but with the other ingredients kept at tree level. A more stringent test is achieved when we take two or more ingredients at higher loop. In this section we consider the *ch*-region which should be compared with the factorized expression

$$\left[J_f^{(1)} \otimes H^{(1)}_{f,\bar f} + J^{(1)}_{f\gamma} \otimes H^{(1)}_{f\gamma,\bar f}\right] \otimes J^{(0)}_{\bar f}\,. \tag{8.55}$$

Let us start again at LP. From the results given in Sec. 7.3, we know that for the *ch*-region the diagrams (b), (d), (f), (g) and (h) have a LP contribution. However, the factorized expression gets only one contribution given by

$$J_f^{(1)} \otimes H^{(1)}_{f,\bar f} \otimes J^{(0)}_{\bar f} =$$

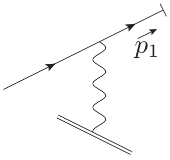

$\otimes$

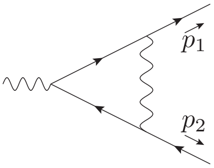

$\otimes\, v(p_2)\,. \qquad (8.56)$

Projecting onto F_1 yields

$$\left(\frac{\mu^2}{m^2}\right)^{\epsilon}\left(\frac{\mu^2}{-\hat s}\right)^{\epsilon}\left[-\frac{2}{\epsilon^4}-\frac{7}{\epsilon^3}-\frac{22}{\epsilon^2}+\frac{16\zeta_3-180}{3\epsilon}+\frac{12\zeta_2^2}{5}+\frac{56\zeta_3}{3}-152\right]+\mathcal{O}(\lambda^2)\,, \tag{8.57}$$

which agrees with the sum of all five diagrams (b), (d), (f), (g) and (h) that have a LP contribution for the *ch*-region.

At NLP, we also get a contribution from

$$J^{(1)}_{f\gamma} \otimes H^{(1)}_{f\gamma,\bar f} \otimes J^{(0)}_{\bar f}$$

$=$

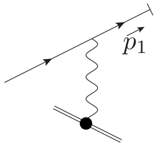

$\otimes \Bigg[$

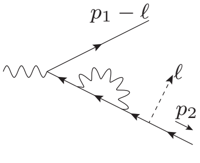

$+$

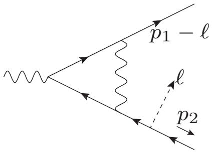

$+$

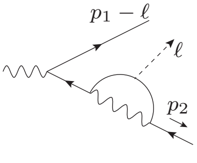

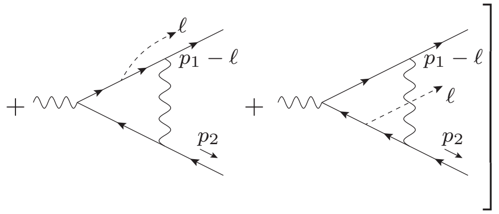

$$\otimes\, v(p_2) \qquad (8.58)$$

We notice that these five contributions show a strong similarity with diagrams (b), (d), (f), (g) and (h) respectively. However, there is no one-to-one relation like we had for most of the diagrams in the *cc*-region. Instead, we have to take all diagrams together before we can compare. To be precise, we project onto F_2, which gives

$$\left(\frac{\mu^2}{m^2}\right)^{\epsilon}\left(\frac{\mu^2}{-\hat{s}}\right)^{\epsilon}\frac{m^2}{\hat{s}}\left[-\frac{4}{\epsilon^3}-\frac{8}{\epsilon^2}+\frac{32\zeta_3-56}{\epsilon}+\frac{320\zeta_3}{3}-280\right], \qquad (8.59)$$

where we also included the contribution coming from Eq. (8.56). Similarly, we can get the order $\mathcal{O}(\lambda^2)$ term of F_1

$$\begin{aligned}\left(\frac{\mu^2}{m^2}\right)^{\epsilon}\left(\frac{\mu^2}{-\hat{s}}\right)^{\epsilon}\frac{m^2}{\hat{s}}\Bigg[&-\frac{4}{\epsilon^4}+\frac{2}{\epsilon^3}+\frac{20\zeta_2-8}{\epsilon^2}+\frac{284\zeta_3-90\zeta_2-66}{3\epsilon}\\&+\frac{568\zeta_2^2}{5}-\frac{322\zeta_3}{3}-92\zeta_2+6\Bigg]. \qquad (8.60)\end{aligned}$$

Using the region results of the previous chapter, one can check that this is the same as the sum of all the *ch*-regions given by diagrams (b), (d), (f), (g) and (h).

8.3.3. $c\bar{c}$-region

The final test for our NLP factorization formula is the comparison with the $c\bar{c}$-region, for which the factorized expression reads:

$$\begin{aligned}&J_f^{(1)}\otimes H_{f,\bar{f}}^{(0)}\otimes J_{\bar{f}}^{(1)}+J_{f\gamma}^{(1)}\otimes H_{f\gamma,\bar{f}}^{(0)}\otimes J_{\bar{f}}^{(1)}\\&\quad+J_f^{(1)}\otimes H_{f,\bar{f}\gamma}^{(0)}\otimes J_{\bar{f}\gamma}^{(1)}+J_{f\gamma}^{(1)}\otimes H_{f\gamma,\bar{f}\gamma}^{(0)}\otimes J_{\bar{f}\gamma}^{(1)}\,. \qquad (8.61)\end{aligned}$$

As usual, we first discuss LP. From the results given in Sec. 7.3, we know that only diagram (h) has a LP contribution for the $c\bar{c}$-region. The factorized expression reads

$$J_f^{(1)} \otimes H^{(0)}_{f,\bar{f}} \otimes J^{(1)}_{\bar{f}} = \qquad (8.62)$$

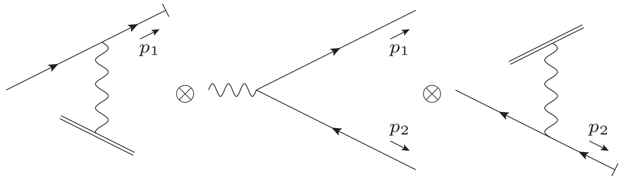

Projecting onto F_1 yields

$$\left(\frac{\mu^2}{m^2}\right)^{2\epsilon}\left[\frac{1}{\epsilon^4}+\frac{4}{\epsilon^3}+\frac{\zeta_2+12}{\epsilon^2}+\frac{12\zeta_2-2\zeta_3+96}{3\epsilon}+\frac{7\zeta_2^2}{10}+12\zeta_2-\frac{8\zeta_3}{3}+80\right]+\mathcal{O}(\lambda^2)\,, \quad (8.63)$$

which agrees with the LP term of diagram (h).

The NLP contribution of the factorized expression Eq. (8.61) currently shows a mismatch with the region analysis – that is, the sum of diagrams (f), (g) and (h). A resolution to this issue appears imminent [4], and as such, we present only a brief outline of the discrepancy below.

The mismatch between the region result and the factorized expression can be seen from diagram (f):

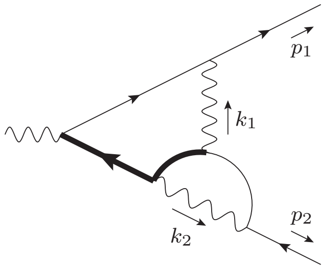

where the bold lines correspond with the hard lines. For clarity, we will work up to order λ, meaning only the first three terms in Eq. (8.61) contribute. The hard lines can be expanded as

$$\begin{aligned}&\frac{-\not{k}_1-\not{p}_2+m}{(k_1+p_2)^2-m^2}\gamma^\rho\frac{-\not{k}_1+\not{k}_2-\not{p}_2+m}{(k_1-k_2+p_2)^2-m^2}\gamma^\sigma\\ &\qquad\qquad =\frac{-\not{k}_1-\not{p}_2+m}{2k_1\cdot p_2^-}\gamma^\rho\frac{-\not{k}_1+\not{k}_2-\not{p}_2+m}{2k_1\cdot(-k_2+p_2)^-}\gamma^\sigma+\mathcal{O}(\lambda^2)\,. \qquad (8.64)\end{aligned}$$

While this expression already factorizes at the integrand level, it cannot be mapped directly onto the factorization formula. The issue arises from the second propagator, which introduces a non-standard eikonal propagator:

$$\frac{1}{2k_1 \cdot (-k_2 + p_2)^-} = \frac{\hat{s}}{[2k_1 \cdot p_2^-][2(-k_2 + p_2) \cdot p_1^+]} \,. \tag{8.65}$$

The hard propagator $1/[(-k_2 + p_2) \cdot p_1^+]$ does not correspond to any ingredient in one of the jet or hard functions (while this propagator is part of $H_{f\gamma,\bar{f}\gamma}$, it only contributes at order λ^2 and, therefore, cannot explain the mismatch already observed at order λ). This analysis is based on a single diagram, so one might expect that the problematic propagator cancels when summing over all relevent diagrams (f), (g) and (h). However, such a cancellation does not occur.

Let us conclude with a short discussion of potential solutions. One possibility is to modify one or more of the hard functions $H^{(0)}_{f,\bar{f}}$, $H^{(0)}_{f\gamma,\bar{f}}$, $H^{(0)}_{f,\bar{f}\gamma}$ or $H^{(0)}_{f\gamma,\bar{f}\gamma}$. However, any modification must preserve the factorization for all other regions, placing strong constraints on allowable changes. Along similar lines, alternations to the jet functions $J_{f\gamma}$ and $J_{\bar{f}\gamma}$ must not disrupt the factorization elsewhere. Furthermore, introducing new jet functions might be necessary, but these too must respect factorization constraints.

At the time of writing, it appears that a proper treatment of fermionic self-energy corrections on the external legs may provide the solution. The problematic propagator $1/[(-k_2 + p_2) \cdot p_1^+]$ seems to cancel when these self-energy contributions are taken into account. To verify this, these self-energy contributions must be incorporated into both the region analysis and the factorization formula Eq. (8.61). Note that no new jet- and hard functions are needed as the self-energy contributions naturally appear in the current operator matrix definitions of the jet functions. We will revisit this potential solution in forthcoming work [4].

Ideally, the solution should have an intuitive interpretation in terms of diagrams or the structures that are already part of the jet functions of above. While this is not strictly required – since hard functions are merly matching functions – it would make the factorization framework applicable to processes beyond those considered in this thesis, see also the discussion around Eq. (8.66).

8.4. Discussion

In this chapter we proposed operator matrix elements for the various jet functions up to NLP. It may be useful to elobarate on the results.

An important point in chapter 7 was that new momentum regions can emerge by shifting loop momenta before applying the expansion by regions. When comparing our factorization formula with the *cc*-region in Sec. 8.3.1, we noticed that the distinct

cc and cc' regions of diagram (h) were reproduced by different jet functions. This observation suggests an alternative perspective: the factorization formula itself can serve as a novel tool for identifying which momentum regions contribute.

A second point worth emphasizing is the universality of the jet functions. While we verified these jet functions by comparing them to the one- and two-loop form factors, it is important to note that they are not limited to this specific process. In fact, a more universal factorization formula holds [25]:

$$\begin{aligned}
\mathcal{M}_n\big|_{\mathrm{LP+NLP}} = {} & \left(\prod_{i=1}^{n} J_f^i\right)\otimes H\,S + \sum_{i=1}^{n}\left(\prod_{j\neq i} J_f^j\right)\left[J^i_{f\gamma}\otimes H^i_{f\gamma} + J^i_{f\partial\gamma}\otimes H^i_{f\partial\gamma}\right] S \\
& + \sum_{i=1}^{n}\left(\prod_{j\neq i} J_f^j\right) J^i_{f\gamma\gamma}\otimes H^i_{f\gamma\gamma}\,S + \sum_{i=1}^{n}\left(\prod_{j\neq i} J_f^j\right) J^i_{fff}\otimes H^i_{fff}\,S \\
& + \sum_{1\leq i\leq j\leq n}\left(\prod_{k\neq i,j} J_f^k\right) J^i_{f\gamma}J^j_{f\gamma}\otimes H^{ij}_{f\gamma,f\gamma}\,S\,,
\end{aligned} \tag{8.66}$$

where the process dependence is captured by the hard functions – now labeled according to the NLP jet functions they pair with. Demonstrating that the factorization formula accurately reproduces the NLP contribution to the $c\bar{c}$-region of the two-loop form factors is crucial in establishing this universality.

Although reversed factorization provides a straightforward method for verifying the factorization formula, calculating the momentum fraction dependence of the jet functions is essential for applications such as resummation. One approach involves rewriting the delta function $\delta(n_+k - n_+\ell)$ in terms of a cut propgator:

$$\begin{aligned}
\delta(n_+k - n_+\ell) &= 2p_2^-\,\delta(2p_2^-\cdot k - x\hat{s}) \\
&= -\frac{2p_2^-}{2\pi i}\left(\frac{1}{2p_2^-\cdot k - x\hat{s} + i\eta} - \frac{1}{2p_2^-\cdot k - x\hat{s} - i\eta}\right).
\end{aligned} \tag{8.67}$$

This reformulation allows the integrals to be evaluated using standard techniques, such as IBP reductions and related methods [180, 181].

A key point in the previous chapter was the need for rapidity regulators for topologies B and X. In this chapter, we added these regulators in a somewhat ad hoc fashion – notably to both the hard functions and the jet functions – to reproduce the results from the region analysis. While this approach suffices for verifying the factorization formula, a more universal description for implementing rapidity regulators is needed. This need can also be seen from the region analysis, where our choice of rapidity regulators broke the c and $\bar{c}$ symmetry of the form factors in diagrams (e) and (h). Ideally, the rapidity regulators should not break such symmetries. Developing a universal description for rapidity regulators is crucial, particularly for applying the factorization formula to other processes where no momentum region results may be available for comparison.

To conclude, we proposed operator matrix elements for the NLP jet functions and verified them by comparing to the various momentum regions of the massive form factors. We showed that the one-loop form factors can indeed be factorized up to NLP. At two loops, the factorization formula successfully matched all regions except the $c\bar{c}$-region, which remains to be fully addressed. Current investigations – which will be reported in [4] – provide strong confidence that the solution to this last challenge is well within reach.

Chapter 9.

Summary and conclusion

The overall theme of this thesis was the concept of power corrections, which we approached from two distinct perspectives: non-perturbative power corrections arising from renormalons, and power corrections to the QED one- and two-loop massive form factors. These were studied using the methods of resurgence and factorization respectively. Let us now briefly summarize the main findings.

After an introduction to resurgence in chapter 2, we considered more formal aspects of the subject in chapter 3. One of the main applications of resurgence is the decoding of non-perturbative physics from asymptotic series, with large order relations serving as a powerful tool for this purpose. We showed that these large order relations themselves form resurgent transseries as well, and in particular we showed that their resurgence structure is inherited from the original transseries. We discussed the Stokes phenomenon for this transseries and the origin of the towers of singularities that appear in the Borel plane. Furthermore, we discussed how one can consistently resum the large order transseries. While large order relations are often analyzed in the asymptotic limit, we showed that they are, in fact, exact. This property allows for the precise resummation of the large order transseries and the exact determination of the perturbative coefficients.

We then proceeded in chapter 4 with one of the key applications of resurgence: renormalons. We briefly introduced the standard lore of renormalons and explained how diagrams with multiple bubble chains can be computed using a convolution integral in the Borel plane. Building on this, we then presented a novel method to study renormalons using resurgence properties of this convolution integral, enabling the calculation of non-perturbative renormalon effects that were previously very challenging to do.

In chapter 5, we studied the renormalon contributions to the Adler function. At leading order in the flavor expansion ($\mathcal{O}(1/N_f)$) – using large order relations and by studying Stokes' automorphism – we constructed the complete resummed two-parameter transseries expression. We then extended our analysis to the Adler function at order $\mathcal{O}(1/N_f^2)$ using the convolution method inroduced in chapter 4. For the diagrams considered, this method enabled us to construct the entire transseries structure. In particular, we identified non-perturbative sectors and alien derivative operators that establish the resurgence relations between these sectors. Furthermore, we observed sectors that exhibit a mixing between UV and IR transmonomials. Additionally, we uncovered a logarithmic type of non-perturbative power correction in the coupling constant plane.

In chapter 6, we shifted our focus from resurgence to aspects of factorization. We first reviewed the power counting formula for massive fermions in QED, that leads to the factorization formula – accurate up to NLP – central to the last three chapters. To verify this factorization formula, we introduced the method of expansion by momentum regions and computed the momentum regions of the one-loop massive form factors in QED. We demonstrated how the factorization formula up to LP was verified by comparing to these momentum regions.

To test the NLP factorization formula, we explained that the momentum regions of the two-loop form factors were required. Chapter 7 was dedicated to this, where we categorized all contributions per region up to NLP. Besided providing the necessary data to verify the factorization formula, we also had the opportunity to test aspects of the region expansion and obtain new perspectives. In particular, we had to define multiple momentum routings in order to uncover all momentum regions. Additionally, we demonstrated how the rapidity divergences canceled in the sum of all regions and subsequently validated our results by reproducing the form factors at NLP as known in the literature. Altough new ultra-(anti-)collinear regions appear at two loops, we showed that these regions cancel in the form factors, so that only the regions already appearing at one loop contribute. This result brings confidence that an all-order factorization can be achieved.

Finally, in chapter 8, we proposed operator matrix definitions for the various NLP jet functions and verified them by comparing to the region results presented in chapter 7. We showed that the momentum regions can be reproduced by these operator matrix definitions. While there are some kinks still to be ironed out for the $c\bar{c}$-region, it appears [4] that this region also fits within the factorization framework. A particularly interresting finding is that the different momentum routings – needed to uncover all regions – can be distinguished by the fact that they correspond to different jet functions. This can therefore also be viewed as a novel approach to identifying new regions.

In conclusion, this thesis highlighted that the resurgence structure in physical problems can be more intricate – and often more intriguing – than in a simplified toy model setting where a bridge equation is available. As a result, many opportunities for further research naturally arise. On the formal side, the transseries structure in the absence of bridge equation can be studied. In applied contexts, resurgence techniques can address challenges in collider and particle physics, such as the determination of non-perturbative effects to the top quark pole mass, or power corrections to the hadronic tau lepton decay which is a key input to determinations of the strong coupling constant. In the direction of factorization, the operator matrix definitions presented in this thesis serve as a starting point for many interesting future investigations. These include the possibility to resum large logarithms at NLP accuracy and the development of radiative jet functions. The results presented in this thesis should meaningfully contribute to these directions.

Appendix A.

Resurgence

A.1. n-Borel transforms

Consider an asymptotic power series

$$\varphi(\alpha) = \sum_{g=0}^{\infty} \varphi_g\, \alpha^g\,, \tag{A.1}$$

where compared to Eq. (2.1), we also included a constant term in α. Comparing Eq. (2.6) and Eq. (2.7) of Example 2.1.1, we see that the difference between a pole and a logarithmic branch cut in the Borel plane lies in an asymptotic coefficient growth proportional to and $g!$ and $(g-1)!$ respectively – or equivalently, in a different value of β in Eq. (2.1). One can turn this observation around by defining different Borel transforms.

We define the 0-*Borel transform* of the sequence φ as

$$\mathcal{B}_0[\varphi](t) \equiv \sum_{g=0}^{\infty} \frac{\varphi_g}{g!}\, t^g\,. \tag{A.2}$$

The 0-Borel transform is a formal power series in the variable t. The 1-*Borel transform* of φ is then defined to be the t-derivative of the 0-Borel transform:

$$\mathcal{B}_1[\varphi](t) \equiv \frac{d}{dt}\mathcal{B}_0[\varphi](t) = \sum_{g=0}^{\infty} \frac{\varphi_{g+1}}{g!}\, t^g\,. \tag{A.3}$$

More generally, we define the n-*Borel transform* of φ to be

$$\mathcal{B}_n[\varphi](t) \equiv \sum_{g=0}^{\infty} \frac{\varphi_{g+n}}{g!}\, t^g\,, \tag{A.4}$$

which can be viewed as the nth derivative of the 0-Borel transform of φ. In fact, for general real (or even complex) ν, one may define

$$\mathcal{B}_\nu[\varphi](t) \equiv \sum_{g=0}^{\infty} \frac{\varphi_g}{\Gamma(g-\nu+1)} t^{g-\nu} \,, \tag{A.5}$$

which for $\nu = n$ integer agrees with Eq. (A.4). It is then generally true that

$$\frac{d}{dt}\mathcal{B}_\nu[\varphi](t) = \mathcal{B}_{\nu+1}[\varphi](t) \,. \tag{A.6}$$

When we start from a sequence that grows factorially as

$$\frac{\varphi_n}{A^{-(n+\beta)}\Gamma(n+\beta)} = \text{const} + \mathcal{O}\left(\frac{1}{g}\right) \qquad \text{as } g \to \infty \tag{A.7}$$

for some nonzero complex constant, and some real choice of β, then $\mathcal{B}_{1-\beta}[\varphi](t)$ has a simple pole at $t = A$. Using Eq. (A.6), we see that similarly, for integer $k \geq 1$, $\mathcal{B}_{k-\beta}[\varphi](t)$ has a pole of order k at $t = A$, and $\mathcal{B}_{-\beta}[\varphi](t)$ has a logarithmic branch point. To keep our formulas concise, we use these facts in this thesis to assume, without too much loss of generality, that our functions in the Borel plane have only simple poles and logarithmic branch points as their singularities, or occasionally even only logarithmic branch points. We can always choose an appropriate n-Borel transform such that this is the case. Extending the results of this thesis so that they also apply to these cases is completely straightforward.

Once a ν-Borel transform is analytically continued beyond the disk of convergence, it can be mapped back to the *Borel sum* via

$$\mathcal{S}_\gamma\varphi(\alpha) = \alpha^{\nu-1} \int_\gamma \mathcal{B}_\nu[\varphi](t)\, \mathrm{e}^{-\frac{t}{\alpha}} \mathrm{d}t \,, \tag{A.8}$$

where to ensure convergence, the contour γ is a straight path starting at the origin and approaching infinity in the half plane where $\Re(t/\alpha) > 0$. Note that the left hand side of this equation is independent of ν. This resummation constructs a function of α which we can asymptotically expand again to retrieve the formal power series $\varphi(\alpha)$.

The Borel transform (and its corresponding Borel sum) that we introduced in chapter 2 and use in practice, will usually be the Borel transform $\mathcal{B}_1$ as this is also the Borel transform one encounters most often in the particle physics literature. However, as discussed in chapter 3, it might be convenient to switch to another Borel transform as some resurgence properties are easier to derive.

A.2. Properties of Stirling transforms

Stirling numbers of the second kind can be defined as [72]

$$\left\{ {n \atop k} \right\} = \frac{1}{k!} \sum_{j=0}^{k} (-1)^j \binom{k}{j} (k-j)^n \, . \tag{A.9}$$

They allow us to express the 0-Borel transform of the Stirling transform $\tilde{\psi}(g)$ defined in Eq. (3.31) in terms of the 0-Borel transform of $\psi(\alpha)$:

$$\mathcal{B}_0[\,\tilde{\psi}\,](t) = \sum_{n=0}^{\infty} \sum_{k=0}^{\infty} \sum_{j=0}^{k} \frac{(-1)^j (k-j)^n a_k}{k! n!} \binom{k}{j} t^n = \mathcal{B}_0[\,\psi\,](\mathrm{e}^t - 1) \, . \tag{A.10}$$

The n-Borel transform is then obtained by simply differentiating both sides n times with respect to t. One finds for example

$$\mathcal{B}_1[\,\tilde{\psi}\,](t) = \mathrm{e}^t \mathcal{B}_1[\,\psi\,](\mathrm{e}^t - 1) \, , \tag{A.11}$$

which can also be obtained by explicitly computing $\mathcal{B}_1[\tilde{\psi}]$ using (A.4) and (A.9), just as we showed for the 0-Borel transform in (A.10). The 0-Borel transform of the rescaled Stirling transform (3.33) is essentially obtained by repeating the computation (A.10), only with a_k replaced by $a_k A^k$, leading to

$$\mathcal{B}_0[\,\hat{\psi}\,](t) = \mathcal{B}_0[\,\psi\,] \left(A(\mathrm{e}^t - 1) \right) \, , \tag{A.12}$$

which again can be differentiated with respect to t to obtain the corresponding n-Borel transforms.

A.3. Stokes phenomenon for gamma functions

In the example of the quartic partition function in Sec. 3.3, the Borel transform $\mathcal{B}[Z^{(1)}] \left(\frac{3}{2}(\mathrm{e}^t - 1) \right)$ induces a Stokes phenomenon as we cross the imaginary t-axis. In order to derive the exact form of this Stokes phenomenon, we start from the exact large order relation as it holds for positive g:

$$\int_0^{\infty} \mathcal{B}[Z^{(1)}] \left(\frac{3}{2}(\mathrm{e}^t - 1) \right) \mathrm{e}^{-gt} \mathrm{d}t = -\frac{2\pi \mathrm{i}}{S_1} \frac{\Gamma(4g+1)}{2^{6g}\, \Gamma(2g+1) \Gamma(g+1)^2} \, . \tag{A.13}$$

Our goal is then to derive the Stokes phenomenon that the gamma functions on the right hand side of this expression undergo and combine them into a Stokes phenomenon for the whole expression. To this end, we use Binet's Log Gamma formula,

$$\log\Gamma(z) = \underbrace{\left(z-\frac{1}{2}\right)\log(z) - z + \frac{1}{2}\log(2\pi)}_{C(z)} + \int_0^\infty \left(\frac{1}{2}-\frac{1}{t}+\frac{1}{\mathrm{e}^t-1}\right)\frac{\mathrm{e}^{-zt}}{t}\mathrm{d}t\,, \quad \text{(A.14)}$$

for $\Re(z) > 0$. This expression consists of singular and constant terms (as $1/z \to 0$) that we collect in the function $C(z)$, and $1/z$ corrections which are resummed using Borel-Laplace resummation. Let us first shift the argument by one:

$$\log\Gamma(z+1) = C(z+1) + \int_0^\infty \left(\left(\frac{1}{2}-\frac{1}{t}+\frac{1}{\mathrm{e}^t-1}\right)\frac{\mathrm{e}^{-t}}{t}\right)\mathrm{e}^{-zt}\mathrm{d}t\,. \quad \text{(A.15)}$$

In the latter term we interpret the integrand as a 1-Borel transform of some formal power series $F(z)$:

$$\mathcal{B}_1[F](t) = \left(\frac{1}{2}-\frac{1}{t}+\frac{1}{\mathrm{e}^t-1}\right)\frac{\mathrm{e}^{-t}}{t}\,. \quad \text{(A.16)}$$

By shifting and rescaling the argument we straightforwardly find that

$$\begin{aligned}
\log\Gamma(z+1) &= C(z+1) + \int_0^\infty \mathcal{B}_1[F]\,(t)\,\mathrm{e}^{-zt}\mathrm{d}t\,,\\
\log\Gamma(2z+1) &= C(2z+1) + \int_0^\infty \frac{1}{2}\mathcal{B}_1[F]\left(\frac{t}{2}\right)\mathrm{e}^{-zt}\mathrm{d}t\,,\\
\log\Gamma(4z+1) &= C(4z+1) + \int_0^\infty \frac{1}{4}\mathcal{B}_1[F]\left(\frac{t}{4}\right)\mathrm{e}^{-zt}\mathrm{d}t\,.
\end{aligned} \quad \text{(A.17)}$$

The large z expansion of the function $C(z)$ has a finite radius of convergence and will therefore not contribute to any Stokes phenomenon that the large z expansion of $\log\Gamma(cz+1)$ undergoes. Let

$$\mathcal{B}_1[\mathcal{F}_n](t) = \frac{1}{n}\mathcal{B}_1[F]\left(\frac{t}{n}\right)\,, \quad \text{(A.18)}$$

then each $\mathcal{B}_1[\mathcal{F}_n](t)$ has simple poles located at $t = 2\pi\mathrm{i}nm$, with residue $1/(2\pi\mathrm{i}m)$, for all nonzero integers m. When we move the contour of integration across the imaginary t-axis – as depicted in Fig. A.1 for $\mathcal{F}_1$ – we therefore pick up poles which lead to the discontinuity

$$\mathrm{disc}_{-\frac{\pi}{2}}\mathcal{F}_n = -\log\left(1-\mathrm{e}^{2\pi\mathrm{i}ng}\right)\,. \quad \text{(A.19)}$$

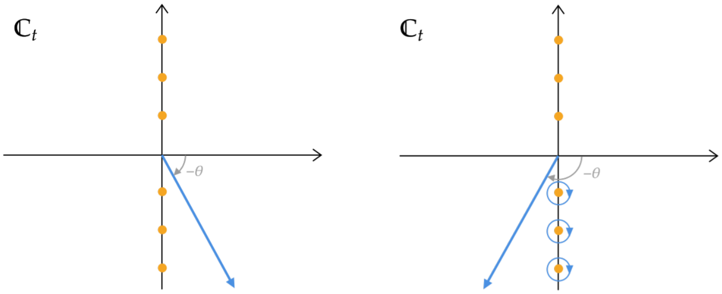

Figure A.1.: The Stokes phenomenon of $\mathcal{F}_1$

Note that the contour of integration runs along an angle $-\theta$ in the lower half plane in order to keep e^{-gt} real and exponentially suppressed. The Stokes automorphism on the product of gamma functions then acts as

$$\mathfrak{S}_{-\frac{\pi}{2}}\mathrm{e}^{\mathcal{F}_4-\mathcal{F}_2-2\mathcal{F}_1} = \left(1-\frac{2\mathrm{e}^{2\pi \mathrm{i} g}}{1+\mathrm{e}^{4\pi \mathrm{i} g}}\right)\mathrm{e}^{\mathcal{F}_4-\mathcal{F}_2-2\mathcal{F}_1}\,. \tag{A.20}$$

This Stokes jump is independent of the Borel transform that we chose. Taking the above jump into account in Eq. (A.13) and now using the 0-Borel transform that we use throughout the paper, we find that after the Stokes transition, i.e. for g in the left half of the complex plane, it becomes

$$\begin{aligned}\int_0^{-\mathrm{i}\infty+\epsilon} &\mathcal{B}_0[Z^{(1)}]\left(\frac{3}{2}(\mathrm{e}^t-1)\right)\mathrm{e}^{-gt}\mathrm{d}t \\ &= \left(1-\frac{2\mathrm{e}^{2\pi \mathrm{i} g}}{1+\mathrm{e}^{4\pi \mathrm{i} g}}\right)\int_0^{-\mathrm{i}\infty-\epsilon}\mathcal{B}_0[Z^{(1)}]\left(\frac{3}{2}(\mathrm{e}^t-1)\right)\mathrm{e}^{-gt}\mathrm{d}t\,.\end{aligned} \tag{A.21}$$

This implements the Stokes phenomenon that we use in Sec. 3.3 to analytically continue the exact large order relation, Eqs. (3.90)-(3.92), when $\frac{\pi}{2}<\theta<\frac{3\pi}{2}$.

Appendix B.

Resurgence analysis of the Adler function at $\mathcal{O}(1/N_f^2)$

B.1. Master integrals

In this appendix we discuss the master scalar integrals we used in the calculation of the diagrams considered in chapter 5. The diagrams given in Figs. 5.1a, 5.7a, 5.7b and 5.7c can be computed using standard one-loop techniques and the one-loop massless master integral

$$\begin{aligned}\hat{I}^{(1,2)}(n_1,n_2) &\equiv (-q^2)^{n_{12}-d/2}\int\frac{d^dk}{\mathrm{i}\pi^{d/2}}\frac{1}{(-k^2)^{n_1}(k-q)^{2n_2}}\\ &=\frac{\Gamma(n_{12}-\frac{d}{2})}{\Gamma(d-n_{12})}\frac{\Gamma(\frac{d}{2}-n_1)}{\Gamma(n_1)}\frac{\Gamma(\frac{d}{2}-n_2)}{\Gamma(n_2)}\,,\end{aligned}\tag{B.1}$$

with d the number of space-time dimensions. We have adopted the following notation: the superscripts for an integral $\hat{I}^{(l,n)}$ indicate the number of loops and the number of propagators. The prefactor ensures that the result is independent of $(-q^2)$ and we do not get factors of π. Furthermore, we introduced the shorthand notation $n_{12}=n_1+n_2$ with its natural extension to the cases with more indices.

For the calculation of the diagrams in Figs. 5.1b and 5.7d, we need to consider the massless two loop two-point function

$$\begin{aligned}&\hat{I}^{(2,5)}(n_1,n_2,n_3,n_4,n_5)\\ &\qquad\equiv(-q^2)^{n_{12345}-d}\int\frac{d^dk_1}{\mathrm{i}\pi^{d/2}}\frac{d^dk_2}{\mathrm{i}\pi^{d/2}}\frac{1}{(-k_1^2)^{n_1}(-k_2^2)^{n_2}(-k_3^2)^{n_3}(-k_4^2)^{n_4}(-k_5^2)^{n_5}}\,,\end{aligned}\tag{B.2}$$

where $k_3=k_2-q$, $k_4=k_1-q$ and $k_5=k_1-k_2$. A general representation for the massless two-point function with arbitrary powers n_i of the propagators can be found in [182]. For a historical overview of this integral, see [183]. For the diagram with one bubble chain, given in Fig. 5.1b, we need the result for

$$\hat{I}^{(2,5)}(1,1,1,1,u+1). \tag{B.3}$$

We should mention here that we can work in $d=4$ dimensions, as the UV and IR divergences are regulated by the power u in the propagator. This integral was first solved using IBP relations and the method of uniqueness in [184], and the result in $d=4$ dimensions reads

$$\hat{I}^{(2,5)}(1,1,1,1,u+1) = -\frac{1}{2u}\left[\psi^{(1)}\left(\tfrac{1+u}{2}\right)-\psi^{(1)}\left(\tfrac{1-u}{2}\right)+\psi^{(1)}\left(\tfrac{2-u}{2}\right)-\psi^{(1)}\left(\tfrac{2+u}{2}\right)\right], \tag{B.4}$$

with $\psi^{(1)}(z)=\frac{\mathrm{d}^2}{\mathrm{d}z^2}\log\Gamma(z)$ the trigamma function.

For the diagram in Fig. 5.7d with two bubble chains, we need the two-loop master integral

$$\hat{I}^{(2,5)}(1,u_2+1,1,1,u_1+1). \tag{B.5}$$

This master was computed in [185, 186] for three arbitrary powers using IBP relations. The result reads[1]

$$\frac{\hat{I}^{(2,5)}(\alpha,\beta,1,1,\gamma)}{\gamma\delta\hat{I}^{(1,2)}(1,\delta+1)} = \frac{\hat{I}^{(1,2)}(\alpha,\gamma+1)}{d-3}S\left(\tfrac{d}{2}-\alpha-1,\beta-1,\tfrac{d}{2}+\alpha-\delta-2,\delta-\beta\right)+(\alpha\leftrightarrow\beta) \tag{B.6}$$

with $\delta=\alpha+\beta+\gamma-\frac{d}{2}$. The function S encapsulates all symmetries of this integral and is given by:

$$S(a,b,c,d)=\frac{\psi(1-c)-\psi(c)}{H(a,b,c,d)}-\frac{1}{c}-\frac{b+c}{bc}F(a+c,-b,-c,b+d) \tag{B.7}$$

where $\psi(z)=\frac{\mathrm{d}}{\mathrm{d}z}\log\Gamma(z)$ is the digamma function and

$$H(a,b,c,d)=\frac{\Gamma(1+a)\Gamma(1+b)\Gamma(1+c)\Gamma(1+d)\Gamma(1+a+b+c+d)}{\Gamma(1+a+c)\Gamma(1+a+d)\Gamma(1+b+c)\Gamma(1+b+d)}, \tag{B.8}$$

$$F(a,b,c,d)=\sum_{n=1}^{\infty}\frac{(-a)_n(-b)_n}{(1+c)_n(1+d)_n}={}_3F_2(-a,-b,1;1+c,1+d;1)-1\,. \tag{B.9}$$

---

[1] In [186], the integral is denoted by $I_4(\alpha,\beta,\gamma,\delta)$.

We have used this result to calculate the expansion of $\hat{I}^{(2,5)}(1, u_2+1, 1, 1, u_1+1)$ in u_1 and u_2. After the expansion, one still needs to carry out the infinite sum in Eq. (B.9). In order to perform the sums, we made use of the package `Summer` [187], which itself relies on `FORM` [188, 189]. The first few terms read

$$\begin{aligned}\hat{I}^{(2,5)}(1, u_2{+}1, 1, 1, u_1{+}1) &= 6\zeta_3 + 5\zeta_5\left(3u_1^2 + 3u_1u_2 + 2u_2^2\right)\\ &\quad - 6\zeta_3^2\left(u_1^2u_2 + u_1u_2^2\right) + \frac{525}{8}\zeta_7 u_1^2u_2^2 + \mathcal{O}\Big(u_1^3, u_2^3\Big). \qquad \text{(B.10)}\end{aligned}$$

Notice that in the limit $u_2 \to 0$ and $u_1 \to u$, one recovers the expansion of Eq. (B.4) around $u = 0$. For the calculation of the full diagram, we want to take the convolution integral, Eq. (4.19), to get the Borel transform in terms of $u = u_1 + u_2$. As

$$\int_0^u du_1\ u_1^m (u - u_1)^n = \frac{m!n!}{(m+n+1)!} u^{m+n+1}, \qquad \text{(B.11)}$$

we see that if we want the Borel transform up to order $m+n+1$, we need all terms where the powers of u_1 and u_2 add up to $m+n$. We have added the expansion in terms of u_1 and u_2 of $\hat{I}^{(2,5)}(1, u_2+1, 1, 1, u_1+1)$ up to combined order $m+n = 18$ in a separate file that is available from the authors upon request. The result can be expressed in terms of regular zeta values and *multiple-zeta values* (MZVs) defined as

$$\zeta_{m_1, m_2, \ldots, m_k} \equiv \sum_{i_1 > i_2 > \ldots > i_k > 0} \frac{1}{i_1^{m_1} i_2^{m_2} \ldots i_k^{m_k}}\,, \qquad \text{(B.12)}$$

for positive integers m_j. The number of indices of the sums is called the *depth* and the sum of the powers, i.e. $m_1 + \ldots + m_k$, the *weight*. Of course, MZVs of depth one are just the regular zeta values. The `Summer` package contains all sums up to weight nine. In order to express the sums of higher weight in terms of MZVs, we made use of the tables in the multiple zeta value data-mine up to the maximal available weight 22 [117]. To give an example, at order $u_1^4 u_2^4$ one finds

$$\zeta_{5,3,3} = \sum_{i_1=1}^{\infty} \frac{1}{i_1^5} \sum_{i_2=1}^{i_1-1} \frac{1}{i_2^3} \sum_{i_3=1}^{i_2-1} \frac{1}{i_3^3}\,, \qquad \text{(B.13)}$$

which in the data file are denoted by `z5z3z3`, with similar notations for sums of higher depth. In general, at higher orders in u_1 and u_2, the weight increases and one also finds MZVs of larger depth. For numerical values of these MZVs, up to 100 decimal places, we have used the EZ-Face calculator [190] that can still be found at http://wayback.cecm.sfu.ca/cgi-bin/EZFace/zetaform.cgi and checked its output up to several decimal places.

B.2. Diagram momentum integrals

Recall the definition of the Adler function (4.1)

$$D(Q^2) = 4\pi^2 Q^2 \frac{\mathrm{d}\Pi(Q^2)}{\mathrm{d}Q^2}\,, \tag{B.14}$$

where $\Pi(Q^2)$ is related to the correlation function of two vector currents $j_\mu = \bar{\psi}\gamma_\mu\psi$ of massless quarks,

$$(-i)\int d^4x e^{-iqx}\langle 0|T\{j_\mu(x)j_\nu(0)\}|0\rangle = (q_\mu q_\nu - \eta_{\mu\nu}q^2)\Pi(Q^2)\,, \tag{B.15}$$

and where $Q^2 = -q^2$. In order to extract $\Pi(Q^2)$, one can use

$$\frac{\eta^{\mu\nu}}{(d-1)Q^2}\,, \tag{B.16}$$

as the projector for $\Pi(Q^2)$. At order $1/N_f$, this yields the following integral expression for the diagram of Fig. 5.1a,

$$\begin{aligned}\mathcal{B}[\Pi_a(Q^2)](u) = -\mathrm{i}\frac{(4\pi)^2(\mu^{2\epsilon})^2}{(d-1)Q^2}\int \frac{d^dk_1}{(2\pi)^d}\frac{d^dk_2}{(2\pi)^d}\mathcal{B}\big[\alpha D^{\rho\sigma}(k_2)\big](u)\\ \times \operatorname{tr}\left[\gamma^\mu \frac{\not{k}_1}{k_1^2}\gamma_\rho \frac{(\not{k}_1-\not{k}_2)}{(k_1-k_2)^2}\gamma_\sigma \frac{\not{k}_1}{k_1^2}\gamma_\mu \frac{(\not{k}_1-\not{q})]}{(k_1-q)^2}\right],\end{aligned} \tag{B.17}$$

where the Borel transform of the bubble chain, $\mathcal{B}\big[\alpha D^{\rho\sigma}(k_2)\big](u)$, is given in Eq. (4.18). After performing the spinor trace, Eq. (B.17) can be written in terms of the master integral of Eq. (B.1). Likewise, for the diagram of Fig. 5.1b we get

$$\begin{aligned}\mathcal{B}[\Pi_b(Q^2)](u) = -\mathrm{i}\frac{(4\pi)^2(\mu^{2\epsilon})^2}{(d-1)Q^2}\int \frac{d^dk_1}{(2\pi)^d}\frac{d^dk_2}{(2\pi)^d}\mathcal{B}\big[\alpha D^{\rho\sigma}(k_1-k_2)\big](u)\\ \times \operatorname{tr}\left[\gamma^\mu \frac{\not{k}_1}{k_1^2}\gamma_\rho \frac{\not{k}_2}{k_2^2}\gamma_\mu \frac{(\not{k}_2-\not{q})}{(k_2-q)^2}\gamma_\sigma \frac{(\not{k}_1-\not{q})]}{(k_1-q)^2}\right],\end{aligned} \tag{B.18}$$

which after the fermion trace has been performed, reduces to the master integrals of Eqs. (B.1) and (B.4).

Let us consider the diagrams of Fig. 5.7 studied in Sec. 5.2 at order $1/N_f^2$. For the diagram of Fig. 5.7a, the loop integral reads

$$\mathcal{B}[\Pi_a(Q^2)](u_1,u_2) = -\mathrm{i}\frac{(4\pi)^4(\mu^{2\epsilon})^3}{(d-1)Q^2}\int \frac{d^dk_1}{(2\pi)^d}\frac{d^dk_2}{(2\pi)^d}\frac{d^dk_3}{(2\pi)^d}\mathcal{B}\big[\alpha D^{\rho\sigma}(k_1-k_3)\big](u_1) \tag{B.19}$$

$$\times\, \mathcal{B}\big[\alpha D^{\alpha\beta}(k_1-k_2)\big](u_2)\mathrm{tr}\left[\gamma^\mu \frac{\not{k}_1}{k_1^2}\gamma_\rho \frac{\not{k}_3}{k_3^2}\gamma_\sigma \frac{\mathrm{i}\not{k}_1}{k_1^2}\gamma_\alpha \frac{\not{k}_2}{k_2^2}\gamma_\beta \frac{\not{k}_1}{k_1^2}\gamma_\mu \frac{(\not{k}_1-\not{q})]}{(k_1-q)^2}\right].$$

After the spinor trace has been performed, the remaining integrals reduce to the master of Eq. (B.1). Likewise, the diagrams of Figs. 5.7b and 5.7c read

$$\begin{aligned}&\mathcal{B}[\Pi_b(Q^2)](u_1,u_2)\\ &\quad= -\mathrm{i}\frac{(4\pi)^4(\mu^{2\epsilon})^3}{(d-1)Q^2}\int \frac{d^dk_1}{(2\pi)^d}\frac{d^dk_2}{(2\pi)^d}\frac{d^dk_3}{(2\pi)^d}\mathcal{B}\big[\alpha D^{\rho\sigma}(k_1-k_3)\big](u_1)\mathcal{B}\big[\alpha D^{\alpha\beta}(k_1-k_2)\big](u_2)\\ &\qquad\times \mathrm{tr}\left[\gamma^\mu \frac{\not{k}_1}{k_1^2}\gamma_\rho \frac{\not{k}_3}{k_3^2}\gamma_\sigma \frac{\not{k}_1}{k_1^2}\gamma_\mu \frac{(\not{k}_1-\not{q})}{(k_1-q)^2}\gamma_\alpha \frac{(\not{k}_2-\not{q})}{(k_2-q)^2}\gamma_\beta \frac{(\not{k}_1-\not{q})}{(k_1-q)^2}\right],\end{aligned} \tag{B.20}$$

and

$$\begin{aligned}&\mathcal{B}[\Pi_c(Q^2)](u_1,u_2)\\ &\quad= -\mathrm{i}\frac{(4\pi)^4(\mu^{2\epsilon})^4}{(d-1)Q^2}\int \frac{d^dk_1}{(2\pi)^d}\frac{d^dk_2}{(2\pi)^d}\frac{d^dk_3}{(2\pi)^d}\mathcal{B}\big[\alpha D^{\rho\sigma}(k_1-k_2)\big](u_1)\mathcal{B}\big[\alpha D^{\alpha\beta}(k_2-k_3)\big](u_2)\\ &\qquad\times \mathrm{tr}\left[\gamma^\mu \frac{\not{k}_1}{k_1^2}\gamma_\rho \frac{\not{k}_2}{k_2^2}\gamma_\alpha \frac{\not{k}_3}{k_3^2}\gamma_\beta \frac{\not{k}_2}{k_2^2}\gamma_\sigma \frac{\not{k}_1}{k_1^2}\gamma_\mu \frac{(\not{k}_1-\not{q})]}{(k_1-q)^2},\right]\end{aligned} \tag{B.21}$$

which reduce to the same master integral of Eq. (B.1). Finally, we studied the diagram of Fig. 5.7d which reads

$$\begin{aligned}&\mathcal{B}[\Pi_d(Q^2)](u_1,u_2)\\ &\quad= -\mathrm{i}\frac{(4\pi)^4(\mu^{2\epsilon})^3}{(d-1)Q^2}\int \frac{d^dk_1}{(2\pi)^d}\frac{d^dk_2}{(2\pi)^d}\frac{d^dk_3}{(2\pi)^d}\mathcal{B}\big[\alpha D^{\rho\sigma}(k_1-k_2)\big](u_1)\mathcal{B}\big[\alpha D^{\alpha\beta}(k_3)\big](u_2)\\ &\qquad\times \mathrm{tr}\left[\gamma^\mu \frac{\not{k}_2}{k_2^2}\gamma_\alpha \frac{(\not{k}_2-\not{k}_3)}{(k_2-k_3)^2}\gamma_\beta \frac{\not{k}_2}{k_2^2}\gamma_\rho \frac{\not{k}_1}{k_1^2}\gamma_\mu \frac{(\not{k}_1-\not{q})}{(k_1-q)^2}\gamma_\sigma \frac{(\not{k}_2-\not{q})}{(k_2-q)^2}\right].\end{aligned} \tag{B.22}$$

This diagram can be written in terms of the master integrals of Eqs. (B.1) and (B.6) where the latter master integral requires the most computational effort. See App. B.1 for the details of this computation. We refer to App. B.3 for a brief discussion on the remaining diagrams at order $1/N_f^2$.

B.3. Remaining $\mathcal{O}(1/N_f^2)$ diagrams

In Sec. 5.2, we considered a subset of the diagrams at order $1/N_f^2$ in the flavour expansion. In this appendix, we briefly discuss the current status of the remaining diagrams at order $1/N_f^2$, given in Fig. B.1. Notice that these are the abelian diagrams and we did not present the diagrams with non-abelian self interactions of the gauge field.

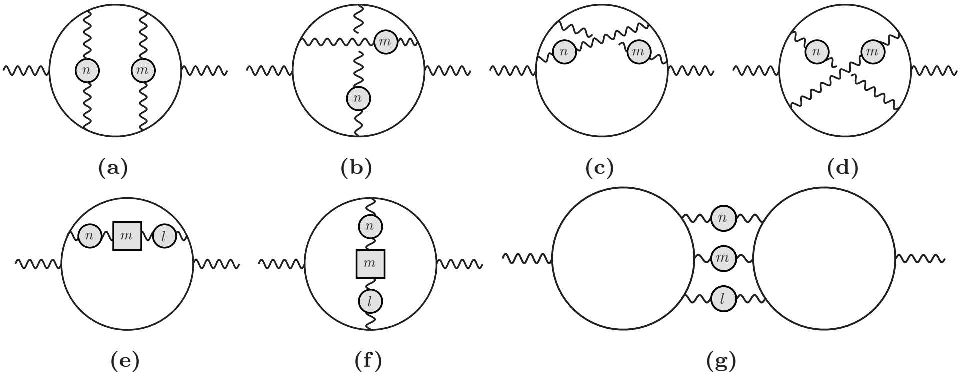

Figure B.1.: Diagrams at order $1/N_f^2$ in the flavour expansion that are not computed in this thesis.

As explained at the end of Sec. 4.1.2, one uses the process of naive non-abelianization, i.e. replace β_{0f} by β_0, to model the non-abelian effects.

The two bubble chain diagrams (a)-(d) of Fig. B.1 were considered in [98]. In particular, these authors focused on the leading UV singularity because a full calculation of these diagrams is not possible yet, as the corresponding master integrals are not known. Notice that the results given are for the vacuum polarization (taking the derivative with respect to Q^2, Eq. (5.2), yields the results for the Adler function). The leading singularity found is[2]

$$\frac{\log(1+u)}{(1+u)^2}\,, \tag{B.23}$$

which would imply the leading order growth of the perturbative coefficients to be

$$d_n \sim (-1)^n \Gamma(n+2)\psi(n+2)\,. \tag{B.24}$$

where ψ is the digamma function. At the level of the transseries, this translates to a non-perturbative contribution of the form

$$\frac{1}{\alpha}\log(\alpha)\, e^{\frac{1}{\alpha}}\,. \tag{B.25}$$

Recall that an exponential like this is typical for UV renormalons and grows exponentially large when $\alpha \to 0$. Possible solutions were already discussed in Sec. 5.1.5: either the transseries parameter in front of such a momomial vanishes, or as long as α

---

[2] The parameter u in [98] is defined with an opposite sign compared to the definition used in this thesis. Here, we present the result in our conventions.

has a definite value, an expression like this still makes sense. Furthermore, we notice that the leading order growth of Eq. (B.24) is enhanced by a factor n compared to leading order growth $\Gamma(n+1)\Psi(n+1)$ of the diagrams considered in Sec. 5.2. In order to construct the transseries, and the relations between the non-perturbative sectors, one either needs access to sufficient perturbative data of these diagrams, or one needs the expansion of the Borel transform around the singularity at $u = -1$ as well as expansions around other singular points in u. In particular, we recall from diagram (d) discussed in Sec. 5.2, that for both procedures one has to compute a number of coefficients that is at least in the double digits, which is a challenging task to perform.

In Figs. B.1e and B.1f, we show the so called nested diagrams, where the square box denotes the LO $(1/N_f)$ diagrams considered in Sec. 5.1, i.e.

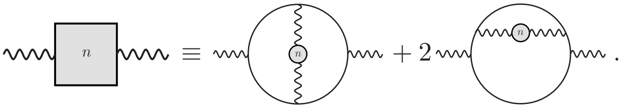

(B.26)

A discussion of the singularity structure in the Borel plane of these diagrams can be found in [116] (where again, the results given are for the vacuum polarization). Using Borel Padé techniques, these authors showed that the singularities for the sum of these two diagrams at $u = 1$ drops out (as expected by OPE arguments). Furthermore, they were able to deduce that the singularities at $u = 2$ and $u = -1$ are branch points, suggesting the presence of further asymptotic sectors. However, is was not possible to compute sufficient perturbative data to determine the precise nature of these branch points.

As far as we know, the diagram of Fig. B.1g has not been considered so far in the literature, as it is a difficult diagram with three bubble chains and its corresponding master integral is not known.

In order to compute the diagrams of Fig. B.1, one needs to compute difficult skeleton diagrams (i.e. the diagrams where the bubble chains are replaced by the analytic regularized propagators of Eq. (4.18)). In particular, this means that diagrams (e) and (f) are two loop skeleton diagrams, diagram (a)-(d) are three loop skeleton diagrams and diagram (g) is a four loop skeleton diagram. We expect that diagrams (d) and (g) are the most challenging diagrams to compute as these, respectively, correspond to three loop, non-planar master integrals with two analytic regularized propagators and a four loop master integral with three analytic regularized propagators.

Appendix C.

Rapidity regulators

In this appendix, we consider the following one-loop integral

$$R = \int [dk] \frac{1}{[k^2 - m^2]} \frac{1}{[(k+p_1)^2]} \frac{1}{[(k-p_2)^2]}\,, \tag{C.1}$$

with $p_i^2 = m^2$ and study three different regulators that can be used to regulate the rapidity divergences that show up once Eq. (C.1) is expanded in momentum regions. Before we discuss these regulators, let us briefly discuss how rapidity divergences appear. For reasons that will become clear in a moment, let us put the mass of the first propagator in Eq. (C.1) to M^2 for now and consider the collinear expansion

$$\begin{aligned} R\Big|_c &= \int [dk] \frac{1}{[k^2 - M^2]} \frac{1}{[(k+p_1)^2]} \frac{1}{[-k^+ p_2^-]} \\ &= \frac{i\mu^{2\epsilon} e^{\epsilon\gamma_E}}{(4\pi)^2} \frac{\Gamma(\epsilon)}{\hat{s}} \int_0^1 dx\, x^{-1} (1-x)^{-\epsilon} \left(-m^2 x + M^2\right)^{-\epsilon}\,, \end{aligned} \tag{C.2}$$

where we performed the loop integral. One can obtain the remaining x-integral after a standard Feynman parametrization. In the limit $M^2 \to m^2$ that we are interested in, the remaining x-integral

$$\int_0^1 dx\, x^{-1}\, (1-x)^{-2\epsilon} \tag{C.3}$$

diverges for $x \to 0$.[1] To be precise, we see that the dimensional regulator ϵ does not regulate all divergences present in the integral in Eq. (C.2). This so-called rapidity divergence can be traced back to the fact that the eikonal propagator only contains the k^+ component and therefore new divergences may arise from the k^+-integral as ϵ only regulates the transverse momentum component $k_\perp$.

---

[1] In fact, the x-integral diverges for all $M \neq 0$.

Eq. (C.2) also shows that in the limit $M^2 \to 0$, the divergence of the remaining x-integral

$$\int_0^1 dx\, x^{-1-\epsilon}\,(1-x)^{-\epsilon} = \frac{\Gamma(-\epsilon)\Gamma(1-\epsilon)}{\Gamma(1-2\epsilon)}\,, \tag{C.4}$$

is fully regulated by ϵ alone. In other words, the presence of rapidity divergences in a Feynman integral is sensitive to propagator masses. This example therefore reflects why topology A, being free of rapidity divergences, is so different from topology B and X, which do have rapidity divergences.

C.1. Full result

To validate that rapidity regulators work, we need to calculate the full integral Eq. (C.1). A straightforward calculation (using e.g. the Schwinger parameterisation followed by one-fold Melin-Barnes integral) yields

$$\begin{aligned} R^{(\text{full})} = \frac{ie^{\epsilon\gamma_E}}{(4\pi)^2}\left(\frac{\mu^2}{m^2}\right)^{\epsilon}\Bigg[&\left(1-\frac{4m^2}{s}\right)^{-\frac{1}{2}+\epsilon}\frac{\pi^2}{s}\frac{\Gamma(1-2\epsilon)\Gamma(1+2\epsilon)}{\Gamma^2(1-\epsilon)\Gamma(1+\epsilon)} \\ &-\frac{\Gamma(-1-2\epsilon)\Gamma(1+\epsilon)}{m^2\Gamma(1-2\epsilon)}\,{}_2F_1(1,1,\frac{3}{2}+\epsilon,\frac{s}{4m^2}) \\ &+\left(\frac{-s}{m^2}\right)^{-\epsilon}\frac{\Gamma^2(1-\epsilon)\Gamma(\epsilon)}{2m^2\Gamma(1-2\epsilon)}\,{}_2F_1(1,1-\epsilon,\frac{3}{2},\frac{s}{4m^2})\Bigg], \end{aligned} \tag{C.5}$$

where we recall that $s = (p_1+p_2)^2 = 2m^2 + \hat{s} + m^4/\hat{s}$. In the small mass limit $m^2 \ll \hat{s}$, we expand Eq. (C.5) up to NNLP as

$$\begin{aligned} R^{(\text{full})}\Big|_{\text{NNLP}} = \frac{i}{(4\pi)^2\hat{s}}\Bigg\{&\left[4\zeta_2+\frac{1}{2}\ln^2\left(-\frac{m^2}{\hat{s}}\right)\right]-\frac{2m^2}{\hat{s}} \\ &+\left(\frac{m^2}{\hat{s}}\right)^2\left[\frac{1}{2}+4\zeta_2+\frac{1}{2}\ln^2\left(-\frac{m^2}{\hat{s}}\right)\right]\Bigg\}+\mathcal{O}\left(\epsilon\right). \end{aligned} \tag{C.6}$$

This expansion can now be compared to the region expansion of Eq. (C.1).

C.2. Analytic regulator

As this is the regulator used throughout the main body of this thesis, we first discuss the analytic regulator, which is implemented by raising the last propagator to a fractional power ν such that Eq. (C.1) is rewritten as [161]

$$R^{(\text{a.r.})} = \int [dk] \frac{1}{[k^2 - m^2]} \frac{1}{[(k+p_1)^2]} \frac{\left(\tilde{\mu}^2\right)^{\nu}}{[(k-p_2)^2]^{1+\nu}} \,. \tag{C.7}$$

For simplicity, we only consider the LP contribution in the remainder of this appendix. The hard contribution is given by

$$\begin{aligned} R^{(\text{a.r.})}\Big|_h &= \int [dk] \frac{1}{[k^2]} \frac{1}{[k^2 + k^- p_1^+]} \frac{\left(\tilde{\mu}^2\right)^{\nu}}{[k^2 - k^+ p_2^-]^{1+\nu}} \\ &= \frac{i}{(4\pi)^2 \hat{s}} \left(\frac{\mu^2}{-\hat{s}}\right)^{\epsilon} \left[\frac{1}{\epsilon^2} - \frac{\zeta_2}{2} + \mathcal{O}(\epsilon, \nu)\right] . \end{aligned} \tag{C.8}$$

We note there is no rapidity divergence in the hard region, so we can safely set $\nu = 0$ either at the beginning or at the end of the calculation. In the collinear region, we have

$$\begin{aligned} R^{(\text{a.r.})}\Big|_c &= \int [dk] \frac{1}{[k^2 - m^2]} \frac{1}{[(k+p_1)^2]} \frac{\left(\tilde{\mu}^2\right)^{\nu}}{[-k^+ p_2^-]^{1+\nu}} \\ &= \frac{i e^{\epsilon \gamma_E}}{(4\pi)^2 \hat{s}} \left(\frac{\mu^2}{m^2}\right)^{\epsilon} \left(\frac{\tilde{\mu}^2}{\hat{s}}\right)^{\nu} \Gamma(\epsilon) \int_0^1 dx \, x^{-1-\nu} (1-x)^{-2\epsilon} . \end{aligned} \tag{C.9}$$

Comparing to Eq. (C.3) we explicitly see how the power ν regulates the rapidity divergence in a similar manner as how ϵ regulates the IR and UV divergences in Eq. (C.4). Carrying out the integral over x yields

$$R^{(\text{a.r.})}\Big|_c = \frac{i}{(4\pi)^2 \hat{s}} \left(\frac{\mu^2}{m^2}\right)^{\epsilon} \left(\frac{\tilde{\mu}^2}{\hat{s}}\right)^{\nu} \left[-\frac{1}{\epsilon\,\nu} + 2\zeta_2 + \mathcal{O}(\epsilon, \nu)\right] . \tag{C.10}$$

Similarly, after expanding Eq. (C.7) in the anti-collinear region, we obtain

$$\begin{aligned} R^{(\text{a.r.})}\Big|_{\bar{c}} &= \int [dk] \frac{1}{[k^2 - m^2]} \frac{1}{[k^- p_1^+]} \frac{\left(\tilde{\mu}^2\right)^{\nu}}{[(k-p_2)^2]^{1+\nu}} \\ &= \frac{i}{(4\pi)^2 \hat{s}} \left(\frac{\mu^2}{m^2}\right)^{\epsilon} \left(\frac{\tilde{\mu}^2}{-m^2}\right)^{\nu} \left[-\frac{1}{\epsilon^2} + \frac{1}{\epsilon\,\nu} + \frac{5\zeta_2}{2} + \mathcal{O}(\epsilon, \nu)\right] . \end{aligned} \tag{C.11}$$

Note that the symmetry of the collinear and anti-collinear region gets broken due to the fact that we added the analytic regulator to the last propagator only.[2] Here, we remark that the natural overall scales for a hard or collinear loop are $(\mu^2/(-\hat{s}))^{\epsilon}$ and $(\mu^2/m^2)^{\epsilon}$ respectively. However, with the analytic regulator, we get slightly different

---

[2] This is similar to diagram (e) as is discussed in Sec. 7.2.2: adding a power ν in a symmetric way, i.e. to both the second and third propagator, does not regulate the rapidity divergences.

overall factors $(\tilde{\mu}^2/\hat{s})^\nu$ and $(\tilde{\mu}^2/(-m^2))^\nu$, see Eqs. (C.10) and (C.11) respectively. This is an effect of the usual Wick rotation to Euclidean space, which produces an additional factor $(-1)^\nu$.

Other regions do not contribute. For example, the semi-hard region leads to a scaleless integral and thus a vanishing contribution

$$R^{(\text{a.r.})}\Big|_{sh} = \int [dk] \frac{1}{[k^2-m^2]} \frac{1}{[k^- p_1^+]} \frac{\left(\tilde{\mu}^2\right)^\nu}{[-k^+ p_2^-]^{1+\nu}} = 0. \tag{C.12}$$

Now, after combining all contributing regions we find that

$$\begin{aligned} R^{(\text{a.r.})}\Big|_{\text{LP}} &= R^{(\text{a.r.})}\Big|_h + R^{(\text{a.r.})}\Big|_c + R^{(\text{a.r.})}\Big|_{\bar{c}} \\ &= \frac{i}{(4\pi)^2 \hat{s}} \left[4\zeta_2 + \frac{1}{2}\ln^2\left(-\frac{m^2}{\hat{s}}\right)\right] + \mathcal{O}(\epsilon), \end{aligned} \tag{C.13}$$

which is the same as the LP result in Eq. (C.6) and we notice that all rapidity divergences have cancelled in the final result, as they should.

C.3. Modified analytic regulator

Instead of raising the power of a propagator by ν, the analytic regulator can also be used to modify the phase space measure as [164]

$$\int d^dk\, \delta\left(k^2\right) \theta\left(k^0\right) \;\rightarrow\; \int d^dk\, \delta\left(k^2\right) \theta\left(k^0\right) \left(\frac{\tilde{\mu}}{k^-}\right)^\nu . \tag{C.14}$$

Here the amplitude itself does not need to be modified. This has the advantage that fundamental properties such as gauge invariance and the eikonal form of the soft and collinear emissions are maintained. The modified analytic regulator is therefore convenient to construct factorization theorems to all orders. To this end, we can modify the measure $[dk]$ as follows [191]

$$\int [dk] \;\rightarrow\; \int [dk] \left(\frac{\tilde{\mu}^2}{-k^+ p_2^- + i0^+}\right)^\nu , \tag{C.15}$$

and define

$$R^{(\text{m.a.r.})} = \int [dk] \frac{1}{[k^2-m^2]} \frac{1}{[(k+p_1)^2]} \frac{1}{[(k-p_2)^2]} \left(\frac{\tilde{\mu}^2}{-k^+ p_2^- + i0^+}\right)^\nu . \tag{C.16}$$

Note that the chosen regulator on the right hand side of Eq. (C.15) leads to $R^{(\text{m.a.r.})}|_h = R^{(\text{a.r.})}|_h$, $R^{(\text{m.a.r.})}|_c = R^{(\text{a.r.})}|_c$ and $R^{(\text{m.a.r.})}|_{sh} = R^{(\text{a.r.})}|_{sh}$. After a direct calculation of $R^{(\text{m.a.r.})}_{\bar{c}}$, we have

$$\begin{aligned} R^{(\text{m.a.r.})}\Big|_{\bar{c}} &= \int [dk] \frac{1}{[k^2-m^2]} \frac{1}{[k^- p_1^+]} \frac{1}{[(k-p_2)^2]} \frac{(\tilde{\mu})^2}{[-k^+ p_2^-]^\nu} \\ &= \frac{i e^{\epsilon \gamma_E}}{(4\pi)^2 \hat{s}} \left(\frac{\mu^2}{m^2}\right)^\epsilon \left(\frac{\tilde{\mu}^2}{-m^2}\right)^\nu \left[\frac{\Gamma(\epsilon)}{\nu} - \Gamma(\epsilon)\left(\psi(1-2\epsilon) - \psi(\epsilon)\right) + \mathcal{O}(\nu)\right] . \end{aligned} \tag{C.17}$$

Comparing $R^{(\text{m.a.r.})}|_{\bar{c}}$ with $R^{(\text{a.r.})}|'_{\bar{c}}$, we find that

$$R^{(\text{m.a.r.})}\Big|_{\bar{c}} - R^{(\text{a.r.})}\Big|_{\bar{c}} = \mathcal{O}(\nu). \tag{C.18}$$

which means that this regulator is also sufficient to reproduce the result of Eq. (C.6).

C.4. δ-regulator

The final regulator we want to discuss is the so-called δ-regulator [192]. It is implemented by adding a small mass to the propagator denominators,

$$R^{(\delta)} = \int [dk] \frac{1}{[k^2 - m^2 - \delta_1]} \frac{1}{[(k+p_1)^2] - \delta_2]} \frac{1}{[(k-p_2)^2 - \delta_3]} . \tag{C.19}$$

The δ_i are regulator parameters that are set to zero unless they are needed to regulate any divergences. Following the discussion below Eq. (C.2), we see that we can immediately put $\delta_1 = 0$ from the beginning as Eq. (C.2) is divergent for all $M \neq 0$. This means that the rapidity divergences have to be regulated by δ_2 and/or δ_3.

We recall from Sec. C.2 that the hard region is free of rapidity divergences, so δ_2 and δ_3 can be set to zero in this region as well, which reproduces Eq. (C.8)

$$R^{(\delta)}\Big|_h = \frac{i}{(4\pi)^2 \hat{s}} \left(\frac{\mu^2}{-\hat{s}}\right)^\epsilon \left[\frac{1}{\epsilon^2} - \frac{\zeta_2}{2} + \mathcal{O}(\epsilon)\right] . \tag{C.20}$$

Next, we consider the collinear expansion

$$\begin{aligned} R^{(\delta)}\Big|_c &= \int [dk] \frac{1}{[k^2-m^2]} \frac{1}{[(k+p_1)^2 - \delta_2]} \frac{1}{[-k^+ p_2^- - \delta_3]} \\ &= \frac{i \mu^{2\epsilon} e^{\epsilon \gamma_E}}{(4\pi)^2} \frac{\Gamma(\epsilon)}{\hat{s}} \int_0^1 dx\ \left(x - \delta_3/\hat{s}\right)^{-1} \left(m^2(1-x)^2 + \delta_2 x\right)^{-\epsilon} . \end{aligned} \tag{C.21}$$

Comparing Eq. (C.21) to Eq. (C.3) we see that δ_3 regulates the rapidity divergence in the remaining x-integral. Furthermore, we notice that δ_2 is not needed to regulate the divergence and can therefore be set to zero. Carrying out the remaining x-integral and performing the ϵ-expansion yields

$$R^{(\delta)}\Big|_{c} = \frac{i}{(4\pi)^2\hat{s}}\left(\frac{\mu^2}{m^2}\right)^{\epsilon}\left[\frac{1}{\epsilon}\ln\left(1-\frac{\hat{s}}{\delta_3}\right)+2\mathrm{Li}_2\left(\frac{1}{1-\delta_3/\hat{s}}\right)+\mathcal{O}(\epsilon)\right]. \tag{C.22}$$

Similarly for the anti-collinear region we now need to keep δ_2 to regulate the rapidity divergence and can set $\delta_3 = 0$. This yields

$$R^{(\delta)}\Big|_{\bar{c}} = \int [dk]\frac{1}{[k^2-m^2]}\frac{1}{[k^-p_1^+ - \delta_2]}\frac{1}{[(k-p_2)^2]} = R^{(\delta)}\Big|_{c}\,(\delta_2 \leftrightarrow \delta_3)\,. \tag{C.23}$$

Next, we take the semi-hard expansion, where both δ_2 and δ_3 need to be kept to regulate the rapidity divergences. Because of the mass-like terms δ_2 and δ_3, this does not lead to a scaleless integral like for the analytic regulator, Eq. (C.12). We get

$$\begin{aligned} R^{(\delta)}\Big|_{sh} &= \int [dk]\frac{1}{[k^2-m^2]}\frac{1}{[k^-p_1^+ - \delta_2]}\frac{1}{[-k^+p_2^- - \delta_3]} \\ &= \frac{i}{(4\pi)^2\hat{s}}\left(\frac{\mu^2}{m^2}\right)^{\epsilon}\left[\frac{1}{\epsilon^2}+\frac{1}{\epsilon}\ln\left(-\frac{m^2\hat{s}}{\delta_2\delta_3}\right)+\frac{\zeta_2}{2}-\mathrm{Li}_2\left(1+\frac{\delta_2\delta_3}{m^2\hat{s}}\right)+\mathcal{O}(\epsilon)\right], \end{aligned} \tag{C.24}$$

where we performed the ϵ-expansion.

Unfortunately, taking the h, c, $\bar{c}$ and sh regions together does not reproduce the LP part of the full result as given in Eq. (C.6) and in particular, the rapidity divergences are not canceled. The reason is that the semi-hard region has overlap with the collinear and anti-collinear regions. To be precise, taking the soft limit of the collinear region, Eq. (C.21) yields

$$R^{(\delta)}\Big|_{c,\emptyset} = \int [dk]\frac{1}{[k^2-m^2]}\frac{1}{[k^-p_1^+ - \delta_2]}\frac{1}{[-k^+p_2^- - \delta_3]} = R^{(\delta)}\Big|_{sh}, \tag{C.25}$$

where we recognize the semi-hard region $R^{(\delta)}|_{sh}$ of Eq. (C.24). To get the full result, we have to perform a so-called zero-bin subtraction where one subtracts the overlapping semi-hard region from the collinear region. Similarly, for the anti-collinear region one has to subtract

$$R^{(\delta)}\Big|_{\bar{c},\emptyset} = R^{(\delta)}\Big|_{sh}. \tag{C.26}$$

Indeed, adding all regions together and including the zero-bin subtractions yields the correct full result of Eq. (C.6)

$$\begin{aligned} R^{(\delta)}\Big|_{\mathrm{LP}} =& R^{(\delta)}\Big|_{h} + R^{(\delta)}\Big|_{c} + R^{(\delta)}\Big|_{\bar{c}} - R^{(\delta)}\Big|_{sh} \\ =& \frac{i}{(4\pi)^2 \hat{s}} \left[4\zeta_2 + \frac{1}{2}\ln^2\left(-\frac{m^2}{\hat{s}}\right)\right] + \mathcal{O}\left(\epsilon, \delta_i\right) \,, \end{aligned} \tag{C.27}$$

where in the last line we were able to take the $\delta_2 \to 0$ and $\delta_3 \to 0$ limits as the rapidity divergences cancel.

C.5. Choosing a rapidity regulator

We found that all three regulators can be used to regulate the rapidity divergence that shows up in the region expansion of the Feynman integral of Eq. (C.1). However, from a calculation point of view, the δ-regulator given in Sec. C.4 is the most complicated one as it leads to additional scales in the integral. Furthermore, it introduces an additional semi-hard region compared to the analytic and modified analytic regulators as discussed in Secs. C.2 and C.3. Regarding the δ-regulator, we showed that a zero-bin subtraction was necessary to avoid double counting momentum regions, which complicated the region analysis even further.

The analytic regulator and the modified analytic regulator are similar to each other. Neither of them increase the number of scales present in the Feynman integral and in case of the example discussed in this appendix, both lead to the same regions. With the specific choice we made for the analytic and modified analytic regulator, the only difference between the two at the integrand level comes from the anti-collinear region, Eq. (C.17). As a result, due to the additional propagator, the calculation of $R^{(\mathrm{m.a.r.})}|_{\bar{c}}$ is more complex than $R^{(\mathrm{a.r.})}|_{\bar{c}}$. This additional complexity that arises from the modified analytic regulator would make the two-loop calculation of the form factor much more difficult as compared to when one would adopt the analytic regulator instead. In this thesis, we therefore used the analytic regulator whenever rapidity divergences showed up.

Appendix D.

Regions in topology $\boldsymbol{X}$

As discussed in detail in Sec. 7.2, finding all momentum regions for a given Feynman integral can be a subtle process. To supplement the discussion given in Sec. 7.2, we provide in this appendix some details about the momentum region analysis for one of the Feynman integrals needed in the calculation of diagram (h), which belongs to topology X. Topology X in particular is difficult because of the complexity of the integrals - we needed two different rapidity regulators and had to route the momenta in three different ways in order to find all regions. The example we consider is $I^{\nu_1,\nu_1,\nu_2,\nu_2}_{X;1,1,1,1,1,1,0}$, which according to the momentum routing given in Eq. (7.3) reads

$$\begin{aligned}\mathcal{I}^X &= \frac{1}{C}\, I^{\nu_1,\nu_1,\nu_2,\nu_2}_{X;1,1,1,1,1,1,0} \\ &= \frac{1}{C}\int [dk_1][dk_2]\frac{1}{k_1^2}\frac{1}{k_2^2}\frac{\tilde{\mu}_1^{2\nu_1}}{[(k_2-p_1)^2-m^2]^{1+\nu_1}}\frac{\tilde{\mu}_1^{2\nu_1}}{[(k_1+k_2-p_1)^2-m^2]^{1+\nu_1}} \\ &\qquad\times\frac{\tilde{\mu}_2^{2\nu_2}}{[(k_1+p_2)^2-m^2]^{1+\nu_2}}\frac{\tilde{\mu}_2^{2\nu_2}}{[(k_1+k_2+p_2)^2-m^2]^{1+\nu_2}}\,,\end{aligned} \tag{D.1}$$

where for convenience we factored out

$$C = \frac{1}{(4\pi)^4\hat{s}^2}\,. \tag{D.2}$$

As discussed in Sec. 7.2.3, both regulators ν_1 and ν_2 are needed to regulate the rapidity divergences once $\mathcal{I}^X$ is expanded in different momentum regions. The full unexpanded integral on the contrary is free of rapidity divergences and therefore ν_1 and ν_2 can be set to zero, and the result can be found in Ref. [132, 170]. In order to compare with the momentum region approach, we expand the full result in the small mass limit up to NLP:

$$\begin{aligned}\mathcal{I}^X_{\text{full}}\Big|_{\text{NLP}} = \left(\frac{\mu^2}{m^2}\right)^{2\epsilon}\Bigg[&-\frac{1}{\epsilon}\left(\frac{1}{3}L^3+\zeta_2 L+\zeta_3\right)-\frac{1}{2}L^4+\zeta_2L^2-\zeta_3L-\frac{37\zeta_2^2}{10} \\ &-\frac{m^2}{\hat{s}}\left(4L^2-8L+4\zeta_2\right)+\mathcal{O}(\epsilon)\Bigg]\,,\end{aligned} \tag{D.3}$$

where we defined

$$L = \ln\left(-\frac{m^2}{\hat{s}}\right) . \tag{D.4}$$

In the remainder of this appendix we first present in App. D.1 all the momentum regions which contribute to the full result of Eq. (D.3) up to NLP. In App. D.2, we then compare these regions to the output of the software package `Asy.m`, which uses a geometric approach to reveal all the relevant regions for a given Feynman integral in parameter space. We finish this appendix with a discussion on a method that can be used to find all regions in momentum space.

D.1. Regions in momentum space

As we have shown in Sec. 7.2.3, there are 12 regions needed for the integrals of topology X.[1] To cover all these regions in momentum space, the region expansion given by the momentum routing of Eq. (7.3) is not sufficient, and one also needs to consider the routings as given in Eqs. (7.9) and (7.10). In what follows, we will show that indeed all three different momenta routings are needed in the region expansion of $\mathcal{I}^X$, Eq. (D.1), to get all the 12 regions that make up the full result of Eq. (D.3).

We first present all the eight different momentum regions given by the first parameterisation of topology X defined by Eq. (7.3). Up to NLP we get

$$\mathcal{I}^X\Big|_{hh} = \left(\frac{\mu^2}{-\hat{s}}\right)^{2\epsilon}\left[-\frac{1}{\epsilon^4}+\frac{6\zeta_2}{\epsilon^2}+\frac{83\zeta_3}{3\epsilon}+\frac{177\zeta_2^2}{10}+\frac{m^2}{\hat{s}}\left(-\frac{3}{\epsilon^2}-\frac{6}{\epsilon}+9\zeta_2+12\right)\right] \tag{D.5}$$

$$\begin{aligned}\mathcal{I}^X\Big|_{cc} = &\left(\frac{\mu^2}{m^2}\right)^{2\epsilon}\left(\frac{\tilde{\mu}_2^2}{\hat{s}}\right)^{2\nu_2}\Bigg[\frac{3}{8\epsilon^4}-\frac{1}{2\epsilon^3\nu_2}+\frac{21\zeta_2}{8\epsilon^2}+\frac{1}{\epsilon}\left(6\zeta_3-\frac{\zeta_2}{2\nu_2}\right)+\frac{\zeta_3}{3\nu_2}+\frac{1177\zeta_2^2}{80}\\ &+\frac{m^2}{\hat{s}}\left(\frac{1}{\epsilon}\left(\frac{2}{\nu_2}+7\right)-14\zeta_2+\frac{10}{\nu_2}+21\right)\Bigg]\end{aligned} \tag{D.6}$$

$$\begin{aligned}\mathcal{I}^X\Big|_{\bar{c}c} = &\left(\frac{\mu^2}{m^2}\right)^{2\epsilon}\left(\frac{\tilde{\mu}_1^2}{-m^2}\right)^{\nu_1}\left(\frac{\tilde{\mu}_1^2}{\hat{s}}\right)^{\nu_1}\left(\frac{\tilde{\mu}_2^2}{-m^2}\right)^{\nu_2}\left(\frac{\tilde{\mu}_2^2}{\hat{s}}\right)^{\nu_2}\Bigg[\frac{1}{4\epsilon^4}+\frac{1}{\epsilon^3}\left(\frac{1}{2\nu_2}+\frac{1}{2\nu_1}\right)\\ &+\frac{1}{\epsilon^2}\left(\frac{5\zeta_2}{4}-\frac{1}{\nu_1\nu_2}\right)+\frac{1}{\epsilon}\left(\frac{3\zeta_2}{2\nu_1}+\frac{3\zeta_2}{2\nu_2}+\frac{17\zeta_3}{6}\right)-\frac{\zeta_2}{\nu_1\nu_2}+\frac{14\zeta_3}{3\nu_1}+\frac{14\zeta_3}{3\nu_2}+\frac{279\zeta_2^2}{40}\\ &+\frac{m^2}{\hat{s}}\left(\frac{1}{\epsilon}\left(\frac{2}{\nu_2}+\frac{2}{\nu_1}+4\right)-4\zeta_2+\frac{2}{\nu_1}+\frac{2}{\nu_2}-4\right)\Bigg]\end{aligned} \tag{D.7}$$

---

[1] Note that we can safely limit ourselves to the Feynman integrals with $n_7 \leq 0$ as only these are needed in the computation of F_1 and F_2 for diagram (h).

$$\mathcal{I}^X\Big|_{hc}=\left(\frac{\mu^2}{-\hat{s}}\right)^{\epsilon}\left(\frac{\mu^2}{m^2}\right)^{\epsilon}\left[\frac{8}{3\epsilon^4}-\frac{8\zeta_2}{\epsilon^2}-\frac{316\zeta_3}{9\epsilon}-\frac{158\zeta_2^2}{5}+\frac{m^2}{\hat{s}}\left(\frac{-4}{3\epsilon^2}+\frac{4}{3\epsilon}+4\zeta_2-\frac{40}{3}\right)\right] \tag{D.8}$$

$$\mathcal{I}^X\Big|_{\bar{c}uc}=\left(\frac{\mu^2}{m^2}\right)^{\epsilon}\left(\frac{\mu^2\hat{s}^2}{m^6}\right)^{\epsilon}\left[\frac{-1}{24\epsilon^4}-\frac{5\zeta_2}{8\epsilon^2}-\frac{7\zeta_3}{18\epsilon}-\frac{493\zeta_2^2}{80}+\frac{m^2}{\hat{s}}\left(\frac{1}{3\epsilon^2}+\frac{5}{3\epsilon}+5\zeta_2+\frac{19}{3}\right)\right] \tag{D.9}$$

Note that the LP of $\mathcal{I}^X|_{hh}$ can be found in [147, 193]. By symmetry, we have

$$\mathcal{I}^X\Big|_{\bar{c}\bar{c}}=\mathcal{I}^X\Big|_{cc}(\nu_1\leftrightarrow\nu_2),\quad \mathcal{I}^X\Big|_{\bar{c}h}=\mathcal{I}^X\Big|_{hc},\quad \text{and}\quad \mathcal{I}^X\Big|_{\overline{uc}c}=\mathcal{I}^X\Big|_{\bar{c}uc}. \tag{D.10}$$

The second parameterisation of topology X, Eq. (7.9), gives two new regions: the cc'-region and the $\bar{c}\bar{c}'$-region. By defining[2]

$$\mathcal{I'}^X=\frac{1}{C}\,I'^{\nu_1,\nu_1,\nu_2,\nu_2}_{X;1,1,1,1,1,1,0}\,, \tag{D.11}$$

the NLP results of these two new regions read

$$\begin{aligned}\mathcal{I'}^X\Big|_{cc'}=&\left(\frac{\mu^2}{m^2}\right)^{2\epsilon}\left(\frac{\tilde{\mu}_1^2}{-m^2}\right)^{\nu_1}\left(\frac{\tilde{\mu}_1^2}{\hat{s}}\right)^{\nu_1}\left(\frac{\tilde{\mu}_2^2}{-m^2}\right)^{2\nu_2}\left[-\frac{29}{4\epsilon^4}+\frac{1}{\epsilon^3}\left(\frac{3}{\nu_2}+\frac{1}{2\nu_1}\right)\right.\\&+\frac{1}{\epsilon^2}\left(\frac{7\zeta_2}{4}-\frac{1}{\nu_2^2}\right)+\frac{1}{\epsilon}\left(\frac{\zeta_2}{2\nu_1}+\frac{83\zeta_3}{6}\right)-\frac{\zeta_2}{\nu_2^2}-\frac{\zeta_3}{3\nu_1}-\frac{7\zeta_3}{\nu_2}+\frac{473\zeta_2^2}{40}\\&\left.+\frac{m^2}{\hat{s}}\left(-\frac{3}{\epsilon^2}+\frac{1}{\epsilon}\left(-\frac{2}{\nu_1}-14\right)-\zeta_2-\frac{10}{\nu_1}-\frac{2}{\nu_2}-42\right)\right]\end{aligned} \tag{D.12}$$

$$\begin{aligned}\mathcal{I'}^X\Big|_{\bar{c}\bar{c}'}=&\left(\frac{\mu^2}{m^2}\right)^{2\epsilon}\left(\frac{\tilde{\mu}_2^2}{-m^2}\right)^{2\nu_1}\left(\frac{\tilde{\mu}_1^2}{-m^2}\right)^{\nu_2}\left(\frac{\tilde{\mu}_1^2}{\hat{s}}\right)^{\nu_2}\left[\frac{2}{\epsilon^4}+\frac{1}{\epsilon^3}\left(-\frac{3}{\nu_2}-\frac{1}{2\nu_1}\right)\right.\\&+\frac{1}{\epsilon^2}\left(3\zeta_2+\frac{1}{\nu_1\nu_2}+\frac{1}{\nu_2^2}\right)+\frac{1}{\epsilon}\left(-\frac{3\zeta_2}{2\nu_1}-\frac{\zeta_2}{\nu_2}+\frac{41\zeta_3}{3}\right)\\&+\frac{\zeta_2}{\nu_1\nu_2}+\frac{\zeta_2}{\nu_2^2}-\frac{14\zeta_3}{3\nu_1}+\frac{2\zeta_3}{\nu_2}+\frac{59\zeta_2^2}{10}\\&\left.+\frac{m^2}{\hat{s}}\left(\frac{4}{\epsilon^2}+\frac{1}{\epsilon}\left(-\frac{4}{\nu_2}-\frac{2}{\nu_1}-4\right)+2\zeta_2-\frac{2}{\nu_1}-\frac{10}{\nu_2}+2\right)\right].\end{aligned} \tag{D.13}$$

---

[2] Recall that the difference between $\mathcal{I'}^X$ and $\mathcal{I}^X$ only arises in the momentum region expansion. The unexpanded integrals are the same.

Finally, to get the full NLP result, two more regions are needed and can be found using the third parametersisation. Recalling Eq. (7.10), we define

$$\mathcal{I}''^{X} = \frac{1}{C}\, I''^{\nu_1,\nu_1,\nu_2,\nu_2}_{X;1,1,1,1,1,1,0}\,. \tag{D.14}$$

These last two missing momentum regions are the ch'' and $\bar{c}h''$ regions and their expressions are given by

$$\mathcal{I}''^{X}\Big|_{ch''} = \left(\frac{\mu^2}{m^2}\right)^{\epsilon}\left(\frac{\mu^2}{-\hat{s}}\right)^{\epsilon}\left[\frac{m^2}{\hat{s}}\left(\frac{2}{\epsilon^2}+2\right)\right], \tag{D.15}$$

and by symmetry

$$\mathcal{I}''^{X}\Big|_{\bar{c}h} = \mathcal{I}''^{X}\Big|_{ch''}\,. \tag{D.16}$$

Note that the ch'' and $\bar{c}h''$ regions do not contribute at LP.

For notational simplicity, we denote $\mathcal{I}^{X}\big|_{\bullet}$ as $\mathcal{I}^{X}_{\bullet}$ from now on. Combining all of the above 12 regions, we obtain the result of the integral Eq. (D.1) up to NLP. That is,

$$\begin{aligned}
&\mathcal{I}^{X}_{hh}+\mathcal{I}^{X}_{cc}+\mathcal{I}^{X}_{\bar{c}\bar{c}}+\mathcal{I}^{X}_{\bar{c}c}+\mathcal{I}^{X}_{hc}+\mathcal{I}^{X}_{\bar{c}h}+\mathcal{I}^{X}_{\bar{c}uc}+\mathcal{I}^{X}_{\overline{uc}c}+\mathcal{I}'^{X}_{cc'}+\mathcal{I}'^{X}_{\bar{c}\bar{c}'}+\mathcal{I}''^{X}_{ch''}+\mathcal{I}''^{X}_{\bar{c}h''}\\
&\quad=\left(\frac{\mu^2}{m^2}\right)^{2\epsilon}\left[-\frac{1}{\epsilon}\left(\frac{1}{3}L^3+\zeta_2 L+\zeta_3\right)-\frac{1}{2}L^4+\zeta_2L^2-\zeta_3L-\frac{37\zeta_2^2}{10}\right.\\
&\qquad\qquad\left.-\frac{m^2}{\hat{s}}\left(4L^2-8L+\frac{4\zeta_2}{3}\right)+\mathcal{O}(\nu_1,\nu_2,\epsilon)\right],
\end{aligned} \tag{D.17}$$

which is the same as Eq. (D.3). We notice that all rapidity divergences have canceled.

D.2. Regions in parameter space

To find all the above 12 regions for $\mathcal{I}^{X}$, we can also use the `Mathematica` package `Asy.m` [144, 145], which implements a geometric approach to reveal the relevant regions for a given Feynman integral and a given limit of momenta and masses. The program relies on the so-called alpha-representation of $\mathcal{I}^{X}$ in Eq. (D.1), which can be written in the following form

$$\mathcal{I}^{X} = C_1\int_0^{\infty}[dy](y_3y_4)^{\nu_1}(y_5y_6)^{\nu_2}A_3^{3\epsilon+2\nu_1+2\nu_2}\left(m^2A_1-s_{12}A_2-i\eta\right)^{-2-2\epsilon-2\nu_1-2\nu_2}, \tag{D.18}$$

where y_i are the so-called alpha parameters and

$$[dy] = \prod_{i=1}^{6} dy_i \delta(1 - y_1 - y_2 - y_3 - y_4 - y_5 - y_6)\,. \tag{D.19}$$

For notational convenience, we defined

$$C_1 = \frac{\hat{s}^2 \mu^{4\epsilon} \tilde{\mu}_1^{4\nu_1} \tilde{\mu}_2^{4\nu_2} e^{2\epsilon\gamma_E} e^{-2i(\nu_1+\nu_2)\pi} \Gamma(2 + 2\epsilon + 2\nu_1 + 2\nu_2)}{\Gamma^2(1+\nu_1)\Gamma^2(1+\nu_2)}\,, \tag{D.20}$$

and

$$\begin{aligned} A_1 =& y_4 y_5(y_4+y_5) + y_5 y_6(y_5+y_6) + y_3^2(y_5+y_6) + y_1(y_3+y_4)^2 + (y_2+y_3)(y_5+y_6)^2 \\ &+ y_3 y_4(y_4+y_5) + y_3 y_4(y_3+y_5) + y_1 y_6^2 + y_2 y_4^2\,, \\ A_2 =& y_1 y_6(y_3+y_4) + y_4 y_6(y_3+y_5) + y_2 y_4(y_5+y_6)\,, \\ A_3 =& y_5(y_4+y_6) + (y_2+y_3)(y_4+y_5+y_6) + y_1(y_2+y_3+y_4+y_6)\,. \end{aligned} \tag{D.21}$$

The package `Asy.m` formulates the expansion by regions of a Feynman integral by studying the scaling of each alpha-parameter y_i, as opposed to the method used in this thesis where we defined the regions by studying the scaling behaviour of loop momentum components. The two methods are closely related, as the scaling of each parameter y_i corresponds directly to the scale of the i-th denominator factor of the original Feynman integral. To find the possible scalings of the parameters y_i that lead to non-vanishing integrals, `Asy.m` uses a geometrical method based on convex hulls [144]. Using the package `Asy.m` for $\mathcal{I}^X$, we get 12 regions listed as

$$\begin{aligned} R =& \big(\{0,0,0,0,0,0\}, \{0,0,0,0,2,2\}, \{0,0,2,2,0,0\}, \{0,0,0,2,0,2\}, \{0,-4,-2,2,0,0\}, \\ & \{0,4,4,4,2,6\}, \{0,-2,-2,0,-2,-2\}, \{0,2,0,0,0,2\}, \{0,0,0,-2,0,0\}, \\ & \{0,0,0,0,0,-2\}, \{0,-2,-2,0,0,0\}, \{0,2,2,2,0,2\}\big)\,. \end{aligned} \tag{D.22}$$

The j-th region of $\mathcal{I}^X$ is now denoted by the vector R_j, which specifies the scales of the alpha parameters. To be precise, one scales $y_i \to y_i \lambda^{R_j^i}$ with $\lambda \ll 1$ and expands Eq. (D.18) around $\lambda = 0$. This yields the alpha representation of $\mathcal{I}^X$ in the j-th region which we denote as $\mathcal{I}_j^X$.

We have checked that the regions as listed by `Asy.m` lead to the same regions as we found in momentum space and listed in App. D.1. For simplicity, we only calculated the LP term of $\mathcal{I}_j^X$, except for $\mathcal{I}_9^X$ and $\mathcal{I}_{10}^X$ as these start at NLP. We find that $\mathcal{I}_1^X$-$\mathcal{I}_{12}^X$ are the same as $\mathcal{I}_{hh}^X$, $\mathcal{I}_{cc}^X$, $\mathcal{I}_{\bar{c}\bar{c}}^X$, $\mathcal{I}_{\bar{c}c}^X$, $\mathcal{I}_{\bar{c}uc}^X$, $\mathcal{I}_{u\bar{c}c}^X$, $\mathcal{I}'^X_{cc'}$, $\mathcal{I}'^X_{\bar{c}\bar{c}'}$, $\mathcal{I}''^X_{ch''}$, $\mathcal{I}''^X_{\bar{c}h''}$, $\mathcal{I}_{hc}^X$ and $\mathcal{I}_{\bar{c}h}^X$, respectively.

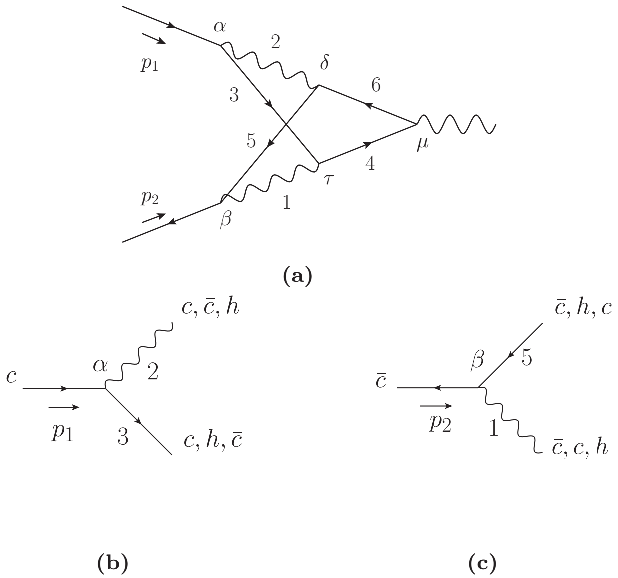

Figure D.1.: We show diagram (h) including labels for the vertices and propagators in Fig. D.1a. The vertices α and β are shown in Figs. D.1b and D.1c with possible momentum modes for each propagator when the loop momenta are regarded as (anti-)collinear.

D.3. Finding regions in momentum space

We finish this appendix by presenting a method that can be used to find all the regions in momentum space of a Feynman integral. In principle, we can use `Asy.m` to find the scale of each propagator in a given region and then obtain the corresponding modes of loop momenta. However, in our case, it is important to apply an independent cross-check to find the regions in momentum space. To illustrate our method, we focus again on the integral $\mathcal{I}^X$, Eq. (D.1), and use the collinear-type region – which means the loop momenta k_1 and k_2 are both collinear or anti-collinear – as an example.

Regardless of whether we perform expansion by region or not, the momentum flowing into a vertex of a Feynman diagram is conserved. We can use this fact to constrain the possible scales of the propagators connected to the same vertex. To make this precise, we labeled the vertices and propagators of $\mathcal{I}^X$ in Fig. D.1a. Vertex α, shown again in Fig. D.1b, includes three lines with one of them being the external fermion line with momentum p_1 which is regarded as the collinear momentum. At present, we only focus on the collinear-type regions such that the momentum of one of the remaining two lines should be collinear or anti-collinear. By momentum conservation, the momentum of the third line is now fixed. That is, if the photon line –

labeled by 2 – has momentum with collinear scaling, then by momentum conservation the fermion line – labeled by 3 – has also collinear momentum. However, if the photon line has anti-collinear scaling, then the momentum of the fermion line should be hard.[3] The only case left for the collinear-type region is when the fermion line has anti-collinear scaling, which leads to a hard momentum scaling for the photon line. In Fig. D.1c, all possibilities are listed for vertex β, which attaches to the fermion line with momentum p_2, regarded as the anti-collinear momentum.

We notice that once we determine the modes of the momenta that flow into the vertices α and β, the momentum scaling of every line in the diagram can be extracted.[4] As discussed above, the momenta of the lines labelled 2 and 3 can have the modes cc, $\bar{c}h$ and $h\bar{c}$ and the momenta of the lines labelled 1 and 5 can have modes $\bar{c}\bar{c}$, ch and hc. Naively, we have 9 different configurations after considering these two vertices. We divide these 9 configurations into 3 categories, which are given by

$$\begin{aligned} R_1^c &= (\bar{c}cc\bar{c}, \bar{c}\bar{c}h\bar{c}, ccch, c\bar{c}hh)\,, \\ R_2^c &= (\bar{c}h\bar{c}\bar{c}, hccc, hh\bar{c}c)\,, \\ R_3^c &= (ch\bar{c}h, h\bar{c}hc)\,. \end{aligned} \tag{D.23}$$

Each configuration, e.g. $\bar{c}cc\bar{c}$ in R_1^c, represents the momentum modes of the lines labelled 1, 2, 3 and 5 respectively. Note that the regions determined by the configurations in R_1^c can be given using the definition of Eq. (7.3), while those in R_2^c can be given using Eq. (7.9). We did not show the definitions of the propagators that can be used to give the configurations in R_3^c. The reason is that these two configurations in R_3^c only give scaleless integrals and hence do not contribute. It is also straightforward to check that the integrals in both configurations $c\bar{c}hh$ and $hh\bar{c}c$ are scaleless. Finally, we find 5 contributing configurations, $\bar{c}cc\bar{c}$, $\bar{c}\bar{c}h\bar{c}$, $ccch$, $\bar{c}h\bar{c}\bar{c}$ and $hccc$ which indeed correspond to the $\bar{c}c$, $\bar{c}\bar{c}$, cc, $\bar{c}\bar{c}'$ and cc' regions given in Sec. 7.3.3, respectively. In principle, one can also choose vertices α and μ or β and μ to analyze the possible collinear-type regions in topology X. However, we did not find any additional collinear-type regions that contributed up to NLP. The other regions in topology X, where the loop momenta have hard or ultra-(anti-)collinear scaling, can be found following a similar procedure.

---

[3] Notice that hard here and h in the following refer to the scaling $\sqrt{\hat{s}}(\lambda^0, \lambda^0, \lambda^1)$ as it is the sum of collinear, which scales as $\sqrt{\hat{s}}(\lambda^0, \lambda^2, \lambda^1)$, and anti-collinear, which scales as $\sqrt{\hat{s}}(\lambda^2, \lambda^0, \lambda^1)$. This is slightly different compared to the hard mode defined in Eq. (6.35).

[4] In fact, one can also pick the vertices α and μ or β and μ.

Bibliography

[1] E. Laenen, C. Marinissen and M. Vonk, *Resurgence analysis of the Adler function at $\mathcal{O}(1/N_f^2)$*, *JHEP* **09** (2023) 103 [`2302.13715`].

[2] J. ter Hoeve, E. Laenen, C. Marinissen, L. Vernazza and G. Wang, *Region analysis of QED massive fermion form factor*, *JHEP* **02** (2024) 024 [`2311.16215`].

[3] C. Marinissen, A. van Spaendonck and M. Vonk, *Resurgence of large order relations*, *Adv. Theor. Math. Phys.* **28** (2024) 2657 [`2312.12497`].

[4] R.v. Bijleveld, E. Laenen, C. Marinissen, L. Vernazza and G. Wang. To appear.

[5] C.B. Marinissen, R. Rahn and W.J. Waalewijn, *..., 83106786, 114382724, 1509048322, 2343463290, 27410087742, ... efficient Hilbert series for effective theories*, *Phys. Lett. B* **808** (2020) 135632 [`2004.09521`].

[6] S. Calò, C. Marinissen and R. Rahn, *Discrete symmetries and efficient counting of operators*, *JHEP* **05** (2023) 215 [`2212.04395`].

[7] L. Di Luzio, S. Hoof, C. Marinissen and V. Plakkot, *Catalogues of Cosmologically Self-Consistent Hadronic QCD Axion Models*, `2412.17896`.

[8] G. 't Hooft and M.J.G. Veltman, *Regularization and Renormalization of Gauge Fields*, *Nucl. Phys. B* **44** (1972) 189.

[9] J. Écalle, *Les fonctions resurgentes*, Publications mathématiques d'Orsay, Université de Paris-Sud. Departement de Mathématique (1985).

[10] E. Borel, *Mémoire sur les séries divergentes*, *Ann. Sc. ENS* **16** (1899) 9.

[11] G. 't Hooft, *Can we make sense out of Quantum Chromodynamics?*, *Subnucl. Ser.* **15** (1979) 943.

[12] C.M. Bender and T.T. Wu, *Anharmonic oscillator*, *Phys. Rev.* **184** (1969) 1231.

[13] C.M. Bender and T.T. Wu, *Anharmonic oscillator. 2: A Study of perturbation theory in large order*, *Phys. Rev. D* **7** (1973) 1620.

[14] G. Sterman, *Summation of large corrections to short distance hadronic cross-sections*, *Nucl. Phys.* **B281** (1987) 310.

[15] S. Catani and L. Trentadue, *Resummation of the QCD perturbative series for hard processes*, *Nucl. Phys.* **B327** (1989) 323.

[16] S. Catani and L. Trentadue, *Comment on qcd exponentiation at large x*, *Nucl. Phys.* **B353** (1991) 183.

[17] G.P. Korchemsky and G. Marchesini, *Structure function for large x and renormalization of wilson loop*, *Nucl. Phys.* **B406** (1993) 225 [`hep-ph/9210281`].

[18] G.P. Korchemsky and G. Marchesini, *Resummation of large infrared corrections using Wilson loops*, *Phys. Lett.* **B313** (1993) 433.

[19] C.W. Bauer, S. Fleming, D. Pirjol and I.W. Stewart, *An effective field theory for collinear and soft gluons: Heavy to light decays*, *Phys. Rev.* **D63** (2001)

114020 [`hep-ph/0011336`].

[20] C.W. Bauer, D. Pirjol and I.W. Stewart, *Soft collinear factorization in effective field theory*, *Phys. Rev. D* **65** (2002) 054022 [`hep-ph/0109045`].

[21] M. Beneke, A.P. Chapovsky, M. Diehl and T. Feldmann, *Soft collinear effective theory and heavy to light currents beyond leading power*, *Nucl. Phys. B* **643** (2002) 431 [`hep-ph/0206152`].

[22] V.V. Sudakov, *Vertex parts at very high-energies in quantum electrodynamics*, *Sov. Phys. JETP* **3** (1956) 65.

[23] J.C. Collins, *Sudakov form-factors*, *Adv.Ser.Direct.High Energy Phys.* **5** (1989) 573 [`hep-ph/0312336`].

[24] L.J. Dixon, L. Magnea and G.F. Sterman, *Universal structure of subleading infrared poles in gauge theory amplitudes*, *JHEP* **0808** (2008) 022 [`0805.3515`].

[25] E. Laenen, J. Sinninghe Damsté, L. Vernazza, W. Waalewijn and L. Zoppi, *Towards all-order factorization of QED amplitudes at next-to-leading power*, *Phys. Rev. D* **103** (2021) 034022 [`2008.01736`].

[26] S. Garoufalidis, A. Its, A. Kapaev and M. Mariño, *Asymptotics of the instantons of Painlevé I*, *Int. Math. Res. Not.* **2012** (2012) 561 [`1002.3634`].

[27] I. Aniceto, R. Schiappa and M. Vonk, *The resurgence of instantons in string theory*, *Commun. Num. Theor. Phys.* **6** (2012) 339 [`1106.5922`].

[28] S. Baldino, R. Schiappa, M. Schwick and R. Vega, *Resurgent Stokes Data for Painleve Equations and Two-Dimensional Quantum (Super) Gravity*, `2203.13726`.

[29] A. van Spaendonck and M. Vonk, *Painlevé I and exact WKB: Stokes phenomenon for two-parameter transseries*, *J. Phys. A* **55** (2022) 454003 [`2204.09062`].

[30] A. Voros, *The return of the quartic oscillator. The complex WKB method*, *Annales de l'I.H.P. Physique théorique* **39** (1983) 211.

[31] E. Delabaere and F. Pham, *Resurgent methods in semi-classical asymptotics*, *Annales de l'I.H.P. Physique théorique* **71** (1999) 1.

[32] J. Zinn-Justin and U.D. Jentschura, *Multi-instantons and exact results I: Conjectures, WKB expansions, and instanton interactions*, *Annals Phys.* **313** (2004) 197 [`quant-ph/0501136`].

[33] G.V. Dunne and M. Unsal, *Uniform WKB, Multi-instantons, and Resurgent Trans-Series*, *Phys. Rev. D* **89** (2014) 105009 [`1401.5202`].

[34] A. van Spaendonck and M. Vonk, *Exact instanton transseries for quantum mechanics*, `2309.05700`.

[35] G.V. Dunne and M. Unsal, *Resurgence and transseries in quantum field theory: the CP(N-1) Model*, *JHEP* **11** (2012) 170 [`1210.2423`].

[36] S. Gukov, M. Marino and P. Putrov, *Resurgence in complex Chern-Simons theory*, `1605.07615`.

[37] M. Mariño and T. Reis, *Renormalons in integrable field theories*, *JHEP* **04** (2020) 160 [`1909.12134`].

[38] L. Di Pietro, M. Mariño, G. Sberveglieri and M. Serone, *Resurgence and $1/N$ expansion in integrable field theories*, *JHEP* **10** (2021) 166 [`2108.02647`].

[39] M.P. Heller and M. Spaliński, *Hydrodynamics Beyond the Gradient Expansion: Resurgence and Resummation*, *Phys. Rev. Lett.* **115** (2015) 072501 [`1503.07514`].

[40] I. Aniceto and M. Spaliński, *Resurgence in Extended Hydrodynamics*, *Phys. Rev. D* **93** (2016) 085008 [`1511.06358`].

[41] P. Gregori and R. Schiappa, *From Minimal Strings towards Jackiw-Teitelboim Gravity: On their Resurgence, Resonance, and Black Holes*, `2108.11409`.

[42] B. Eynard, E. Garcia-Failde, P. Gregori, D. Lewanski and R. Schiappa, *Resurgent Asymptotics of Jackiw-Teitelboim Gravity and the Nonperturbative Topological Recursion*, `2305.16940`.

[43] M. Marino, R. Schiappa and M. Weiss, *Nonperturbative effects and the large-order behavior of matrix models and topological strings*, 2008.

[44] M. Marino, *Nonperturbative effects and nonperturbative definitions in matrix models and topological strings*, *JHEP* **12** (2008) 114 [`0805.3033`].

[45] R. Couso-Santamaría, J.D. Edelstein, R. Schiappa and M. Vonk, *Resurgent Transseries and the Holomorphic Anomaly*, *Annales Henri Poincare* **17** (2016) 331 [`1308.1695`].

[46] J. Gu, A.-K. Kashani-Poor, A. Klemm and M. Marino, *Non-perturbative topological string theory on compact Calabi-Yau 3-folds*, `2305.19916`.

[47] I. Aniceto, G. Basar and R. Schiappa, *A Primer on resurgent transseries and their asymptotics*, *Phys. Rept.* **809** (2019) 1 [`1802.10441`].

[48] M. Mariño, *Lectures on non-perturbative effects in large N gauge theories, matrix models and strings*, *Fortsch. Phys.* **62** (2014) 455 [`1206.6272`].

[49] D. Dorigoni, *An introduction to resurgence, transseries and alien calculus*, *Annals Phys.* **409** (2019) 167914 [`1411.3585`].

[50] D. Sauzin, *Introduction to 1-summability and resurgence*, 2014. https://arxiv.org/abs/1405.0356.

[51] G.G. Stokes, *On the numerical calculation of a class of definite integrals and infinite series*, in *Mathematical and Physical Papers*, vol. 2 of *Cambridge Library Collection - Mathematics*, p. 329–357, Cambridge University Press (2009), DOI.

[52] G.G. Stokes, *On the discontinuity of arbitrary constants which appear in divergent developments (1857)*, in *Mathematical and Physical Papers*, vol. 4 of *Cambridge Library Collection - Mathematics*, p. 77–109, Cambridge University Press (2009), DOI.

[53] G. Edgar, *Transseries for beginners*, *Real Analysis Exchange* **35** (2010) 253.

[54] M. Borinsky and D. Broadhurst, *Resonant resurgent asymptotics from quantum field theory*, *Nucl. Phys. B* **981** (2022) 115861 [`2202.01513`].

[55] C.M. Bender and S.A. Orszag, *Advanced mathematical methods for scientists and engineers*, McGraw-Hill (1978).

[56] L.F. Richardson, *The approximate arithmetical solution by sinite sifferences of physical problems involving differential equations, with an application to the stresses in a masonry dam*, *Philosophical Transactions of the Royal Society of London Series A* **210** (1911) 307.

[57] L.F. Richardson and J.A. Gaunt, *The deferred approach to the limit*, *Philosophical Transactions of the Royal Society of London Series A* **226** (1927) 299 .

[58] H. Padé, *Sur la représentation approchée d'une fonction par des fractions rationnelles*, *Annales scientifiques de l'École Normale Supérieure* **3e série, 9** (1892) 3.

[59] G. Frobenius, *Ueber relationen zwischen den näherungsbrüchen von potenzreihen*, *Journal für die reine und angewandte Mathematik* **90** (1881) 1.

[60] O. Costin and G.V. Dunne, *Physical Resurgent Extrapolation*, *Phys. Lett. B* **808** (2020) 135627 [`2003.07451`].

[61] O. Costin and G.V. Dunne, *Conformal and uniformizing maps in Borel analysis*, *Eur. Phys. J. ST* **230** (2021) 2679 [`2108.01145`].

[62] E. Brézin, G. Parisi and J. Zinn-Justin, *Perturbation theory at large orders for a potential with degenerate minima*, *Phys. Rev. D* **16** (1977) 408.

[63] S. Hikami and E. Brezin, *Large-order behaviour of the 1/n expansion in zero and one dimensions*, *Journal of Physics A: Mathematical and General* **12** (1979) 759.

[64] J.C. Le Guillou and J. Zinn-Justin, eds., *Large order behavior of perturbation theory*, North Holland, Amsterdam (1990).

[65] O. Costin and M.D. Kruskal, *On optimal truncation of divergent series solutions of nonlinear differential systems*, *Proceedings of the Royal Society of London. Series A: Mathematical, Physical and Engineering Sciences* **455** (1999) 1931–1956.

[66] S. Garoufalidis and M. Marino, *Universality and asymptotics of graph counting problems in nonorientable surfaces*, 2009.

[67] J. Écalle and S. Sharma, *Power series with sum-product Taylor coefficients and their resurgence algebra*, in *Asymptotics in dynamics, geometry and PDEs. Generalized Borel summation. Vol. I. Proceedings of the conference, CRM, Pisa, Italy, October 12–16, 2009*, pp. 35–200, Pisa: Edizioni della Normale (2011).

[68] C. Mitschi and D. Sauzin, *Divergent series, summability and resurgence, I: Monodromy and resurgence*, Springer, Switzerland (2016), https://doi.org/10.1007/978-3-319-28736-2.

[69] D. Sauzin, *Large order asymptotics on an example*, 2020, unpublished – private communication.

[70] S. Garoufalidis, J. Gu and M. Marino, *Peacock patterns and resurgence in complex Chern-Simons theory*, `2012.00062`.

[71] I. Aniceto, G. Başar and R. Schiappa, *A primer on resurgent transseries and their asymptotics*, *Physics Reports* **809** (2019) 1.

[72] "*NIST Digital Library of Mathematical Functions: Combinatorial Analysis - Set Partitions: Stirling Numbers*." `https://dlmf.nist.gov/26.8`, Release 1.1.11 of 2023-09-15.

[73] Y. Takei, *Wkb analysis and stokes geometry of differential equations*, pp. 263–304 (2017), DOI.

[74] C. Howls, P. Langman and A. Olde Daalhuis, *On the Higher-Order Stokes Phenomenon*, *Proceedings: Mathematical, Physical and Engineering Sciences* **460** (2004) 2285–.

[75] D.J. Gross and A. Neveu, *Dynamical symmetry breaking in asymptotically free field theories*, *Phys. Rev. D* **10** (1974) 3235.

[76] B.E. Lautrup, *On high order estimates in QED*, *Phys. Lett. B* **69** (1977) 109.

[77] S.L. Adler, *Some simple vacuum-polarization phenomenology: $e^+e^- \to$ hadrons; the muonic-atom x-ray discrepancy and $g_\mu - 2$*, *Phys. Rev. D* **10** (1974) 3714.

[78] P. Argyres and M. Unsal, *A semiclassical realization of infrared renormalons*, *Phys. Rev. Lett.* **109** (2012) 121601 [`1204.1661`].

[79] P.C. Argyres and M. Unsal, *The semi-classical expansion and resurgence in gauge theories: new perturbative, instanton, bion, and renormalon effects*, *JHEP* **08** (2012) 063 [`1206.1890`].

[80] G.V. Dunne and M. Ünsal, *Continuity and Resurgence: towards a continuum definition of the $\mathbb{CP}$(N-1) model*, *Phys. Rev. D* **87** (2013) 025015 [`1210.3646`].

[81] M. Shifman, *Infrared renormalons in supersymmetric theories*, *Phys. Rev. D* **107** (2023) 045002 [`2211.05090`].

[82] T. Reis, *On the resurgence of renormalons in integrable theories*, Ph.D. thesis, U. Geneva (main), 2022. `2209.15386`.

[83] M. Beneke, *Renormalons*, *Phys. Rept.* **317** (1999) 1 [`hep-ph/9807443`].

[84] M. Shifman, *New and old about renormalons: in Memoriam Kolya Uraltsev*, *Int. J. Mod. Phys. A* **30** (2015) 1543001 [`1310.1966`].

[85] M. Beneke, *Large order perturbation theory for a physical quantity*, *Nucl. Phys. B* **405** (1993) 424.

[86] D.J. Broadhurst, *Large N expansion of QED: Asymptotic photon propagator and contributions to the muon anomaly, for any number of loops*, *Z. Phys. C* **58** (1993) 339.

[87] M. Neubert, *Scale setting in QCD and the momentum flow in Feynman diagrams*, *Phys. Rev. D* **51** (1995) 5924 [`hep-ph/9412265`].

[88] A.H. Mueller, *On the structure of infrared renormalons in physical processes at high-energies*, *Nucl. Phys. B* **250** (1985) 327.

[89] G. Parisi, *Singularities of the Borel transform in renormalizable theories*, *Phys. Lett. B* **76** (1978) 65.

[90] D.J. Broadhurst and A.G. Grozin, *Matching QCD and HQET heavy - light currents at two loops and beyond*, *Phys. Rev. D* **52** (1995) 4082 [`hep-ph/9410240`].

[91] P. Ball, M. Beneke and V.M. Braun, *Resummation of $(\beta_0\alpha_s)^n$ corrections in QCD: techniques and applications to the tau hadronic width and the heavy quark pole mass*, *Nucl. Phys. B* **452** (1995) 563 [`hep-ph/9502300`].

[92] M. Beneke and V.M. Braun, *Naive non-Abelianization and resummation of fermion bubble chains*, *Phys. Lett. B* **348** (1995) 513 [`hep-ph/9411229`].

[93] G.V. Dunne and M. Ünsal, *Generating nonperturbative physics from perturbation theory*, *Phys. Rev. D* **89** (2014) 041701 [`1306.4405`].

[94] I. Krichever and N. Nekrasov, *Towards Lefschetz Thimbles in sigma models, I*, *J. Exp. Theor. Phys.* **132** (2021) 734 [`2010.15575`].

[95] M. Beneke, *Renormalization scheme invariant large order perturbation theory and infrared renormalons in QCD*, *Phys. Lett. B* **307** (1993) 154.

[96] D.J. Broadhurst and A.L. Kataev, *Connections between deep inelastic and annihilation processes at next to next-to-leading order and beyond*, *Phys. Lett. B* **315** (1993) 179 [`hep-ph/9308274`].

[97] A.I. Vainshtein and V.I. Zakharov, *Ultraviolet renormalon calculus*, *Phys. Rev. Lett.* **73** (1994) 1207 [`hep-ph/9404248`].

[98] M. Beneke and V.A. Smirnov, *Ultraviolet renormalons in Abelian gauge theories*, *Nucl. Phys. B* **472** (1996) 529 [`hep-ph/9510437`].

[99] S. Peris and E. de Rafael, *Low-energy QCD and ultraviolet renormalons*, *Nucl. Phys. B* **500** (1997) 325 [`hep-ph/9701418`].

[100] G. Parisi, *On infrared divergences*, *Nucl. Phys. B* **150** (1979) 163.

[101] G. Cvetič, *Renormalon-motivated evaluation of QCD observables*, *Phys. Rev. D* **99** (2019) 014028 [`1812.01580`].

[102] C. Ayala, G. Cvetic and D. Teca, *Determination of perturbative QCD coupling from ALEPH τ decay data using pinched Borel–Laplace and Finite Energy Sum Rules*, *Eur. Phys. J. C* **81** (2021) 930 [`2105.00356`].

[103] C. Ayala, G. Cvetic and D. Teca, *Borel-Laplace Sum Rules with τ decay data, using OPE with improved anomalous dimensions*, `2206.05631`.

[104] D. Boito, P. Masjuan and F. Oliani, *Higher-order QCD corrections to hadronic τ decays from Padé approximants*, *JHEP* **08** (2018) 075 [`1807.01567`].

[105] I. Caprini, *Conformal mapping of the Borel plane: going beyond perturbative QCD*, *Phys. Rev. D* **102** (2020) 054017 [`2006.16605`].

[106] E. Cavalcanti, *Renormalons beyond the Borel plane*, *Phys. Rev. D* **103** (2021) 025019 [`2011.11175`].

[107] A. Maiezza and J.C. Vasquez, *Resurgence of the QCD Adler function*, *Phys. Lett. B* **817** (2021) 136338 [`2104.03095`].

[108] A. Maiezza and J.C. Vasquez, *The QCD Adler function and the muon $g-2$ anomaly from renormalons*, *Symmetry* **14** (2022) 1878 [`2111.06792`].

[109] A. Maiezza and J.C. Vasquez, *Non-local Lagrangians from renormalons and analyzable functions*, *Annals Phys.* **407** (2019) 78 [`1902.05847`].

[110] J. Bersini, A. Maiezza and J.C. Vasquez, *Resurgence of the renormalization group equation*, *Annals Phys.* **415** (2020) 168126 [`1910.14507`].

[111] M. Marino, R. Miravitllas and T. Reis, *New renormalons from analytic trans-series*, *JHEP* **08** (2022) 279 [`2111.11951`].

[112] S.V. Mikhailov and N.I. Volchanskiy, *Renormalon-Chain Contributions to Two-Point Correlators of Nonlocal Quark Currents*, *Phys. Part. Nucl. Lett.* **20** (2023) 296 [`2301.01806`].

[113] J. Gu and M. Marino, *On the resurgent structure of quantum periods*, `2211.03871`.

[114] M. Marino, R. Miravitllas and T. Reis, *On the structure of trans-series in quantum field theory*, `2302.08363`.

[115] C. Kozçaz, T. Sulejmanpasic, Y. Tanizaki and M. Ünsal, *Cheshire Cat resurgence, self-resurgence and Quasi-Exact Solvable Systems*, *Commun. Math. Phys.* **364** (2018) 835 [`1609.06198`].

[116] N.A. Dondi, G.V. Dunne, M. Reichert and F. Sannino, *Towards the QED beta function and renormalons at $1/N_f^2$ and $1/N_f^3$*, *Phys. Rev. D* **102** (2020) 035005 [`2003.08397`].

[117] J. Blumlein, D.J. Broadhurst and J.A.M. Vermaseren, *The Multiple Zeta Value data mine*, *Comput. Phys. Commun.* **181** (2010) 582 [`0907.2557`].

[118] J. Fuster, C. Marinissen and M. Vonk. To appear.

[119] H. Gervais, *Soft photon theorem for high energy amplitudes in Yukawa and scalar theories*, *Phys. Rev.* **D95** (2017) 125009 [`1704.00806`].

[120] J.-w. Qiu and G.F. Sterman, *Power corrections in hadronic scattering. 1. Leading 1/Q**2 corrections to the Drell-Yan cross-section*, *Nucl. Phys. B* **353** (1991) 105.

[121] J.-w. Qiu and G.F. Sterman, *Power corrections to hadronic scattering. 2. Factorization*, *Nucl. Phys. B* **353** (1991) 137.

[122] L.D. Landau, *On analytic properties of vertex parts in quantum field theory*, *Nucl. Phys.* **13** (1959) 181.

[123] S. Coleman and R.E. Norton, *Singularities in the physical region*, *Nuovo Cim.* **38** (1965) 438.

[124] W. Bernreuther, R. Bonciani, T. Gehrmann, R. Heinesch, T. Leineweber, P. Mastrolia et al., *Two-loop QCD corrections to the heavy quark form-factors: The Vector contributions*, *Nucl. Phys. B* **706** (2005) 245 [`hep-ph/0406046`].

[125] J. Ablinger, A. Behring, J. Blümlein, G. Falcioni, A. De Freitas, P. Marquard et al., *Heavy quark form factors at two loops*, *Phys. Rev. D* **97** (2018) 094022 [`1712.09889`].

[126] M. Beneke and V.A. Smirnov, *Asymptotic expansion of Feynman integrals near threshold*, *Nucl. Phys.* **B522** (1998) 321 [`hep-ph/9711391`].

[127] V.A. Smirnov, *Applied asymptotic expansions in momenta and masses*, *Springer Tracts Mod. Phys.* **177** (2002) 1.

[128] B. Jantzen, *Foundation and generalization of the expansion by regions*, *JHEP* **1112** (2011) 076 [`1111.2589`].

[129] D. Bonocore, E. Laenen, L. Magnea, L. Vernazza and C.D. White, *The method of regions and next-to-soft corrections in Drell-Yan production*, *Phys. Lett.* **B742** (2015) 375 [`1410.6406`].

[130] N. Bahjat-Abbas, J. Sinninghe Damsté, L. Vernazza and C.D. White, *On next-to-leading power threshold corrections in Drell-Yan production at N^3LO*, *JHEP* **1810** (2018) 144 [`1807.09246`].

[131] A.V. Manohar and I.W. Stewart, *The Zero-Bin and Mode Factorization in Quantum Field Theory*, *Phys. Rev. D* **76** (2007) 074002 [`hep-ph/0605001`].

[132] J. Gluza, A. Mitov, S. Moch and T. Riemann, *The QCD form factor of heavy quarks at NNLO*, *JHEP* **07** (2009) 001 [`0905.1137`].

[133] J.M. Henn, A.V. Smirnov and V.A. Smirnov, *Analytic results for planar three-loop integrals for massive form factors*, *JHEP* **12** (2016) 144 [`1611.06523`].

[134] J. Henn, A.V. Smirnov, V.A. Smirnov and M. Steinhauser, *Massive three-loop form factor in the planar limit*, *JHEP* **01** (2017) 074 [`1611.07535`].

[135] R.N. Lee, A.V. Smirnov, V.A. Smirnov and M. Steinhauser, *Three-loop massive form factors: complete light-fermion corrections for the vector current*, *JHEP* **03** (2018) 136 [`1801.08151`].

[136] R.N. Lee, A.V. Smirnov, V.A. Smirnov and M. Steinhauser, *Three-loop massive form factors: complete light-fermion and large-N_c corrections for vector, axial-vector, scalar and pseudo-scalar currents*, *JHEP* **05** (2018) 187 [`1804.07310`].

[137] J. Ablinger, J. Blümlein, P. Marquard, N. Rana and C. Schneider, *Heavy quark form factors at three loops in the planar limit*, *Phys. Lett. B* **782** (2018) 528 [`1804.07313`].

[138] J. Blümlein, P. Marquard and N. Rana, *Asymptotic behavior of the heavy quark form factors at higher order*, *Phys. Rev. D* **99** (2019) 016013 [`1810.08943`].

[139] J. Blümlein, P. Marquard, N. Rana and C. Schneider, *The Heavy Fermion Contributions to the Massive Three Loop Form Factors*, *Nucl. Phys. B* **949** (2019) 114751 [`1908.00357`].

[140] M. Fael, F. Lange, K. Schönwald and M. Steinhauser, *Massive Vector Form Factors to Three Loops*, *Phys. Rev. Lett.* **128** (2022) 172003 [`2202.05276`].

[141] M. Fael, F. Lange, K. Schönwald and M. Steinhauser, *Singlet and nonsinglet three-loop massive form factors*, *Phys. Rev. D* **106** (2022) 034029 [`2207.00027`].

[142] M. Fael, F. Lange, K. Schönwald and M. Steinhauser, *Massive three-loop form factors: Anomaly contribution*, *Phys. Rev. D* **107** (2023) 094017 [`2302.00693`].

[143] J. Blümlein, A. De Freitas, P. Marquard, N. Rana and C. Schneider, *Analytic results on the massive three-loop form factors: Quarkonic contributions*, *Phys. Rev. D* **108** (2023) 094003 [`2307.02983`].

[144] A. Pak and A. Smirnov, *Geometric approach to asymptotic expansion of Feynman integrals*, *Eur.Phys.J.* **C71** (2011) 1626 [`1011.4863`].

[145] B. Jantzen, A.V. Smirnov and V.A. Smirnov, *Expansion by regions: revealing potential and Glauber regions automatically*, *Eur. Phys. J.* **C72** (2012) 2139 [`1206.0546`].

[146] E. Gardi, F. Herzog, S. Jones, Y. Ma and J. Schlenk, *The on-shell expansion: from Landau equations to the Newton polytope*, *JHEP* **07** (2023) 197 [`2211.14845`].

[147] V.A. Smirnov and E.R. Rakhmetov, *The Strategy of regions for asymptotic expansion of two loop vertex Feynman diagrams*, *Theor. Math. Phys.* **120** (1999) 870 [`hep-ph/9812529`].

[148] V.A. Smirnov, *Problems of the strategy of regions*, *Phys. Lett. B* **465** (1999) 226 [`hep-ph/9907471`].

[149] T. Becher and K. Melnikov, *Two-loop QED corrections to Bhabha scattering*, *JHEP* **06** (2007) 084 [`0704.3582`].

[150] C. Studerus, *Reduze-Feynman Integral Reduction in C++*, *Comput. Phys. Commun.* **181** (2010) 1293 [`0912.2546`].

[151] W.H. Furry, *A symmetry theorem in the positron theory*, *Phys. Rev.* **51** (1937) 125.

[152] J. Collins, *Foundations of Perturbative QCD*, Cambridge Monographs on Particle Physics, Nuclear Physics and Cosmology, Cambridge University Press (2023), 10.1017/9781009401845.

[153] M.G. Echevarria, A. Idilbi and I. Scimemi, *Factorization Theorem For Drell-Yan At Low q_T And Transverse Momentum Distributions On-The-Light-Cone*, *JHEP* **07** (2012) 002 [`1111.4996`].

[154] M.G. Echevarría, A. Idilbi and I. Scimemi, *Soft and Collinear Factorization and Transverse Momentum Dependent Parton Distribution Functions*, *Phys. Lett. B* **726** (2013) 795 [`1211.1947`].

[155] M.G. Echevarria, I. Scimemi and A. Vladimirov, *Transverse momentum dependent fragmentation function at next–to–next–to–leading order*, *Phys. Rev. D* **93** (2016) 011502 [`1509.06392`].

[156] M.G. Echevarria, I. Scimemi and A. Vladimirov, *Universal transverse momentum dependent soft function at NNLO*, *Phys. Rev. D* **93** (2016) 054004 [`1511.05590`].

[157] M.G. Echevarria, I. Scimemi and A. Vladimirov, *Unpolarized Transverse Momentum Dependent Parton Distribution and Fragmentation Functions at next-to-next-to-leading order*, *JHEP* **09** (2016) 004 [`1604.07869`].

[158] J.-y. Chiu, A. Jain, D. Neill and I.Z. Rothstein, *The Rapidity Renormalization Group*, *Phys. Rev. Lett.* **108** (2012) 151601 [`1104.0881`].

[159] J.-Y. Chiu, A. Jain, D. Neill and I.Z. Rothstein, *A Formalism for the Systematic Treatment of Rapidity Logarithms in Quantum Field Theory*, *JHEP* **05** (2012) 084 [`1202.0814`].

[160] Y. Li, D. Neill and H.X. Zhu, *An exponential regulator for rapidity divergences*, *Nucl. Phys. B* **960** (2020) 115193 [`1604.00392`].

[161] M. Beneke and T. Feldmann, *Factorization of heavy to light form-factors in soft collinear effective theory*, *Nucl. Phys. B* **685** (2004) 249 [`hep-ph/0311335`].

[162] J.-y. Chiu, F. Golf, R. Kelley and A.V. Manohar, *Electroweak Sudakov corrections using effective field theory*, *Phys. Rev. Lett.* **100** (2008) 021802 [`0709.2377`].

[163] T. Becher and M. Neubert, *Drell-Yan Production at Small q_T, Transverse Parton Distributions and the Collinear Anomaly*, *Eur. Phys. J. C* **71** (2011) 1665 [`1007.4005`].

[164] T. Becher and G. Bell, *Analytic Regularization in Soft-Collinear Effective Theory*, *Phys. Lett. B* **713** (2012) 41 [`1112.3907`].

[165] M.A. Ebert, I. Moult, I.W. Stewart, F.J. Tackmann, G. Vita and H.X. Zhu, *Subleading power rapidity divergences and power corrections for q_T*, *JHEP* **04** (2019) 123 [`1812.08189`].

[166] J. Klappert, F. Lange, P. Maierhöfer and J. Usovitsch, *Integral reduction with Kira 2.0 and finite field methods*, *Comput. Phys. Commun.* **266** (2021) 108024 [`2008.06494`].

[167] R.N. Lee, *LiteRed 1.4: a powerful tool for reduction of multiloop integrals*, *J. Phys. Conf. Ser.* **523** (2014) 012059 [`1310.1145`].

[168] R. Bonciani, P. Mastrolia and E. Remiddi, *QED vertex form-factors at two loops*, *Nucl. Phys. B* **676** (2004) 399 [`hep-ph/0307295`].

[169] J.-y. Chiu, F. Golf, R. Kelley and A.V. Manohar, *Electroweak Corrections in High Energy Processes using Effective Field Theory*, *Phys. Rev. D* **77** (2008) 053004 [`0712.0396`].

[170] R. Bonciani, P. Mastrolia and E. Remiddi, *Vertex diagrams for the QED form-factors at the two loop level*, *Nucl. Phys. B* **661** (2003) 289 [`hep-ph/0301170`].

[171] D. Maitre, *HPL, a mathematica implementation of the harmonic polylogarithms*, *Comput. Phys. Commun.* **174** (2006) 222 [`hep-ph/0507152`].

[172] D. Maitre, *Extension of HPL to complex arguments*, *Comput. Phys. Commun.* **183** (2012) 846 [`hep-ph/0703052`].

[173] S. Moch, J. Vermaseren and A. Vogt, *The Quark form-factor at higher orders*, *JHEP* **0508** (2005) 049 [`hep-ph/0507039`].

[174] T. Gehrmann, E.W.N. Glover, T. Huber, N. Ikizlerli and C. Studerus, *Calculation of the quark and gluon form factors to three loops in QCD*, *JHEP* **06** (2010) 094 [`1004.3653`].

[175] V. Pilipp, *Semi-numerical power expansion of Feynman integrals*, *JHEP* **09** (2008) 135 [`0808.2555`].

[176] T.Y. Semenova, A.V. Smirnov and V.A. Smirnov, *On the status of expansion by regions*, *Eur. Phys. J. C* **79** (2019) 136 [`1809.04325`].

[177] B. Ananthanarayan, A. Pal, S. Ramanan and R. Sarkar, *Unveiling Regions in multi-scale Feynman Integrals using Singularities and Power Geometry*, *Eur. Phys. J. C* **79** (2019) 57 [`1810.06270`].

[178] G. Heinrich, S. Jahn, S.P. Jones, M. Kerner, F. Langer, V. Magerya et al., *Expansion by regions with pySecDec*, *Comput. Phys. Commun.* **273** (2022) 108267 [`2108.10807`].

[179] M. Beneke, M. Garny, R. Szafron and J. Wang, *Anomalous dimension of subleading-power N-jet operators*, *JHEP* **03** (2018) 001 [`1712.04416`].

[180] C. Anastasiou and K. Melnikov, *Higgs boson production at hadron colliders in nnlo qcd*, *Nucl. Phys.* **B646** (2002) 220 [`hep-ph/0207004`].

[181] S.E. Jaskiewicz, *Factorization and Resummation at Subleading Powers*, Ph.D. thesis, Munich, Tech. U., Munich, Tech. U., 5, 2021.

[182] I. Bierenbaum and S. Weinzierl, *The massless two loop two point function*, *Eur. Phys. J. C* **32** (2003) 67 [`hep-ph/0308311`].

[183] A.G. Grozin, *Massless two-loop self-energy diagram: historical review*, *Int. J. Mod. Phys. A* **27** (2012) 1230018 [`1206.2572`].

[184] D.I. Kazakov, *Multiloop calculations: method of uniqueness and functional equations*, *Teor. Mat. Fiz.* **62** (1984) 127.

[185] A.V. Kotikov, *The Gegenbauer polynomial technique: The Evaluation of a class of Feynman diagrams*, *Phys. Lett. B* **375** (1996) 240 [`hep-ph/9512270`].

[186] D.J. Broadhurst, J.A. Gracey and D. Kreimer, *Beyond the triangle and uniqueness relations: Nonzeta counterterms at large N from positive knots*, *Z. Phys. C* **75** (1997) 559 [`hep-th/9607174`].

[187] J.A.M. Vermaseren, *Harmonic sums, Mellin transforms and integrals*, *Int. J. Mod. Phys. A* **14** (1999) 2037 [`hep-ph/9806280`].

[188] J.A.M. Vermaseren, *New features of FORM*, `math-ph/0010025`.

[189] B. Ruijl, T. Ueda and J. Vermaseren, *FORM version 4.2*, `1707.06453`.

[190] J.M. Borwein, D.M. Bradley, D.J. Broadhurst and P. Lisonek, *Special values of multiple polylogarithms*, 1999.

[191] S. Gritschacher, A. Hoang, I. Jemos and P. Pietrulewicz, *Two loop soft function for secondary massive quarks*, *Phys. Rev. D* **89** (2014) 014035 [`1309.6251`].

[192] J.-y. Chiu, A. Fuhrer, A.H. Hoang, R. Kelley and A.V. Manohar, *Soft-Collinear Factorization and Zero-Bin Subtractions*, *Phys. Rev. D* **79** (2009) 053007 [`0901.1332`].

[193] R.J. Gonsalves, *Dimensionally regularized two-loop on-shell quark form factor*, *Phys. Rev. D* **28** (1983) 1542.

Samenvatting

Fundamentele natuurkunde richt zich op het begrijpen van de fundamentele wetten van de natuur. Binnen de deeltjesfysica heeft deze zoektocht geleid tot een krachtige theorie, genaamd het Standaardmodel. Dit model beschrijft de kleinste deeltjes van materie – bekend als elementaire deeltjes – die alles om ons heen vormen, van atomen tot sterrenstelsels. Het Standaardmodel is meer dan alleen een opsomming van deeltjes; het verklaart ook hoe deze deeltjes met elkaar interacteren. Het maken van voorspellingen op basis van deze interacties is echter buitengewoon complex.

Om dit te vereenvoudigen, gebruiken natuurkundigen een methode genaamd *storingsrekening* – ook wel *perturbatietheorie* genoemd. Deze methode begint met een eenvoudiger systeem en voegt kleine correcties toe om complexere interacties mee te nemen. Deze correcties vormen een reeks waarmee voorspellingen steeds nauwkeuriger kunnen worden gemaakt.

Ondanks het succes van storingsrekening in de natuurkunde, heeft deze methode een groot probleem: het leidt vaak tot wiskundige oneindigheden die voorspellingen onmogelijk maken. Een van deze problemen, bekend als ultraviolet-oneindigheden, wordt aangepakt via een proces genaamd renormalisatie. Dit proces verwijdert de oneindigheden door de parameters van de onderliggende theorie aan te passen. Maar zelfs na renormalisatie groeit de storingsreeks op een manier die het verkrijgen van nauwkeurige resultaten bemoeilijkt. De reeks gaat zich gedragen als een divergente, *asymptotische reeks*, waarbij de eerste termen de nauwkeurigheid verbeteren, maar latere termen de nauwkeurigheid juist weer verminderen.

Dit probleem betekent niet dat storingsrekening nutteloos is. Wiskundigen hebben een methode ontwikkeld genaamd *resurgence*, waarmee dergelijke asymptotische reeksen kunnen worden omgezet in zinvolle functies. Resurgence laat zien dat de storingsreeks alleen niet genoeg is, er ontbreken zogenoemde *niet-perturbatieve* effecten. Dit zijn effecten die niet beschreven kunnen worden door de gebruikelijke storingsreeks, maar wel cruciale informatie over het systeem bevatten.

In het eerste deel van dit proefschrift, hoofdstuk 2-5, onderzoeken we zowel formele aspecten van resurgence als ook de praktische toepassingen ervan: *renormalons*. Renormalons zijn niet-perturbatieve effecten die voorkomen in theorieën zoals het Standaardmodel en worden vaak *power corrections* genoemd.

Om te beginnen, in hoofdstuk 2 en 3, bestuderen we zogenoemde *grote-orde-relaties* met behulp van resurgence. Deze grote-orde-relaties laten zien hoe in de divergente storingsreeks niet-perturbatieve effecten verborgen zitten. Bovendien laten we zien hoe deze niet-perturbative effecten uit de storingsreeks gedestilleerd kunnen worden. Dit maakt het een belangrijk hulpmiddel voor natuurkundigen, aangezien zij vaak alleen een directe manier hebben om de storingsreeks te berekenen, en geen andere eenvoudige manier voor de niet-perturbatieve effecten.

In hoofdstuk 4 en 5 passen we deze methoden vervolgens toe om renormalons te bestuderen. Met behulp van resurgence kunnen we de berekeningen van renormalon effecten – effecten die vaak worden genegeerd – vereenvoudigen. We passen deze technieken toe op de Adler-functie – een belangrijke functie in de deeltjesfysica – en onderzoeken hoe renormalons hierop van invloed zijn. Door resurgence methoden te gebruiken, kunnen we een nauwkeurige formule opstellen die deze niet-perturbatieve renormalon effecten beschrijft.

In het tweede deel van dit proefschrift verschuift de focus naar een ander type power correction door gebruik te maken van *factorisatie*. Factorisatie is een methode die een complex proces – waarbij verschillende fysische schalen betrokken zijn – opsplitst in eenvoudigere delen, die van een enkele schaal afhangen en afzonderlijk kunnen worden berekend. Deze techniek is cruciaal voor het begrijpen van het gedrag van deeltjes in hoogenergetische botsingen, zoals die in deeltjesversnellers.

In hoofdstuk 6-8 passen we factorisatie toe op een verstrooiingsproces waarbij een foton vervalt in twee deeltjes met een relatief kleine massa. Met behulp van een techniek genaamd *expansie in momentumregio's* laten we zien hoe de factorisatieformule voor dit proces op verschillende niveaus van precisie kan worden geverifieerd. Op leidende orde van precisie, ook wel de *leading power* correctie genoemd, laten we zien hoe de berekening van deze correcties kan worden opgesplitst in een procesafhankelijk deel, het zogenoemde *harde deel*, en in universele functies genaamd *jet functies*. Het harde deel in factorisatie beschrijft de interactie op korte afstand waarbij de fundamentele deeltjes met elkaar botsen. Een jet functie beschrijft hoe een hoogenergetisch deeltje, geproduceerd in een botsing, zich ontwikkelt tot een smalle bundel van deeltjes, een *jet*. Omdat jet functies universeel zijn, kunnen ze in veel verschillende berekeningen opnieuw worden gebruikt en hoeven ze slechts één keer te worden uitgerekend. Om de precisie verder te verhogen, onderzoeken we ook de *next-to-leading power* correcties. In het bijzonder laten we zien hoe nieuwe jet functies kunnen worden gedefinieerd om deze next-to-leading power correcties nauwkeurig te beschrijven.

Kort samengevat gaat het onderzoek gepresenteerd in dit proefschrift over het concept van "power corrections" – vandaar de titel van deze thesis – die ons kunnen helpen de interacties tussen elementaire deeltjes beter te begrijpen en bovendien nauwkeuriger te beschrijven. Dit gebeurt vanuit twee invalshoeken. Allereerst kijken we naar power correcties die voortkomen uit niet-perturbatieve effecten, zoals in het geval van renormalons. Vervolgens bestuderen we power correcties in berekeningen waarbij meerdere fysische schalen betrokken zijn. Deze twee onderwerpen worden respectievelijk benaderd met behulp van de methoden van resurgence en factorisatie.

Summary

Fundamental physics focuses on understanding the fundamental laws of nature, and in the realm of particle physics, this quest has led to a powerful theory called the Standard Model. This model describes the smallest particles of matter – known as elementary particles – which make up everything around us, from atoms to galaxies. The Standard Model does more than list particles; it also explains how these particles interact. However, making predictions based on these interactions is extremely complex.

To make things easier, physicists use a method called *perturbation theory*, which simplifies the problem by starting with a simpler system and adding small corrections to account for more complex interactions. These corrections form a series that allows predictions to be made more precisely.

Despite its success in all areas of physics, perturbation theory faces a significant problem: it often leads to mathematical infinities that make predictions impossible. One of these issues, known as ultraviolet infinities, is handled through a process called renormalization. This process removes the infinities by adjusting the parameters of the underlying theory. However, even after renormalization, the mathematical series still grows out of control in a way that makes it difficult to get accurate results. The series begins to behave like a divergent, *asymptotic series*, where early terms improve the accuracy, but later terms on the other hand worsen the accuracy.

This challenge does not mean that perturbation theory is useless. In fact, mathematicians have developed a way to turn these divergent series into meaningful functions through a method called *resurgence*. Resurgence indicates that the perturbative series is not enough, there are *non-perturbative* effects missing. These effects cannot be described by the usual perturbative series, but can provide crucial information about the system.

In the first part of this thesis, chapters 2-5, we explore formal aspects of resurgence as well as one of the more practical applications of resurgence: *renormalons*. Renormalons are non-perturbative effects that appear in theories like the Standard Model and are often referred to as *power corrections*.

First, in chapters 2 and 3, we study so-called *large-order relations* with resurgence. These large-order relations show how in the divergent perturbative series, non-perturbative effects are hidden. In particular, we show how these non-perturbative effects can be obtained using the perturbative series alone. This makes it a valuable tool for physicists, as they often only have a way to calculate the perturbative series, and no direct simple way to calculate the non-perturbative effects.

Then, these methods are applied to study renormalons in chapters 4 and 5. Using resurgence, we are able to simplify how we calculate renormalon effects, which are parts of calculations that often get ignored. We apply these techniques to the Adler function, a key quantity in particle physics, and look at how renormalons affect it. By using resurgence methods, we are able to build an accurate formula that describes these non-perturbative renormalon effects.

The second part of the thesis shifts focus to another type of power correction in particle physics using factorization. Factorization is a method that separates a complex process – in which multiple physical scales are involved – into simpler parts, each of which depend on a single scale and can be calculated independently. This technique is crucial for understanding the behavior of particles in high-energy collisions, such as those in particle accelerators.

In chapters 6-8, we apply factorization to the study of a scattering process in which a photon decays into a pair of particles with a relatively small mass. Using a tool called *expansion by momentum regions*, we show how the factorization formula for this process can be verified at different levels of precision. At leading order of precission, also called the *leading power* correction, we show how the calculation of these corrections can be factorized into a process dependent part, the so-called *hard part*, and into universal functions called *jet functions*. The hard part in factorization represents the short-distance, high-energy interaction where the fundamental particles scatter off each other. A jet function describes how a highly energetic particle, produced in a collision, transforms into a narrow spray of particles called a jet. Furthermore, being universal, the jet functions can be reused for many different processes and therefore only need to be calculated once. To go even further, and increase the precision, we also explore the *next-to-leading power* corrections. In particular, we show how new jet functions can be defined to accurately describe the next-to-leading power corrections.

In summary, this thesis explores the idea of "power corrections" – hence the title of this thesis – which help in our understanding of particle interactions and describe their behavior more accurately. First, it delves into power corrections that come from non-perturbative effects, like renormalons, and second, it examines power corrections in calculations that involve multiple physical scales. These two topics are approached using methods known as resurgence and factorization respectively.

Dankwoord

Allereerst wil ik graag mijn beide begeleiders, Eric en Marcel, bedanken voor hun advies en enthousiaste begeleiding gedurende de afgelopen jaren. De vrijheid en het vertrouwen dat jullie mij gaven hebben een onmisbare rol gespeeld in mijn ontwikkeling tot zelfstandig onderzoeker. Ik kan dan ook niet anders zeggen dan dat ik onze samenwerking als zeer plezierig heb ervaren.

I would also like to thank the members of my dissertation committee, Miranda Cheng, Wouter Waalewijn, Jordy de Vries, Thomas Grimm and Leonardo Vernazza for their time and effort reading this somewhat long thesis (I admit, I could have kept it shorter).

Nikhef has been an amazing place to work. The theory group has always been an active and stimulating environment where I immediately felt at home. I am particularly happy that I can stay for two more years as a postdoc. I would like to thank all current and past members of the Nikhef theory group: Robin, Pieter, Jelle, Max, Peter, Giacomo, Jaco, Heleen, Vaisakh, Anders, Tommaso, Lemonia, Avanish, Sachin, Guanghui, Maximilian, Ankita, Lukás, Juraj, Philipp, Johannes Maria, Tanjona, Tomasso, Andrea, Rudi, Michael, Robert, Melissa, Marieke, Juan, Jordy and Wouter. Van de emiriti wil ik in het bijzonder Jos bedanken. Ik heb altijd genoten van uw bezoekjes aan Nikhef en kijk ernaar uit om in de toekomst nauwer samen te werken.

I would also like to express my gratitude to my collaborators, without whom this thesis may never have seen the light of day. Leonardo and Guoxing, I truly enjoyed working with you and fondly remember our countless enthusiastic discussions, where we tackled many problems and formulated new interesting questions. A special thanks to Rudi – you were already in the acknowledgements for my master thesis, and you certainly deserve a place here as well. Your enthousiasm is boundless (not just for physics, but for almost everything, it seems) and it was therefore great to supervise Simon together – also a big thanks to you, Simon. I also want to thank the other (former) master students I had the pleasure to work with: Paul, Jaime, Boudewijn and Nicolo.

Alexander, ondanks dat we op twee verschillende plekken ons kantoor hadden, was ik altijd ontzettend blij dat er nog iemand in Amsterdam aan resurgence werkte. We wisten elkaar altijd te vinden als het nodig was en ik koester warme herinneringen aan onze eindeloze discussies op Nikhef, de UvA en het CWI, onze tripjes naar onder andere de ARA workshop en de momenten dat we samen gewoon even een koffie deden.

Van samen inlevers maken tot zelfs het schrijven van een paper – Jaco, ik heb genoten van alle momenten samen sinds de master. Ondanks de grotere fysieke afstand ben ik blij dat onze vriendschap verder gaat en ik kijk er nu al naar uit om samen (een deel van) de North Coast 500 te gaan fietsen.

Robin en Max, jullie zijn de afgelopen jaren goede vrienden geworden. Naast inhoudelijke goede discussies hebben we denk ik voornamelijk veel lol gehad, met onze roadtrip naar Freiburg als een van de hoogtepunten. Ik hoop dat er nog veel meer van zulke avonturen volgen.

Ik wil graag mijn dierbare vrienden bedanken. Zowel diegenen met wie ik de fascinatie voor natuurkunde heb kunnen delen gedurende onze studie, waaronder TP-boys Maarten en Miguel, als diegenen waarbij ik ook even natuurkunde kon vergeten. Jullie hebben altijd geholpen een juiste balans te behouden tussen werk en ontspanning en boden steun wanneer dat nodig was.

Ook mijn (schoon)familie wil ik bedanken voor hun interesse in mijn vakgebied. Het uitleggen van mijn onderzoek in grote lijnen bleek telkens een bron van hernieuwd enthousiasme. In het bijzonder hebben natuurlijk mijn ouders hier aan bijgedragen, wiens liefde, betrokkenheid en vertrouwen het fundament vormen onder dit proefschrift.

Bovenal wil ik Jette en Kalle bedanken. Jette, ik had het nooit zonder jouw steun en eindeloze geduld kunnen doen. En Kalle, ondanks dat je mij ook soms een slapeloze nacht opleverde, ben je een groot onderdeel geworden van mijn promotietraject – met als fysiek bewijs de omslag van dit proefschrift.

Coenraad Marinissen
Amersfoort, Maart 2025